# VIIRS – A New Operational Cloud Imager

by

Keith D. Hutchison[1] and Arthur P. Cracknell[2]

[1] Center for Space Research
The University of Texas at Austin
3925 W. Braker Lane, Suite 200
Austin, Texas
USA

[2] Division of Electronic Engineering and Physics
University of Dundee
Dundee DD1 4HN
Scotland, UK

Deleted: epartment

# Table of Contents


**TABLE OF CONTENTS** ..... **II**

**LIST OF TABLES** ..... **VI**

**LIST OF FIGURES** ..... **VIII**

**LIST OF FIGURES** ..... **VIII**

**SUN GLINT** ..... **XI**

**PREFACE** ..... **XII**

**PREFACE** ..... **XII**

**CHAPTER 1** ..... **15**

**INTRODUCTION** ..... **15**

**SATELLITE METEOROLOGY** ..... **15**

1.1 OVERVIEW OF NUMERICAL WEATHER PREDICTION MODELING ..... 15
1.2 EVOLUTION OF OBSERVATIONAL DATA FOR NWP MODELING ..... 16
1.3 ADDITIONAL APPLICATIONS OF METEOROLOGICAL SATELLITE DATA ..... 21
*1.3.1 Sea Surface Temperature Analyses* ..... *22*
*1.3.2 Climate Modeling* ..... *26*
*1.3.3 Tropical Storm Monitoring* ..... *28*
*1.3.4 Satellite-Derived Wind Fields* ..... *30*

**CHAPTER 2** ..... **33**

**METEOROLOGICAL SATELLITE SYSTEMS** ..... **33**

2.1 EVOLUTION OF SATELLITES AND SENSORS ..... 33
*2.1.1 Polar-Orbiting Environmental Satellite (POES) Systems* ..... *34*
2.1.1.1 The Advanced TIROS-N (ATN) Satellite Series ..... 36
2.1.1.2 Defense Meteorological Satellite Program (DMSP) ..... 40
2.1.1.3 NASA Earth Observing System (EOS) Program ..... 47
2.1.1.4 Other Polar-Orbiting Meteorological Satellite Systems ..... 51
2.1.1.5 The Proposed Eumetsat MetOp Series ..... 53


**Deleted:** *22*
**Deleted:** *27*
**Deleted:** *29*
**Deleted:** *31*

*2.1.2 Geostationary Meteorological Satellite Systems* ..... *56*
2.2 THE NATIONAL POLAR-ORBITING OPERATIONAL ENVIRONMENTAL SATELLITE SYSTEM (NPOESS) ..... 60

**CHAPTER 3** ..... **65**

**VIIRS IMAGERY DESIGN ANALYSIS** ..... **65**

3.1 VIIRS EDR REQUIREMENTS OVERVIEW ..... 65
3.2 VIIRS IMAGERY REQUIREMENTS ..... 66
3.3 CLOUD APPLICATIONS-RELATED IMAGERY REQUIREMENTS ..... 68
*3.3.1 Cloud Cover* ..... *69*
*3.3.2 Cloud Type* ..... *70*
3.4 VALUE OF MANUALLY-GENERATED CLOUD ANALYSES ..... 71
*3.4.1 Performance Verification of Automated Cloud Models* ..... *71*
*3.4.2 Quality Control of Automated Cloud Analyses* ..... *72*

**CHAPTER 4** ..... **76**

**VIIRS IMAGERY REQUIREMENTS ANALYSIS** ..... **76**

4.1 THEORETICAL BASIS FOR MANUAL CLOUD ANALYSES ..... 76
4.2 OVERVIEW OF APPROACH TO INSTRUMENT DESIGN ..... 79
4.3 CLOUD TRUTH DATA SETS TO FLOWDOWN SENSOR REQUIREMENTS ..... 82
*4.3.1 Cloud Truth from Manual Interpretation of Multispectral Imagery* ..... *83*
*4.3.2 Cloud Truth in Simulated Imagery* ..... *86*
4.4 DERIVATION OF SENSING REQUIREMENTS FROM ANALYSIS REQUIREMENTS ..... 88
4.5 OVERVIEW OF VIIRS HARDWARE DESIGN ..... 98
*4.5.1 VIIRS Sensor Overview* ..... *98*
*4.5.2 Detailed VIIRS Design Capabilities* ..... *101*
4.5.2.1 VIIRS Spectral Design Requirements ..... 102
4.5.2.2 VIIRS Spatial Capabilities ..... 103
4.5.2.3 VIIRS Horizontal Sampling Interval ..... 104
4.5.2.4 VIIRS Dynamic Range Capability ..... 107
4.5.2.5 VIIRS Sensitivity Capability ..... 108
4.5.2.6 VIIRS Sensor Polarization Sensitivity ..... 109
4.5.2.7 Detector Performance ..... 110
4.5.2.8 Band to Band Registration or Co-registraton ..... 112
4.5.2.9 VIIRS Calibration ..... 114
4.5.2.9.1 VIIRS Absolute Radiometric Calibration – Uniform Scene ..... 114
4.5.2.9.2 VIIRS Relative Radiometric Calibration – Uniform Scene ..... 115
4.5.2.9.3 VIIRS Relative Radiometric Calibration – Structure Scene ..... 115

**CHAPTER 5** ..... **117**

**PRINCIPLES IN IMAGE INTERPRETATION** ..... **117**

5.1. INTRODUCTION ..... 117
5.2. VIIRS IMAGERY DATA ..... 120
*5.2.1. VIIRS Imagery Band I1 (0.64 ± 0.040 μm)* ..... *122*
*5.2.2. VIIRS I2 Band (0.865 ± 0.020 μm)* ..... *125*
*5.2.3. VIIRS I3 and M10 Bands (1.61 ± 0.03 μm)* ..... *128*
*5.2.5. VIIRS I5 Band (11.45 ± 0.95 μm)* ..... *147*
*5.2.6. VIIRS Day Night Band (DNB)* ..... *152*
5.3. VIIRS IMAGERY ASSIST DATA ..... 155

**Deleted:** 86
**Deleted:** 86
**Deleted:** *86*
**Deleted:** *86*
**Deleted:** 86
**Deleted:** 86
**Deleted:** 86
**Deleted:** 86
**Deleted:** 86
**Deleted:** 86
**Deleted:** 86
**Deleted:** 86
**Deleted:** 86
**Deleted:** 86
**Deleted:** 86
**Deleted:** 86
**Deleted:** 86
**Deleted:** 86
**Deleted:** 86
**Deleted:** *86*
**Deleted:** *86*
**Deleted:** *86*
**Deleted:** *86*
**Deleted:** 86

*5.3.1. VIIRS M1 – M4 Bands (0.412 ± 0.010 μm, 0.445 ± 0.009 μm, 0.488 ± 0.010 μm, 0.555 ± 0.010 μm)* ..... *156*
*5.3.2. VIIRS M9 Band (1.378 ± 0.0075 μm)* ..... *159*

**CHAPTER 6** ..... **163**

**MULTICOLOR COMPOSITES OF MULTISPECTRAL IMAGERY** ..... **163**

6.1. INTRODUCTION ..... 163
6.2. COLOR COMPOSITES OF (0.64μM, 0.865μM, AND 12.0 μM) SURFACE VEGETATION AND CLOUD CLASSIFICATIONS ..... 165
6.3 COLOR COMPOSITES (3.7 μM ALBEDO, 0.865μM, 12.0 μM) FOR SNOW DETECTION ..... 167
6.4. COLOR COMPOSITES OF (0.64 μM, 0.64μM, 3.7μM ALBEDO) SNOW MAPPING THROUGH THIN CIRRUS CLOUDS ..... 169
6.5. COLOR COMPOSITES OF (0.412 μM, 0.865 μM, AND 0.64 μM) CLOUDS OVER ARID REGIONS ..... 171

**CHAPTER 7** ..... **173**

**CASE STUDIES IN THE USE OF MULTICOLOR COMPOSITES FOR SCENE INTERPRETATION** ..... **173**

7.1 OVERVIEW ..... 173
7.2 MAS DATA OVER ALASKA ..... 174
*COLOR COMPOSITE #1: IDENTIFICATION OF VEGETATED SURFACES* ..... *176*
*COLOR COMPOSITE #2: IDENTIFICATION OF SNOW AND ICE FEATURES* ..... *178*
*COLOR COMPOSITE #3: CLOUD TYPE CLASSIFICATION – PART I* ..... *180*
*COLOR COMPOSITE #4: CLOUD TYPE CLASSIFICATION – PART II* ..... *183*
7.3 MAS SUCCESS DATA COLLECTED OVER COLORADO ..... 185
*COLOR COMPOSITE #1: IDENTIFICATION OF VEGETATED SURFACES* ..... *187*
*COLOR COMPOSITE #2: IDENTIFICATION OF SNOW AND ICE FEATURES* ..... *189*
*Color Composite #3: CLOUD TYPE CLASSIFICATION – PART I* ..... *191*
*Color Composite #4: CLOUD TYPE CLASSIFICATION – PART II* ..... *194*

**CHAPTER 8** ..... **197**

**AUTOMATED 3-DIMENSIONAL CLOUD ANALYSES FROM NPOESS** ..... **197**

8.1 ARCHITECTURE FOR 3-DIMENSIONAL CLOUD ANALYSES ..... 197
8.2 AUTOMATED CLOUD DETECTION ..... 199
*8.2.1 Single Channel Cloud Detection Algorithms* ..... *200*
*8.2.2 Multispectral Channel Cloud Detection Algorithms* ..... *200*
*8.2.3 Spatial Cloud Classifier Algorithms* ..... *203*
8.3 CLOUD TOP PHASE CLASSIFICATIONS ..... 204
8.4 CLOUD OPTICAL (THICKNESS AND PARTICLE SIZE) PROPERTIES ..... 209
*8.4.1 Retrieval for Water Clouds During Daytime Conditions* ..... *209*
*8.4.2 Retrieval for Ice Clouds Microphysical Properties* ..... *213*
8.4.2.1 Retrieval of Ice Cloud Properties in Daytime Imagery ..... 214
8.4.2.2 Retrieval of Ice Cloud Properties in Nighttime Imagery ..... 215
8.5 CLOUD TOP (TEMPERATURE, PRESSURE, AND HEIGHT) PARAMETERS ..... 218
8.6 CLOUD BASE HEIGHTS ..... 219
*8.6.1 Cloud base heights retrieved for water clouds* ..... *219*
*8.6.2 Cloud base heights retrieved for ice clouds* ..... *220*
*8.6.3 Ancillary Data and Products from Other Sensors* ..... *220*
*8.6.4 Integration of VIIRS, CMIS, and Conventional Cloud Base Observations* ..... *221*

**Deleted:** *86*
**Deleted:** *86*
**Deleted:** **86**
**Deleted:** **86**
**Deleted:** 86
**Deleted:** 86
**Deleted:** 86
**Deleted:** 86
**Deleted:** 86
**Deleted:** **86**
**Deleted:** **86**
**Deleted:** 86
**Deleted:** 86
**Deleted:** *86*
**Deleted:** *86*
**Deleted:** *86*
**Deleted:** *86*
**Deleted:** 86
**Deleted:** *86*
**Deleted:** *86*
**Deleted:** *86*
**Deleted:** *86*
**Deleted:** **86**
**Deleted:** **86**
**Deleted:** 86
**Deleted:** 86
**Deleted:** *86*
**Deleted:** *86*
**Deleted:** 86
**Deleted:** 86
**Deleted:** 86
**Deleted:** *86*
**Deleted:** 86
**Deleted:** 86
**Deleted:** 86
**Deleted:** 86
**Deleted:** 86
**Deleted:** *86*
**Deleted:** *86*
**Deleted:** *86*
**Deleted:** *86*
**Deleted:** *86*

**REFERENCES** ..... 224

Deleted: 86

Deleted: **TABLE OF CONTENTS** II¶
**LIST OF TABLES** VIII¶
**LIST OF FIGURES** XI¶
**LIST OF FIGURES** XI¶
**PREFACE** XX¶
**PREFACE** XX¶
**CHAPTER 1** 23¶
**INTRODUCTION** 23¶
**SATELLITE METEOROLOGY** 23¶
1.1 OVERVIEW OF NUMERICAL WEATHER PREDICTION MODELING 23¶
1.2 EVOLUTION OF OBSERVATIONAL DATA FOR NWP MODELING 24¶
1.3 ADDITIONAL APPLICATIONS OF METEOROLOGICAL SATELLITE DATA 30¶
*1.3.1 Sea Surface Temperature Analyses* 30¶
*1.3.2 Climate Modeling* 35¶
*1.3.3 Tropical Storm Monitoring* 37¶
*1.3.4 Satellite-Derived Wind Fields* 39¶
**CHAPTER 2** 42¶
**METEOROLOGICAL SATELLITE SYSTEMS** 42¶
2.1 EVOLUTION OF SATELLITES AND SENSORS 42¶
*2.1.1 Polar-Orbiting Environmental Satellite (POES) Systems* 43¶
2.1.1.1 The Advanced TIROS-N (ATN) Satellite Series 45¶
2.1.1.2 Defense Meteorological Satellite Program (DMSP) 49¶
2.1.1.3 NASA Earth Observing System (EOS) Program 52¶
2.1.1.4 Other Polar-Orbiting Meteorological Satellite Systems 52¶
2.1.1.5 The Proposed Eumetsat MetOp Series 52¶
*2.1.2 Geostationary Meteorological Satellite Systems* 52¶
2.2 THE NATIONAL POLAR-ORBITING OPERATIONAL ENVIRONMENTAL SATELLITE SYSTEM (NPOESS) 52¶
**CHAPTER 3** 52¶
**VIIRS IMAGERY DESIGN** ... [1]

Deleted: **TABLE OF CONTENTS** II¶
**LIST OF TABLES** VI¶
**LIST OF FIGURES** VIII¶
**LIST OF FIGURES** VIII¶
**PREFACE** XIII¶
**PREFACE** XIII¶
**CHAPTER 1** 16¶
**INTRODUCTION** 16¶
**SATELLITE METEOROLOGY** 16¶
1.1 OVERVIEW OF NUMERICAL WEATHER PREDICTION MODELING 16¶
1.2 EVOLUTION OF OBSERVATIONAL DATA FOR NWP MODELING 17¶
1.3 ADDITIONAL APPLICATIONS OF METEOROLOGICAL SATELLITE DATA 23¶
*1.3.1 Sea Surface Temperature Analyses* 23¶
*1.3.2 Climate Modeling* 28¶
*1.3.3 Tropical Storm Monitoring* 30¶
*1.3.4 Satellite-Derived Wind Fields* 31¶
**CHAPTER 2** 34¶
**METEOROLOGICAL SATELL** ... [2]

# List of Tables


TABLE 1.1 GUAM DMSP TROPICAL CYCLONE POSITION STATISTICS FOR 1972. ..... 29
TABLE 2.1 – OVERVIEW OF THE US CIVILIAN POLAR METEOROLOGICAL PROGRAMS (KRAMER 2002). ..... 35
TABLE 2.2 – SPECTRAL BAND WAVELENGTHS OF THE AVHRR . ..... 39
TABLE 2.3 CHRONOLOGICAL OVERVIEW OF DMSP SERIES SATELLITES. ..... 43
TABLE 2.4 COMPARISON OF TWO SENSORS – NOAA AVHRR/2 AND DMSP/OLS (KRAMER 2002). ..... 46
TABLE 2.5 BAND CHARACTERISTICS FOR MODIS DATA PRODUCTS (NASA MODIS WEBSITE). ..... 48
TABLE 2.6 MODIS DATA PRODUCTS ACCORDING TO APPLICATION CLASS. ..... 50
TABLE 2.7 - OVERVIEW OF POLAR-ORBITING METEOROLOGICAL SATELLITE SERIES (KRAMER 2002). ..... 52
TABLE 2.8 OVERVIEW OF METOP-1 PAYLOAD COMPLIMENT (KRAMER 2002). ..... 55
TABLE 2.9 OVERVIEW OF GEOSTATIONARY METEOROLOGICAL SATELLITES (KRAMER 2002). ..... 57
TABLE 3.1 ATTRIBUTE REQUIREMENTS FOR EACH VIIRS BAND CLASSIFIED AS IMAGERY. ..... 67
TABLE 3.2. NPOESS REQUIREMENTS FOR MANUALLY-GENERATED CLOUD COVER EDR. ..... 70
TABLE 3.3. NPOESS REQUIREMENTS FOR MANUALLY-GENERATED CLOUD TYPE EDR. ..... 70
TABLE 4.1. COMPARISONS OF MANUALLY-GENERATED CLOUD MASK AND SIMULATION BINARY CLOUD MASK FOR SYNTHETIC VIIRS IMAGERY SHOWN IN FIGURE 4.7. ..... 88
TABLE 4.2. VIIRS IMAGERY CHANNELS NEEDED TO SATISFY EACH NPOESS VIIRS REQUIREMENT FOR MANUALLY-GENERATED CLOUD COVER AND CLOUD TYPE EDRS. ..... 95
TABLE 4.3. VIIRS IMAGERY AND IMAGERY ASSIST BAND SELECTED TO SATISFY NPOESS REQUIREMENTS. ..... 96
TABLE 4.4 VIIRS SPECTRAL BAND OPTICAL REQUIREMENTS. ..... 102
TABLE 4.5 OPTICALLY BLURRED IFOV REQUIREMENTS. ..... 104
TABLE 4.6 MODERATE RESOLUTION BAND MTF REQUIREMENTS ..... 105
TABLE 4.7. CROSS-TRACK AGGREGATION FACTORS. ..... 106
TABLE 4.8. HSI REQUIREMENTS FOR SINGLE-GAIN MODERATE RESOLUTION BANDS. ..... 106
TABLE 4.9 HSI REQUIREMENTS FOR DUAL-GAIN MODERATE RESOLUTION BANDS. ..... 107
TABLE 4.10 HSI REQUIREMENTS FOR IMAGING BANDS ..... 107
THE DYNAMIC RANGE OF THE VIIRS REFLECTIVE AND EMISSIVE BANDS IS SHOWN IN TABLES 4.17 AND 4.18. ..... 107
TABLE 4.11 DYNAMIC RANGE REQUIREMENTS FOR VIIRS SENSOR REFLECTIVE BANDS. ..... 107
TABLE 4.12 DYNAMIC RANGE REQUIREMENTS FOR VIIRS SENSOR EMISSIVE BANDS. ..... 108
TABLE 4.13 SENSITIVITY REQUIREMENTS FOR VIIRS SENSOR REFLECTIVE BANDS. ..... 108
TABLE 4.14 SENSITIVITY REQUIREMENTS FOR VIIRS SENSOR EMISSIVE BANDS. ..... 109
TABLE 4.15 POLARIZATION SENSITIVITY REQUIREMENTS. ..... 110
TABLE 4.16 VIIRS DETECTOR NEΦ REQUIREMENTS. ..... 111
TABLE 4.17 BANDS AND DETECTORS DEFINED ..... 112
TABLE 4.18 ABSOLUTE RADIOMETRIC CALIBRATION UNCERTAINTY OF SPECTRAL RADIANCE FOR MODERATE RESOLUTION EMISSIVE BANDS. ..... 115
TABLE 4.19 RADIOMETRIC CALIBRATION UNCERTAINTY FOR IMAGING EMISSIVE BANDS. ..... 115
TABLE 4.20 RADIOMETRIC CALIBRATION UNCERTAINTY FOR DAY/NIGHT BAND ..... 115
TABLE 4.21 STRUCTURED SCENE REQUIREMENTS. ..... 116
TABLE 5.1. BANDPASSES OF INSTRUMENTS THAT APPROXIMATE VIIRS IMAGERY RESOLUTION BANDS. ..... 120
TABLE 5.2. BANDPASSES OF SENSORS THAT CLOSELY APPROXIMATE VIIRS MODERATE RESOLUTION BANDS. ..... 155
TABLE 7.1. FEATURE DETECTION AND IDENTIFICATION BASED UPON INTERPRETATION OF FIGURE 7.1. ..... 177
TABLE 7.2. FEATURE DETECTION AND IDENTIFICATION BASED UPON INTERPRETATION OF FIGURE 7.3. ..... 179
TABLE 7.3. FEATURE DETECTION AND IDENTIFICATION BASED UPON INTERPRETATION OF FIGURE 7.4. ..... 182
TABLE 7.4. FEATURE DETECTION AND IDENTIFICATION BASED UPON INTERPRETATION OF FIGURE 7.5. ..... 184
TABLE 7.5. FEATURE DETECTION AND IDENTIFICATION BASED UPON INTERPRETATION OF FIGURE 7.7. ..... 188
TABLE 7.6. FEATURE DETECTION AND IDENTIFICATION BASED UPON INTERPRETATION OF FIGURE 7.8. ..... 190
TABLE 7.7. FEATURE DETECTION AND IDENTIFICATION BASED UPON INTERPRETATION OF FIGURE 7.9. ..... 193
TABLE 7.8. FEATURE DETECTION AND IDENTIFICATION BASED UPON INTERPRETATION OF FIGURE 7.10. ..... 195
TABLE 8.1 FREQUENCY OF OCCURRENCE OF CLOUD TYPES FROM CURRENT MODIS ALGORITHMS AND THOSE DEVELOPED BY PAVOLONIS AND HEIDINGER (2004) FOR 8-DAY PERIOD. ..... 207


**Deleted:** 30
**Deleted:** 86
**Deleted:** 86
**Deleted:** 86
**Deleted:** 86
**Deleted:** 86
**Deleted:** 86
**Deleted:** 86
**Deleted:** 86
**Deleted:** 86
**Deleted:** 86
**Deleted:** 86
**Deleted:** 86
**Deleted:** 86
**Deleted:** 86
**Deleted:** 86
**Deleted:** 86
**Deleted:** 86
**Deleted:** 86
**Deleted:** 86
**Deleted:** 86
**Deleted:** 86
**Deleted:** 86
**Deleted:** 86
**Deleted:** 86
**Deleted:** 86
**Deleted:** 86
**Deleted:** 86
**Deleted:** 86
**Deleted:** 86
**Deleted:** 86
**Deleted:** 86
**Deleted:** 86
**Deleted:** 86

TABLE 8.2. PREDICTED CLOUD THICKNESS FOR EXPECTED OPTICAL DEPTHS, (10 FOR ICE AND 64 FOR WATER CLOUDS) WHICH MIGHT BE RETRIEVED FROM MODIS IMAGERY..... 221
TABLE 8.3 CHARACTERISTICS OF CLOUD BASE HEIGHT OBSERVATIONS..... 222

**Deleted:** 86

**Deleted:** 86

**Deleted:** TABLE 1.1 GUAM DMSP TROPICAL CYCLONE POSITION STATISTICS FOR 1972. 38¶
TABLE 2.1 – OVERVIEW OF THE US CIVILIAN POLAR METEOROLOGICAL PROGRAMS (KRAMER 2002). 44¶
TABLE 2.2 – SPECTRAL CHANNEL WAVELENGTHS OF THE AVHRR . 48¶
TABLE 2.3 CHRONOLOGICAL OVERVIEW OF DMSP SERIES SATELLITES. 52¶
TABLE 2.4 COMPARISON OF TWO SENSORS – NOAA AVHRR/2 AND DMSP/OLS (KRAMER 2002). 52¶
TABLE 2.5 BAND CHARACTERISTICS FOR MODIS DATA PRODUCTS (NASA MODIS WEBSITE). 52¶
TABLE 2.6 MODIS DATA PRODUCTS ACCORDING TO APPLICATION CLASS. 52¶
TABLE 2.7 - OVERVIEW OF POLAR-ORBITING METEOROLOGICAL SATELLITE SERIES (KRAMER 2002). 52¶
TABLE 2.8 OVERVIEW OF METOP-1 PAYLOAD COMPLIMENT (KRAMER 2002). 52¶
TABLE 2.9 OVERVIEW OF GEOSTATIONARY METEOROLOGICAL SATELLITES (KRAMER 2002). 52¶
TABLE 3.1 ATTRIBUTE REQUIREMENTS FOR EACH VIIRS BAND CLASSIFIED AS IMAGERY. 52¶
TABLE 3.2. NPOESS REQUIREMENTS FOR MANUALLY-GENERATED CLOUD COVER EDR. 52¶
TABLE 3.3. NPOESS REQUIREMENTS FOR MANUALLY-GENERATED CLOUD TYPE EDR. 52¶
TABLE 4.1. COMPARISONS OF MANUALLY-GENERATED CLOUD MASK AND SIMULATION BINARY CLOUD MASK FOR SYNTHETIC VIIRS IMAGERY SHOWN IN FIGURE 4.7. 52¶
TABLE 4.2. VIIRS IMAGERY BANDS NEEDED TO SATISFY EACH NPOESS VIIRS REQUIREMENT FOR MANUALLY-GENERATED CLOUD COVER AND CLOUD TYPE EDRS. 52¶
TABLE 4.3. VIIRS IMAGERY AND IMAGERY ASSIST BAND SELECTED ... [3]

**Deleted:** TABLE 1.1 GUAM DMSP TROPICAL CYCLONE POSITION STATISTICS FOR 1972. 31¶
TABLE 2.1 – OVERVIEW OF THE US CIVILIAN POLAR METEOROLOGICAL PROGRAMS (KRAMER 2002). 36¶
TABLE 2.2 – SPECTRAL CHANNEL WAVELENGTHS OF THE AVHRR . 40¶
TABLE 2.3 CHRONOLOGICAL OVERVIEW OF DMSP SERIES SATELLITES. 44¶
TABLE 2.4 COMPARISON OF TWO SENSORS – NOAA AVHRR/2 AND DMSP/OLS (KRAMER 2002). 47¶
TABLE 2.5 BAND CHARACTERISTICS FOR MODIS DATA PRODUCTS (NASA MODIS WEBSITE). 49¶ ... [4]

# List of Figures


FIGURE. 1.1 COMPARISON OF THE NORTHERN HEMISPHERE (NH) ANOMALY CORRELATION FROM OPERATIONAL AND REANALYSIS FORECASTS FOR 500 MB. (KALNAY, 1998)..... 21
FIGURE 1.2 COMPARISON OF OPERATIONAL AND REANALYSIS 5-DAY FORECAST ANOMALY CORRELATIONS FOR THE NORTHERN HEMISPHERE (NH) AND THE SOUTHERN HEMISPHERE (SH) AT 500 MB. (KALNAY, 1998). ..... 21
FIGURE 1.3 SIMULATIONS DEMONSTRATE THE IMPACT OF SENSOR NEΔT ON SST ANALYSES USING 2-CHANNEL AND 3-CHANNEL MULTICHANNEL SEA SURFACE TEMPERATURE ALGORITHMS..... 25
FIGURE 1.4 SIMULATIONS DEMONSTRATE THE IMPACT OF AN IMPERFECT CLOUD MASK ON MEETING SEA SURFACE TEMPERATURE (SST) REQUIREMENTS OF 0.5 K. SST ACCURACY IS STRONGLY IMPACTED IF CLOUDS FAIL TO BE DETECTED IN THE CLOUD MASK BUT NO IMPACT IS NOTED IF THE MASK OVER-DETECTS THEM..... 26
FIGURE 1.5 CONCENTRATION OF ATMOSPHERIC $CO_2$ AT MAUNA LOA OBSERVATORY, HAWAII EXPRESSED AS A MOLE FRACTION IN PARTS PER MILLION OF DRY AIR FOR THE PERIOD 1958-1990 (LIOU 1992). ..... 27
FIGURE 1.6 MODEL ON THE EVOLUTION OF TROPICAL STORMS USED IN INTENSITY ANALYSIS BASED UPON THE DVORAK METHOD (RAO, 1990)..... 29
FIGURE 1.7 MODIS TERRA WATER VAPOR IMAGERY OVER NORTHERN POLAR REGIONS (LEFT PANEL) AND WIND FIELDS (~~LOW-LEVEL WIND, MID-LEVEL WIND, HIGH-LEVEL WIND~~) DERIVED FROM ANALYSES (RIGHT PANEL) OF CLOUD MOVEMENTS OBSERVED IN SUCCESSIVE ORBITS..... 32
FIGURE 1.8 IMPROVEMENTS IN FORECAST SCORES (ANOMALY CORRELATION) AT ECMWF FOR THE 1000 HPA (LEFT) AND 500 HPA (RIGHT) GEOPOTENTIAL HEIGHT OVER THE ARCTIC (TOP) AND NORTHERN HEMISPHERE (BOTTOM), FOR MODEL FORECASTS WITH (RED) AND WITHOUT (BLUE) THE MODIS POLAR WINDS. ..... 32
FIGURE 2.1 ILLUSTRATION OF THE AVHRR INSTRUMENT (FROM KRAMER, 2002). ..... 38
FIGURE 2.2 SCHEMATIC ILLUSTRATION OF DMSP BLOCK 5D-3 SPACECRAFT MODEL ( KRAMER, 2002)..... 43
FIGURE 2.3 ILLUSTRATION OF THE EOS AQUA SATELLITE AND SENSORS (KRAMER, 2000)..... 48
FIGURE 2.4 INTEGRATED CONCEPT OF NOAA/EUMETSAT METEOROLOGICAL POLAR SATELLITES (KRAMER,2002). 54
FIGURE 2.5. SKETCH OF METOP-1 (FROM FIGURE 204 OF KRAMER, 2002) ..... 55
FIGURE 2.6 COVERAGE OF THE GEOSYNCHRONOUS SATELLITES ASSOCIATED WITH THE COORDINATION OF GEOSTATIONARY METEOROLOGICAL SATELLITES (RAO, 2000)..... 59
FIGURE 2.7 METEOROLOGICAL SATELLITES SUPPORTING THE WMO WORLD WEATHER WATCH PROGRAMME (WMO WEBSITE)..... 60
FIGURE 2.8 TRANSITION OF NPOESS SATELLITES WITH EXISTING US POES SATELLITE SYSTEMS (IPO WEBSITE)..... 63
FIGURE 3.1. HRCP CLOUD FORECAST RELIABILITY ESTABLISHED DURING THE CMEP STUDY (HUTCHISON AND JANOTA, 1989)..... 72
FIGURE 4.1. SOLAR SPECTRAL IRRADIANCE DISTRIBUTION FOR TOP OF THE ATMOSPHERE (TOA) AND SEA LEVEL ALONG WITH PRIMARY ATMOSPHERIC ABSORPTION BANDS AND SPECIES. (FIGURE 2.6 FROM LIOU, 1980)..... 82
FIGURE 4.2. CLOUDS AND SNOW ARE BRIGHT IN AVHRR IMAGERY CHANNEL 2 (0.9 μM) AT PANEL (A) AND CHANNEL 5 (12.0 μM) AT PANEL (B) OF A NOAA-12 SCENE COLLECTED ON MARCH 19, 1996 (HUTCHISON ET AL, 1997). 84
FIGURE 4.3. CLOUDS SEEN IN THE 0.6 μM BAND (CHANNEL 1) OF THE AVHRR IMAGERY IN PANEL (A) ARE CONTAINED THE MANUALLY-GENERATED CLOUD ANALYSIS, ARE SHOWN AS RED, IN PANEL (B)..... 84
FIGURE 4.4. SNOW NOW APPEARS BLACK IN PANEL (A) CONTAINING THE ALBEDO COMPONENT OF THE 3.7 μM BAND (CHANNEL 3) OF THE AVHRR IMAGERY WHILE PANEL (B) CONTAINS THE MANUALLY-GENERATED CLOUD ANALYSIS MADE USING THIS IMAGE..... 85
FIGURE 4.5. EXAMPLE OF A TOTAL CNC ANALYSIS CREATED BY MERGING CNC ANALYSES FROM INDIVIDUAL SPECTRAL BANDS SHOWN IN FIGURE 4.3 AND FIGURE 4.4 INTO A SINGLE CNC ANALYSIS. ..... 85
FIGURE 4.6. SYNTHETIC BACKGROUND SHOWN IN PANEL (A) ARE USED WITH CLOUD MASK, SHOWN IN PANEL (B) TO GENERATE SYNTHETIC VIIRS IMAGERY..... 86
FIGURE 4.7. SYNTHETIC 12.0 μM VIIRS IMAGE, MANUAL AND SYNTHETIC CLOUD MASKS, AND DIFFERENCE FIELDS SHOW LOCATIONS OF INACCURACIES IN MANUALLY-GENERATED CLOUD DATA PRODUCT..... 87
FIGURE 4.8. SPECTRAL SIGNATURES OF CLOUD PARTICLES AND SURFACE BACKGROUNDS IN 0.3 - 1.0 MICRON RANGE. (KEY: REFLECTIVITIES: VEGETATED LAND = GREEN, OCEAN = DARK BLUE, SNOW = WHITE, BARE SOIL OR SAND = YELLOW., SOLAR ILLUMINATION = GOLD AND ATMOSPHERIC TRANSMISSION = BLACK. VIIRS BANDS BLUE,


**Deleted:** 22
**Deleted:** 27
**Deleted:** 30
**Deleted:** 60
**Deleted:** 85
**Deleted:** 86
**Deleted:** 86

SOLID TURQUOISE = INDEX OF REFRACTION FOR WATER DROPLETS, AND DASHED TURQUIOSE = INDEX OF REFRACTION FOR ICE.) ..... 91
FIGURE 4.9. SPECTRAL SIGNATURES OF CLOUD PARTICLES AND SURFACE BACKGROUNDS IN 1.0 - 3.0 MICRON RANGE. (KEY: REFLECTIVITIES OF, VEGETATED LAND = GREEN, OCEAN = DARK BLUE, SNOW = WHITE, BARE SOIL OR SAND = YELLOW. SOLAR ILLUMINATION = GOLD AND ATMOSPHERIC TRANSMISSION = BLACK. VIIRS BANDS ARE SHOWN IN LIGHTER BLUE SOLID TURQUOISE = INDEX OF REFRACTION FOR WATER DROPLETS, AND DASHED TURQUIOSE = INDEX OF REFRACTION FOR ICE.) ..... 92
FIGURE 4.10. SPECTRAL SIGNATURES OF CLOUD PARTICLES AND SURFACE BACKGROUNDS IN 3.0 - 5.0 MICRON RANGE. (KEY: REFLECTIVITIES OF, VEGETATED LAND = GREEN, OCEAN = DARK BLUE, SNOW = WHITE, BARE SOIL OR SAND = YELLOW. SOLAR ILLUMINATION = GOLD AND ATMOSPHERIC TRANSMISSION = BLACK. VIIRS BANDS ARE SHOWN IN LIGHTER BLUE SOLID TURQUOISE = INDEX OF REFRACTION FOR WATER DROPLETS, AND DASHED TURQUIOSE = INDEX OF REFRACTION FOR ICE.) ..... 93
FIGURE 4.11. SPECTRAL SIGNATURES OF CLOUD PARTICLES AND SURFACE BACKGROUNDS IN 5.0.- 15.0 MICRON RANGE. (KEY: REFLECTIVITIES OF, VEGETATED LAND = GREEN, OCEAN = DARK BLUE, SNOW = WHITE, BARE SOIL OR SAND = YELLOW. SOLAR ILLUMINATION = GOLD AND ATMOSPHERIC TRANSMISSION = BLACK. VIIRS BANDS ARE SHOWN IN LIGHTER BLUE SOLID TURQUOISE = INDEX OF REFRACTION FOR WATER DROPLETS, AND DASHED TURQUIOSE = INDEX OF REFRACTION FOR ICE.) ..... 94
FIGURE 4.12 VIIRS SENSOR BLOCK DIAGRAM (KRAMER, 2002). ..... 98
FIGURE 4.13 SUMMARY OF VIIRS DESIGN CONCEPTS AND HERITAGE (BYERLY ET AL., 2000). ..... 99
FIGURE 4.14 VIIRS DETECTOR FOOTPRINT AGGREGATION SCHEME FOR BUILDING IMAGERY "PIXELS" ..... 100
FIGURE 4.15 HORIZONTAL SAMPLING INTERVAL (HSI) FOR IMAGERY BANDS (AGGREGATION IN SCAN DIRECTION). 101
FIGURE 4.16 VIIRS AGGREGATION AND BOW TIE PIXEL REDUCTION. ..... 101
FIGURE 4.17 DEPICTION OF SENSOR OPTICAL PERFORMANCE PARAMETERS. ..... 102
FIGURE 4.18 HSI FOR SINGLE-GAIN MODERATE RESOLUTION BANDS ..... 106
FIGURE 4.19 HSI FOR DUAL-GAIN MODERATE RESOLUTION BANDS. ..... 107
FIGURE 5.1. NORMALIZED DISTRIBUTION OF EMISSION SPECTRA FOR THREE BLACKBODIES WITH ABSOLUTE TEMPERATURES OF 6000 K (SUN), 770 K (FOREST FIRES), AND 300 K (EARTH'S SURFACE) SHOWS PRIMARY ENERGY SOURCES FOR EACH OF THE VIIRS SPECTRAL BANDS (SCORER, 1990). ..... 118
FIGURE 5.2. SIGNATURES OF CLOUDS AND LAND SURFACES TYPICAL OF THOSE PRESENT IN THE VIIRS I1 BAND ARE SEEN IN THE NOAA-12 AVHRR CHANNEL 1 IMAGERY COLLECTED NEAR SAN FRANCISCO, CA ON FEBRUARY 19, 1996 (HUTCHISON ET AL., 1997(A)). ..... 124
FIGURE 5.3. SIGNATURES OF CLOUDS AND LAND SURFACES TYPICAL OF THOSE PRESENT IN THE VIIRS I2 BAND ARE SEEN IN THE NOAA-12 AVHRR CHANNEL 1 IMAGERY COLLECTED NEAR SAN FRANCISCO, CA ON FEBRUARY 19, 1996 (HUTCHISON ET AL., 1997(A)). ..... 126
FIGURE 5.4. SIGNATURES OF CLOUDS AND LAND SURFACES TYPICAL OF THOSE PRESENT IN THE VIIRS I2 BAND ARE SEEN IN THE SEAWIFS DATA COLLECTED OVER SOUTHWESTERN US ON JULY 13, 2001 ..... 127
FIGURE 5.5. THEMATIC MAPPER DATA COLLECTED OVER THE SIERRA NEVADA MOUNTAINS SHOW THE VALUE OF 1.61 µM IMAGERY FOR DIFFERENTIATING BETWEEN WATER CLOUDS (BRIGHT IN BOTH BANDS) AND SNOW (BLACK IN ONLY THE 1.61 µM IMAGE). ..... 129
FIGURE 5.6. ATMOSPHERIC ATTENUATION IN AVHRR 3.7, 10.8, AND 11.8 µM BANDS AS A FUNCTION OF TOTAL ATMOSPHERIC WATER VAPOR (HUTCHISON ET AL., 1995). ..... 131
FIGURE 5.7. SUN GLINT IN AVHRR CHANNEL 2 AND CHANNEL 3 BANDS OF NOAA-15 MISSION OVER SOUTHEASTERN UNITED STATES ..... 135
FIGURE 5.8. STRATUS OVER SAN FRANCISCO BAY AND COASTAL CALIFORNIA IN NIGHTTIME 3.7 µM AND 11 µM IMAGERY COLLECTED BY NOAA-14 ..... 137
FIGURE 5.9. CHANNELS 1,3, AND 5 OF NOAA-12 IMAGERY COLLECTED AT ABOUT 7:05 AM PST ON MARCH 19, 1996 OVER WESTERN UNITED STATES AND PACIFIC COASTAL REGIONS. ..... 138
FIGURE 5.10. NOAA-12 SCENE COLLECTED AT ABOUT 7:05 AM LOCAL PST (1505 GMT) ON ..... 140
MARCH 19, 1996 OVER WESTERN UNITED STATES AND PACIFIC COASTAL REGIONS (HUTCHISON AND LOCKE, 1997). ..... 140
FIGURE 5.11. NOAA-12 SCENE COLLECTED AT ABOUT 7:58 AM LOCAL (1558 GMT) ON MARCH 12, 1996 OVER WESTERN UNITED STATES AND PACIFIC COASTAL REGIONS (HUTCHISON ET AL., 1997(B)). ..... 141
FIGURE 5.12. AMBIGUITIES IN SPECTRAL SIGNATURES CAN IMPACT A-PRIORI CLOUD TOP PHASE ANALYSES OF THIS NOAA-12 AVHRR SCENE COLLECTED AT 1558 GMT ON MARCH 12, 1996. ZOOMING IN ON THE LOWER-RIGHT QUADRANT OF CHANNEL 5, (A), AND CHANNEL 3A, (B), SHOWS THE DIFFICULTY IN MANUALLY CLASSIFYING

Deleted: 86
Deleted: 86
Deleted: 86
Deleted: 86
Deleted: 86
Deleted: 86
Deleted: 86
Deleted: 86
Deleted: 86
Deleted: 86
Deleted: 86
Deleted: 86
Deleted: 86
Deleted: 86
Deleted: 86
Deleted: 86
Deleted: 86
Deleted: 86
Deleted: 86
Deleted: 86
Deleted: 86
Deleted: 86

CIRRUS SINCE ICE APPEARANCE CHANGES AS OPTICAL THICKNESS DECREASES FROM (A) TO (B) (HUTCHISON ET AL, 1997). ..... 142 Deleted: 86
FIGURE 5.13. SIMULATED AVHRR ($T_{3.7}$-$T_{11.0}$) BRIGHTNESS TEMPERATURE DIFFERENCE VERSUS OPTICAL THICKNESS OF CIRRUS IN MID-LATITUDE WINTER ATMOSPHERE WITH CLOUD TEMPERATURE OF 236 K AND RADII OF 20 AND 40 MICRONS (HUTCHISON ET AL., 1997). ..... 144 Deleted: 86
FIGURE5.14. SIMULATED AVHRR (CHANNEL 3 MINUS CHANNEL 5) BRIGHTNESS TEMPERATURE DIFFERENCE VERSUS CHANNEL 4 TEMPERATURE FOR CIRRUS OF VARIABLE EMISSIVITY (E) AT 10 KM IN SUB-ARCTIC WINTER ATMOSPHERE (HUTCHISON ET AL., 1997). ..... 144 Deleted: 86
FIGURE 5.15. SMOKE PLUMES FROM SEVERAL FOREST FIRES (INCLUDING THE ONE NEAR LOS ALAMOS, NEW MEXICO) ARE EVIDENT IN CHANNEL 2 OF THE NOAA-12 AVHRR SCENE COLLECTED AT 2319 GMT ON MAY 11, 2000. ..... 145 Deleted: 86
FIGURE 5.16. HOT SPOTS IN THE FOREST FIRES ARE EVIDENT IN CHANNEL 3 OF THE NOAA-12 AVHRR SCENE COLLECTED AT 2319 GMT ON MAY 11, 2000. SEVERAL IN THE MOUNTAINS OF MEXICO SHOW NO PLUMES. .. 146 Deleted: 86
FIGURE 5.17. GOES-EAST VISIBLE AND IR IMAGERY OF TEXAS ON APRIL 4, 2001 AT 1600 GMT SHOW EXTENSIVE WATER CLOUDS OVER THE EASTERN AND THIN CIRRUS CLOUDS OVER WESTERN TEXAS. ..... 149 Deleted: 86
FIGURE 5.18. BRIGHTNESS TEMPERATURES IN AVHRR CHANNEL 4 IMAGERY OF VARIOUS CLOUDS LOCATED OVER TEXAS AT 1127 GMT ON APRIL 4, 2001. ..... 150 Deleted: 86
FIGURE 5.19. RADIOSONDE FOR CORPUS CHRISTI, TEXAS AT 1200 UTC ON APRIL 4, 2001 ALONG WITH THERMODYNAMIC (SKEWT-LOGP) CHART OF THESE DATA SHOW CLOUD TOP TEMPERATURE OF 19.6 $^0$C. ..... 151 Deleted: 86
FIGURE 5.20. SPECTRAL RESPONSE OF THE DAYTIME/NIGHTTIME VISIBLE IMAGERY BAND, COMPARED WITH THE LUNAR SIGNAL. ..... 152 Deleted: 86
FIGURE 5.21. SIGNAL TO NOISE RATIO PERFORMANCE OF THE DAYTIME/NIGHTTIME VISIBLE IMAGERY UNDER QUARTER-MOON ILLUMINATION CONDITIONS, AS A FUNCTION OF SCAN ANGLE. ..... 153 Deleted: 86
FIGURE 5.22 – F13 OLS VISIBLE (HRD) IMAGE FOR THE FIRST TERMINATOR CROSSING OF THE JULY 20, 2001 1131 UT ORBIT. ..... 154 Deleted: 86
FIGURE 5.23. SEAWIFS DATA FROM THE 0.412 µM AND 0.488 µM BANDPASSES ARE SHOWN FOR THE WESTERN US AND NORTHERN MEXICO ON JULY 13, 2001 AT 1954 GMT. ..... 157 Deleted: 86
FIGURE 5.24. SEAWIFS DATA IN THE 0.555 µM AND 0.765 µM BANDS ARE SHOWN FOR THE SCENE OVER THE WESTERN US AND NORTHERN MEXICO ON JULY 13, 2001 AT 1954 GMT. ..... 158 Deleted: 86
FIGURE 5.25. THE TWO-WAY CLEAR-SKY TRANSMITTANCES FOR ENERGY ARRIVING AT SATELLITE ALTITUDE IN THE 1.38 µM REGION FOR A PERFECT REFLECTOR LOCATED AT DIFFERENT ALTITUDES. CALCULATIONS BASED UPON SUB-ARCTIC SUMMER ATMOSPHERE AND LOWTRAN. (GAO ET AL., 1993). ..... 160 Deleted: 86
FIGURE 5.26. AVIRIS IMAGERY FOR VIIRS I2 AND M9 CHANNELS OVER COFFEVILLE, KANSAS SHOWS VALUE OF MASKING SURFACE FEATURES FOR MANUAL INTERPRETATION OF THIN CIRRUS. ..... 161 Deleted: 86
FIGURE 5.27. AVIRIS IMAGERY FOR VIIRS I1 AND M9 CHANNELS OVER TEXAS GULF COAST REVEALS THAT LOW-LEVEL WATER CLOUDS ARE MASKED IN 1.38 µM IMAGERY. ..... 162 Deleted: 86
FIGURE 6.1. COLOR COMPOSITE TO EMPHASIZE VEGETATED LAND SURFACES CREATED BY ASSIGNING 0.64 µM BAND ASSIGNED TO RED AND GREEN GUNS OF CRT AND 0.865 µM ALBEDO BAND ASSIGNED TO BLUE GUN. ..... 164 Deleted: 86
FIGURE 6.2. PLACING THE 12.0 µM BAND IN THE BLUE GUN OF FIGURE 6.1 PROVIDES VALUABLE DATA ON CLOUD TOP TEMPERATURES NEEDED FOR CLOUD TYPING. WARM, LOW LEVEL WATER CLOUDS APPEAR YELLOW WHILE COLDER ICE CLOUDS ARE BLUE. ..... 165 Deleted: 86
FIGURE 6.3. REPLACING THE BAND IN THE RED GUN OF FIGURE 6.2 WITH THE AVHRR 3.7 ALBEDO CHANNEL ALLOWS SNOW TO BE DIFFERENTIATED FROM LOWER-LEVEL WATER CLOUDS, THIN CIRRUS, AND THICKER CIRRUS WHILE MAINTAINING INFORMATION ON CLOUD TOP TEMPERATURES AND VEGETATED LAND SURFACES (RED = 3.7 µM ALBEDO, GREEN = 0.865 µM, BLUE = 12.0 µM). ..... 167 Deleted: 86
FIGURE 6.4. COLOR COMPOSITE RED = 0.64 µM BAND, GREEN = 0.64 µM BAND, BLUE = 3.7 µM ALBEDO BAND) FOR THE MANUAL DETECTION AND MAPPING OF SNOW THROUGH CIRRUS CLOUDY CONDITIONS (HUTCHISON AND LOCKE, 1997). ..... 169 Deleted: 86
FIGURE 6.5. COMPOSITE IMAGE (RED = 0.412 µM, GREEN = 0.865 µM, BLUE = 0.64 µM) FOR THE DETECTION CLOUDS OVER HIGHLY REFLECTIVE, ARID OR SEMI-ARID REGIONS. ..... 172 Deleted: 86
FIGURE 7.1. GRAY-SCALE MAS IMAGERY COLLECTED OVER THE NORTH SLOPE OF ALASKA DURING FLIGHT TRACK #01 ON JUNE 7, 1995. DATA SHOWN ARE THOSE MODIS AND VIIRS BANDS NEEDED TO INTERPRET CLOUD AND SURFACE FEATURES IN THE SCENE. ..... 175 Deleted: 86

FIGURE 7.2. COLOR COMPOSITE (RED = 0.645μM, GREEN = 0.845 μM, BLUE = 0.645 μM) SHOWS MOST OF THE SURFACE IS (GREEN) HIGHLY VEGETATED. ..... 176
FIGURE 7.3. COLOR COMPOSITE (RED = 0.645μM, GREEN = 0.845 μM, BLUE = 1.61 μM) SHOWS SNOW, ICE, AND GLACIATED CLOUDS AS YELLOW. NOTICE THE SMOOTH TEXTURE ASSOCIATED WITH CIRRUS CLOUDS. ..... 178
FIGURE 7.4. COLOR COMPOSITE (RED = 0.645 μM, GREEN = 1.88 μM, BLUE = 11.45 μM) PROVIDES VALUABLE INFORMATION FOR CLOUD TYPE, SURFACE, AND ATMOSPHERIC MOISTURE CLASSIFICATIONS. ..... 181
FIGURE 7.5. COLOR COMPOSITE (RED = 0.645 μM, GREEN = 0.865 μM, BLUE = 11.45 μM) PROVIDES USEFUL INFORMATION ON SURFACE FEATURES AND CLOUD TOP TEMPERATURES AND HEIGHTS. ..... 183
FIGURE 7.6. GRAY-SCALE IMAGERY COLLECTED OVER COLORADO DURING FLIGHT TRACK #26 OF THE MODIS AIRBORNE SIMULATOR ON JULY 5, 1995. DATA SHOWN ARE THOSE MODIS AND VIIRS BANDS NEEDED TO INTERPRET FEATURES IN THE SCENE. ..... 186
FIGURE 7.7. COLOR COMPOSITE (RED = 0.645μM, GREEN = 0.845 μM, BLUE = 0.645 μM) SHOWS MOST OF THE SURFACE IS NOT (GREEN) HIGHLY VEGETATED. ..... 187
FIGURE 7.8. COLOR COMPOSITE (RED = 0.645μM, GREEN = 0.845 μM, BLUE = 1.61 μM) SHOWS SNOW, ICE, AND GLACIATED (OPTICALLY-THIN) CLOUDS AS YELLOW. THICKER CLOUDS REMAIN WHITE. ..... 189
FIGURE 7.9. COLOR COMPOSITE (RED = 0.645 μM, GREEN = 1.88 μM, BLUE = 11.45 μM) PROVIDES INFORMATION ON CLOUD TYPE, SURFACE, AND ATMOSPHERIC MOISTURE CLASSIFICATIONS. ..... 191
FIGURE 7.10. COLOR COMPOSITE (RED = 0.645 μM, GREEN = 0.865 μM, BLUE = 11.45 μM) PROVIDES USEFUL INFORMATION ON SURFACE FEATURES AND CLOUD TOP TEMPERATURES AND HEIGHTS. ..... 194
FIGURE 8.1 OVERVIEW OF AN APPROACH TO RETRIEVING 3-DIMENSIONAL CLOUD FIELDS FROM SATELLITE DATA (HUTCHISON, 2002). ..... 199
FIGURE 8.2 BI-SPECTRAL REFLECTANCES RATIO (BSRR) IN THE FORWARD AND NON-FORWARD SCATTERING DIRECTIONS FOR OPTICALLY-THICK CLOUDS (▲)AND CLOUD–FREE PIXELS (+) OVER OCEAN SURFACES AS A FUNCTIONS OF COSINE SOLAR ZENITH ANGLE (FROM HUTCHISON AND HARDY, 1995). ..... 202
FIGURE 8.3 BRIGHTNESS TEMPERATURE DIFFERENCES (BTD) BETWEEN NIGHTTIME 3.7 μM MINUS 11.0 μM FOR THIN CIRRUS CLOUDS (▲) AND CLOUD CLOUD–FREE PIXELS (+) ARE SHOWN IN THE LEFT PANEL AS A FUNCTION OF TOTAL ATMOSPHERIC WATER CONTENT. IN THE RIGHT PANEL, 11.0 μM MINUS 3.7 μM BTDS ARE SHOWN FOR STRATUS CLOUDS (▲) AND CLOUD-FREE (+) PIXELS IN NIGHTTIME AVHRR IMAGERY (FROM HUTCHISON AND HARDY, 1995). ..... 202
FIGURE 8.4 CLOUD PHASE CLASSIFICATION FROM THE FUSION OF SPECTRAL SIGNATURES IN AVHRR IMAGERY AND CLOUD TOP PRESSURES FROM $CO_2$ SLICING OF HIGH RESOLUTION IR SOUNDER DATA. (FROM HUTCHISON ET AL., 1997A) S & K = SAUNDERS AND KRIEBEL (1988); BSRR = BISPECTRAL REFLECTANCE RATIO ..... 206
FIGURE 8.5 ANALYSIS OF CLOUD PHASE CLASSES FROM GLOBAL TERRA MODIS DATA USING CURRENT MODIS ALGORITHM (MENZEL ET AL., 2002). ..... 207
FIGURE 8.6 ANALYSIS OF CLOUD PHASE CLASSES FROM GLOBAL TERRA MODIS DATA USING PAVOLONIS AND HEIDINGER ALGORITHM (PAVOLONIS AND HEIDINGER 2004). ..... 207
FIGURE 8.7. ARCHITECTURE FOR THE RETRIEVAL OF WATER CLOUD MICROPHYSICAL PROPERTIES DURING DAYTIME AND NIGHTTIME CONDITIONS. CTT = CLOUD TOP TEMPERATURE (OU ET AL., 2002) ..... 210
FIGURE 8.8. OVERVIEW OF THE WATER CLOUD SOLAR RETRIEVAL ALGORITHM. $A_G(\lambda)$ = SURFACE ALBEDO FOR WAVELENGTH λ (OU ET AL., 2002) ..... 211
FIGURE 8.9. SUN SATELLITE GEOMETRY. (OU ET AL., 2002) ..... 211
FIGURE 8.10. THEORETICAL RELATIONSHIP BETWEEN THE REFLECTION FUNCTION AT 0.664 μM AND (A) 1.621 μM AND (B) 2.142 μM FOR VARIOUS VALUES OF $\tau_C$ (AT 0.664 μM) AND $R_E$ WHEN $\theta_0$ =26°, θ = 40° AND ϕ = 42°. (KING ET AL., 1997) ..... 212
FIGURE 8.11. ARCHITECTURE FOR THE RETRIEVAL OF ICE CLOUD MICROPHYSICAL PROPERTIES FROM VIIRS DATA DURING DAYTIME CONDITIONS AND VIIRS DATA DURING NIGHTTIME. $T_C$, AND $D_E$ ARE CLOUD TOP TEMPERATURE AND ICE CRYSTAL DIAMETER (FIGURE 4.11 FROM OU ET AL., 2002). ..... 214
FIGURE 8.12 PROCESSING SEQUENCE FOR RETRIEVAL OF ICE CLOUD OPTICAL PROPERTIES IN DAYTIME CONDITIONS. 215
FIGURE 8.13 PROCESSING SEQUENCE FOR RETRIEVAL OF ICE CLOUD OPTICAL PROPERTIES IN NIGHTTIME CONDITIONS. ..... 217
FIGURE 8.14 GEOMETRY FOR RETRIEVAL OF CLOUD BASE HEIGHT USING CLOUD TOP HEIGHT ALONG WITH CLOUD OPTICAL PROPERTIES THE OBTAIN CLOUD THICKNESS (HUTCHISON, 2002). ..... 219

**Deleted:** 86
**Deleted:** 86
**Deleted:** 86
**Deleted:** 86
**Deleted:** 86
**Deleted:** 86
**Deleted:** 86
**Deleted:** 86
**Deleted:** 86
**Deleted:** 86
**Deleted:** 86
**Deleted:** 86
**Deleted:** 86
**Deleted:** 86
**Deleted:** 86
**Deleted:** 86
**Deleted:** 86
**Formatted:** French (France)
**Field Code Changed**
**Deleted:** 86
**Formatted:** French (France)
**Deleted:** 86
**Deleted:** 86
**Deleted:** 86
**Deleted:** 86
**Deleted:** 86
**Deleted:** FIGURE. 1.1 COMPARISON OF THE NH ANOMALY CORRELATION FROM OPERATIONAL AND REANALYSIS FORECASTS FOR 500 MB. (KALNAY, 1998). 29¶
FIGURE 1.2 COMPARISON OF OPERATIONAL AND REANALYSIS 5-DAY FORECAST ANOMALY CORRELATIONS FOR THE NORTHERN HEMISPHERE AND THE SOUTHERN HEMISPHERE AT 500 MB. (KALNAY, 1998). 30¶
FIGURE 1.3 SIMULATIONS DEMONSTRATE THE IMPACT OF SENSOR NEΔT ON SST ANALYSES USING 2-CHANNEL AND 3-CHANNEL MULTICHANNEL SEA SURFACE TEMPERATURE ALGORITHMS. 33¶
FIGURE 1.4 SIMULATIONS DEMONSTRATE THE IMPACT OF AN IMPERFECT CLOUD MASK ON MEETING SEA SURFACE ... [5]
**Formatted:** English (U.S.)
**Deleted:** FIGURE. 1.1 COMPARIS ... [6]
**Deleted:** SUN GLINT
**Deleted:** IN AVHRR CHANNEL ... [7]

# PREFACE

Meteorological satellites have been flown in near-Earth orbit since the launch of Television and Infrared (IR) Observing System (TIROS)-1 by the National Aeronautics and Space Administration (NASA) of the United States (US) in 1960 and in the mid-1960s, the US Department of Defense (DoD) launched its first meteorological satellite under the Defense Meteorological Satellite Program (DMSP). These early satellite sensors collected data in only one broad visible band and one broad IR band, e.g. 0.5-1.0 and 10-12 μm regions of the electromagnetic spectrum. Early applications of these data included their use in automated cloud models at the US Air Force Weather Central and the manual interpretation of meteorological conditions by weather forecasters around the globe. A satellite meteorological handbook was developed as the first significant attempt to document the manual interpretation of clouds and weather patterns in satellite imagery (Dickenson, et al., 1974; Brandli, 1976).

In recent decades, there has been an ever-increasing wealth of information collected by meteorological satellites that carry multispectral sensors to view the Earth-atmosphere system in a large number of discrete wavelengths. The Advanced Very High Resolution Radiometer (AVHRR) was the first truly operational cloud imaging instrument to be flown on a polar-orbiting meteorological satellite. The first AVHRR was carried on the experimental TIROS-N spacecraft in 1978 and it then became an operational system when flown on the National Oceanographic and Atmospheric Administration (NOAA)-6 spacecraft in 1979. In addition to providing imagery of clouds and the development of weather systems in the visible and near-infrared wavelength ranges, the AVHRR was also designed to provide improved data for sea surface temperature analyses. In the early 1980's, NASA began preparations to build a new sensor to collect higher quality data suitable for climate change studies and the 36-band MODerate-resolution Imaging Spectroradiometer (MODIS) was first launched in 2000.

**Deleted:** VIIRS, the Visible/Infrared Imager/Radiometer Suite,

In 1994, there was a Presidential Decision Directive in the US to combine the DMSP and NOAA polar-orbiting meteorological satellite systems into a single system, the (US) National Polar-orbiting Operational Environmental Satellite System (NPOESS). The NPOESS Integrated Program Office (IPO), consisting of personnel from NOAA, DoD and NASA, was created to develop, acquire, and operate this next generation of US polar-orbiting meteorological satellites. In the meantime, EUMETSAT, the European organization which has a long track record in operating geostationary meteorological satellites, had begun planning MetOp, a Meteorological Operational series of polar-orbiting spacecraft similar to the US NOAA spacecraft. In 1998 a cooperation agreement was signed with the objective of joining the space segment of the emerging MetOp program with the NPOESS program to form a fully coordinated service, thus sharing the costs between the US and Europe.

A new era in Earth observations will soon be ushered in with the first launch of the Visible/Infrared Imager/Radiometer Suite (VIIRS), an electro-optical imager specifically designed to meet a subset of the totality of user requirements defined by NPOESS. The first VIIRS instrument is scheduled to fly on the NASA NPOESS Preparatory Project (NPP) in 2006 and further VIIRS instruments are planned to be flown on all the spacecraft of the NPOESS program collecting global cloud imagery and environmental data for the next two decades.

VIIRS will collect data in 22 spectral bands in the visible, near-IR, mid-IR, and long-wave IR regions of the electromagnetic spectrum and at two resolutions: 375 m at nadir for imagery and 750 m at nadir for radiometric data. In addition, the unique VIIRS design restricts resolution growth to no more the 2:1 as the sensor scans from nadir to the 3000 km edge of swath. Thus, VIIRS draws its heritage from the AVHRR, the DMSP OLS, and the more sophisticated Sea-viewing Wide Field-of-view Sensor (SeaWiFS) and MODIS instruments. However, lacking has been a reference text to help introduce users to the next generation instrument or help those new in the field to exploit more fully these multispectral data once they become available.

Thus, our purpose in writing this book is threefold. First, we discuss, in Chapters 1 and 2 respectively, the evolution of satellite meteorology in the broader field of operational meteorology and provide background information on the previous optical and near-infrared (IR) imaging instruments flown by key international agencies. Secondly, since VIIRS was designed to satisfy user requirements for data products, rather than just satellite observations, we provide in Chapters 3 and 4 an overview of these requirements and the type of very detailed studies that were undertaken to convert product specifications into sensor design parameters. Thirdly, in Chapters 5 – 8, we seek to provide future users of VIIRS data with the fundamental concepts needed to fully exploit VIIRS data for a variety of cloud studies which ranges from image interpretation to retrieval of three-dimensional cloud fields. With regard to the third point, if we had waited for the launch of the first spacecraft carrying a VIIRS instrument in order to obtain actual VIIRS data for inclusion in this book, then it could not have been published until several years after the VIIRS data first became available. Therefore, in order to be able to put this book into the hands of the scientific community in readiness for them to be able to analyze VIIRS data as soon as it became available, we have had to make use of simulated or surrogate data from other instruments with specifications of spectral bands and of spatial resolutions as close as we could find to those of VIIRS. The match is obviously not perfect, but it should be sufficient for most purposes.

In this text, we attempt to introduce the reader to the fundamental principles necessary for the interpretation of surface and cloud features in multispectral meteorological satellite imagery. Therefore, parts of the text are aimed at those familiar with calculus and offer such individuals detailed insights into the signatures of clouds and land surfaces in both daytime and nighttime imagery along with background material that could be useful in the design of future satellites sensors. Those with a less extensive mathematical background can also become very knowledgeable in the interpretation of multispectral imagery through the careful review of the many illustrative examples contained in the text.

We are indebted to the NPOESS IPO and Northrop Grumman Space Technology for their assistance in publishing this text. In addition, we pay special thanks to Raytheon Santa Barbara Remote Sensing and Information Technology and Scientific Services (ITSS) for funding used to prepare the original manuscript that forms the core segment of this book *and source material regarding VIIRS system design. We thank* Ms. Nikki Goodfellow, of the Center for Space Research at The University of Texas at Austin, for spending many hours of her own time making this material more legible. Special thanks also are extended to Dr. Neal Baker for his meticulous review of the text on behalf of the NPOESS IPO. We also thank current and former employers that supported our work, including the Lockheed Martin Advanced Technology Center, which

**Deleted:** is poised to become an important satellite-flown cloud imager for a decade or two. O
**Deleted:** propose to recall
**Deleted:** background in terms
**Deleted:** on meteorological satellites.
**Deleted:** shall relate the principal outlines
**Deleted:**
**Deleted:** involved in the
**Deleted:** and
**Deleted:** stages of VIIRS
**Deleted:** The specification and design were guided by a very detailed set of requirements identified by the user community.
**Deleted:** aim to
**Deleted:** readers
**Deleted:** a manual or handbook for the visual analysis of
**Deleted:** or
**Deleted:** going to be
**Deleted:** good enough
**Deleted:** This
**Deleted:**
**Deleted:** s
**Deleted:**
**Deleted:** manual
**Deleted:** P
**Deleted:** ¶ Meteorological satellites have been flown in near-Earth orbit since the launch of Television and Infrared (IR) Obse ... [8]
**Deleted:** O
**Deleted:** D) launched its first ... [9]
**Deleted:** O
**Deleted:** D and NASA, was cr ... [10]
**Deleted:** sensor
**Deleted:** s.¶ ... [11]
**Deleted:** l
**Deleted:** ispectral sensors to vi ... [12]
**Formatted** ... [13]
**Formatted** ... [14]
**Formatted** ... [15]
**Deleted:** providing the funding ... [16]
**Deleted:** In addition, w

funded research that resulted in many of the publications referenced in this text. Finally, we thank our families for their patience and support during the time required to complete this endeavor.

Keith D. Hutchison
Arthur P. Cracknell

# Chapter 1

# INTRODUCTION

## SATELLITE METEOROLOGY

In this chapter, the evolution of satellite meteorology is highlighted to demonstrate the role played by space-based meteorological observations and data products in advancing our understanding of the Earth-atmosphere system. Specifically, the value of satellite derived atmospheric profiles to numerical weather prediction (NWP) modeling is provided based largely upon the publication of Kalnay et al (1998). In addition, a general overview is presented on the use of remotely-sensed satellite data for other meteorological and oceanographic applications. We shall not attempt to discuss non-meteorological applications of meteorological satellite data (see, for example, Cracknell 1997). As this chapter concludes, the rationale should become evident for the National Polar-orbiting Operational Environmental Satellite System (NPOESS) becoming the first satellite built to emphasize product requirements rather than hardware design, since it is these data products that are needed to further improve our understanding of the Earth-atmosphere system and continue advances in weather and climate modeling.

## 1.1 OVERVIEW OF NUMERICAL WEATHER PREDICTION MODELING

Kalnay et al (1998) discussed the evolution of NWP and included the foundations that were laid early in the 20th century by some of the greatest names in meteorology. Highlights from this early work include:

- The concept of linearized perturbation of the equations of motion for weather prediction was demonstrated in 1939 by Carl-Gustaf Rossby. He assumed that the atmospheric velocity was horizontal and non-divergent, so that potential vorticity was conserved and developed the formula for the phase speed of large-scale atmospheric (Rossby) waves (Rossby et al. 1939; Rossby 1940). (Confirm with papers.)
- The first successful numerical forecasts were made by Charney et al. (1950), using Rossby's model. Charney also discussed the importance of initial conditions on forecasts.
- Charney (1951) discussed the importance of Richardson's (1922) experiment and the influence that Rossby's model had on the development of the quasi-geostrophic model used on the first computer. He reviewed the theoretical basis of numerical modeling, the importance of boundary conditions, and the advances he foresaw in NWP modeling. For example, he predicted replacing the quasi-geostrophic equations by the primitive equations, balancing of initial conditions, needing to parameterize small-scale physical processes, and developing automatic data assimilation and quality control procedures. (Confirm with papers.)
- Lorenz (1963, 1965, 1969) discussed the chaotic nature of the atmosphere and predicted it would impose an upper limit of about 14 days on the predictability of the weather forecasts even if perfect models and observations were available.

**Deleted:** upon

**Deleted:** (Confirm with papers.)

**Deleted:** 8

**Deleted:** with

**Formatted:** Font color: Auto

**Deleted:** (Confirm with papers.)

Thus, there are three avenues for continuing to improve NWP forecast performance: (1) developing better atmospheric models, (2) improving observational data, and (3) employing better methods for data assimilation. All are important because NWP is an initial value problem, i.e. NWP forecasts start with the initial state of the atmosphere and predict future states using the physics in the model. Thus, NWP forecasts could be improved by (1) representing better the physics of the atmosphere, or (2) specifying better initial atmospheric conditions through improved observational data. Since conventional weather observations are made less frequently than satellite observations, especially over the broad ocean areas, the use of satellite data in regions where ground-based observations are not collected should represent an obvious area to further improve NWP predictions. Improvements that exploit satellite data have generally been associated with advances in computer technology since global NWP models are computationally intensive. However, for the purpose of this text, attention focuses on the improvements in observational data, specifically those made by satellite-based systems.

Deleted: s

## 1.2 EVOLUTION OF OBSERVATIONAL DATA FOR NWP MODELING

Prior to the launch of the first of the first artificial satellite by the former Soviet Union on 4 October 1957, NWP was based largely upon the analysis of surface and atmospheric observations collected at ground-based weather stations around the world. Unlike the networks of automated observing systems used today, initially these conventional weather reports of surface conditions were typically made by skilled weather observers who routinely reported on surface temperature, pressure, sky conditions (e.g. cloud cover), visibility, and wind speed/direction. A similar set of vertical profile observations, excluding sky condition and visibility, was made at multiple heights above the surface by instruments (radiosondes) as they were carried aloft by weather balloons or during descent after being carried high into the atmosphere by rockets (rocketsondes). A large number of surface-based observations sites, that reported surface weather observations almost every hour, were located around the globe while a small subset of these stations made rawinsonde (trophosperic) observations, typically twice daily at 1200 and 2400 UTC.

Deleted: ,

The importance of conventional weather observations to NWP and climate modeling was recognized in the middle of the 20th century when the United Nations contended that no country's national weather service could operate effectively with only indigenous data. Therefore, the sharing of weather data was a logical step for members of the world community. The World Meteorological Convention, by which the World Meteorological Organization (WMO) was created, was adopted at the Twelfth Conference of Directors of the International Meteorological Organization (IMO), which met in Washington, D.C. in 1947. Although the Convention became active in 1950, the WMO commenced operations as the successor to IMO in 1951 and, later that year, was established as a specialized agency of the United Nations by agreement between the UN and WMO.

Deleted: early

Today, the stated purposes of the 185-member WMO include (a) facilitating international cooperation in the establishment of networks of stations for making meteorological,

hydrological and other related observations and (b) promoting the rapid exchange of meteorological information, the standardization of meteorological observations and the uniform publication of observations and statistics. The WMO furthers the application of meteorology to aviation, shipping, water problems, agriculture and other human activities, promotes operational hydrology and encourages research and training in meteorology. Among the WMO's major scientific and technical programs is the World Weather Watch (WWW), which is the backbone of WMO's activities. The WWW currently provides information from about 10,000 land-based surface observations, 7,000 ship-based stations, and 300 moored and drifting buoys carrying automatic weather stations. Each day, high-speed links transmit over 15 million data characters and 2,000 weather charts through 3 World, 35 Regional and 183 National Meteorological Centers co-operating with each other in preparing weather analyses and forecasts. It is through the WMO that the complex agreements on standards, codes, measurements and communications are established internationally (See WMO website http://www.wmo.ch/index-en.html.)

The evolution of space-based meteorology has its genesis in the rocket technology developed by Germany during the late stages of World War II. By the late 1940s, German V-2 and Viking rockets, captured by allied forces, were fitted with instruments and cameras and launched into sub-orbital space to gather meteorological data and cloud images. These photographs of the Earth fueled scientific discussions on the feasibility of space-based weather observations systems.

The successful launch of Sputnik-1 by the former Soviet Union on 4 October 1957 and a challenge subsequently issued by the US President, for national excellence in science and technology, propelled space-based weather observation from discussions into reality. The US launched its first successful satellite, Explorer-1, on 31 January 1958, just prior to the formation of the NASA on 1 October 1958. The Suomi Radiometer became the first successful meteorological sensor flown in space when it was launched on 13 October 1959 by the NASA Explorer 7 mission (Kidder and Vonder Haar, 1995). Data collected by the Suomi Radiometer provided coarse maps of the solar energy reflected by the Earth and the thermal energy emitted from it (Vaughan, 1982 –have Warnecke edited by Vaughan - 1987).

The first dedicated meteorological satellite was launched by the US on April 1, 1960 and lasted for 79 days. This system was officially named the Television and Infrared Observation Satellite (TIROS)-1 since it carried a vidicon camera that was an adaptation of a standard television camera. Data from the camera were transmitted to the ground where an image of 500 lines each with 500 elements was constructed. The initial observations from the TIROS-1 created immense excitement as scientists sought applications for these new data. For the first time, cloud patterns over ocean regions, e.g. the Gulf of Alaska, could be seen advancing upon continents, such as the Northwestern US (Fuller, 1990; add from Vaughan). With the launch of TIROS-8 on 21 December 1963, users around the globe were provided with the ability to receive imagery via the Automated Picture Transmission (APT) direct broadcast system. Thus began a US tradition of providing meteorological satellite data, at no cost, to those in the international

community who had acquired the equipment necessary to receive direct broadcast transmissions from US meteorological satellites.

With the launch of the first meteorological satellites, attention focused on the manual interpretation of image content to assist in manually-generated weather forecasts, including cloud elements, cloud systems, and synoptic weather patterns. The interpretation of data from these early satellites contained many challenges since image geolocation and rectification was crude, data were collected in just a single band, and composites of multiple images were needed to view synoptic-scale weather patterns (Fuller, 1990). Thus, one branch of satellite meteorology originated from the need to interpret cloud and weather patterns manually in these early cloud images in order to improve weather forecasts. Eventually, satellite interpretation guides were created to help instruct the novice in the exploitation of these data. (Dickenson et al., 1974; Brandli, 1976). However, these manuals became outdated as more sophisticated, multispectral imagers became operational and this became a strong motivation for the present text.

**Deleted:** ssue

On 28 August 1964, NASA launched the first satellite in the Nimbus series, which were experimental satellites that carried advanced sensors designed to improve operational systems. Nimbus-1 carried the first High resolution Infrared Radiometer, the forerunner to the Advanced Very High Resolution Radiometer (AVHRR), the first truly multispectral cloud imager. The first AVHRR was carried on the experimental TIROS-N spacecraft in 1978 and it then became an operational system when flown on the National Oceanic and Atmospheric Administration's NOAA-6 spacecraft in 1979. In addition to providing imagery of clouds, the AVHRR was also designed to provide improved data for sea surface temperature analyses.

**Deleted:** ograph

On 16 September 1966, the US Air Force (USAF) launched the first in its series of polar-orbiting meteorological satellites under the Defense Meteorological Satellite Program (DMSP). Data collected by the DMSP provided several major improvements over TIROS and Nimbus data, including more favorable orbital characteristics that produced imagery of much higher resolution (0.33 nm), better sensors that produced data with near-constant resolution from nadir to edge of scan, and superior processing equipment (Fuller, 1990). In addition, since DMSP imagery were precisely registered and contained infrared data, valuable information could be obtained on cloud top heights, which allowed satellite meteorologists to create the first global, computer-generated cloud analysis models (Hamill et al., 1992; Keiss and Cox, 1985; Frye, 1978) which formed the basis for global forecasts (Crum, 1987). From 1976 onwards, the DMSP spacecraft carried the Operational Linescan System (OLS) which has two spectral bands, one in the visible and near-infrared wavelength range and one in the thermal infrared wavelength range.

**Deleted:** canner

**Deleted:** channels

While the USAF initially excelled in the exploitation of cloud information contained in DMSP imagery, NASA focused on the development of new technologies needed for NWP and climate prediction modeling. The Environmental Science Services Administration (ESSA), a forerunner to the National Oceanic and Atmospheric Administration (NOAA), focused on the retrieval of data products and their integration into NWP models. NASA flew the first atmospheric sounding sensor on NIMBUS-X

**Deleted:** ograph

**Deleted:** in 19xx

Similar IR sounders became an operational component on all NOAA satellites starting in 1972. The USAF also became a leader in the design of microwave imagers and sounders as shown in Chapter 2.

In 1994 there was a Presidential Decision Directive in the US to combine the DMSP and NOAA polar-orbiting meteorological satellite systems into a single system, the (US) National Polar-orbiting Operational Environmental Satellite System (NPOESS). The NPOESS Integrated Program Office (IPO) was created to develop, acquire and operate the next generation of US polar-orbiting meteorological satellites. In the meantime EUMETSAT, the European organization which has a long track record in operating geostationary meteorological satellites, had begun planning MetOp, a Meteorological Operational series of polar-orbiting spacecraft similar to the US NOAA spacecraft. In 1998 a cooperation agreement was signed with the objective of joining the space segment of the emerging MetOp programme with the NPOESS program to form a fully coordinated service, thus sharing the costs between the US and Europe.

The electro-optical imager known as the Visible/Infrared Imager/Radiometer Suite (VIIRS), which is the subject of this book, has been specifically designed to meet a subset of the totality of NPOESS requirements. The first VIIRS instrument is scheduled to fly on the NASA's NPOESS Preparatory Project (NPP) and further VIIRS instruments are planned to be flown on all the operational spacecraft of the NPOESS program. VIIRS has 22 channels or bands, but some of these are duplicate between the imagery and radiometry bands, so that the total number of different spectral bands is 20 that extend across wavelengths in the visible, near-IR, mid-IR, and long-wave IR regions of the electromagnetic spectrum. Its heritage is from MODIS, AVHRR, the DMSP OLS, and SeaWiFS sensors.

**Deleted:** will collect data in

**Deleted:** channel

**Deleted:** Operational Linescan System (

**Deleted:** )

We now return to Kalnay et al. (1998) to examine the impact of satellite-based data products upon NWP forecasts. As the accuracy of NWP models improved, the initial atmospheric conditions used to generate forecasts were estimated by a statistical interpolation between a short-range forecast from the model, sometimes called a first guess, and observed conditions. In fact, a whole new specialty in meteorology developed just to address this data assimilation problem. For example, a multi-dimensional method is used operationally in regional and global NWP forecast models at the National Center for Environmental Prediction (NCEP) and requires the solution of extremely large systems of equations, with matrices on the order of the number of degrees of the model, e.g. about $10^6$. A more complex system is used at the European Centre for Medium-Range Weather Forecasts (ECMWF) (Kalnay et al., 1998).

Climate researchers prefer uniform gridded fields over manual interpretation of conventional weather observations for use in their studies. However, every change in a model or the data assimilation scheme could produce a discontinuity in the initial atmosphere conditions which would appear as a climate fluctuation. Consequently, "reanalysis" projects are common to ensure the full data set is generated by a single data assimilation scheme. For example, 40 years of data (1958–97) have been reanalyzed at NCEP to produce initial atmosphere conditions four times daily (Kalnay et al.1996).

**Deleted:** -

**Deleted:** 4-

Once new forecasts are generated with these data, the "re-forecasts" can be used to isolate changes in the forecast skill due solely to changes in the observing systems.

Anomaly correlations are used to assess the impact of changes in models or initial conditions on forecast skill. In this case, anomalies are defined as the difference between an analysis of a forecast field and the corresponding climatology for that month. Thus, the anomaly correlation is the pattern correlation between the forecast anomalies and the verifying analysis anomalies. Experience has shown that a forecast is useful only if the anomaly correlation is greater than about 60% (Kalnay et al., 1998).

Deleted: up

Figure 1.1 compares the anomaly correlation for the 5-day forecasts over the northern hemisphere, north of 20°N, for the operational and reanalysis forecasts at 500 mb. The 5-day forecasts based upon the reanalysis (dashed curve) are skillful (i.e. have an anomaly correlation above 60%) as early as 1958. The improvements in the observing systems, which are the only factor affecting the reanalysis, increase the anomaly correlation from about 65% in the 1950s and 1960s to about 70% by the late 1990s. Thus, if the present-day NWP modeling and data assimilation systems had been available many decades ago, skillful northern hemisphere 5-day forecasts would have been possible with the ground-based surface and upper-air observation network of the late 1950s.

Deleted:

Figure 1.1 also shows the operational 5-day forecasts (solid curves). It is evident that these 5-day forecasts were of little use until the 1980s since anomaly correlation values were less than 60% until that time. However, the skill in these forecasts has dramatically improved to a level of about 75%. In fact, the operational forecasts became better than those of the reanalysis starting in 1991, when the spatial resolution of the operational forecast model was increased to about 100 km, compared to 200-km resolution used in the reanalysis system. Thus, changes in observational data, starting in the mid-1970s, have greatly improved operational 5-day forecasts issued by NCEP.

Deleted: ncreased

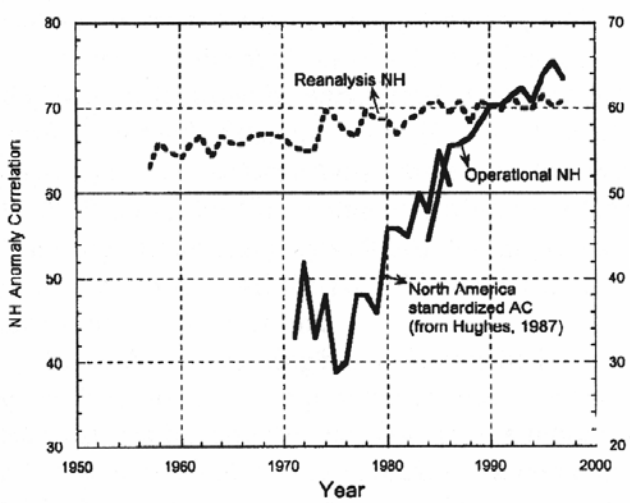

Figure. 1.1 Comparison of the Northern Hemisphere (NH) anomaly correlation from operational and reanalysis forecasts for 500 mb. (Kalnay, 1998).

**Deleted:** (Query: What are the numbers up the right-hand side of the figure?)

Figure 1.2 shows the anomaly correlation scores for both the northern hemisphere and southern hemisphere reanalysis (solid curves) and operational 5-day forecasts (dashed curves). Changes in the observing system have produced a much larger effect in the southern hemisphere than in the northern hemisphere, where there are far fewer surface-based observations. Thus, the improvement in the southern hemisphere anomaly correlation is due to the use of meteorological satellite data. (The use of satellite-derived temperature retrievals started in 1975 from the TIROS Vertical Temperature Profile Radiometer (VTPR) sensor, which was first launched in 1972, and subsequently from the TIROS Operational Vertical Sounder (TOVS), after its first launch in December 1978.) Thus, the marked improvements in the reanalysis forecasts for the southern hemisphere are mostly due to better operational atmospheric profile retrievals from TOVS, as well as some improvements in the cloud-tracked wind, which is discussed in a later section of this chapter.

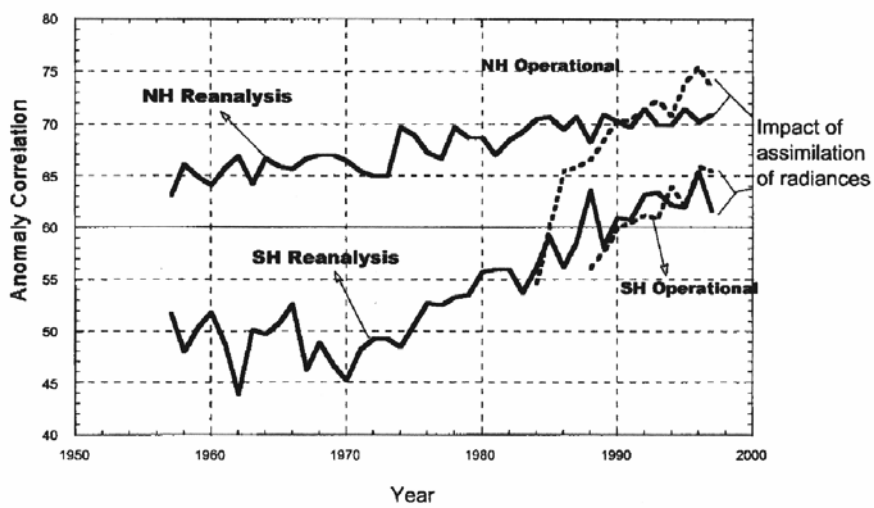


Figure 1.2 Comparison of operational and reanalysis 5-day forecast anomaly correlations for the northern hemisphere (NH) and the southern hemisphere (SH) at 500 mb. (Kalnay, 1998).

## 1.3 ADDITIONAL APPLICATIONS OF METEOROLOGICAL SATELLITE DATA

While NWP forecasts have profited from the use of satellite-based meteorological observations of radiances as well as temperature and moisture profiles from atmospheric sounders flown in polar-orbits, additional applications, of equal importance, have been developed using other sensors and observing platforms. The scope of this text limits the discussion of this topic to a brief overview of several key data products. Rao et al. (1990) provided more details on the numerous satellite data products developed by NOAA.

### 1.3.1 Sea Surface Temperature Analyses

As noted earlier, NWP is an initial value problem in which computer models of the atmosphere start from the best estimate of the present state of the atmosphere and integrate forward in time to predict the evolution of the atmosphere. The ocean's surface satisfies one set of the boundary conditions for NWP models and oceanography models alike. Since oceans cover 75% of the Earth's surface, it is no surprise that considerable effort has been made to generate highly accurate, global sea surface temperature (SST) analyses.

The longest data set of SST observations is based on observations initially made from ships (capturing buckets of seawater and measuring the temperature with a thermometer). From about 1870 onwards these ship observations were sufficiently frequent to permit a global SST analysis to be made but not at the horizontal and temporal resolution needed to support NWP and climate modeling.

Remote sensing techniques have been applied to radiometric data to retrieve SST analyses after correcting for atmospheric attenuation due primarily to water vapor. Saunders (1967) was the first to report on such a method to retrieve SST using an aircraft to make two measurements of a single location through different viewing geometries. Anding and Kauth (1970) proposed a method to obtain SST values based on measurements in two different wavelengths. While some disagreements were noted in the literature (Maul and Sidran, 1972; Anding and Kauth, 1972), a more complete theoretical justification for the method was demonstrated by McMillin (1971).

Subsequently, NOAA began providing global SST estimates with the launch of the first Improved TIROS Operational Satellite (ITOS) in 1970 (See Chapter 2) using the single 11 μm band. Histogram procedures were developed both for cloud detection and reducing instrument noise but only crude empirical estimates of water vapor could be obtained with this single band. After the launch of NOAA-2 in the ITOS series (late 1972) satellite sounder data became available from the VTPR. Profiles of temperature and humidity were calculated and used to make atmospheric corrections for use in SST analyses from the 11 μm band (McClain et al., 1985). However, because the VTPR data were dependent upon the derived SST and vice versa, and because the resolutions of the profiles data (400 km) was much lower than the SST data (100 km), the resulting values of the SST were relatively poor. In 1976, NOAA changed to a multiple band approach to retrieve SST fields by combining several radiometer pixels along with VTPR data to eliminate the use of temperature and moisture profiles in correcting for atmospheric water vapor (Walton et al., 1976).

These early successes in the retrieval of SST with remotely-sensed data were deemed sufficiently promising that the AVHRR instrument was designed, built, and flown to obtain operational sea surface temperatures from space. With the launch of NOAA-7 in 1981, which carried the first 5-channel AVHRR sensor, NOAA implemented the multi-channel sea surface temperature (MCSST) algorithms which gave the NWP community access to global SST fields with an estimated accuracy of 1 K or better (McMillin and

**Deleted:** channel

**Deleted:** channel

**Deleted:** channel

**Deleted:** Nevertheless, t

**Deleted:**

**Deleted:** less

Crosby, 1984). Statistics now show a capability to retrieve global analyses with these algorithms to an accuracy of 0.78 K with daytime and 0.58 K with nighttime AVHRR imagery (McClain et al., 1983; McClain et al., 1985). While various approaches have been taken to further improve upon the accuracy of SST analyses from AVHRR data (Emery et al., 1994; Walton, 1988), there was little improvement in this global analysis capability during the previous decade (Barton, 1995).

For climate modeling, the minimum error required of SST is specified as between ± 0.2 - 0.3 K (Webster and Fieux, 1984; Minnett, 1986; Watts et al., 1996). Thus, it became evident that further improvements in global SST analyses required the use of advanced satellite data with technologies superior to those of the AVHRR sensor. Thus, the NPOESS program established minimum system-level SST accuracy requirements of 0.5 K with a goal of achieving accuracy in the 0.1 - 0.35 K range (NPOESS VIIRS SRD, 2000).

Simulations have shown that improved SST analyses can be also achieved using the MCSST algorithms with higher quality satellite measurements (Hutchison et al., 1999). Results shown in Figure 1.3 suggest that reducing sensor noise from 0.12 K, the design specification of AVHRR, to 0.07 K would allow the minimum NPOESS SST requirements to be met with the existing 3-channel MCSST algorithm, assuming a perfect cloud mask. NASA's MODIS sensor contains an NEΔT design specification of 0.05 K for bands used to retrieve SST. However, further improvement in algorithm and/or sensor technology might be needed to meet the NPOESS SST goal for the climate community.

Alternatively, improved satellite measurements, based upon lower sensor noise, can be achieved by taking multiple observations of each field-of-view (Stewart, 1985). This approach is reminiscent of the method of Saunders (1967) and has been implemented in the Along-Track Scanning Radiometer (ATSR) flown on the European Remote Sensing Satellite (ERS) series (Za'vody et al., 1995).

While the feasibility of retrieving improved SST fields was demonstrated soon after the launch of the AVHRR sensor (McMillin and Crosby, 1984; McClain et al., 1985, Minnett, 1986), there remained the challenge of detecting cloud contaminated pixels and removing them from the SST analyses (Schluessel et al., 1987), especially stratus in nighttime imagery and thin cirrus in both daytime and nighttime imagery. Undetected clouds can be especially problematic in the more coarse resolution AVHRR satellite data, i.e. global area coverage (GAC), which has a nominal resolution of 4-km at nadir that degrades to nearly 6-times larger at edge of scan. Methods were developed early on to help detect fractional cloud-filled pixels and eliminate them from SST analyses (Coakley and Bretherton, 1982). Bell and Wong (1981) demonstrated that the contrast between nighttime stratus and ocean surfaces was greatly enhanced in the AVHRR 3.7 μm band over that present in the 11 μm band that was used by most meteorologists to identify clouds in imagery. The improved contrast between a stratus cloud and its cloud-free surroundings was due to the lower emissivity of water droplets in the stratus clouds at the shorter wavelength compared to the longer, which will be discussed later in the text. Thus, the signature of stratus clouds was greatly increased in a composite image made

**Deleted:** h

**Deleted:** been

**Deleted:** past

**Deleted:** accuracy

**Deleted:** +/-

**Deleted:** channels

from the brightness temperature (BT) difference of these two AVHRR bands centered at 3.7 μm and 11.0 μm (i.e. $T_{B3.7}$ - $T_{B11.0}$). Subsequently, Inoue (1985) demonstrated that the contrast between cirrus and its cloud-free surrounding region could be greatly enhanced by looking at a composite (difference) image made with the 11 μm and 12 μm AVHRR bands (i.e. by looking at feature $TB_{11.0}$ - $TB_{12.0}$). Saunders and Kriebel (1988) combined these and other methods into a new formalism that exploits multiple "bi-spectral" cloud signatures that resulted in significantly improved cloud screening for SST analyses. Their approach was incorporated into the cloud model AVHRR Processing scheme Over Land, Clouds, and Ocean or APOLLO (Kreibel and Saunders, 1988; Gesell, 1989). A short time later, NOAA began implementing its own multi-spectral, automated cloud analyses model, known as CLouds from AVHRR (CLAVR), as described by Stowe et al. (1991; 1999) while the US Air Force began a similar program known as Support of Environmental Requirements for Cloud Analyses and Archive or SERCAA (Gustafson et al., 1994). Most recently, National Aeronautics and Space Administration (NASA) scientists developed another global cloud detection model for use with data collected by the MODerate Resolution Imaging Spectroradiometer (MODIS) sensor flow on Earth Observing System (EOS) spacecraft (Ackerman et al., 1998).

Cloud-contaminated pixels have been identified as a major error source in SST analyses of AVHRR data (Schluessel et al., 1987; Minnett, 1986). Undetected clouds can be especially problematic in the more coarse resolution AVHRR satellite data, i.e. global area coverage (GAC), which has a nominal resolution of 4-km at nadir that degrades to nearly 6-times larger at edge of scan. Methods were developed early to help detect fractional cloud-filled pixels and eliminated them from SST analyses (Coakley and Bretherton, 1982). But the first comprehensive cloud detection algorithms were published much later by Saunders and Kriebel (1988) and, as previously noted, NOAA used this approach in the development of the CLAVR algorithms specifically to eliminate cloud-contaminated pixels from SST analyses.

**Deleted:** channels

**Deleted:** channels

**Deleted:** for

**Deleted:** Ref.

**Deleted:** .

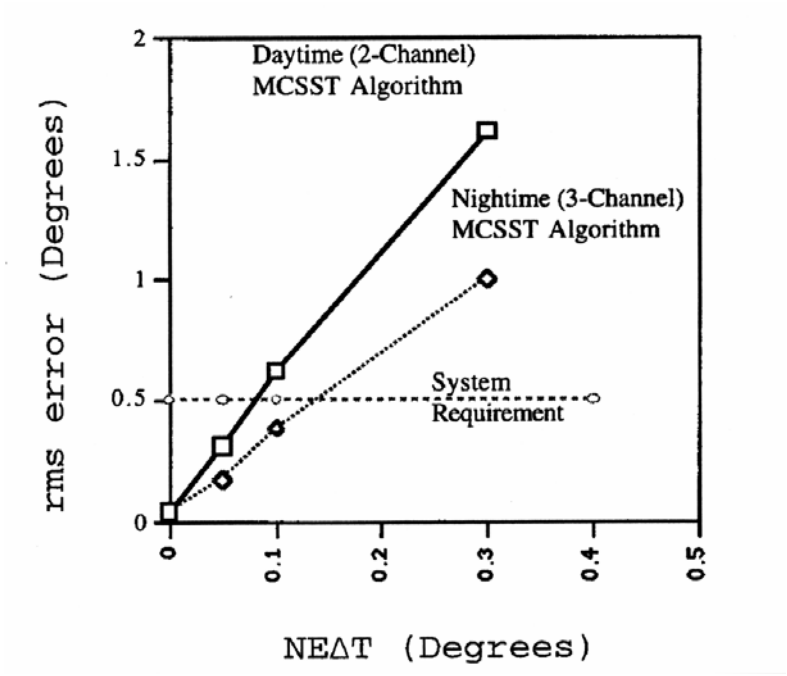


Figure 1.3 Simulations demonstrate the impact of sensor NEΔT on SST analyses using 2-channel and 3-channel multichannel sea surface temperature algorithms.

Since an imperfect cloud mask has been identified as a key error source in the retrieval of SST fields, additional simulations were completed to quantify this effect. In these simulations, a synthetic stratocumulus cloud and SST field was created and satellite-based observations created using the MODTRAN radiative transfer model (Berk et al., 1989). Next, numerous automated cloud masks were systematically generated and SST analyses retrieved on all pixels classified as cloud-free. The accuracy of a particular automated cloud and SST analysis (each dot on the curve) was created by pixel-level comparisons with the cloud mask and the SST field used to generate the synthetic data.

The results, shown in Figure 1.4, quantitatively demonstrate the impact of undetected cloud-contaminated pixels on SST analyses (Hutchison, unpublished) It is interesting to note that the most accurate SST analysis does not coincide with the most accurate cloud mask. The best SST analysis is realized when the cloud mask is slightly pessimistic, i.e. no sub-pixel clouds are introduced into the SST analysis. However, the most accurate automated cloud analysis, shown in Figure 1.4 to exceed 95%, produces an SST analysis that fails to meet NPOESS requirements of 0.5 K (horizontal dashed line). Additionally, a cloud analysis of 90% accuracy (the vertical dashed line) produces a totally unacceptable (~1.3 K) SST accuracy, if the errors are due to too few clouds being detected ; however, the same cloud mask accuracy produces an SST analysis that meets requirements (~0.4 K) if errors result only from too many clouds being detected in the mask. Thus, these simulations show convincingly the dynamics between a cloud and SST analysis – the

**Deleted:** which would meet NPOESS system-level requirements,

**Deleted:** minimum

**Deleted:** mask

**Deleted:** that meets minimum NPOESS requirements for cloud cover

**Deleted:** horizontal

**Deleted:** nalysis

**Deleted:**

**Deleted:** un

**Deleted:** clouds

optimum SST analysis is obtained when no pixels containing fractional cloud cover are introduced into the analysis. (Note: impacts of clouds on SST fields would be more severe if the clouds were optically thin cirrus, since the difference between ocean surface and cloud top temperatures would be larger for these clouds than the stratocumulus cloud used in these simulations.)

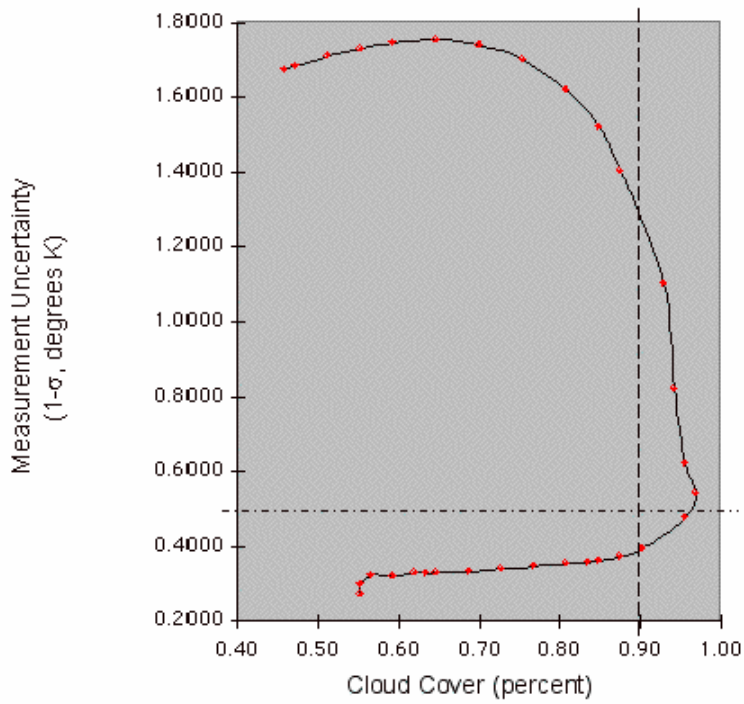


Figure 1.4 Simulations demonstrate the impact of an imperfect cloud mask on meeting sea surface temperature (SST) requirements of 0.5 K. SST accuracy is strongly impacted if clouds fail to be detected in the cloud mask but no impact is noted if the mask over-detects them.

**Deleted:** satisfying

**Deleted:** NPOESS SST

**Deleted:** accuracy

SST analyses derived from NPOESS sensor data will further improve upon existing analyses due to the improved characteristics of the VIIRS global data, e.g. spatial resolution of 750 m resolution at NADIR and 1.5 km at edge of scan. In addition, SSTs generated from NPOESS passive microwave radiometers will also achieve a 0.5 K accuracy under cloudy conditions, except for precipitating clouds. Thus, the NPOESS provides, for the first time, a global SST analyses generated under all weather conditions.

### 1.3.2 Climate Modeling

A very active global research program led to numerous operational applications for meteorological satellite data and the value of these data for climate monitoring and prediction has become indispensable. For example, the discovery of the ozone hole over

**Deleted:** ,

Antarctica (Farman et al., 1985) placed new emphasis on research directed toward improved understanding of anthropogenic activities on climate modeling. In addition, scientists have long been aware of the steady increase in greenhouse gases in the atmosphere, based upon in situ measurement such as those made on carbon dioxide levels from observations at Mauna Loa Observatory, Hawaii, as shown in Figure 1.5 (Liou, 2002). As record temperatures became common across the world, predictions of global warming and melting of the polar ice-caps sounded alarms throughout the scientific community. Also, the recognition of El Ninõ and its effects upon precipitation patterns further reduced the gap between long-term climatic and near-term NWP forecasting.

Deleted: o

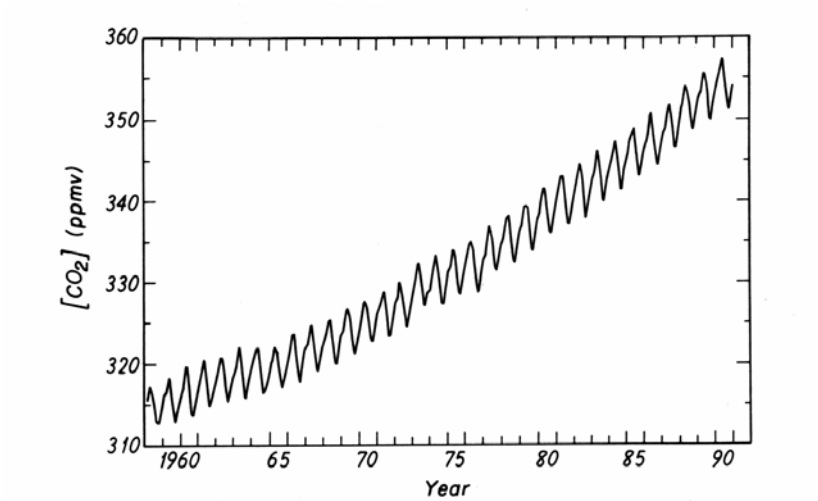


Figure 1.5 Concentration of atmospheric $CO_2$ at Mauna Loa Observatory, Hawaii expressed as a mole fraction in parts per million of dry air for the period 1958-1990 (Liou 1992).

Deleted: s

Early studies to predict, with certainty, changes in the Earth's climate caused by the aforementioned and other mechanisms was impacted by the absence of high-quality, global environmental data products. While AVHRR IR bands provided the highly-calibrated measurements needed to generate SST analyses, similar data were not available in the visible and near-infrared bands. Thus, calibration of these AVHRR bands was based upon pre-launch sensor characterizations which were found to be inadequate for quantitative applications (Abel, 1991) and changed with time on orbit (Che and Price, 1992). Special procedures were developed to obtain on-orbit updates to the pre-launch calibration using special airborne, ground, and space-based observations. However, it became most difficult to create highly correlated data products from multiple AVHRR sensors flown on different satellites, as required to establish long-term knowledge of the Earth-atmosphere system (Rao and Chen, 1993).

Deleted: channels

Deleted: channels

Thus, the importance of long-term, highly accurate observations of the entire Earth-atmosphere system was identified by members of the WMO as critical to understanding natural and anthropogenic changes in the global climate system. For example, clouds are the single largest regulator in the Earth's energy budget and it is estimated that the Earth

is approximately 50 percent cloud covered at any give time (Liou, 1980). However, global cloud climatologies vary greatly depending on the data and algorithms used to construct them (Hughes, 1984). Uncertainty in global cloud cover estimates arise, in part, from difficulties associated with the accurate detection of optically thin cirrus clouds. Initial cloud climatologies were based solely upon surface observations (London, 1957) and the specification of cirrus clouds was among the problems inherent in these data (Hughes, 1984; Stowe, 1984). In addition, these cirrus clouds have historically represent difficulties for global cloud climatologies derived from meteorological satellite data due to difficulties in accurately detecting them with current operational satellite sensors, due to the lack of spectral resolution of these sensors (Hutchison et al., 1995; Hutchison and Hardy, 1995; Hutchison and Choe, 1996). Cirrus clouds also have highly variable radiative properties which are poorly known (Wylie et al., 1994) and thus represented the largest area of uncertainty in modeling atmospheric radiative transfer processes (Liou, 1986). To make matters worse, studies have shown that a four percent error in global cloud cover could offset the predicted warming due to a doubling of the $CO_2$ content in the atmosphere (Randall et al., 1984). Thus, the absence of reliable, accurate measurements on the status of the Earth-atmosphere system is an obstacle to climate modeling.

**Deleted:** Jones

**Deleted:** 92

**Deleted:** ed

**Deleted:** the

**Deleted:** ,

Since it was widely recognized that an accurate global cloud cover climatology suitable for use in climate change studies did not exist, the International Satellite Cloud Climate Project (ISCCP) was established by the WMO as the first project of the World Climate Research Program (Schiffer and Rossow, 1983; Rossow et al., 1985). Subsequently, advances were made in cloud detection methodologies, based upon bi-spectral techniques (Inoue, 1985; Saunders and Kriebel, 1988; Hutchison and Hardy, 1995) and new sensor technologies were recommended to obtain improved contrast between cloud signatures, atmospheric water vapor, and surface features (Ackerman et al., 1990; Gao et al., 1993). Thus, a primary goal of the NASA EOS program was to obtain high-quality satellite-based observations throughout a 15-year period that can be used to derive products suitable for climate change research. Central to this data collection effort were the EOS Terra spacecraft, launched in December 1999, and the EOS Aqua spacecraft, launched in May 2002. MODIS was a key sensor on both spacecraft and collected data in 36-spectral bands having horizontal resolution of 250, 500, and 1000m. Both EOS Terra and Aqua missions were designed to collect data over at least a 5-year lifetime (King and Greenestone, 1999). MODIS data and products would be augmented by VIIRS, with the first VIIRS instrument scheduled to be launched in 2006 as part of the NASA NPOESS Preparatory Project (NPP) as a replacement for EOS Terra. Subsequent VIIRS launches are to begin in 2009 with the launch of NPOESS-1 to extend the collection of high spatial and spectral resolution imagery needed to further improve upon current global cloud climatological statistics.

### 1.3.3 Tropical Storm Monitoring

Faced with programmed reductions in weather reconnaissance aircraft, due to budgetary cutbacks, a DMSP direct broadcast readout site was established at the Joint Typhoon Warning Center on Guam in May, 1971 to provide tropical cyclone surveillance coverage of the broad Pacific Ocean area. Coincident with the activation of the DMSP site,

research was conducted to quantify the potential value of DMSP data as an alternative to aircraft reconnaissance (Arnold, 1975). The objective of this research program was to assess the viability of satellite-derived storm characteristics, i.e. accurately determining the location of the circulation center, assessing the current intensity of the storm, and predicting the storm's intensification or weakening during the following 24 hours. Storm intensity analyses and prediction were based upon the characteristics observed in the storm and its recent history using techniques developed by Dvorak (1973) as illustrated in Figure 1.6.

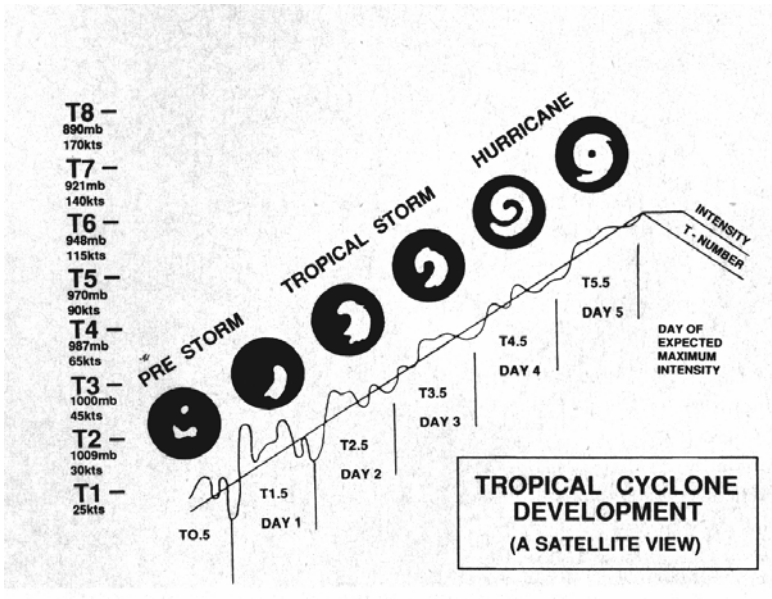


Figure 1.6 Model on the evolution of tropical storms used in intensity analysis based upon the Dvorak method (Rao, 1990).

Deleted: 2000

Confidence levels were established to assess the accuracy of location of the tropical storm circulation center based upon the ability of the satellite meteorologist to observe a well-defined eye or circulation center and the type of gridding used, i.e. geographic or ephemeris. The Position Code Number (PCN) is defined as (1) visible eye and geographic gridding, (2) visible eye, ephemeris gridding, (3) well-defined circulation center, geographic gridding, (4) well-defined circulation center, ephemeris gridding, (5) poorly-defined circulation center, geographic center, and (6) poorly-defined circulation center, ephemeris gridding. Satellite derived analyses were compared with aircraft reconnaissance reports to determine the mean error in storm positions as a function of PCN as shown in Table 1.1.

Deleted: s

Deleted: were

Table 1.1 Guam DMSP tropical cyclone position statistics for 1972.

| Position Code Number | Mean Error (km) | Sample Size |
|---|---|---|

| | | |
|---|---|---|
| 1 | 26.3 | 104 |
| 2 | 29.3 | 53 |
| 3 | 39.4 | 100 |
| 4 | 37.4 | 39 |
| 5 | 55.6 | 137 |
| 6 | 56.3 | 157 |
| Total | 44.4 | 590 |

Ultimately, the satellite-derived analyses of tropical storms became an integral part of the Joint Typhoon Warning Center's operations and resulted in greater use by the US across the Pacific Ocean and ultimately in the Atlantic Ocean region where storms directly affect major populations centers from Central to North America. The judicious use of limited tropical storm reconnaissance aircraft with satellite-derived analyses of these storms at the Joint Typhoon Warning Center's became known as the Selective Reconnaissance Program (Arnold, 1975).

### 1.3.4 Satellite-Derived Wind Fields

Satellite-derived wind fields can be obtained by tracking the movement of cloud features and patterns in a sequence of two or more images and these remotely sensed data have made a positive contribution to NWP modeling (Kalnay et al., 1998). While satellite-derived wind fields are typically based upon data collected by satellites in geostationary orbit, data from successive polar-orbits can be used to retrieve wind fields over high latitude regions (Key et al., 2003).

**Deleted:** 2

Figure 1.7 shows MODIS band 31 (11 μm) data for two 5-minute granules over part of Arctic (left) and Antarctic (right) regions collected during August 27 and 28, 2003 respectively. Cloud and water vapor targets were identified with an automated technique using three sets of images from consecutive overpasses about 1.5 hours apart. Winds are shown for three levels, i.e. low, middle, and high. Since the procedure exploits thermal emissions, these data products can be created during daytime and nighttime conditions, i.e. including the polar night.

**Deleted:** and 27

**Deleted:** (Reference xxxx)

The European Centre for Medium Range Weather Forecasting (ECMWF) has demonstrated a positive impact from the use of MODIS polar winds in their short-range forecast models. Figure 1.8 shows sample results. These panels show forecast scores in terms of anomaly correlation for the 1000 hPa (left) and 500 hPa (right) geopotential height over the Arctic (top) and Northern Hemisphere (bottom), for model forecasts with (red) and without (blue) the MODIS polar winds. The forecast score is the anomaly correlation between the forecast and its verifying analysis (model run with other data

assimilated), expressed as a percent. The figures show that forecasts of geopotential height are improved when the MODIS winds are assimilated for the Arctic, Northern Hemisphere, and the Antarctic (not shown).

Figure 1,7 and Figure 1.8 were obtained from the website of the Cooperative Institute for Meteorological Satellite Studies (CIMSS) at:
http://stratus.ssec.wisc.edu/projects/polarwinds/polarwinds.html).

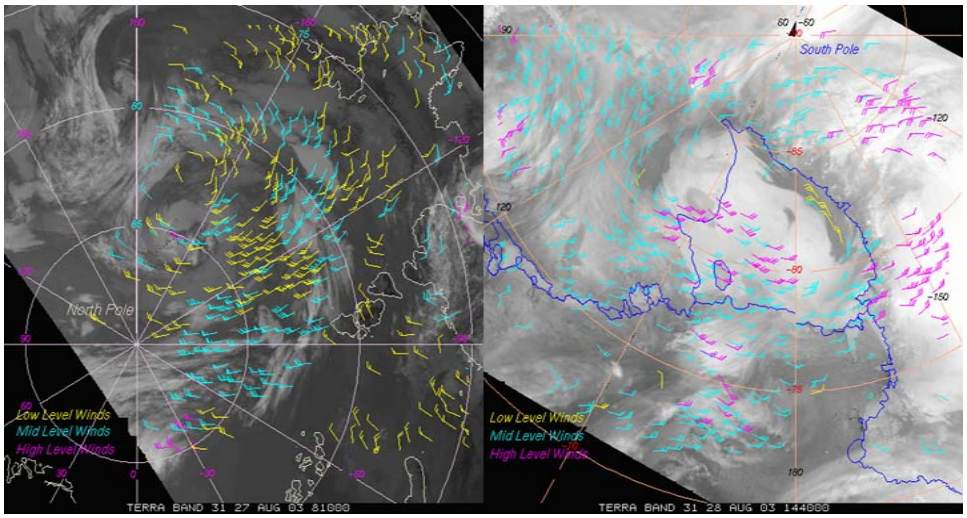


Figure 1.7 MODIS Terra water vapor imagery over northern polar regions (left panel) and wind fields (low-level wind, mid-level wind, high-level wind) derived from analyses (right panel) of cloud movements observed in successive orbits

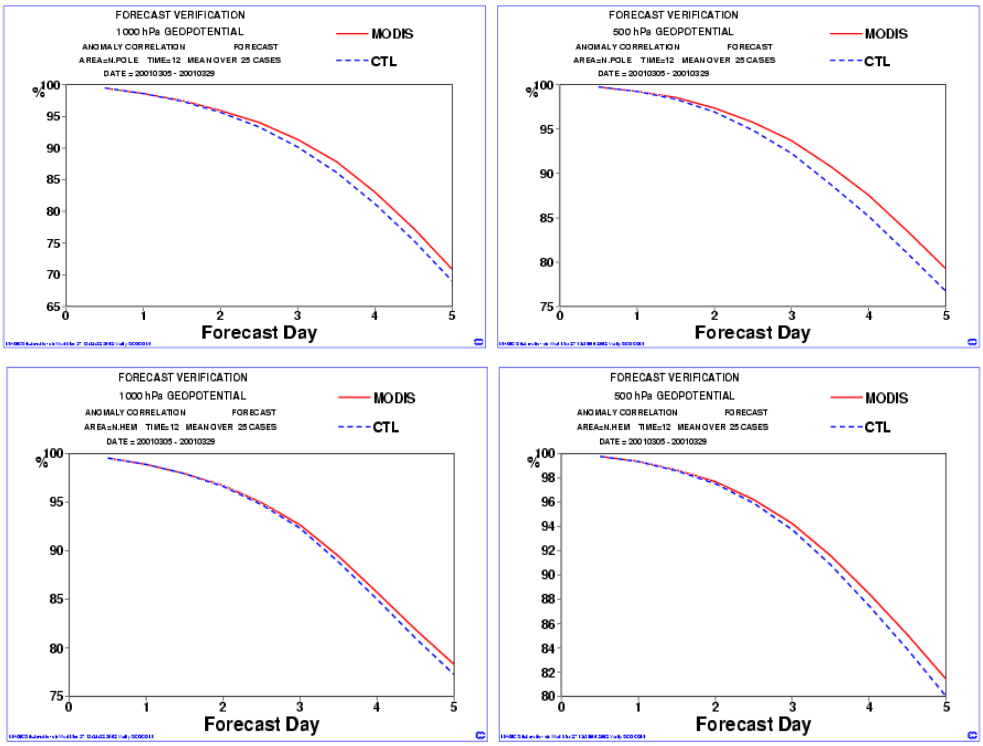


Figure 1.8 Improvements in forecast scores (anomaly correlation) at ECMWF for the 1000 hPa (left) and 500 hPa (right) geopotential height over the Arctic (top) and Northern Hemisphere (bottom), for model forecasts with (red) and without (blue) the MODIS polar winds.

# Chapter 2

## METEOROLOGICAL SATELLITE SYSTEMS

### 2.1 EVOLUTION OF SATELLITES AND SENSORS

This section relies heavily on two major sources: the book by Rao *et al.* (1990), which describes the first 30 years of meteorological satellites, and another by Kramer (2002), which describes all the primary Earth-observing satellite systems that have been launched by member nations of the WMO. Before discussing the evolution of satellite sensors, a brief overview is provided on the principal orbits used to collect meteorological satellite data.

While in principle many different types of orbits can be constructed, in practice only two types are important for meteorological and other environmental satellite systems: polar and geostationary orbits. Polar-orbiting operational environmental satellites are commonly referred to as POES systems and are typically positioned into orbits at an altitude between 700 -1000 km above the surface of the Earth with an orbital period of approximately 100 minutes. POES systems are generally in a sun-synchronous orbit, that is characterized by an inclination angle close to $90^o$ in which the satellite precesses slowly so that the relative orientation of the orbit and the line joining the Sun to the Earth remains constant. Consequently, each of consecutive orbits of the satellite passes over the equator at approximately the same local (sun) time and it passes over a given point on the surface of the Earth at approximately the same local time each day. POES satellites orbit the Earth about 14 times each day; thus, a given point near the equator will be viewed once in daylight and again during nighttime conditions. Data products from POES systems are most widely used in meteorological, oceanographic, and hydrological applications. For example, products generated from satellites flying in these orbits are used to obtain the atmospheric soundings of temperature and humidity profiles for numerical weather prediction modeling as well as sea surface temperatures as discussed in Chapter 1. On 28 August 1964 Nimbus-1 became the first environmental satellite to be launched into a sun-synchronous orbit; but, today all operational, meteorological polar-orbiting, satellites fly in this type of orbit.

Geostationary meteorological satellites are launched into orbits at a height of approximately 36,000 km above the Earth. Such an orbit is equatorial, circular, and has a period of exactly one day. Satellites in this type of orbit remain relatively constantly above a point on the Earth's surface. These meteorological satellites are commonly referred to as GOES systems and provide full-disk images of the Earth every 30 to 60 minutes, but images of smaller regions can be obtained more frequently. Geostationary satellite data are highly valuable for monitoring severe weather features such as thunderstorms throughout their lifecycle. In addition, multiple geostationary satellite images can be used to create time-lapse sequences and to derive wind vectors from cloud motions in lower-latitude regions for numerical weather prediction models as discussed in Chapter 1. Time lapse images are very valuable for education and training purposes

(Warnecke and Zick 1981, Warnecke 1987, Warnecke *et al.* 1987, Zick 1987) and they routinely appear on TV weather broadcasts.

**Formatted:** Font color: Auto

**Formatted:** Font color: Auto

**Deleted:** NASA's Applications Technology Satellite (ATS-1) was the first system launched into geostationary orbit on 7 December 1966. (Is this statement in contradiction with beginning sentence in Section 2.1.2?)

### 2.1.1 Polar-Orbiting Environmental Satellite (POES) Systems

Responsibility for US operational civilian meteorological satellites was assigned by Congress to the US Weather Bureau in 1962. In 1965 the Bureau, renamed the National Weather Service, was made part of a newly created Environmental Science Services Administration (ESSA) which, in 1970, became the National Oceanic and Atmospheric Administration (NOAA). The evolution to NOAA was reflected in the names given to the spacecraft as increased importance was place upon space-based weather observations. Many details of the individual spacecraft and the instruments carried on them are given in Kramer (2002). Brief highlights are provided herein.

Following the launch of the first Television InfRared Observation Satellite (TIROS-1) in 1960, there have been five generations of polar-orbiting meteorological satellites developed by NASA and flown by NOAA as outlined in Table 2.1.

- The first generation Television InfRared Observation Satellites, TIROS-1 – TIROS-10, were developmental satellites since they were used to mature the technologies needed for subsequent operational observing systems. Satellites in this series had a short life-span, e.g. TIROS-1 was operational for only 78 days. The main instruments flown on this satellite series were TV cameras which provided daily cloud cover pictures. Direct broadcast started when an APT camera was introduced with the launch of TIROS-8 on 21 December 1963. The first TIROS system to fly in sun-synchronous orbit was TIROS-9 launched on 22 January 1965. Earlier satellites flew at inclination angles of ~ 48-58 degrees.
- The second generation was marked by the creation of the US Environmental Science Services Administration (ESSA) and the launch of ESSA-1 on 3 February 1966. This was the beginning of the world's first operational weather satellite system which consisted of two POES spacecraft in sun-synchronous orbit crossing the equator during local morning and afternoon. The even-numbered satellites of ESSA carried APT cameras to provide direct broadcasts to the ground.
- In 1970, the National Oceanic and Atmospheric Administration (NOAA) was created within the Department of Commerce (DoC) to operate the US POES system which coincided with the third generation of POES satellites, known as the Improved TIROS Operational System (ITOS). The first ITOS satellite was launched on 11 December 1970 and carried the Scanning Radiometer which measured reflected radiation in the 0.52-0.72 μm band and emitted terrestrial energy in the 10.5-12.5 μm atmospheric window. (Many people thought that the Scanning Radiometer (SR) provided the first daytime and nighttime global coverage of the Earth. In reality, that capability was first provided by DMSP satellites which will be discussed later.) The SR also provided highly calibrated IR radiances across the temperature range of 185 – 330 K. The NASA ITOS-D or NOAA-2 carried the first IR atmospheric sounder, the Vertical Temperature Profile Radiometer (VTPR), when it was launched on 15 October 1972. In addition, this satellite also carried the first Very High Resolution Radiometer

**Deleted:** O

(VHRR) that provided improved resolution over the SR, i.e. 0.9 km compared to 4 km.

- The NOAA fourth generation of POES satellites was inaugurated by the launch of TIROS-N on 13 October 1978. The later spacecraft of this generation (from NOAA-8 onwards) were designated the Advanced TIROS-N (ATN) series. The ATN series used a larger satellite bus that enabled additional sensors to be carried along with operational sensors.
- The fifth generation of POES satellites continued the progression to more advanced systems technology. These satellites carried the 3rd version of the AVHRR, known as AVHRR/3, along with a new generation of microwave sounders known as the Advanced Microwave Sounder Unit - Temperature (AMSU-A) and Advanced Microwave Sounder Unit - Moisture (AMSU-B).

Table 2.1 – Overview of the US civilian polar meteorological programs (Kramer 2002).

| | |
|---|---|
| 1st generation launched between 1 April 1960 and 2 July 1965 | Television InfRared Observation Satellite (TIROS) series [TIROS-1 (1960) to TIROS-10 (1965)] |
| 2nd generation launched between 3 February 1966 and 26 February 1969 | TOS (TIROS Operational System) series as pre-launch designation. The in-orbit satellite designation was ESSA [ESSA-1 (1966) to ESSA-9 (1969)], after the spacecraft's operating agency. |
| 3rd generation launched between 11 December 1970 and 16 March 1976 | ITOS (Improved TIROS Operational System) series as pre-launch designation. The in-orbit satellite designation was NOAA [NOAA-1(1970) to NOAA-5 (1976)] |
| 4TH generation launched between 13 October 1978 and 30 December 1994 | After TIROS-N (1978) the pre-launch designation changed to NOAA-A (the corresponding in-flight name was NOAA-6). The pre-launch letter designation was kept throughout. NOAA-8 to NOAA-14 were designated ATN (Advanced TIROS-N) spacecraft, equipped for S&R (Search and Rescue) and development instruments. |
| 5th generation launched between 13 May 1998 and present. To be followed by NPOESS | NOAA-15 (pre-launch NOAA-K,), NOAA-L, -M, -N, and –N' incorporate advanced instrumentation and are designated "NOAA next". |

Thus, during its first 20 years, the evolution of sensor technology was a key characteristic of the US civilian POES program. In the first half of this period, the imaging capability was first provided by simple TV cameras to obtain cloud cover during sunlight conditions while the APT camera was added to TIROS-8 in 1963 to provide this information directly to weather forecasters in field units. Later, POES spacecraft flew in sun-synchronous orbits to obtain added daytime imagery. During the second half of this period, it became apparent that satellite-based observations could also be used for other applications, such as the retrieval of sea surface temperature fields for numerical weather prediction and climate models as discussed in Chapter 1. Thus, the 1970s saw further development in sensor technology. First came the two-band SR flown on NOAA-1 which delivered cloud imagery during daytime and nighttime conditions. Shortly thereafter, the VHRR sensor was flown on NOAA-2 to provide improvements in resolution and global coverage, i.e. it had an IFOV of 0.9 km, a swath width of 2580 km and two spectral bands (0.6-0.7 µm and 10.5-12.5 µm). However, as we shall see shortly, TIROS-N brought unique new data to the international community and helped to propel a flurry of

**Deleted:** s

**Deleted:** channel

research into new applications for POES data. The reason for this increased emphasis of remotely-sensed data was due, at least in part, to the availability of high quality data, at no cost, to all who could build for themselves, or afford to purchase from a commercial source, the equipment needed to track the satellite, receive its direct broadcast data, and process them in real-time as the POES satellites orbited the Earth. Thus, began a US tradition of providing a direct broadcast capability on operation meteorological satellites that continued on NASA EOS satellites, although the data rates have grown immensely. A similar capability will continue during the NPOESS era; however, before turning toward the future of POES, which includes NPOESS and ESA's MetOP systems, the ATN satellite series will be examined in greater detail.

Deleted:

#### 2.1.1.1 The Advanced TIROS-N (ATN) Satellite Series

The launch of TIROS-N on 13 October 1978 marked the start of the fourth generation of TIROS systems due to the significant advancement in technology used with these operational environmental satellites. As previously noted, TIROS-N carried the first AVHRR instrument. After it, next were launched NOAA-6 on 27 June 1979 followed by NOAA-7 on 23 June 1981. Satellites from NOAA-8 to NOAA-14 were called the Advanced TIROS-N (ATN) series because these spacecraft were enlarged and provided with additional solar panels that provided more power. The additional space enabled ATN spacecraft to carry extra instruments. Additionally, these systems provided higher quality, continuous S-band direct broadcast to the user community.

Deleted: hroug

Deleted: h

Deleted: DB

The TIROS-N satellite and its successors carried instrument that were provided through collaboration with several nations, including the US, the UK, and France. These satellites carried the TIROS Operational Vertical Sounder (TOVS), the ARGOS data collection system, the Space Environment Monitor (SEM), and the Advanced Very High Resolution Radiometer (AVHRR).

Deleted: a

TOVS consisted of an integrated, three-instrument system used to retrieve atmospheric temperature and moisture profiles from the Earth's surface into the stratosphere. This suite consists of:

Deleted: s

Deleted: ed

- The High-resolution InfRared Sounder (HIRS/2). The HIRS/2 was a 20-band instrument that sampled the atmosphere at wavelengths from about 3.75 to 15 μm in bands selected to penetrate to different depths of the atmosphere. One band was included in the visible region, at about 0.7 μm to view the Earth's surface. The data acquired could be used to compute atmospheric profiles of temperature and humidity at heights up to about 40 km. The HIRS/2 was replaced by the HIRS/3, which provides slightly higher spatial resolution data, i.e. 16 km versus 30 km.

Deleted:

Deleted: channel

Deleted: eventually

Deleted: d

- The Stratospheric Sounding Unit (SSU). The SSU was a three-band IR instrument, provided by the UK, which used a selective absorption technique. The pressure in a $CO_2$ gas cell in the optical path determined the spectral characteristics of each band, and the mass of $CO_2$ in each cell determined the atmospheric level at which the weighting function of each band peaked. The SSU allowed temperatures profiles to be retrieved from about 25 km up to about 50 km. Unfortunately, changes in the pressure of this gas require periodic calibration

Deleted:

Deleted: channel

Deleted: channel

Deleted: s

Deleted: channel

of the sensor using data collected by rocketsondes and this eventually proved too costly.

- The Microwave Sounding Unit (MSU). This four-band Dicke radiometer made passive microwave measurements in the 50-60 GHz $O_2$ band. Unlike the infrared instruments of TOVS, the MSU was little influenced by clouds in the field of view and could provide temperature profiles to about 20 km. It was also used to help assess cloud contamination in the HIRS/2 pixels since the brightness temperature of the surface would be lower in HIRS/2 than in the MSU if clouds were present, neglecting differences in surface emissivity.

**Deleted:** channel

The ARGOS Data Collection System (DCS) was provided by France and collected environmental data from fixed and moving platforms, e.g. buoys, free-floating balloons, and other remote and inaccessible platforms and transmitted these data to central stations for processing and relay to users.

The SEM consisted of two separate instruments and a data processing unit. The Total Energy Detector (TED) measured the flux of particles from outer space in 11 energy bins that ranged from 0.3 keV to 20.0 keV. The Medium Energy Proton and Electron Detector (MEPED) measured the fluxes of protons, electrons and ions with energies from 30 keV to several tens of MeV.

**Deleted:** a

**Deleted:** d

The AVHRR instrument served as the main cloud and surface imaging instrument on the TIROS-N and its successors. Key attributes of the AVHRR instrument were its relatively high temporal resolution, multi-spectral imaging capability, and global coverage of data collected by a digital scanner. The AVHRR has a swath-width of more than 2600 km, (scanning to $\pm$ 55.4$^{o}$) and provides imagery of about 1.1 km spatial resolution at nadir from a near-polar orbit with a nominal altitude of 833 km. However, the spatial resolution of these data becomes degraded to ~ 6 km at the edge of the scan (EOS). A sketch of the AVHRR is shown in Figure 2.1. Differences between the three versions of the AVHRR were primarily based upon the number of spectral bands in each instrument, as shown in Table 2.2, which was taken from the NOAA website: http://www2.ncdc.noaa.gov/docs/podug/html/c3/sec3-0.htm

**Deleted:** rather than the analogue data collected by its predecessors

**Deleted:** d

**Deleted:** see

**Deleted:** ,

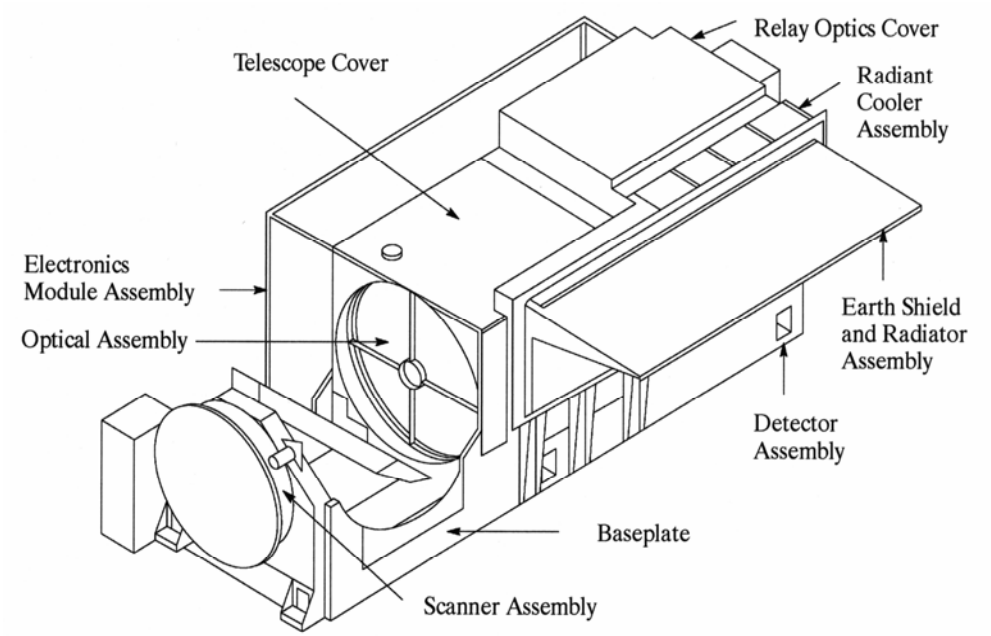


Figure 2.1 Illustration of the AVHRR instrument (from Kramer, 2002).

The original AVHRR sensor (AVHRR/1) had only four spectral bands. Data in the fifth band were simply a repeat of band 4 and therefore were redundant. Soon the longwave IR band was split into two bands to improve the atmospheric corrections needed for the SST retrievals. This version of the sensor was known as AVHRR/2. However, as noted in Chapter 1, the AVHRR/2 NEΔT of 0.12K in these IR bands limited the accuracy of SST analyses that could be retrieved with this instrument. Later AVHRR/2 data were further exploited to improve the detection of thin cirrus clouds (Inoue, 1985; Saunders and Kriebel, 1988).

**Deleted:** channel

**Deleted:** channels

The first AVHRR/3 sensor was carried into space with the launch of NOAA-15 on 13 May 1998. This third generation AVHRR sensor, which is a payload on the ESA MetOp-1 satellite, has an extra spectral band in the 1.58 -1.64 µm band to provide improved discrimination between clouds and snow/ice fields. It was designed as channel 3A. However, on the ATN spacecraft, channels 3A and 3B could not operate simultaneously. Therefore, the 1.6 µm band was transmitted during the daytime while the 3.7 µm band was typically transmitted only during nighttime condition. However, channel 3B had proved to be very valuable for studying certain kinds of clouds and, prior to the launch of NASA's EOS MODIS sensor, the band was used for detection of intensive sources of heat such as forest fires. A more complete discussion of these and other non-meteorological applications for AVHRR data may be found in the book by Cracknell (1997).

**Deleted:** (see section XXX below)

**Deleted:** channel

**Deleted:** Channel

**Deleted:** C

**Deleted:** C

**Deleted:** channel

Table 2.2 – Spectral band wavelengths of the AVHRR .

| | AVHRR/1 | | AVHRR/2 | | AVHRR/3 |
|---|---|---|---|---|---|
| Channel No. | TIROS-N (μm) | NOAA-6, -8, -10 (μm) | NOAA-7, -9, -11, -12, -14 (μm) | NOAA-13 | NOAA – 15, -16, through series (μm) |
| 1 | 0.55 - 0.90 | 0.55 - 0.68 | 0.55 - 0.68 | 0.55 - 0.68 | 0.58 – 0.68 |
| 2 | 0.725 - 1.10 | 0.725 - 1.10 | 0.725 - 1.10 | 0.725 - 1.00 | 0.725 – 1.00 |
| 3 (A) | n/a | n/a | n/a | n/a | 1.58 – 1.64 |
| 3 (B) | 3.55 - 3.93 | 3.55 - 3.93 | 3.55 - 3.93 | 3.55 - 3.93 | 3.55 – 3.93 |
| 4 | 10.5 –11.5 | 10.5 - 11.5 | 10.3 -11.3 | 10.3 - 11.3 | 10.30 – 11.30 |
| 5 | Repeat of Channel 4 | Repeat of Channel 4 | 11.5 -12.5 | 11.4 -12.4 | 11.50 – 12.50 |

The channel 2 wavelength range is often given as 0.725-1.1 μm but 1.0 μm would be a better value of the upper limit, see the NOAA website or Figure 2.8 or Cracknell (1997).

As previously noted, the larger spacecraft and additional solar panels provided ATN satellites with more power and space for extra instruments to be carried into space. Some of the instruments carried included the Earth Radiation Budget Experiment (ERBE), the Solar Backscatter Ultraviolet instrument (SBUV/2), a Search and Rescue System (S&RSAT), and the Advanced Microwave Sounding Units.

- The Earth Radiation Budget Experiment (ERBE) was a NASA research instrument used to improve the understanding of the total and seasonal planetary albedo and Earth Radiation balances, across latitude zones. This information was valuable for recognizing and interpreting seasonal and annual climate variations and contributes to long-term climate monitoring, research, and prediction.
- The Solar Backscatter UltraViolet radiometer (SBUV) was a non-scanning, nadir viewing instrument designed to measure scene radiance in the spectral region from 160 to 400 nm. SBUV data were used to determine the vertical distribution of ozone and the total ozone in the atmosphere, and solar spectral irradiance. The instrument was normally flown on POES missions with afternoon northbound Equator crossing times.
- S&RSAT was part of an international program to save lives. This S&RSAT equipment was provided by Canada and France. Similar Russian equipment, called COSPAS (Space System for the Search of Distressed Vessels), has been carried on the Russian polar-orbiting spacecraft. S&RSAT and COSPAS spacecraft relayed emergency radio signals from aviators, mariners and land travelers in distress to ground stations, or Local User Terminals (LUT), where the location of the distress signal transmitter cloud be determined by Doppler shift techniques. Information on the nature and location of the emergency could then be passed to a Mission Control Center that alerted the Rescue Coordination Center closest to the emergency.

**Deleted:** channe

**Deleted:** 1

**Formatted:** Font: Not Bold

**Formatted:** Font: Not Bold

**Formatted:** Font: Not Bold

**Formatted:** Font: Not Bold

**Formatted:** Font: Not Bold

**Formatted:** Font: Not Bold

- The Advanced Microwave Sounding Unit (AMSU) was a 20-band radiometer designed to obtain global temperature and humidity profiles. It replaced the MSU and SSU components of the TOVS sensor suite. It consisted of three separate components: AMSU-A1 (which had sounding bands in the 50-60 GHz oxygen band), the AMSU-A2 (with window bands at 23.8 and 31.4 GHz), and the AMSU-B (which had bands in the 183 GHz water vapor absorption band). (See NOAA websites: http://www2.ncdc.noaa.gov/docs/klm/html/c3/sec3-3.htm and http://www2.ncdc.noaa.gov/docs/klm/html/c3/sec3-4.htm.) The AMSU-A has a heritage in the DMSP Special Sensor Microwave – Temperature, which was originally known as SSM/T but which was renamed SSM/T-1 after the launch of the SSM/T-2 which is the DMSP humidity sounder. AMSU-A has a much smaller IFOV than SSM/T-1 (50 km vs 200 km) to provide improved horizontal resolution and many more bands (17 versus 7) for improved vertical resolution in retrieved atmospheric profiles. In addition, the use of bands in the 23.8 and 31.4 GHz window provide better surface temperature information than was available from SSM/T-1, which relied only upon bands in the 50-60 GHz range. The AMSU-A sensor was designed to provide temperature profiles for heights up to 50 km. AMSU-B has its heritage in the DMSP Special Sensor Microwave – Water Vapor Profiler (SSM/T-2), discussed in the next section. Three copies of the AMSU-B were provided by the UK to fly on NOAA-K, -L, and M or NOAA-15, -16, and -17 respectively. The AMSU-B will be replaced by the Microwave Humidity Sounder (MHS), also provided by the UK. The MHS sensor will fly on NOAA-N and N' as well as the ESA MetOp satellite series. These new microwave moisture profiling sensors provide high quality moisture profiles under cloudy conditions, except in regions of precipitation.

**Deleted:**

**Deleted:** channel

**Deleted:** channels

**Deleted:** channels

**Deleted:** channels

**Deleted:** SSM/T-2

**Deleted:** channels

**Deleted:** channels

**Deleted:** channels

The data collected by the TIROS-N and ATN instruments, like those from all NOAA polar orbiting spacecraft, were stored onboard the satellite for transmission to the NOAA central processing facility at Suitland, Maryland, through the Wallops and Fairbanks command and data acquisition stations. The AVHRR data could be recorded at 1.1 km resolution (the basic resolution of the AVHRR instrument) or at 4 km resolution. The stored high resolution (1.1 km) imagery is known as Local Area Coverage (LAC). Due to the large number of data bits, only about 11 minutes of LAC data was accommodated on a single recorder. By contrast, 115 minutes of the lower resolution (4 km) imagery, called Global Area Coverage (GAC) data, was stored on a recorder and this was sufficient to cover an entire 102 minute orbit. As previously noted, satellite data are also transmitted in real-time through a direct broadcast capability at VHF and S-band frequencies in the Automatic Picture Transmission (APT) and High Resolution Picture Transmission (HRPT) modes, respectively. The HRPT capability provided full 1.1 km (nadir) resolution data to those users with the equipment necessary to track the satellite and to process its transmission.

**Deleted:** es

#### 2.1.1.2 Defense Meteorological Satellite Program (DMSP)

In parallel with the civilian POES program, the US Department of Defense (DoD) built a separate polar-orbiting meteorological satellite which became known as the Defense Meteorological Satellite Program or DMSP System. It was originally known as the

**Deleted:** O

Defense System Applications Program and the Defense Acquisition and Processing Program (Kramer, 2000). Like the NOAA series of satellites, all DMSP satellites were flown in sun-synchronous orbits. There have normally been two satellites in operation at any one time (one in an early morning and one in a late morning orbit) with nodal times of 0530 and 1030 (Fuller, 1990).

The series of satellites known as the Block 4 series started with a launch on 19 January 1965 and continued through to 1967, see Table 2.3. These were followed by the Blocks 5A, 5B and 5C series from 23 May 1968 until the last satellite of Block 5C was launched on 19 February 1976. From mid-1965 to early 1970, the Block 4 series carried two cameras to collect high resolution TV pictures at 2.4 km (nadir) and 16 km (edge of scan) in the 0.4-4.0 μm region. Some of these early spacecraft also carried an IR sensor (8.0-12.0 μm) to collect data at night. Block 4 data initially consisted of Polaroid prints which were hand analyzed into cloud reports (Meyer, 1985). The spacecraft of the Blocks 5A, 5B and 5C series carried as their imaging instruments a three- then a four-band scanning radiometer. The visible bands had a spectral band of 0.4-1.1 μm and the lower resolution band (i.e. 3.6 km at nadir) also had a low-light level amplification system that provided useful nighttime visible imagery. These two enhancements provided imagery with good land-sea contrast and nighttime visible data by lunar illumination. In addition, the sensor provided the demographics of nighttime city lights and the display of the aurora borealis was used immediately in assess the strength and character of solar activity. The Blocks 5A, 5B, and 5C series continued with only minor increases in size, power, and capability until 1977, see Table 2.3. The changes were made for two reasons: to increase the amount and types of data and to increase spacecraft life through redundant systems such as onboard tape recorders and data transmitters. Block 5B was the first to carry an 8-band IR vertical temperature profiler. Block 5C added a fourth image band which provided IR imagery at roughly the same resolution as the highest resolution visible band, i.e. 0.5 km at nadir (Meyer, 1985).

**Deleted:** IV
**Deleted:** .
**Deleted:** channel
**Deleted:** channels
**Deleted:** channel
**Deleted:** channel
**Deleted:** channel
**Deleted:** channel

During the mid-1970s, the DMSP Block 5D satellite was designed and the first one in the series was launched on 11 September 1976, see Table 2.3. Block 5D-1 carried a totally programmable onboard computer, the first of its kind on an operational satellite. The Block 5D satellites also carried a new cloud imager called the Operational Linescan System (OLS) sensor which collected data in the same wavelength ranges as the VHRR, i.e. two bands at 0.4-1.1 μm and 10.5-12.6 μm (8-13 μm before 1979). In addition, the resolution of the nighttime imagery was improved to 2.4 km at nadir. Finally, the 8-band IR temperature sounder was enhanced to 16-bands, and became known as the SSH. Block 5D satellites also carried the 7-band microwave temperature sounder, Special Sensor Microwave Temperature (SSM/T) in addition to improved energetic electron and proton spectrometers and a plasma monitor to measure the in situ plasma (Meyer, 1985).

**Deleted:** channels
**Deleted:** channel
**Deleted:** channels
**Deleted:** channel

The OLS was revolutionary in restricting pixel growth as the sensor scanned from nadir to the edge of the scan. Using a unique detector switching technique, the OLS restricted growth of horizontal resolution as the sensor scanned the cross-track direction to produce data with a spatial resolution at the edge of the scan that was only approximately twice the resolution at nadir, compared to the nearly 5-6 pixel growth factor in AVHRR

imagery. The OLS continuous analog signal was sampled at a constant rate so that the Earth-located center of each pixel was roughly equidistant, i.e. 0.65 km apart and 7,322 pixels (according to system specification) were digitized in the cross track direction. The nearly constant resolution across the swath was accomplished through a combination of the natural rotation of the detector footprint and detector segment switching, i.e. to a smaller IFOV at approximately ± 40 degrees. Perhaps this is the reason that DMSP data were considered superior to those acquired by the civilian POES system since they had higher (0.5 km) spatial resolution in both visible and infrared wavelengths along with better Earth location which supported improved gridding and data rectification (Fuller, 1990). Certainly, the improved registration and high spatial resolution of the DMSP visible data made them invaluable for tropical storm analyses in support of the US Navy Joint Typhoon Warning Center (JTWC) as discussed in Chapter 1 (Arnold, 1975). However, the multispectral capability of AVHRR was far superior to that of the OLS. A comparison between the characteristics of the NOAA AVHRR/2 and the DMSP OLS is given in Table 2.4.

The first satellite in the Block 5D-1 series, known as F-1, experienced an uncorrectable spacecraft yaw and consequently OLS data quality suffered. This made it difficult to use the data to perform tropical storm analyses in support of JTWC, as described in Chapter 1. The yaw was sufficient so that gridding from ephemeris based data could not be used; therefore, geographic gridding techniques were refined locate the coordinates of storm centers (Hutchison, personal experience).

Another major contribution of the DMSP series satellites was the pioneering work in the area of microwave radiometry which was considered important to the "all-weather" operational requirements of the military community.

- While IR temperature sounders were carried on the Block 5D-1 satellites, these sensors were short-lived in the DMSP program and were soon replaced by microwave temperature sounders. First, the SSM/T or SSM/T-1 was carried into space on 18 December 1983 with the launch of F-7, a Block 5D-2 spacecraft. As noted previously, this sensor was a 7-band temperature sounder with a horizontal resolution of about 200 km.
- Next, came the Special Sensor Microwave Imager (SSM/I) with the launch of F-8 on 18 June 1987. As its name implies, the SSM/I collected (vertically and horizontally polarized) data in the microwave window regions from about 19-85 GHz using a 45° conical scan which gave it an incident angle of 53.1° degrees at the Earth's surface. From its nominal altitude of 833 km, this scan geometry provided a data swath of only about 1400 km while about 3000 km is needed for contiguous coverage at the equator. Thus, large gaps appeared in SSM/I data sets. Data from the SSM/I were used to obtain a variety of environmental data products , mostly over ocean surfaces, that were not products from other sensors, including sea surface winds (speed only), rain rates, cloud liquid water, and precipitable water to name a few.
- Then, another new sensor, the SSM/T-2, was launched with DMSP F-11 on 28 November 1991. As previously noted in the discussion of the AMSU-B sensor

**Deleted:** ue

**Deleted:** 5

**Deleted:** +

**Deleted:** to render

**Deleted:** al

**Deleted:** s

**Deleted:** channel

**Deleted:** lination

above, the SSM/T-2 was the first microwave moisture profiling sensor to fly on operational weather satellites.

- Most recently, DMSP launched its Special Sensor Microwave Imager Sounder (SSMIS) with the Block 5D-3 F-16 spacecraft on 18 October 2003. The SSMIS was designed to provide the combined capabilities of the SSM/T-1, SSM/T-2, and SSM/I sensors. This design also exploited the Zeeman splitting of the oxygen line to create weighting functions that peaked much higher in the atmosphere than earlier sensors with a goal of extending atmospheric temperature sounding to 70 km. (Stogryn, 1989a and 1989b)

Deleted: ed

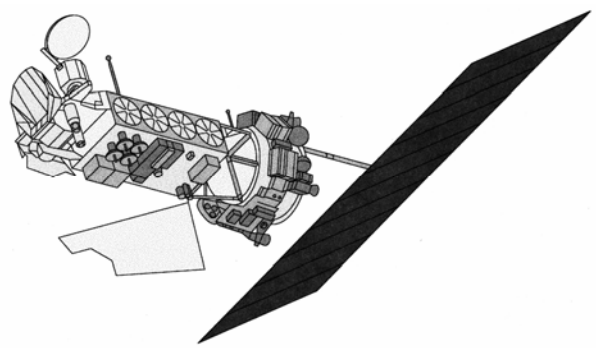

Figure 2.2 Schematic illustration of DMSP Block 5D-3 spacecraft model ( Kramer, 2002).

Originally it was planned to produce a DMSP Block 6 satellite series and indeed contracts were awarded to competing US aerospace contractors in the 1991 timeframe. Work was done on developing the Lockheed design for the legacy OLS sensor and the approach to create automated cloud analyses from imagery collected by the new sensor (Hutchison and Hardy, 1995). However, the merger of the NOAA and DMSP programs into NPOESS meant that the Block 6 satellites were never built and so documentation on them is difficult to locate. However, a significant advancement in the microwave remote-sensing methods was evaluated with a goal of increasing the incidence angle of the conical scan from 53.1° to as much as 70°. This was proposed to extend the data swath and products that could be generated by this new sensor suite. The trail of these investigations is evident in the literature (Wilheit et al., 1994; Rosenkranz et al., 1994).

Deleted: .

Table 2.3 Chronological overview of DMSP series satellites.

Formatted: Font: Not Bold

| Space-craft Bus | Spacecraft Series | Launch Date/Mission End | Sensor Complement | Space-craft mass (kg) |
|---|---|---|---|---|
| Block 4A | F-1 | 19 January 1965 | | 150 |
| | F-2 | 18 March 1965 | | 130 |
| | F-3 | 20 May 1965 | | 130 |
| | F-4 | 10 September 1965 | | 130 |
| | F-5 | 6 January 1965 | | 130 |

| | | | | |
|---|---|---|---|---|
| | F-6 | 30 March 1966 | | 130 |
| | F-7 | 16 September 1966 | | 125 |
| | F-8 | 8 February 1967 | | 130 |
| | F-9 | 23 August 1967 | | 195 |
| | F-10 | 11 October 1967 | | 195 |
| Block 5A | F-1 | 23 May 1968 | | 195 |
| | F-2 | 23 October 1968 | | 195 |
| | F-3 | 23 July 1969 | | 195 |
| | F-4 | 11 February 1970 | | 195 |
| | F-5 | 3 September 1970 | | 195 |
| | F-6 | 17 February 1971 | | 195 |
| Block 5B | F-1 | 14 October 1971 | | 195 |
| | F-2 | 24 March 1972 | | 195 |
| | F-3 | 9 November 1972 | | 195 |
| | F-4 | 17 August 1973 | | 195 |
| | F-5 | 16 March 1974 | | 195 |
| | F-6 | 9 August 1974 | | 195 |
| Block 5C | F-1 | 24 May 1975 | | 194 |
| | F-2 | 19 February 1976 | | 175 |
| Block 5D-1 | F-1 | 11 September 1976 - 17 September 1979 | OLS , SSH, SSJ/3, SSB, Contamination Monitor | 450 |
| | F-2 | 4 June 1977 - 19 March 1978 | OLS, SSH, SSJ/3, SSB, SSB/0, IFM, SSI/E, SSI/P | 450 |
| | F-3 | 30 April 1978 - December 1979 | OLS, SSH, SSJ/3, SSB, GFE-3R | 513 |
| | F-4 | 6 June 1979 - 29 August 1980 | OLS, SSH, SSJ/3, SSI/E, SSM/T, SSC, SSD | 513 |
| | F-5 | 14 July 1980 (failed) | OLS, SSH-2, SSJ/3, SSI/E, SSB/O, SSR | 513 |
| Block 5D-2 | F-6 | 20 December 1982 - 24 August 1987 | OLS, SSH-2, SSI/E, SSJ/4, SSB/A | 750 |
| | F-7 | 18 December 1983 - 17 October 1987 | OLS, SSM/T, SSI/E, SSJ/4, SSB, SSJ*, SSM | 750 |
| | F-8 | 18 June 1987 - 13 August 1991 | OLS, SSM/I, SSM/T, SSI/ES, SSJ/4, SSB/X-M | 750 |
| | F-9 | 3 February 1988 | OLS, SSM/T, SSI/ES, SSJ/4, SSK | 750 |
| | F-10 | 1 December 1990 - February 1995 | OLS, SSM/I SSM/T, SSI/ES, SSJ/4, SSB/X-2 | 750 |
| | F-11 | 28 November 1991 - August 2000 | OLS, SSM/I, SSM/T, SSM/T-2, SSJ/4, SSI/ES-2, SSB/X-2 | 830 |
| | F-12 | 29 August 1994 | OLS, SSM/I, SSM/T, SSM/T-2, SSJ/4, SSI/ES-2, SSB/X-2, SSM | 830 |

**Deleted:** SSM/1

**Deleted:** SSM/1

| | | | | |
|---|---|---|---|---|
| | F-13 | 24 March 1995 | OLS, SSM/I, SSM/T, SSJ/4, SSI/ES-2, SSB/X-2, SSM, SSZ | 750 |
| | F-14 | 4 April 1997 | OLS, SSM/I, SSM/T, SSM/T-2, SSJ/4, SSI/ES-2, SSM | 750 |
| Block 5D-3 | F-15 | 12 December 1999 | OLS, SSM/I, SSJ/4, SSI/ES-2, SSM-Boom, SSZ | 1125 |
| | F-16 | 18 October 2003 | OLS, SSMIS, SSI/ES-3, SSJ5, SSM-Boom, SSULI, SSUSI, SSF | 1125 |
| | S-17 | To become F-17 | OLS, SSMIS, SSI/ES-3, SSJ5, SSM-Boom, SSULI, SSUSI, SSF | 1125 |
| | S-18 | To become F-18 | OLS, SSMIS, SSI/ES-3, SSJ5, SSM-Boom, SSULI, SSUSI, SSF | 1125 |
| | S-19 | To become F-19 | OLS, SSMIS, SSI/ES-3, SSJ5, SSM-Boom, SSULI, SSUSI, SSF | 1125 |
| | S-16 | To become F-20 | OLS, SSMIS, SSI/ES-3, SSJ5, SSM-Boom, SSULI, SSUSI, SSF | 1125 |

**Deleted:** SSM/1

**Deleted:** SSM/1

**Deleted:** SSM/1

Table 2.4 Comparison of two sensors – NOAA AVHRR/2 and DMSP/OLS (Kramer 2002).

| N0AA/AVHRR-2 Sensor | System Parameter/ (Applications) | DMSP/OLS Sensor |
|---|---|---|
| 1.1 km LAC<br>4.0 km GAC (degraded at edges)<br>good<br>good | spatial resolution<br><br>(sea ice leads)<br>(meteorology) | 0.55 km 'fine'<br>2.7 km 'smooth' (constant across swath)<br>better<br>better |
| 5 narrow bands<br>Ch1: 0.55-0.68 µm<br>Ch2: 0.725-1.0 µm<br>Ch3: 3.55-3.93 µm<br>Ch4: 10.30-11.30 µm<br>Ch5: 11.50-12.50 µm<br>good<br>good | Spectral resolution<br><br>(sea surface temp.)<br>(vegetation index) | 2 broad bands<br>VIS: 0.4-1.1 µm<br>IR: 10.5-12.5 µm<br><br>Marginal<br>N/A |
| IR yes (10 bit)<br>VIS no (pre-launch, drifts) | absolute calibration | IR yes (older units had 7 bit IR and VIS, which was changed to 8 and 6; the 8 bits are digitized in temperature and not radiance)<br>VIS no (continuous gain adjustment) |
| No<br><br>N/A<br>developmental<br><br>N/A | visible-band dynamic range/<br>night time operation<br>(auroral characteristics)<br>(biomass burning,)<br>NESDIS, NASA<br>(moonlit clouds/snow) | Yes<br><br>Yes<br>added potential with unique visible band<br><br>good |
| No<br><br>N/A<br><br>N/A | coincident passive microwave<br>(snow/ice, rain rate)<br>(surface wind/soil moisture) | Yes<br><br>good<br>good |
| No<br><br>No | coincident space environment measurements<br>(auroral image feature + electron flux) | Yes<br><br>Yes |

**Deleted:** channels
**Deleted:** channels
**Formatted:** English (U.S.)
**Deleted:** band
**Formatted:** English (U.S.)
**Formatted:** English (U.S.)
**Deleted:** 8
**Deleted:** ed
**Deleted:** (Note this is an SSM/I capability not OLS!!)¶
**Deleted:** (Note this is an SSM/I capability not OLS!!)
**Formatted:** Left

#### 2.1.1.3 NASA Earth Observing System (EOS) Program

The Earth Observing System (EOS) was the centerpiece of NASA's Earth Science Enterprise (ESE). It was composed of a series of satellites, a science component, and a data system supporting a coordinated series of polar-orbiting and low inclination satellites for long-term global observations of the land surface, biosphere, solid Earth, atmosphere, and oceans. The following series of spacecraft were planned: http://www.jpl.nasa.gov/earth/missions

Deleted: (NASA JPL website)¶

- EOS AM-1
- Landsat-7
- EOS PM-1
- EOS Laser ALT-1
- EOS CHEM-1
- EOS AM-2
- EOS PM-2A
- EOS Laser ALT-2
- EOS CHEM-2 Monitor
- EOS CHEM-2 Process

The EOS program began in the early 1980s when it became evident that improved remotely-sensed data were critical to a better understanding of the Earth's climate system and the impacts of anthropogenic activities upon it. The objectives of the EOS mission were (1) to create an integrated scientific observing system that would enable multidisciplinary study of the Earth's critical, life-enabling, interrelated processes involving the atmosphere, oceans, land surfaces, polar regions, and solid Earth, and the dynamic and energetic interactions among them and (2) to develop a comprehensive data and information system, including a data retrieval and processing system, to serve the needs of scientists performing an integral, multidisciplinary study of planet Earth. (See EOS website: http://modis.gsfc.nasa.gov/.)

While the EOS program changed considerably over the 1990-2000 decade, it maintained its key components. EOS AM-1, which became known as Terra, was launched on 18 December 1999. Landsat-7 was launched on 15 April 1999. The EOS PM-1 satellite (known as Aqua) was launched on 4 May 2002. The EOS Laser ALT-1 mission (known as the Geoscience Laser Altimeter System or the GLAS mission) was launched on 12 January 2003. The EOS CHEM-1 mission (known as Aura) was launched on 17 June 2004.

The Terra mission carried sensors from the US (CERES, MISR, and MODIS), Japan (ASTER), and Canada (MOPITT) while the EOS Aqua satellite carried several sounders to obtain atmospheric profiles to benefit numerical weather prediction modeling. For example, the Atmospheric IR Sounder (AIRS) was purported to provide global temperature and moisture profiles, in clear and fractionally cloud-filled pixels, as accurately as conventional rawinsonde data. In addition, Aqua carried the AMSR-E (built by Japan in collaboration with the US) and Humidity Sounder Brazil, sponsored by

Brazilian Space Agency and built in the UK. An illustration of the Aqua satellite is shown in Figure 2.3.

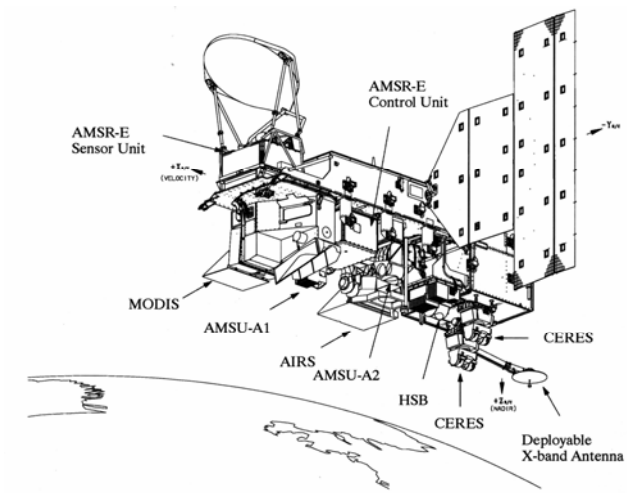


Figure 2.3 Illustration of the EOS Aqua satellite and sensors (Kramer, 2000).

The key EOS sensor relevant to this text is MODIS and it will be discussed in some detail since it was a key VIIRS heritage sensor. (See Kramer (2002) for information on other EOS sensors.) MODIS provides high radiometric sensitivity (12 bit) in 36 spectral bands ranging in wavelength from 0.4 µm to 14.4 µm. The responses are custom tailored to the individual needs of the user community and provide exceptionally low out-of-band response. Two bands are imaged at a nominal resolution of 250 m at nadir, with five bands at 500 m, and the remaining 29 bands at 1 km. A ±55° scanning pattern at the EOS orbit of 705 km achieves a 2,330-km swath and provides global coverage every one to two days. MODIS band characteristics are shown in Table 2.5 along with the primary application for each. (See MODIS website: http://modis.gsfc.nasa.gov/about/specs.html .)

Table 2.5 Band characteristics for MODIS data products (NASA MODIS website).

| Primary Use (Solar Bands) | Band | Bandwidth (nm) | Spectral Radiance ($W m^{-2} \mu m^{-1} sr^{-1}$) | Signal-to-Noise Ratio |
|---|---|---|---|---|
| Land/Cloud/Aerosols Boundaries | 1 | 620 - 670 | 21.8 | 128 |
| | 2 | 841 - 876 | 24.7 | 201 |
| | 26 | 1360 - 1390 | 6.00 | 150 |
| Land/Cloud/Aerosols Properties | 3 | 459 - 479 | 35.3 | 243 |
| | 4 | 545 - 565 | 29.0 | 228 |
| | 5 | 1230 - 1250 | 5.4 | 74 |
| | 6 | 1628 - 1652 | 7.3 | 275 |
| | 7 | 2105 - 2155 | 1.0 | 110 |

Deleted: /

Deleted: -

Deleted: -

| | | | | |
|---|---|---|---|---|
| Ocean Color/ Phytoplankton/ Biogeochemistry | 8 | 405 - 420 | 44.9 | 880 |
| | 9 | 438 - 448 | 41.9 | 838 |
| | 10 | 483 - 493 | 32.1 | 802 |
| | 11 | 526 - 536 | 27.9 | 754 |
| | 12 | 546 - 556 | 21.0 | 750 |
| | 13 | 662 - 672 | 9.5 | 910 |
| | 14 | 673 - 683 | 8.7 | 1087 |
| | 15 | 743 - 753 | 10.2 | 586 |
| | 16 | 862 - 877 | 6.2 | 516 |
| Atmospheric Water Vapor | 17 | 890 - 920 | 10.0 | 167 |
| | 18 | 931 - 941 | 3.6 | 57 |
| | 19 | 915 - 965 | 15.0 | 250 |
| Primary Use (Thermal Bands) | Band | Bandwidth (μm) | Spectral Radiance (W $m^{-2}$ $\mu m^{-1}$ $sr^{-1}$) | Noise-Equivalent Temperature Difference (K) |
| Surface/Cloud Temperature | 20 | 3.660 - 3.840 | 0.45(300K) | 0.05 |
| | 21 | 3.929 - 3.989 | 2.38(335K) | 2.00 |
| | 22 | 3.929 - 3.989 | 0.67(300K) | 0.07 |
| | 23 | 4.020 - 4.080 | 0.79(300K) | 0.07 |
| Atmospheric Temperature | 24 | 4.433 - 4.498 | 0.17(250K) | 0.25 |
| | 25 | 4.482 - 4.549 | 0.59(275K) | 0.25 |
| | 27 | 6.535 - 6.895 | 1.16(240K) | 0.25 |
| | 28 | 7.175 - 7.475 | 2.18(250K) | 0.25 |
| Cloud Properties | 29 | 8.400 - 8.700 | 9.58(300K) | 0.05 |
| Ozone | 30 | 9.580 - 9.880 | 3.69(250K) | 0.25 |
| Surface/Cloud Temperature | 31 | 10.780 - 11.280 | 9.55(300K) | 0.05 |
| | 32 | 11.770 - 12.270 | 8.94(300K) | 0.05 |
| Cloud Top Altitude | 33 | 13.185 - 13.485 | 4.52(260K) | 0.25 |
| | 34 | 13.485 - 13.785 | 3.76(250K) | 0.25 |
| | 35 | 13.785 - 14.085 | 3.11(240K) | 0.25 |
| | 36 | 14.085 - 14.385 | 2.08(220K) | 0.35 |

**Deleted:** /$m^2$ -μm-sr

A number of standard products were generated from MODIS data, shown in Table 2.6, for scientists involved in the study of global climate change. These products were created

and made available at no cost to the international community through the EOS Data and Information System (EOSDIS). The algorithms to create these products were developed by an international team of experts from the US, UK, Australia, and France and used by scientists from a variety of disciplines, including oceanography, biology, and atmospheric science.

Table 2.6 MODIS data products according to application class.

| Application Class | Product Name | Product Description |
|---|---|---|
| Calibration | MOD 01 | Level 1A Radiance Counts |
| | MOD 02 | Level 1B Calibrated Geolocated Radiance |
| | MOD 03 | Geolocation Data Set |
| Atmosphere | MOD 04 | Aerosol Product |
| | MOD 05 | Total Precipitable Water (Water Vapor) |
| | MOD 06 | Cloud Product |
| | MOD 07 | Atmospheric Profiles |
| | MOD 08 | Gridded Atmospheric Product |
| | MOD 35 | Cloud Mask |
| Land | MOD 09 | Surface Reflectance |
| | MOD 11 | Land Surface Temperature and Emissivity |
| | MOD 12 | Land Cover/Land Cover Change |
| | MOD 13 | Gridded Vegetation Indices (Max NDVI & Integrated MVI) |
| | MOD 14 | Thermal Anomalies, Fires, and Biomass Burning |
| | MOD 15 | Leaf Area Index & FPAR |
| | MOD 16 | Evapotranspiration |
| | MOD 17 | Net Photosynthesis & Primary Productivity |
| | MOD 44 | Vegetation Cover Conversion |
| Cryosphere | MOD 10 | Snow Cover |
| | MOD 29 | Sea Ice Cover |
| Ocean | MOD 18 | Normalized Water-leaving Radiance |
| | MOD 19 | Pigment Concentration |
| | MOD 20 | Chlorophyll Fluorescence |
| | MOD 21 | Chlorophyll_a Pigment Concentration |
| | MOD 22 | Photosynthetically Available Radiation (PAR) |
| | | |
| | MOD 23 | Suspended Solids Concentration |
| | MOD 24 | Organic Matter Concentration |
| | MOD 25 | Coccolith Concentration |
| | MOD 26 | Ocean Water Attenuation Coefficient |
| | MOD 27 | Ocean Primary Productivity |
| | MOD 28 | Sea Surface Temperature |
| | MOD 31 | Phycoerythrin Concentration |
| | MOD 36 | Total Absorption Coefficient |

| | | |
|---|---|---|
| | MOD 37 | Ocean Aerosol Properties |
| | MOD 38 | Clear Water Epsilon |

In keeping with the discussion of this text, it is noted that MODIS provided new spectral data to improve the quality global cloud analyses and subsequently SST analyses. For example, MODIS was the first sensor to carry all bands available in the AVHRR/3 sensor plus the 8.3, 1.375 μm bands for improved cirrus detection in nighttime and daytime conditions respectively. In addition, MODIS provided several bands in the 13-15 μm ranges to support the retrieval of cloud top pressures at 1-km resolution using the $CO_2$ slicing method (Menzel et al., 2002). One can develop arguments against placing sounding bands in an imager and alternative methods have been developed to fuse cloud top pressures from more coarse resolution sounder data with higher resolution imager data (Hutchison, 1999; Hutchison et al., 1997a; Hutchison et al., 1997b). The MODIS Aqua mission is the first to collect all the sensor data needed to determine the value of this data fusion technique compared to using sounding bands directly in an image; however, this analysis has not yet been completed.

**Deleted:** channels

**Deleted:** channels

**Deleted:** ry

However, MODIS Band 26 was too wide, i.e. 1360 – 1390 nm. This band was centered on a strong water vapor absorption line with the intent of blocking reflected energy from lower-level clouds and surfaces (Gao et al., 1993). However, even when 10 nm bandpass data were analyzed, surface features could be observed in this band (Hutchison and Choe, 1996). The VIIRS design reduced the problems in this MODIS band to some degree by narrowing the bandwidth of this band from 30 to 15 nm. Improved cirrus detection means improved SST analyses through better cloud screening. Coupled with the higher NEΔT values of 0.05 K for SST bands (i.e. band 20, 31, and 32) and alternative bands with 0.07 K for auxiliary bands 22 and 23, we expect both daytime and nighttime SST analyses to approach the climate modeling goal of 0.2-0.3K.

**Deleted:** channel

**Deleted:** channel

**Deleted:** ,

**Deleted:** channels

Clearly, MODIS is an exceptional sensor for numerical weather prediction, climate research and many other applications. While there are currently over 40 products produced on a routine basis, we expect many more to be developed in the future. In fact, this author developed two products that were not part of the original MODIS data product lists have already been developed; they are cloud base heights (Hutchison, 2002) and air quality monitoring data products (Hutchison, 2003).

#### 2.1.1.4 Other Polar-Orbiting Meteorological Satellite Systems

In addition to the US, there are now a number of other countries involved in polar orbiting meteorological satellite programs, see Table 2.7. In parallel with the U.S. development of polar-orbiting meteorological satellites the former USSR launched 14 experimental satellites in the Cosmos series between 1962 and 1966 (see Table III-2-1 of Rao *et al.* 1990). Cosmos-144 and Cosmos-156, which were launched in 1967, were designated as the first spacecraft of the operational Meteor system. The Meteor system, which was operated by ROSHYDROMET, the Soviet Committee, now the Russian Federal Service, for Hydrometeorology and Environmental Monitoring, included weather satellites, ground stations to receive and process the data, a service to control the operations of the satellites and a regular prediction service. The data were recorded and

stored for transmission to Earth when the satellites were over Soviet or Russian territory. Later satellites carried Automatic Picture Transmission (APT) equipment making real-time pictures available anywhere within receiving range. Following the launch of Cosmos-144 and Cosmos-156 there were several more Cosmos spacecraft launched in 1967 and 1968 before the first spacecraft of the Meteor-1 series was launched in 1969. Altogether 25 spacecraft of the Meteor-1 series were launched from 1969 to 1977 (see Table 361 of Kramer 2002). These were followed by the Meteor-2 series (first spacecraft Meteor-2-1 launched on 11 July 1975, last one Meteor-2-22 launched on 31 August 1993) and Meteor-3 series (first spacecraft launched on 24 October 1985 and the series is still ongoing) (see also Table 361 of Kramer 2002). Further details of the Meteor System are given by Rao *et al.* (1990) and Kramer (2002).

The Feng-Yun (Feng Yun = wind and cloud) meteorological satellite program of the People's Republic of China includes both polar-orbiting and geostationary spacecraft. The Feng-Yun-1 series are polar-orbiting spacecraft; the launch dates of the first three spacecraft in the series are given in Table 2.7 and further information is given in Section G of Kramer (2002).

Table 2.7 - Overview of polar-orbiting meteorological satellite series (Kramer 2002).

| Satellite Series (Agency) | Launch | Major Instruments | Comments |
|---|---|---|---|
| NOAA-2 to -5 (NOAA) | 21 October 1971, 29 July 1976 | VHRR | 2580 km swath |
| TIROS-N (NOAA-POES)<br>NOAA-15 to -L, M, N, N' | 13 October 1978<br>13 May 1998 – 2007 | AVHRR<br>AVHRR/3 | >2600 km swath<br>>2600 km swath |
| DMSP Block 5D-1 (DoD)<br>DMSP Block 5D-2 (DoD)<br>DMSP Block 5D-3 (DoD) | 11 September 1976 –14 July 1980<br>20 December 1982 – 4 April 1997<br>12 December 1999 | OLS<br>OLS, SSM/I<br>OLS, SSM/I | 3000 km swath<br>SSMIS replaces SSM/I<br>Starting with F-16 (2001) |
| Meteor-3 series of Russia | 24 October 1985 | MR-2000M, MR-900B | 3100 km, 2600 km swath |
| Meteor-3M series of Russia | 2001 (Meteor-3M-1) | | |
| FY-1A,-1B,-1C (CMA) China Meteorological Administration) | 7 September 1988, 3 September 1990, 10 May 2000 | MVISR | 2800 km swath |
| MetOp-1 (EUMETSAT) | 2005 | AVHRR/3, MHS, IASI | PM complement to NOAA-POES series |

Formatted: Font: Not Bold

Deleted: SSM/I

Deleted: , China

| | | | |
|---|---|---|---|
| NPP, (NASA/IPO) | 2005 | VIIRS, CrIS, ATMS,OMPS | NPOESS Preparatory Project |
| NPOESS (IPO) | 2008 | VIIRS, CMIS, CrIS, ATMS, OMPS | Successor to NOAA-POES and DMSP series |

#### 2.1.1.5 The Proposed Eumetsat MetOp Series

EUMETSAT, the European meteorological satellite data service provider, has had a long-established involvement in the operation of geostationary meteorological satellites in the Meteosat series (see section 2.1.2). The EUMETSAT Polar System (EPS) has been in the plans since mid 1980s and consists of the ESA-developed Meteorological Operational (MetOp) series of spacecraft and an associated ground segment for meteorological and climate monitoring. Since the early 1990s, NOAA and EUMETSAT have been discussing future cooperation in flying a polar-orbiting meteorological satellite constellation. A co-operation agreement between NOAA and EUMETSAT was signed in November 1998.

The basic tenet of this cooperation is to join the space segment of the emerging MetOp program of EUMETSAT with the existing NPOESS program into a fully coordinated service, thus sharing the costs of a program for synergetic reasons. The plans came to a common baseline and agreement, referred to as the IJPS (Initial Joint Polar System), in 1998. IJPS comprises two series of independent, but fully coordinated polar satellite systems, namely POES and MetOp, to provide for the continuous and timely collection and exchange of environmental data from space. EUMETSAT plans to include its satellites MetOp-1, -2 and -3 for the morning orbit, while the US would start with its NOAA-N and N' spacecraft for the afternoon orbit of the coordinated system. The MetOp program, as successor to the NOAA POES morning series, is required to provide a continuous broadcast of its meteorological data to the world-wide user community, so that any ground station in any part of the world can receive local data when the satellite passes over that receiving station. This implies continued long-term provision of the low rate picture transmission (LRPT) and VHF downlink services. Both services are coordinated and integrated, on the basis of exchange of data, instruments and operational services, see Figure 2.4.

The prime objectives of the EPS MetOp mission series are: (1) to ensure continuity of availability for operational purposes of polar meteorological observations from the "morning" orbit to the global user community and (2) to provide enhanced monitoring capabilities (complementary to ENVISAT) to fulfill the requirements to study the Earth climate system as expressed in a number of international co-operative programs such as the GCOS (Global Climate Observing System), IGBP (International Geosphere and Biosphere Program) and WCRP (World Climate Research Program). The aim is to provide continuous, long-term data sets. Plans call for MetOp-1 to be launched in 2005, see Figure 2.5. The anticipated MetOp-1 payload is identified in Table 2.8. Within the European framework, the ESA program developing MetOp-1, and the EUMETSAT procurement of MetOp-2, -3, is under the responsibility of a joint ESA/EUMETSAT team. EUMETSAT is also directly responsible for the delivery of some of the payloads,

while several payloads are contributed by NOAA and CNES (the French Centre National d'Etudes Spatiales) and shown in Table 2.8).

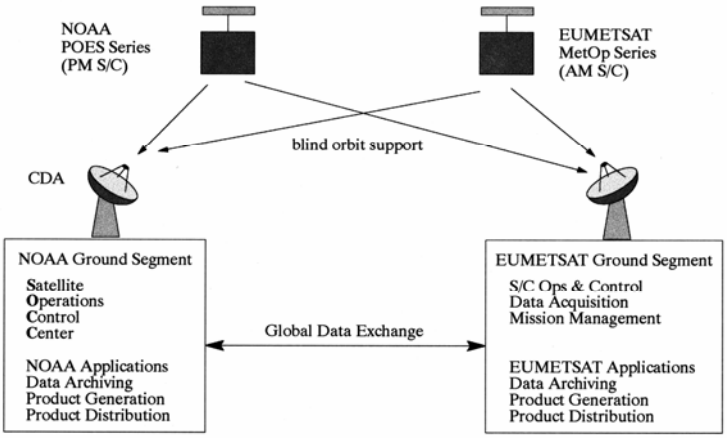


Figure 2.4 Integrated concept of NOAA/EUMETSAT meteorological polar satellites (Kramer,2002).

MetOp-1 will have a VHF low-rate digital direct broadcast service, the LRPT (Low-Rate Picture Transmission) which employs a JPEG data compression scheme to ensure high-quality images to APT users. This digital service provides three bands of AVHRR data at the full instrument spatial and radiometric resolution. There will also be a high-rate HRPT (High-Rate Picture Transmission) broadcast service, very similar to the existing NOAA POES service, to enable regional users to receive all direct broadcast data in real time as currently provided by NOAA POES and NASA EOS systems.

**Deleted:** channels

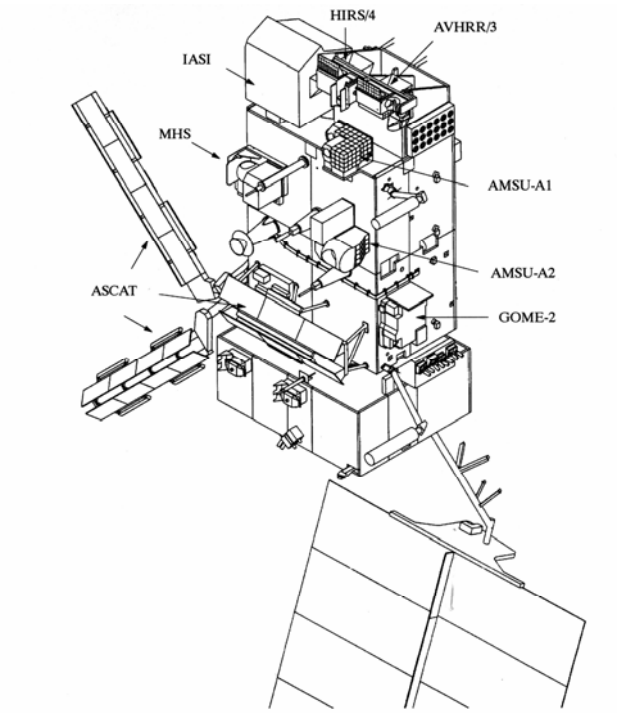


Figure 2.5. Sketch of MetOp-1 (from Figure 204 of Kramer, 2002)

Table 2.8 Overview of MetOp-1 payload compliment (Kramer 2002).

| Payload Sensor | Mission Objectives | Instrument Provider |
|---|---|---|
| AVHRR/3 (Advanced Very High Resolution Radiometer) | Global imagery, global sounding, ocean measurements (SST), clouds and Earth radiation budget, land measurements | NOAA |
| HIRS/4 (High Resolution Infrared Sounder) | Global sounding, atmospheric minor constituents, (ozone) | NOAA |
| AMSU-A (Advanced Microwave Sounding Unit-A-A1 & A2) | Global sounding, sea ice | NOAA |
| MHS (Microwave Humidity Sounder) | Global sounding, clouds and Earth radiation budget, sea ice | EUMETSAT |
| IASI (Improved Atmospheric Sounder Interferometer) | Global sounding, ocean measurements (SST), clouds and Earth radiation budget, some atmospheric trace constituents, land measurements | CNES/ EUMETSAT |
| ASCAT (Advanced Scatterometer | Ocean measurements, surface stress and surface wind | ESA |
| GOME 2 (Global Ozone Monitoring Experiment-2) | Atmospheric trace gases (ozone content and profile) | ESA/ EUMETSAT |

| | | |
|---|---|---|
| GRAS (GNSS Receiver for Atmospheric Sounding) | Atmospheric refractive index measurement in limb sounding mode | ESA/ EUMETSAT |
| ARGOS (Remote Data Collection System). | Data collection and location; ADCS on-board, PTTs and DCPs in the ground segment | CNES |
| S&R = Search and Rescue System | Cooperative satellite-based radiolocation system for search and rescue operations. Relay of emergency radio signals to ground stations from aviators, mariners and land travellers in distress. | CNES/NOAA |
| SEM-2 (Space Environment Monitor-2) | Monitoring of the S/C environment (solar terrestrial) | NOAA |

Deleted:

### 2.1.2 Geostationary Meteorological Satellite Systems

In May 1966 the former Soviet Union adopted the geostationary orbit for meteorological purposes by placing television cameras on the third and fourth Molniya-1 communications satellites (in highly elliptical orbits with apogee at approximately 40,000 km above the northern hemisphere). The first picture was taken on 18 May 1966.

The NOAA GOES (Geostationary Operational Environmental Satellite) Program was a direct descendant of the NASA research and development Applications Technology Satellite (ATS) program. This program was initiated on 7 December 1966 with the launch of ATS-1 to demonstrate communications technology by the use of a satellite in a geostationary orbit. The excess capacity of the spacecraft suggested the inclusion of meteorological sensors for experimental observations of the Earth from the geostationary orbit at 35,800 km above the Earth's surface. The ATS-1 imagery gave convincing proof of the ability of geostationary spacecraft to monitor in real-time the evolution of weather systems, particularly severe weather. ATS-1 was followed by five additional satellites, ATS-2 to ATS-6, which were all developmental satellites used to mature the technology needed to make geostationary satellites into an operational system.

The success of the ATS geostationary satellites led to the development by NASA of an operational spacecraft designed specifically for meteorology. Five spacecraft were built for this series, two Synchronous Meteorological Satellites (SMS) and three GOES. NASA's demonstration of two SMS systems began with the launch of SMS-1 on 17 May 1974 while NOAA's operation of the GOES series followed with the launch of GOES-1 on 16 October 1975. The SMS satellites carried the VISSR (Visible Infrared Spin-Scan Radiometer) as the prime instrument. The VISSR consisted of a cylinder covered with solar cells, containing most of the instrumentation and with its axis parallel to the axis of rotation of the Earth; there was an antenna assembly that remains directed towards the Earth. Scanning in the East-West direction along a scan line was achieved by the spinning of the whole spacecraft about its axis. The gathering of data from successive scan lines was achieved by tilting a mirror within the optical system. The VISSR provided high-quality day/night cloud cover data and made radiance temperature measurements of the Earth-atmosphere system. The evolution of ATS into SMS and

eventually into the GOES series permitted the implementation of new services like the routine tracking of clouds, with infrared imagery available for cloud height determination and night-time tracking capabilities.

GOES spacecraft were equipped to observe the Earth's disc (See Figure 2.6) in the visible and infrared regions of the spectrum and provided near-continuous, repetitive observations needed to observe, track, and predict mesoscale, severe weather systems through their evolution cycle. GOES spacecraft also were used to retrieve cloud cover, surface conditions, snow and ice cover, surface temperatures from imagery, along with vertical distributions of atmospheric temperature and humidity from sounding sensors. These satellites were also instrumented to measure solar X-rays and high energy particles, collect and relay environmental data from platforms, and broadcast instrument data and environmental information products to ground stations.

GOES spacecraft continue to operate at the geostationary altitude of 35,800 km above the surface of the Earth. The full constellation consists of two spacecraft that provide overlapping coverage that centers on the United States and extends over the eastern Atlantic Ocean and the western Pacific Ocean. GOES-East is located over the Equator at 75°W; GOES-West is at 135°W. To date twelve satellites in the GOES series have been launched, see Table 2.9.

Japan began its geostationary meteorological satellite program with the launch of GMS-1 (Geostationary Meteorological Satellite-1, referred to as Himawari-1 in Japan) by the Japan Meteorological Agency (JMA) and the National Space Development Agency of Japan (NASDA) on 7 July 1977. Its planned replacement, the Multi-functional Transport Satellite is expected to serve a dual role by providing navigation data to air-traffic control services in the Asia Pacific region and as well as the meteorological data. A launch failure of the H-2 vehicle occurred with the initial launch of MTSAT-1 on 15 November 1999 and a replacement satellite, MTSAT-1R, has been build and is awaiting launch. The prime instrument of the meteorology mission on MTSAT-1R is the Japanese Advanced Meteorological Imager (JAMI) which was built by Raytheon Santa Barbara Remote Sensing. (Insert comments from SBRS)

**Deleted:** s

**Deleted:**

**Deleted:**

**Deleted:** was launched in 2003

Table 2.9 Overview of geostationary meteorological satellites (Kramer 2002).

| Spacecraft Series (Agency) | Launch | Major Instrument | Comment |
|---|---|---|---|
| ATS-1 to ATS-6 (NASA) | 6 December 1966 - 12 August 1969 | SSCC (MSSCC ATS-3) | Technical demonstration |
| GOES-1 to –7 (NOAA) | 16 October 1975 - 26 February 1987 | VISSR | 1st generation |
| GOES-8 to –12 (NOAA) | 13 April 1994 - 23 July 2001 | GOES-Imager, Sounder | 2nd generation |
| GMS-1 to -5 (JMA) | 14 July 1977, 18 March 1995 | VISSR (GOES heritage) | 1st generation |
| MTSAT-1 (JMA *et al.*) | 15 November 1999 (launch failure of H-2 | JAMI | 2nd generation |

| | | | |
|---|---|---|---|
| MTSAT-1R (JMA) | vehicle)<br>re-planned for 2003 | JAMI | |
| Meteosat-1 to -7 (EUMETSAT)<br>MSG-1 (EUMETSAT) | 23 November 1977, 3 September 1997<br>28 August 2002 | VISSR<br><br>SEVIRI, GERB | 1st generation<br><br>2nd generation |
| INSAT-1B to -1D (ISRO)<br>INSAT-2A to -2E (ISRO)<br>INSAT-3B (ISRO)<br><br>INSAT-3A (ISRO)<br>MetSat-1 (ISRO) | 30 August 1983 – 12 June 1990<br>9 July 1992 - 2 April 1999<br>21 March 2000<br><br>planned for 2001<br>planned for Oct. 2001 | VHRR<br><br>VHRR/2<br><br><br><br>VHRR/2 | <br><br>Starting with -2E<br><br>Communications only<br>Weather Satellite only |
| GOMS-1 (Russia/Planeta)<br>Electro-M (Russia) | 31 October 1994<br><br>2005/6 | STR | 1st Generation<br><br>2nd Generation |
| FY-2A, -2B (CMA, China) | 10 June 1997, 26 July 2000 | S-VISSR | |
| AVStar (Astro Vision Inc.,Pearl River, MS, USA) | 2003 | Suite of 5 cameras | First commercial GEO weather satellite |

The METEOSAT program of Europe was initiated by ESA in 1972 followed by a launch of METEOSAT-1, as a demonstration satellite on 23 November 1977. The EUMETSAT convention was signed on 24 May 1983 by 16 countries. On 1 January 1987, responsibility for the operation of the METEOSAT spacecraft was transferred from ESA to EUMETSAT. The METEOSAT Second Generation (MSG) series, with the launch of the first satellite in the program on 28 August 2003, provided considerable improvements.

India started planning of the INSAT series of geostationary satellites in the 1970s with the launch of INSAT-1B on 30 April 1983, see Table 2.9. INSAT is a multi-purpose operational geostationary satellite system series employed for meteorological observation over India and the Indian Ocean, as well as for domestic telecommunications (nationwide direct TV broadcasting, TV program distribution, meteorological data distribution, etc.). The prime instrument, the Very High-Resolution Radiometer (VHRR), was enhanced several times to provide high-quality data of 2 km spatial resolution in the visible band and 18 km resolution in the near infrared and thermal infrared bands. India approved a dedicated geostationary weather satellite named MetSat (Meteorological Satellite) which was launched in October 2001.

Russia launched GOMS-1 (Geostationary Operational Meteorological Satellite-1) on 31 October 1994. The Scanning TV Radiometer (STR) is the prime instrument to observe clouds and the cloud-free surfaces in the visible and infrared bands. GOMS-1, also referred to as Electro-1, ended operations in November 2000. Russia plans to launch Electro-M (Modified) by 2006. Until that time, the Russian weather service is dependent on the services provided by METEOSAT of EUMETSAT for its access to geostationary weather satellite data.

China joined the group of nations with geostationary meteorological satellites with the launch of FY-2A (Feng-Yun-2A) on 10 June 1997. The prime sensor, the Stretched-Visible and Infrared Spin-Scan Radiometer (S-VISSR), is an optomechanical system, providing observations in three bands (at resolutions of 1.25 km in the visible and 5 km in the infrared and water vapor bands).

As the value of meteorological satellite data became increasingly apparent, the WMO incorporated them into the World Weather Watch (WWW) program, to provide members access to real-time, world-wide weather information through member-operated observation systems and telecommunication links. It was eventually agreed that to provide complete coverage in the tropics, two geostationary satellites would be furnished by the United States (GOES-E and GOES-W) and one each by Japan (GMS), the European Space Agency (Meteosat) and the former Soviet Union (GOMS), as shown in Figure 2.7. For more detailed information about the various polar-orbiting and geostationary meteorological satellites, the reader is referred to texts by Rao *et al* (1990) and Kramer (2002).

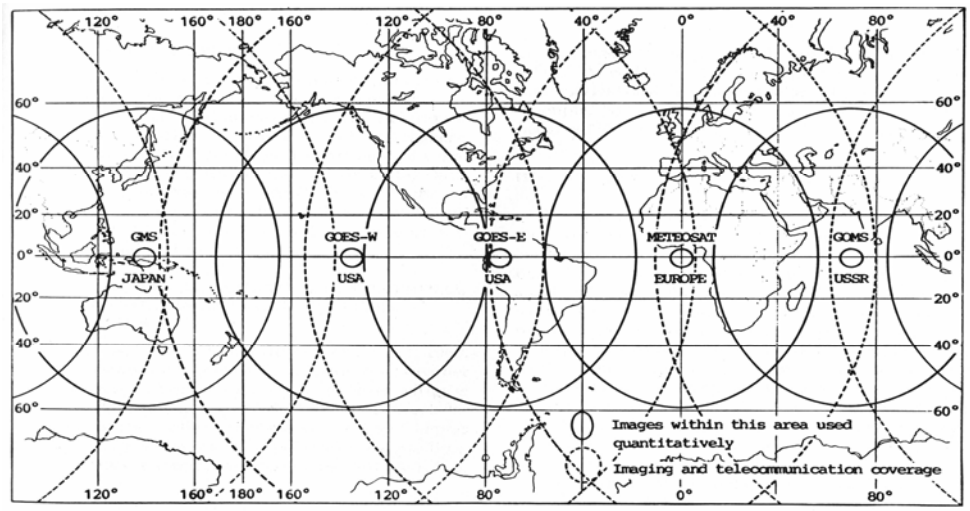


Figure 2.6 Coverage of the geosynchronous satellites associated with the Coordination of Geostationary Meteorological Satellites (Rao, 2000).

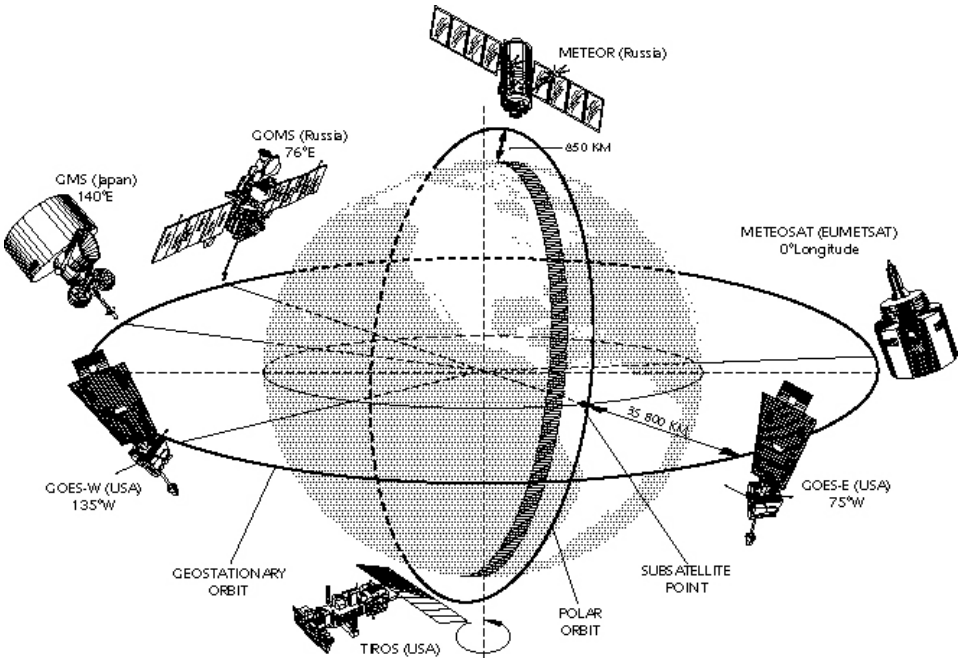


Figure 2.7 Meteorological satellites supporting the WMO World Weather Watch programme (WMO website).

## 2.2 THE NATIONAL POLAR-ORBITING OPERATIONAL ENVIRONMENTAL SATELLITE SYSTEM (NPOESS)

The US National Polar-Orbiting Operational Environmental Satellite System (NPOESS) is an Executive branch agency established by a 1994 Presidential Decision Directive to bring together the DMSP and TIROS POES systems under a single national program. The NPOESS Integrated Program Office (IPO) was created to develop, acquire, manage, and operate the next generation of US polar-orbiting environmental satellites. The IPO is composed of representatives from the Department of Commerce (DoC), Department of Defense, and NASA. Program oversight is exercised by the DoC, system acquisition by the DoD, and NASA provides technical oversight and guidance.

Deleted: o

Deleted: o

Deleted: o

The NPOESS system represents the first US operational environmental satellite designed specifically to meet product requirements, known as Environmental Data Records (EDRs), as defined by the NPOESS user community. These requirements were flowed from the various DoC, DoD, and NASA users to the NPOESS IPO where they were grouped into sensing requirements and summarized in Sensor Requirement Documents (SRDs). For example, requirements for high-resolution cloud imagery were outlined in the VIIRS SRD. The requirement for the highest accuracy atmospheric temperature profiles was contained in the Cross-track Infrared Sounder (CrIS) SRD while requirements for atmospheric profiles in cloudy conditions were assigned to the Conical

Deleted: o

Deleted: o

Scanning Microwave Imager/Sounder (CMIS) SRD. Sensors developed by the NPOESS IPO include:

- CMIS (Conical-scanning Microwave Imager/Sounder). This instrument collects global microwave radiometry and sounding data to produce microwave imagery and other meteorological and oceanographic data. CMIS is the primary instrument for satisfying 20 EDRs (NPOESS CMIS SRD, 2001). It has its heritage in the DMSP SSMI/I, and SSMIS, and the NASA Tropical Rainfall Measurement Mission (TRMM) Microwave Imager (TMI). The contract to build the CMIS instrument was awarded to Boeing Satellite Systems of El Segundo, California.
- CrIS (Cross-Track Infrared Sounder). This instrument measures the Earth's radiation to determine the vertical distribution of temperature, moisture and pressure in the atmosphere; thus, it is the primary instrument for satisfying these 3 EDRs (NPOESS CrIS SRD, 1999). The heritage of CrIS is from the NASA Atmospheric Infrared Sounder (AIRS), the EUMETSAT Infrared Atmospheric Sounding Interferometer Radiometer (IASI), and the NOAA HIRS sensors. The contract to build the CrIS instrument was awarded to ITT Aerospace of Ft. Wayne, Indiana.
- OMPS (Ozone Mapping and Profiler Suite). This instrument collects data to permit the calculation of the vertical and horizontal distribution of Ozone in the Earth's atmosphere and is the primary instrument for satisfying 1 EDR (NPOESS OMPS SRD, 1999). Heritage sensor for the OMPS include the Total Ozone Mapping Spectrometer (TOMS), the Solar Backscatter UltraViolet (SBUV), and the Global Ozone Monitoring Experiment (GOME) sensors. The contract to build the OMPS instrument was awarded to Ball Aerospace of Boulder, Colorado.
- VIIRS (Visible/Infrared Imager/Radiometer Suite). This instrument collects visible and infrared radiometric data of the Earth's atmosphere and is the primary instrument for satisfying 26 EDRs (NPOESS VIIRS SRD, 2000). Heritage sensors for the VIIRS include the DMSP OLS, the TIROS AVHRR/3, and NASA's MODIS, and SeaWiFS sensors. The contract to build the VIIRS instrument was awarded to Raytheon Santa Barbara Remote Sensing of Goleta, California.
- SESS (Space Environment Sensor Suite). This instrument suite measures the near-Earth space environment in terms of neutral and charged particles, electron and magnetic fields, and optical signatures of aurora. SESS is the primary sensor suite for satisfying X EDRs (NPOESS SESS SRD, 1999). The heritage instruments for the SES include the DoD DMSP Space Sensor and the NOAA series Space Environment Monitor. The contract to build the SESS instrument was awarded to Ball Aerospace of Boulder, Colorado.

Detailed specifications for product attributes (e.g. accuracy, precision, measurement uncertainty, reporting interval, refresh rate, etc.) for each EDR were contained in the individual SRD developed for each sensor. All NPOESS system-level requirements were then consolidated into Appendix D to the NPOESS Technical Requirements Document (NPOESS TRD, 2001). Subsequently, competing instrument sub-contractors developed their sensor designs and retrieval algorithms concepts to satisfy these SDR requirements.

**Deleted:** e

**Deleted:** ,

**Deleted:** <#>GPSOS (GPS Occultation Sensor). This instrument measures the refraction of radiowave signals from the GPS and Russia's Global Navigation Satellite System (GLONASS) to characterize the ionosphere. The instrument is also used for spacecraft navigation. It is the primary instrument for satisfying 2 ionospheric EDRs and, in addition, has growth potential to support 2 tropospheric EDRs (NPOESS GPSOS SRD, 2000). The heritage for this instrument is in the GRAS [GNSS (Global Navigation Satellite System) Receiver for Atmospheric Sounder] and the GPS/MET (Global Positioning System/ Meteorology) sensors. The contract to build the GPSOS instrument was awarded to Saab Ericsson Space AB, Gothenburg, Sweden. ¶

**Deleted:** O

**Deleted:** ?????

After several years of development, each competing sensor vendor conducted a Preliminary Design Review to present its design concept and retrieval algorithms. After competing vendors completed their preliminary design reviews, proposals to manufacture instrument were solicited and the NPOESS IPO selected the winning instrument vendor to begin full-scale production. The first stage of this production process was the issuance of a non-competitive contract to the winning instrument vendor to mature their design and retrieval algorithms needed to meet EDR requirements and present this work at a Critical Design Review.

At the start of the instrument vendor competition, the NPOESS IPO awarded competitive contracts to two large aerospace companies to design the complete NPOESS system. This "prime" contractor would be required to provide the spacecraft, integrate all the instrument into the system, develop the data transmission concept, and ground processing system to ensure all attributes of EDR requirements were satisfied. Upon downselect, the prime contractor also assumed control of sub-contracts with instrument vendors selected by the IPO to ensure that these systems were smoothly integrated into the spacecraft environment. TRW (Thompson Ramo Wooldridge), Inc. was selected by the NPOESS IPO as the prime contractor for the NPOESS system but was subsequently acquired by Northrop Grumman so the NPOESS system contractor became Northrop Grumman Space Technology.

**Formatted:** Space Before: 12 pt

**Deleted:** ,

The schedule for the transition from the current operational system to NPOESS is shown in Figure 2.8. NPOESS-1 is currently scheduled to be launched in 2009 and the NPOESS program will extend to at least 2018. Northrop Grumman Space Technology will build much of the NPOESS system in preparation for the launch of the NPOESS Preparatory Project (NPP) mission in 2006. The NPP spacecraft is a transitional system that will fill the gap between NASA's EOS AM (Terra) mission and supplement measurements for the NASA EOS PM (Aqua) spacecraft. Key objectives of the NPOESS Preparatory Project are: (1) to conduct instrument risk reduction by offering early instrument and system level testing, (2) to learn lessons for design modifications in time to ensure NPOESS launch readiness, (3) to reduce risk in the ground system data processing, to include conducting early user evaluation of NPOESS data products, such as algorithms and instrument verification, opportunities for instrument calibration. Northrop Grumman Space Technology will conduct system-level testing and verification of all EDRs, using data collected by the NPOESS Preparatory Project, to ensure products will meet system requirements with data acquired by NPOESS-1.

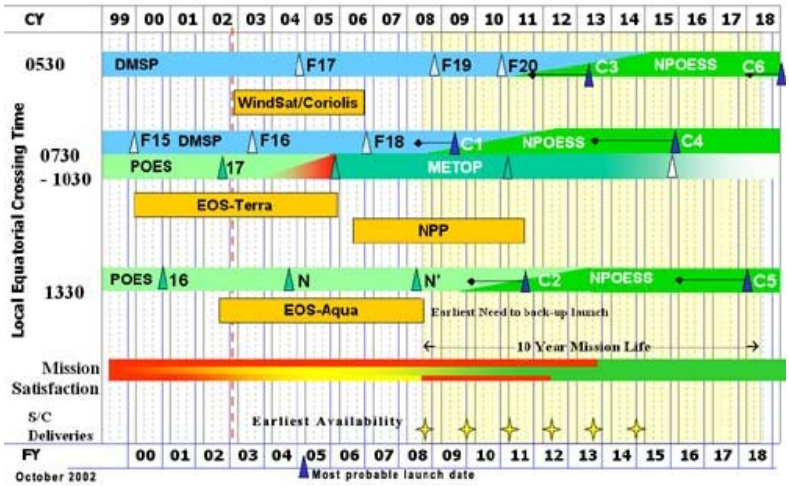


Figure 2.8 Transition of NPOESS satellites with existing US POES satellite systems (IPO website).

Thus, we can see that the NPOESS system is clearly a program that is driven by Environmental Data Record (EDR) requirements and that VIIRS is a key sensor that will be carried first on the NPOESS Preparatory Project satellite and every subsequent NPOESS satellite. With a nominal data swath width of 3,000 km, VIIRS has been designed to provide contiguous coverage at the equator every four hours based upon the plan to fly three NPOESS spacecraft in Sun-synchronous orbits at nominal altitudes of 833 km with ascending nodal times of 1330, 1730, and 2130.

The initial NPOESS system specification listed over 60 Environmental Data Records to be generated from multiple instruments, including imagers and sounders designed specifically to meet a subset of these product requirements. The electro-optical imager, known as the Visible/Infrared Imager/Radiometer Suite, VIIRS, was required to collect data needed to retrieve 27 NPOESS Environmental Data records The design process used to ensure that VIIRS imagery satisfies NPOESS requirements for manually-generated cloud products is a focus of this book and in Chapter 3, this process is demonstrated in detail along with specifications for the resulting VIIRS design. (In 1997 Raytheon Santa Barbara Remote Sensing (SBRS) entered the competition to build the VIIRS instrument and was awarded the contract in 2000 to build the instrument. Dr Keith D. Hutchison served as a principal investigator for SBRS to flowdown the sensing requirements necessary to meet the VIIRS Imagery Environmental Data Records.) In Chapters 5, 6, and 7 detailed insights are provided on the manual interpretation of cloud and background signatures in these VIIRS bands. In addition, Dr. Hutchison also developed the approach to retrieve the Cloud Base Heights Environmental Data Record solely from VIIRS data. The algorithms that retrieve Cloud Base Heights are discussed at length in Chapter 8 along with other automated cloud algorithms that can be used to create automated, 3-dimensional cloud fields from data collected by VIIRS and other NPOESS sensors.

**Deleted:** channels

# Chapter 3

# VIIRS IMAGERY DESIGN ANALYSIS

As noted in the last chapter, the VIIRS instrument was designed to meet EDR product requirements as specified in the VIIRS Sensor Requirements Document (NPOESS VIIRS SRD, 2002). In this chapter, all VIIRS EDR requirements are identified and in-depth information is provides on those requirements that impact the Imagery EDR. The next chapter discusses the process used to ensure that the VIIRS design satisfies these user requirements.

## 3.1 VIIRS EDR REQUIREMENTS OVERVIEW

The VIIRS sensor was designed by Raytheon Santa Barbara Remote Sensing to collect data sufficient to create EDRs that comply with specifications defined by the NPOESS IPO as outlined in the VIIRS Sensor Requirements Document (NPOESS VIIRS SRD, 2002). The following EDRs and Application-Related Requirements are listed as primary products of the VIIRS sensor in that document:

Deleted: R

- Imagery (except microwave imagery)
- Sea Surface Temperature
- Soil Moisture
- Aerosol Optical Thickness
- Aerosol Particle Size Parameter
- Suspended Matter
- Cloud Base Height (Derived)
- Cloud Cover/Layers
- Cloud Effective Particle Size
- Cloud Optical Thickness
- Cloud Top Height (Derived)
- Cloud Top Pressure (Derived)
- Cloud Top Temperature
- Albedo (Surface)
- Land Surface Temperature
- Vegetation Index (VI)
- Snow Cover/Depth
- Surface Type
- Ice Surface Temperature
- Net Heat Flux (Derived)
- Ocean Color/Chlorophyll
- Sea Ice Age/Edge Motion

- Fresh Water Ice
- Active Fires

Deleted: ¶

Deleted: Listed in parentheses after each EDR is a reference to Appendix D to the NPOESS Technical Requirements Document (NPOESS TRD, 2001) which specifies system-level requirements that also must be satisfied by the NPOESS system integrator, Northrop Grumman Corporation, possibly using data acquired by more than one of the NPOESS sensors.

## 3.2 VIIRS IMAGERY REQUIREMENTS

The VIIRS SRD states that Imagery EDR requirements fall into three classes: (a) explicit requirements on the EDR content, quality, reporting frequency, and timeliness (b) application-related requirements based on utilizing the imagery EDR, such as manual generation of cloud and sea ice data, and (c) derived requirements to be derived by the VIIRS contractor based on requirements for other EDRs supported by the imagery. A brief overview of these requirements includes:

Deleted: s

(1) Explicit EDR Requirements for each Imagery band include the following two data products, both generated by ground processing of VIIRS data:
   (a) a two-dimensional array of locally averaged absolute in-band radiances at the top of the atmosphere measured in the direction of the viewing instrument, and
   (b) the corresponding array of equivalent blackbody temperatures (EBBT) if the band is primarily emissive, or the corresponding array top-of-the-atmosphere (TOA) reflectances if the band is primarily reflective during the daytime. The form of the spatial weighting function that determines the local averaging of the absolute TOA radiance is constrained by the Horizontal Spatial Resolution (HSR) requirement. The number of spectral bands, band limit values, measurement ranges, and measurement uncertainty (or accuracy and precision) requirements are to be derived based on the manually-generated, application-related requirements and on the requirements of other EDRs supported by the imagery.
   (c) In addition to these products, the Imagery EDR includes a daytime/nighttime visible imagery product that maintains apparent contrast under daytime, nighttime, and terminator region illumination conditions.
   (d) At a minimum, at least one daytime visible, one daytime/nighttime visible, and one IR channel shall meet the explicit imagery requirements.
(2) Application-related Imagery requirements are based on specific applications utilizing the imagery EDR, such as manual-generation of cloud and sea ice data as outlined in the next section.
(3) Derived Imagery requirements are requirements necessary to satisfy threshold requirements of other "primary" EDRs supported by the imagery.

All VIIRS spectral bands that are classified as imagery channels in order to meet the explicit, applications-related, or derived Imagery EDR requirements listed above must also meet the additional requirements shown in Table 3.1. Thresholds are considered

minimum acceptable NPOESS system-level performance requirements and objectives are preferred NPOESS system-level performance requirements. Typically, much more stringent design requirements and significantly increased costs are needed to attain Objective performances levels. For example, worst-case Horizontal Spatial Resolution decreases from 0.8 km for the Threshold requirement to 0.1 km for the Objective requirement at the VIIRS edge of scan. Obviously, the much higher resolution of this Objective requirement would greatly increase both hardware design costs, to measure sufficient energy 1500 km from nadir and to store much larger data sets on-board the satellite, as well as increased communication costs, associated with the transmission of a much larger data volume to the satellite operations ground station.

Table 3.1 Attribute Requirements for Each VIIRS Band Classified as Imagery.

| Attribute | Thresholds | Objectives |
|---|---|---|
| a. Horizontal Spatial Resolution (HSR), both in-track and cross-track | | |
| 1. At nadir | 0.4 km | To be determined |
| 2. Worst case | 0.8 km | 0.1 km |
| 5. Daytime/Nighttime Visible, worst case | 2.6 km | 0.65 km |
| b. Horizontal Reporting Interval | Derived (gapless or near gapless coverage required) | Derived (gapless or near gapless coverage required) |
| c. Horizontal Coverage | Global | Global |
| d. Measurement Range | | |
| 1. Daytime/Nighttime visible | 4E-9 - 3E-2 W cm$^{-2}$-sr$^{-1}$ in the 0.4-1.0 µm band, or equivalent in another band | Includes threshold range |
| 2. Other bands | Derived | Derived |
| e. Measurement Uncertainty | Derived | Derived |
| f. Mapping Uncertainty | | |
| 1. At nadir | 3 km | (TBD) |
| 2. Worst case | 4 km | 0.5 km |
| g. Maximum Local Average Revisit Time | 4 hrs | (TBD) |
| h. Maximum Local Refresh | 6 hrs | (TBD) |
| i. Fraction of Revisit Times Less Than a Specified Value | At any location at least 75% of the revisit times will be 4 hours or less. | (TBD) |
| j. Minimum Swath Width (All other EDR thresholds met) | 3000 km | (TBD) |

**Deleted:** (TBD)

**Deleted:** /

**Deleted:** 2

**Deleted:** (TBR)

Thus, the VIIRS Imagery requirement specifies that: (a) at least one daytime visible, nighttime visible, and IR band will be Imagery channels, (2) all bands needed to meet Threshold requirements for manually-generated cloud and sea ice analyses will be Imagery channels, and (3) any band that requires Imagery attributes listed in Table 3.1 to meet the Threshold requirements of another VIIRS EDR will be an Imagery channel.

## 3.3 CLOUD APPLICATIONS-RELATED IMAGERY REQUIREMENTS

As noted above, the VIIRS SRD states that the content and quality of VIIRS Imagery shall be adequate to allow application-related requirements to be satisfied. These requirements include manually-generated cloud and manually-generated sea ice data. The requirement for manually-generated cloud analyses includes the capability to detect or identify clouds and manually classify them as discussed below. *Therefore, a primary goal of this book is to demonstrate the capability and procedures to manually detect and classify clouds in spectral data similar to those identified as VIIRS Imagery bands.*

- Manually Generated Cloud Data. Manually generated cloud data are estimates of cloud cover and cloud type generated by a trained human analyst. This is done by viewing either or both of the unprocessed and the processed imagery derived from the unprocessed imagery, e.g., by data fusion, spatial re-scaling, image enhancement, etc.

- Manually Generated Cloud Type. Cloud type is defined as follows:

(1) Altocumulus (AC)
(2) Altocumulus Castellanus (ACCAS)
(3) Altocumulus (Standing lenticular) (ACSL)
(4) Altostratus (AS)
(5) Cirrocumulus (CC)
(6) Cirrocumulus (Standing lenticular) (CCSL)
(7) Cirrostratus (CS)
(8) Cirrus (CI)
(9) Cumulonimbus (CB)
(10) Cumulus (CU)
(11) Cumulus Fractus (CUFRA)
(12) Towering Cumulus (TCU)
(13) Stratus Fractus (STFRA)
(14) Nimbostratus (NS)
(15) Stratocumulus (SC)
(16) Stratocumulus (Standing lenticular) (SCSL)
(17) Stratus (ST)

The determination of cloud type not only entails a capability to distinguish between clouds of different type, but also a capability to distinguish clouds from other features, such as snow, cold water, cold land, haze, smoke, dust, etc. Therefore, the following additional types are defined:
(18) Obscured/not cloudy
(19) Clear

- Sea Ice Data. Sea ice data may be generated interactively by a trained human analyst viewing unprocessed or processed imagery at a computer workstation, or automatically via an algorithm. In addition to the determination of ice edge location and ice concentration as described below, analysts will attempt to determine the thickness and size of leads and polynyas based on the imagery.

- Ice Edge Location and Ice Concentration. An ice edge is defined as the boundary between ice-covered sea water (ice concentration > 0.1) and sea water not covered by ice (ice concentration ≤ 0.1). Ice concentration is defined as the fraction of a given area of sea water covered by ice. An ice edge is typically provided as a contour on a map or in digital form as a set of latitude/longitude coordinates. The ice edge location error is defined as the distance between the estimated locations of an ice edge and the nearest location of a true ice edge.

**Deleted:** (TBR)

**Deleted:** (TBR)

### 3.3.1 Cloud Cover

The NPOESS requirements for manually-generated cloud cover are shown in Table 3.2. Cloud cover is defined as the fraction of a given area, i.e., of a horizontal cell, on the Earth's surface for which a locally normal line segment, extending between two given altitudes, intersects a detectable cloud. For manual analyses, cloud cover is estimated for a single atmospheric layer. Specifically, the minimum and maximum altitudes of this layer are defined to be the surface of the Earth and the altitude where the pressure is 0.1 mb. Haze, smoke, dust, and rain are not to be considered clouds. For the purpose of validating this requirement, cloud cover estimates are to be generated by a trained human analyst viewing unprocessed and/or processed imagery for contiguous square areas having side length equal to the horizontal cell size specified below.

*Thus, the requirement for the manually-generated cloud cover EDR translates into identifying the minimum set of VIIRS Imagery channels needed to accurately differentiate between cloud and cloud-free pixels under a global set of conditions***.** "Accurately" is defined by the attributes listed in Table 3.2. From a sensor design perspective, this requirement includes quantifying the spatial, spectral, and sensor (e.g. noise) model needed to meet the threshold requirements. Chapter 3, "*Theoretical Basis for Manual Cloud Analyses*," demonstrates the procedures used to define the VIIRS design parameters needed to satisfy requirements for the manually-generated cloud cover EDR.

Table 3.2. NPOESS requirements for Manually-Generated Cloud Cover EDR.

| Attribute | Thresholds | Objectives |
|---|---|---|
| a. Horizontal Cell Size | 3 times the Imagery HSR | 2 times the Imagery HSR |
| b. Horizontal Reporting Interval | Horizontal cell size | Horizontal cell size |
| c. Measurement Range | 0 - 1, in 0.1 increments | 0 - 1, in 0.1 increments |
| d. Measurement Uncertainty | 0.1 | 0.1 |

**Deleted:** (TBR)

### 3.3.2 Cloud Type

The NPOESS Requirements for the manually-generated cloud type EDR are shown in Table 3.3. For the purpose of validating this requirement, typing is to be performed by a trained human analyst viewing either or both unprocessed and processed imagery for contiguous square areas having side length equal to the horizontal cell size specified below. The probability of correct typing is defined as the probability that a cell reported as being of type *x* is in fact of type *x*, where *x* is any of the 19 cloud types specified above.

Table 3.3. NPOESS requirements for Manually-Generated Cloud Type EDR.

| | Thresholds | Objectives |
|---|---|---|
| a. Horizontal Cell Size | 3 times Imagery HSR (1.2 km at nadir) | 2 times Imagery HSR |
| b. Horizontal Reporting Interval | Horizontal cell size | Horizontal cell size |
| c. Measurement Range | Clear, obscured/not cloudy, ST, CU, CI | Clear, obscured/not cloudy, all 17 cloud types |
| d. Probability of Correct Typing | 85 % at 95 % (TBR) confidence level | 90 % at 95 % (TBR) confidence level |

**Deleted:** (TBD)

**Deleted:** (TBD)

During the design phase of the VIIRS project, it was demonstrated that only three spectral bands were required to satisfy the threshold requirements for the VIIRS Imagery Application-Related manually-generated cloud products. These bands included one visible (~0.64 μm), one mid-IR (~3.74 μm), and one longwave-IR (~11.45 μm) band. With the additional NPOESS-Explicit EDR requirement for a nighttime visible Imagery band, known as the day-night band (DNB), and derived requirements for imagery resolution bands at 0.865 μm and 1.6 μm, there came to be six total imagery resolution channels in the VIIRS sensor design.

**Deleted:** channels

From Table 3.1, it is seen that VIIRS imagery bands must have a nadir resolution of no worse than 400m – the VIIRS design is 375 m. This resolution must be near-constant in the cross-track direction, i.e. it can degrade to no worse than 800 m at the edge of scan. (Typically, AVHRR Local Area Coverage degrades from a nominal 1.1 km at nadir to over 5 km at the edge of its scan.)

All remaining bands needed to support the retrieval of VIIRS EDRs shown in Section 2.2 are called moderate resolution bands. For the purpose of constructing manually-generated cloud analyses, they are referred to as "*Imagery-Assist*" bands. The importance of Imagery Assist bands are two fold: (1) it is possible to achieve much higher signal to noise with moderate resolution bands, since the horizontal spatial resolution of 750 m at nadir is double that of the imagery bands and (2) lower bandwidth is needed to transmit data collected in moderate resolution bands compared to imagery bands.

NPOESS required that all VIIRS bands needed to satisfy threshold requirements for applications-related imagery products, e.g. manually-generated cloud cover, would be at Imagery resolution, i.e. 0.4 km at nadir. However, Imagery Assist bands could be used with Imagery bands to advance toward performance objectives, as shown in the far right columns of Tables 3.2 and 3.3. The use of Imagery and Imagery Assist bands together in performing manually-generated cloud analyses is demonstrated in Chapter 6.

## 3.4 VALUE OF MANUALLY-GENERATED CLOUD ANALYSES

Manually-generated cloud analyses can serve several important functions in operational meteorology. Cloud cover analyses generated from the human interpretation of multispectral imagery can be defined as "ground truth" and then used to make quantitative comparisons with the results obtained with automated cloud analysis algorithms or models. In addition, manual analyses can be used to validate the accuracy of cloud forecast models or other numerical weather prediction models by creating manual analyses of imagery coincident with forecast verification time.

Deleted:

### 3.4.1 Performance Verification of Automated Cloud Models

In the 1990 timeframe, cloud cover analyses were generated from OLS imagery collected by the DMSP satellite series and ingested into the Real-time Cloud Nephanalysis (RTNEPH) Model (Keiss and Cox, 1985) at Air Force Weather Agency (AFWA). These automated cloud analyses were then used to initialize a cloud forecast model known as the High Resolution Cloud Prognosis (HRCP). The goal of the Cloud Model Enhancement Program (CMEP) was to determine the accuracy of the HRCP model and identify enhancements to improve the accuracy of forecasts. To accomplish the task, raw satellite imagery, automated cloud analyses, and automated cloud forecasts were collected for two 30 day periods. Manual cloud analyses were generated for each satellite image. These ground truth cloud, no cloud (CNC) analyses were compared against time-coincident automated cloud analyses and forecasts. Sample results from this study are shown in shown Figure 3.1 for the 0-hour cloud analysis used to initialize the HRCP model and 3-hour HRCP cloud forecast. Similar results were obtained at each of the HRCP forecast verification times, e.g. covering 24 hours at 3-hour intervals.

Figure 3.1 shows that the RTNEPH failed to detect clouds, especially in regions that were less than 50% cloud covered. It was not a surprise to find that the under-specification of cloud cover in the 0-hour analysis resulted in an under-specification of clouds at each of the HRCP forecast verification times. This ability to detect clouds manually and create

highly accurate CNC analyses from DMSP imagery allowed scientists to evaluate automated cloud forecast model performance quantitatively and resulted in a major improvement in cloud forecast accuracy, according to Air Force personnel. In addition, quantifying the impact of automated cloud analysis on performance of the HRCP model led to a program initiative, known as the Cloud Depiction and Forecast System (CDFS) II project, to update the RTNEPH cloud analysis model (Hutchison and Janota, 1989).

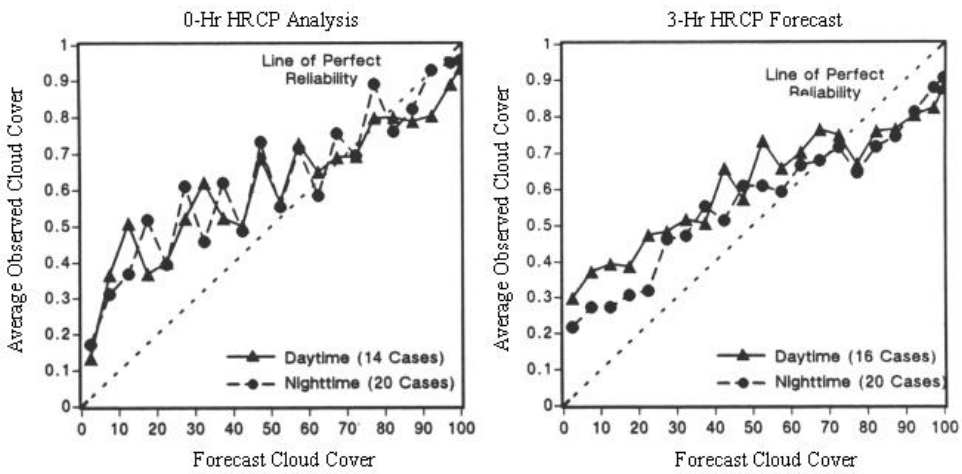


Figure 3.1. HRCP cloud forecast reliability established during the CMEP Study (Hutchison and Janota, 1989).

**Deleted:** C

**Deleted:** F

**Deleted:** R

**Deleted:** E

**Deleted:** D

**Deleted:** 1990

### 3.4.2 Quality Control of Automated Cloud Analyses

While VIIRS imagery can be used to create manual cloud analyses for quantifying the performance of cloud forecast models, it can also be used *to quality control automated cloud analyses, not to generate manual CNC analyses as discussed in the previous section*. The typical sequence of steps in the generation of automated cloud forecasts at Air Force Weather Agency (AFWA) includes:

1) Data ingestion functions:

- Process imagery by the satellite processing mainframe computer
- Process the imagery into the Satellite Data Handling System which does an ingest function separate from the mainframe computer

2) Generate Automated Cloud Analysis with Real-time Nephanalysis (RTNEPH) Model

**Deleted:** providing

**Deleted:** for

**Deleted:** ly-generated

**Deleted:** has great value

**Deleted:** to

**Deleted:** *the primary use of VIIRS imagery at the US Air Force Weather Agency (AFWA) is*

**Deleted:** *Therefore, the implied VIIRS requirement for manually-generated cloud products is to provide imagery that supports the quality control of automated cloud analysis models in a highly time-constrained environment.*

- Generate cloud analysis with the RTNEPH (Hamill et al., 1992)
- Manual Quality Control of the RTNEPH analyses (the so-called "RTNEPH Bogus" process)

3) Generate Automated Cloud Forecasts Cloud Advection (ADVCLD) Model

- ADVCLD (Five-Layer) forecast model (+00 to +36 hours)
- Manual quality control of Forecast Products (the so-called "Forecast Bogus" process)

The entire process is accomplished within time constraints typical of an operational weather central. First, the DMSP spacecraft begins transmitting data to the command readout site. Based upon the DMSP system, data ingestion typically requires several minutes. Automated cloud analyses are accomplished next; however, these algorithms do not always produce high-quality cloud analyses. Therefore, quality control by trained forecasters is an important part of the RTNEPH process. Preparation for the RTNEPH Bogus occasionally begins prior to data readout (e.g., pre-mapping grid coordinates to satellite image space). The manual quality control (Bogus) process generally allows two or more quarter-orbits of data to be processed in parallel. At Bogus completion, RTNEPH edits are sent to the satellite processing mainframe to update the RTNEPH database. This database is used to initialize the various forecast models (Hamill, et al., 1992). Output cloud cover forecasts are displayed on the Satellite Data Handling System over the DMSP imagery alongside ancillary forecast aids (e.g., height, temperature, and moisture fields) and reviewed for correctness by forecasters. Forecast edits are retransmitted to the satellite processing mainframe for database update and final forecast product generation.

Historically, the RTNEPH Bogus on the Satellite Data Handling System was accomplished by displaying only two DMSP bands of smooth (1.5 nautical miles) broadband infrared and visible imagery for a quarter-orbit of data simultaneously on two monitors at 1024x1024 resolution in the nominal satellite projection. A third monitor displays a 4:1 reduced view of the entire quarter orbit to provide the analyst with an overview of the entire scene. On the high resolution monitors, digits are displayed over the imagery at RTNEPH grid point locations to represent the automated cloud cover analysis. Only the total cloud amount, in eighths, is displayed. Cloud cover of zero eighths is not displayed; this is to emphasize the distinctiveness of clear-cloud regions. Because digits are spaced closely in image space (typically no more than 16 pixels from center to center), a special character set is used to display digits with a minimum number of pixels. Additionally, the capability to toggle digits on or off rapidly is available.

Analysts use a multiple monitor slaved draw mode with a digitizing tablet to circumscribe cloud edits around sets of digits which are deemed unrepresentative of the true cloud field. Each single cloud edit label takes the form of a closed curve and may include up to three pairs of cloud amount and cloud type; one each for low, middle and/or high clouds. For example, one Bogus label might include 3-eighths of cumulus, 5-eighths of altocumulus, and 6-eighths of cirrus. Analysts generally estimate lower altitude cloud amounts based on their meteorological understanding of the scene. The

**Deleted:** Model

**Deleted:** referred to in the literature as

**Deleted:** long range

**Deleted:** 3

**Deleted:** 3

**Deleted:** <#>HRCP (High-Resolution Cloud Prognosis) short range cloud forecast model¶

**Deleted:** nominally

**Deleted:**

**Deleted:** less than an hour

**Deleted:** This time starts when

**Deleted:** only a few

**Deleted:** i

**Deleted:** is

**Deleted:**

**Deleted:**

**Deleted:** channels

**Deleted:** Up to four sets of these displays are 'scanned' in sequence from the northernmost to the southernmost sections of the quarter-orbit.

**Deleted:**

**Deleted:**

**Deleted:**

RTNEPH bogus edit post-processor uses cloud type labels to assign default cloud base and top altitudes.

After a review of the displayed 1024x1024 frame for the quarter orbit is complete, another analyst performs a "quick" review of the edits; then, quality control of the next frame of the quarter-orbit begins. The quality control time schedule only allows the analyst approximately additional time for each 1024x1024 frame to ensure that a single quarter-orbit is processed within the required timeline. At the end of the allotted time or when the quarter orbit is completely reviewed, all edits are concatenated and shipped to the satellite processing mainframe to update the database.

**Deleted:** A hardcopy of the edits is generated and filed for subsequent review. Given the typical time budget to review and correct a quarter orbit cloud analysis, the analysts typically are reviewing and correcting 1.5 million square kilometers per minute.

The integration of NPOESS data in general, and VIIRS data in particular, should significantly improve the cloud analysis and forecast system. Expected enhancements include:

**Deleted:** will

**Deleted:** this

- *The use of VIIRS imagery will significantly improve the quality of automated cloud analyses, resulting in fewer operations being needed to perform the quality control, Bogus function.* Earlier studies quantified the accuracy of the cloud forecast system at AFWA and recommended further improvements in the cloud analysis and forecast system (Hutchison and Janota, 1989; Hutchison et al., 1990). Recommended enhancements were made to the cloud forecast models and subsequently the time required to perform quality control of the automated cloud forecasts became negligible. These studies concluded that "After the recommended enhancements to cloud forecast models were made, the next major step necessary to improve the cloud forecast accuracy was to upgrade the cloud analysis model." Subsequently, the Support of Environmental Requirements for Cloud Analysis and Archive (SERCAA) Program was undertaken to improve automated cloud analyses (Gustafson et al., 1994). Continued improvement in automated cloud analysis accuracy is expected with the added spectral data provided by VIIRS.

**Deleted:** n

- *The use of VIIRS imagery will provide analysts with the capability to more readily distinguish between clouds and cloud-free surfaces, using color composites, which will improve the speed and accuracy of the quality control, Bogus processes.* It is assumed that the current Satellite Data Handling System terminals will have the capability to display VIIRS imagery as color composites (i.e. different VIIRS imagery bands, imagery assist bands, band differences, and/or band ratios assigned to each gun of a color display) to exploit the unique spectral signatures of cloud and backgrounds and enhance the analysts' capability to perform the quality control process on automated cloud analyses quickly and accurately. As experience is gained in using and interpreting these color composites, the capability to quality control the automated analyses more accurately and quickly will be possible using a minimum of VIIRS color composites. *Again, it is a primary purpose of this text to provide future users of VIIRS imagery with the fundamental knowledge and skills of image interpretation to exploit fully the spectral signatures in*

**Deleted:** During the NPOESS era, at a minimum, i

**Deleted:** expected

**Deleted:** all

**Deleted:** been upgraded

**Deleted:** channels

**Deleted:** channels

**Deleted:** channel

**Deleted:** channel

**Deleted:** *manual*

*VIIRS imagery and improve support to various missions, including overall performance of the Cloud Depiction and Forecast System.*

Attention now turns to the primary focus of this text, which is to analyze the spectral signatures of clouds and various cloud-free surfaces in VIIRS bands. The analysis will include a brief overview of the phenomenology that characterizes signatures of clouds and surface features in meteorological satellite imagery and sample imagery of each VIIRS band that demonstrates this theory. A thorough representation of this phenomenology is important to fully understand the fundamental principles of meteorological satellite data interpretation. Mastery of this basic knowledge will allow users of VIIRS imagery to apply these concepts to their unique applications that will ultimately extend the information base provided in this text. It is our hope that future users of VIIRS data will freely share their new knowledge with us so we may include additional applications in future revisions of this text.

**Deleted:** channels

# Chapter 4

# VIIRS IMAGERY REQUIREMENTS ANALYSIS

The VIIRS Imagery bands were derived from an analysis of the Imagery EDR requirements contained in the VIIRS Sensor Requirements Document, as discussed in Chapter 3. The Raytheon Santa Barbara Remote Sensing company philosophy for satisfying this EDR was to design the VIIRS sensor with the minimum number of spectral bands needed to meet threshold performance requirements. Attempts to achieve objective level performance would be attempted using Imagery Assist bands, also known as radiometric bands.

**Deleted:** Channe

**Deleted:** l

**Deleted:** Channels

**Deleted:** R

**Deleted:** Channels

Synthetic images that contained different cloud types and various backgrounds were generated to establish the performance expected of the VIIRS design. A manual cloud analysis was created for each synthetic image using procedures that are discussed in this chapter. The cloud, no cloud analysis for each image was then compared against the cloud masks used in the simulation and performance quantitatively established for each of the candidate sensor models. This process was followed to obtain the most cost-effective design that satisfied the VIIRS Imagery EDR requirements. This chapter discusses this process in detail and concludes with a summary of the imagery requirements levied upon the VIIRS sensor designers.

## 4.1 THEORETICAL BASIS FOR MANUAL CLOUD ANALYSES

The ability to manually identify clouds in any given spectral band is based upon the contrast, measured in radiance, between the cloud and the surrounding cloud-free background. More precisely:

$$C = I_\nu(0)_{cloud} \ / \ I_\nu(0)_{background} \tag{4.1}$$

Depending upon the wavenumber ($\nu$) of the radiation viewed in a given band, the top of the atmosphere radiance, $I_\nu(0)$, may be composed of reflected solar radiation, emitted thermal radiation, or both solar and thermal radiation when observations are made in the 3-5 μm wavelength interval under daytime conditions. (By convention, E-O imagers use wavelength rather than wavenumber; however, this presentation stays with the latter to conform with presentations in Liou (1980). In addition, $\nu$ is used to represent wavenumber for simplicity, not frequency. The reader is referred to Chapter 1 of this reference to understand the transformations between wavelength, wavenumber, and frequency.)

**Deleted:** by

**Deleted:** channel

**Deleted:** of the VIIRS sensor

For simplicity, consider the case of thermal (infrared) radiation as a narrow (monochromatic) beam of energy emitted from a surface through a cloud-free atmosphere to space. The monochromatic, upwelling infrared energy arriving at the sensor is given by:

**Deleted:** aperture of the VIIRS

**Deleted:** (Liou, 1980)

$$I_\nu(0) = \varepsilon_\nu B_\nu[\mathrm{T}_s]T_\nu(p_s) + \int_{p_s}^{0} B_\nu[\mathrm{T}(p)]\frac{\partial T_\nu(p)}{\partial p}\,dp + (1-\varepsilon_\nu)\int_0^{p_s} B_\nu[\mathrm{T}(p)]\frac{\partial T_\nu(p)}{\partial p}\,dp \qquad (4.2)$$

where: $\nu$ = wavenumber of emission

$B_\nu[\mathrm{T}(p)]$ = Planck function at wavenumber ($\nu$) for temperature (T) in K

$\varepsilon_\nu$ = emissivity of surface at wavenumber ($\nu$)

$T_\nu(p_s)$ = atmospheric transmittance between pressure level ($p_S$) and space

$I_\nu(0)$ = monochromatic radiance arriving at satellite.

$p_s$ = surface pressure

$T_s$ = surface temperature

For imaging sensors, as opposed to sounders, the difference in atmospheric transmittance between adjoining pressure levels (p) is very small which makes the atmosphere a secondary source of energy arriving at the sensor, as described in the integral terms in Equation (4.2). Thus, for the purpose of creating a manual cloud analysis, Equation (4.2) may be closely approximated by:

$$I_\nu(0) = \varepsilon_\nu B_\nu[\mathrm{T}_s]T_\nu(p_s) \qquad (4.3)$$

Equation (4.3) states that the vast majority of energy arriving at the satellite sensor is dependent on three primary components: the blackbody emission from the Earth's surface, the emissivity of the surface, and the atmospheric transmission from the surface to the sensor.

**Deleted:** B

Planck's Law for blackbody radiation defines the total energy of the emission as a function of monochromatic wavelength and surface skin temperature (Liou, 1980). The emissivity is unity if the surface is a blackbody and less than unity otherwise as described by Kirchoff's Law (Liou, 1980). The transmission is unity if the atmosphere is completely transparent at the wavelength ($\nu$), exactly zero if the atmosphere completely absorbs all energy emitted by the surface at the wavelength ($\nu$), and greater than zero but less than unity otherwise, as is typically the case. A similar equation can be written when the feature is a thick (blackbody) cloud rather than a cloud-free surface. In the cloudy case, the emissivity and temperature represent the cloud top rather than the surface and atmospheric transmissivity refers to the column of air extending from the cloud top to the top of the atmosphere.

For the case of solar radiation, the amount of monochromatic energy reflected by the Earth-atmosphere system into the sensor aperture is far more complex and given by Equation (4.4) as described by Liou (1980):

$$I(0;\mu,) = I(\tau_{1;\mu,}\phi)e^{-\tau_1/\mu} + \int_0^{\tau_1} J(\tau;\mu,\phi)e^{-\tau/\mu}\frac{d\tau}{\mu} \qquad (4.4)$$

**Deleted:** $I(0;\mu,) = I(\tau_{1;\mu,}\phi)^{-\tau_1}$

Term A Term B

where:

$I_\nu(0)$ = monochromatic radiance arriving at satellite

$\tau$ = optical depth of each $\tau'$ layer, while the atmosphere is $\tau_1$ thick

Term A = surface energy contribution attenuated to space

Term B = internal atmospheric contributions attenuated to space

$\mu$ = cosine of the angle between radiation stream and the local zenith angle

$\phi$ = azimuth angle.

The complexity of this calculation lies in the source function term, $J(\tau;\mu,\phi)$, which is described for solar radiation by Liou as (1980):

$$J(\tau;\mu,\phi) = \frac{\omega}{4\pi}\int_0^{2\pi}\int_{-1}^{1} I(\tau;\mu',\phi')P(\mu,\phi;\mu',\phi')d\mu'\,d\phi' \tag{4.5}$$

Term C

$$+\frac{\bar{\omega}}{4\pi}\pi F_0 P(\mu,\phi;-\mu_0,\phi_0)e^{-\tau/\mu_0}$$

Term D

where:

Term C = multiple scattering of diffuse (scattered) energy

Term D = single scattering of direct solar irradiance, $F_0$

Deleted: $_o$

and:

$\omega$ = single scattering albedo

$P(\mu,\phi;\mu',\phi')$ = phase function

$F_0$ = solar irradiance

$\mu_0$ = cosine of solar zenith angle

$\phi_0$ = solar azimuth angle

In reality, monochromatic radiation does not exist because of line broadening from natural, pressure (collision), and Doppler (thermal velocity) effects. Also, since an

instrument can distinguish only a finite bandwidth, the upwelling radiance measured by the satellite is integrated over the sensor transmission filter, which is also called the sensor response function, and is given by (Liou, 1980):

$$I_\nu(0) = \int_{\nu_1}^{\nu_2} [I_\nu(0)_\nu \phi_\nu d\nu] / \int_{\nu_1}^{\nu_2} \phi_\nu d\nu \qquad (4.6)$$

Deleted: $I_\nu(0) = \int_{\nu_1}^{\nu_2} [I_\nu(0)_\nu d\nu]$

where: $\phi_\nu$ = filter (sensor) response function at wavenumber (ν)

$\nu_1, \nu_2$ = wavenumber range of filter response

In summary, the ability of the human to observe a cloud in imagery consisting of terrestrial (infrared) radiation is enhanced under the following conditions:

(1) exploiting strong temperature contrasts between the cloud and its surrounding background in a single infrared band in which the emissivities of the cloud and the surface are nearly the same,

Deleted: channel

(2) viewing the cloud and its surrounding background that have the same temperature in a spectral band in which the cloud and background have significantly different emissivities, and

(3) viewing features in a band in which atmospheric transmissivity is much less than unity such that the surface feature is masked by the atmosphere but the cloud is not.

The ability to observe the cloud in imagery containing solar radiation is enhanced under the following conditions:

(1) exploiting strong contrasts in reflectivity between the cloud and its surrounding background in a single band,

Deleted: channel

(2) viewing features in a band in which atmospheric transmissivity is much less than unity such that the surface feature is masked by the atmosphere but the cloud is not. The latter case is typical of the phenomenology exploited in the 1.378 μm band, which suppresses the signatures of low-level cloud and surfaces features and thus enhances the signatures of higher level clouds.

Deleted: channel

Finally, the capability to distinguish a cloud from its surrounding background is also enhanced by viewing the features in multiple spectral bands where the cloud and surface emissivities or reflectivities are significantly different. Examples of these cases will be presented in Chapter 5.

## 4.2 OVERVIEW OF APPROACH TO INSTRUMENT DESIGN

The sensor design process requires extensive trade studies to optimize the VIIRS system parameters needed to meet NPOESS system requirements while maintaining financial

responsibility. For example, a hyperspectral sensor can easily be designed that collects hundreds or even thousands of bands of data; however, major flaws of this design might include the expenses incurred to store the data on the spacecraft, communication downlinks to transmit the data from the satellite to the satellite readout facility, and computer resources necessary to prepare and fully utilize these data in an operational environment. Therefore, the Raytheon VIIRS design philosophy was to minimize the number of imagery bands required to meet NPOESS Imagery EDR requirements, discussed in Section 2.3, and to make all remaining VIIRS bands of lower spatial resolution to satisfy the remaining EDR requirements shown in Section 2.2. Key differences between imagery and moderate resolution bands or imagery assist bands are spatial resolution and band sensitivity, as emphasized in Chapter 3. The effect of spatial resolution is straightforward in that the higher the spatial resolution, the larger the data volume and higher the communication costs necessary to transmit and process the data sets. The impact of band sensitivity on system cost may not be so straightforward, so it is discussed in some detail.

Deleted: channels

Deleted: channels

The sensitivity of radiometers depends on the ratio of their internally generated signal to that produced by incoming radiation (Stewart, 1985). The power available to the instrument is given by:

$$\Phi_{IN} = A\, d\Omega\, d\lambda\, L(\lambda) \tag{4.7}$$

where A is the aperture of the instrument, $d\Omega$ is the angular extent of the area viewed by the instrument, $d\lambda$ is the bandwidth, and $L(\lambda)$ is the spectral radiance of the area viewed. The power is usually focused on a detector that converts radiant power into electrical power which is then amplified and either recorded or transmitted to the ground. The output of the detector $\Phi_{out}$ is the sum of the incoming signal $\Phi_{IN}$ plus the noise, $\Delta\Phi$, generated within the transducer and is represented as:

$$\Phi_{OUT} = A\, d\Omega\, d\lambda\, L(\lambda) + \Delta\Phi \tag{4.8}$$

The signal-to-noise ratio, SNR or $S_n$, of an instrument or an individual band in a multispectral scanner is a common measure of performance for bands operating in the solar spectrum region (e.g. 0 - 5 μm). For example, each MODIS band has a different signal to noise ratio ranging between 57 for channel 18 (0.931-0.941 μm) and 1087 for channel 14 (0.673-0.683 μm). Signal to noise ratio is given by:

Deleted: ensor

Deleted: channel

$$S_n = \Phi_{IN} / \Delta\Phi \sim [A\, d\Omega\, d\lambda\, L(\lambda)] / \Delta\Phi \tag{4.9}$$

Sensor designers seek to maximize $S_n$ in a cost effective manner, which may only be done in a couple of ways. First, $S_n$ may be enlarged by increasing: the size of the aperture A; the field of view $d\Omega$; and/or the bandwidth $d\lambda$. Secondly, it is possible to increase $S_n$ by reducing sensor or individual band noise, $\Delta\Phi$, which is done with improved detector performance.

Deleted: s

Deleted: channel

By convention, instrument noise is inserted into the Planck equation and converted to an apparent change in temperature, $\Delta T$, or Noise Equivalent $\Delta T$ (NE$\Delta$T) for bands operating in the thermal infrared spectrum region, e.g. 5-100 μm. In this case, the optimal sensor design minimizes NE$\Delta$T in a cost effective manner. For MODIS, values of NE$\Delta$T range from 0.05 K for channel 20 (3.660-3.840 μm) to 2.00 K for channel 21 (3.929 – 3.989 μm). In general, an increase in the bandpass, $d\lambda$, is a cost-effective way to lower the NE$\Delta$T of a given band and improve EDR retrieval accuracy (Hutchison, et. al., 1999).

Deleted: ,

Deleted: channel

Deleted: channel

Another option to maximize the function, $S_n$, is to observe the area many times, N, with the same instrument, assuming $L(\lambda)$ does not change between observations, as is done with the along-track scanning radiometer (ATSR) flown on the ERS satellite series (Za'vody et al., 1995). The average of these observations converges toward $\Phi_{IN}$ as N increases. If the noise in different observations is not correlated, then on average:

Deleted: ultiple

$$S_n = (N)^{0.5} [A \ d\Omega \ d\lambda \ L(\lambda)] / \Delta\Phi \qquad (4.10)$$

Thus, the optimum NPOESS VIIRS sensor design becomes a trade study in 3-dimensional space: system capabilities, program costs, and user EDR requirements. For example, the aperture (A) can also be increased to maximize signal to noise $S_n$ at the expense of making the instrument larger and heavier but cannot exceed weight allocations provided for VIIRS on the NPOESS satellite. The field of view can also be increased; however, spatial resolution must be balanced against the increase in $d\Omega$ and horizontal cell size, which relates to field-of-view, as defined by the NPOESS program. Cooling VIIRS sensor detectors to lower temperatures can be used to decrease the NE$\Delta$T but must be limited to NPOESS satellite power allocations. Finally, the band-center and bandwidth of each channel is constrained by (1) availability of solar/terrestrial radiation, (2) atmospheric transmission, and (3) phenomenology associated with the retrieval of a given EDR product. For example, shown in Figure 4.1 is the spectral irradiance distribution for solar illumination at the top of the Earth's atmosphere and at sea level. Darkened areas represent regions of strong atmospheric absorption while the scale shows gaseous species absorbing the solar energy. If only solar irradiance was important, much higher values of $S_n$ could be achieved by placing a band-center near 0.5 μm rather than at 2.5 μm. However, there are phenomenological issues in addition to available energy that must be considered before making bandpass selections, including atmospheric transmission and the interaction of radiation with a variety of surface features and cloud ice and water particles.

Deleted: each channel

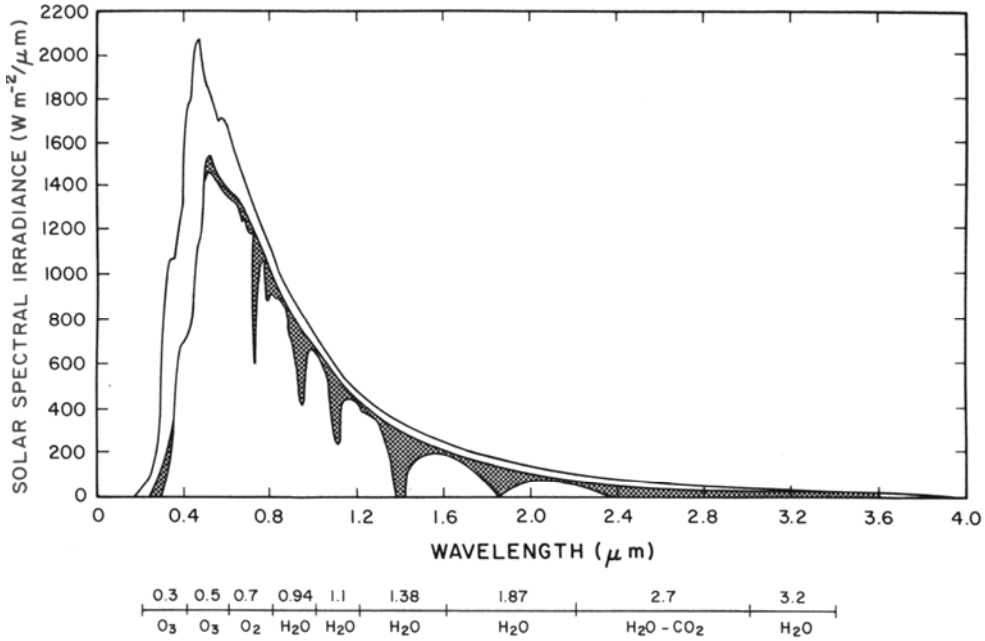


Figure 4.1. Solar spectral irradiance distribution for top of the atmosphere (TOA) and sea level along with primary atmospheric absorption bands and species. (Figure 2.6 from Liou, 1980).

The final set of design issues that must be considered involves interactions between the sensor hardware and the "observed" radiation impinging upon the optics of the sensor. Among these sensor hardware issues are efficiency of detector materials and size of focal planes to name a few. An overview of the VIIRS sensor hardware is provided in Section 4. 5.

## 4.3 CLOUD TRUTH DATA SETS TO FLOWDOWN SENSOR REQUIREMENTS

It is now apparent that the VIIRS sensor must include bandpasses in which major cloud types emit or reflect energy with characteristics that are significantly different from the major surface classes to support manually-generated cloud data analyses. Before examining the phenomenology needed to select VIIRS bandpasses, it is useful to examine the methodology used in the VIIRS sensor design phase to quantify the accuracy of manually-generated cloud analyses based upon simulated VIIRS imagery.

The process of quantitatively defining the accuracy of manually-generated cloud analyses requires the creation of cloud "truth" data sets. There are two methods frequently used to create cloud truth data sets: (1) build a ground truth by manually-generating cloud/no cloud (CNC) analyses from the human interpretation of clouds in the multispectral imagery or (2) define the ground truth by constructing a synthetic CNC map that is used in the simulation of VIIRS imagery assuming some characteristic sensor model. Examples of both are provided since the VIIRS design process used truth CNC masks as

**Deleted:** ,

**Deleted:** , preferably using temporally and spatially coincident imagery of much higher resolution than the sensor being evaluated, e.g. use 30 m Landsat imagery to create a ground truth CNC analysis for a coincident 375 m VIIRS scene,

**Deleted:** and

**Deleted:** which

**Deleted:** then

**Deleted:** as an input field to

**Deleted:** ed

**Deleted:** for

**Deleted:** a particular

**Deleted:** sensor

**Deleted:** "constructed" ground truth

input fields to simulate numerous sets of synthetic VIIRS images for a variety of scenes and sensor models and human interpretation of each simulated VIIRS data set to produce a manually-generated CNC analysis. Thus, pixel-by-pixel comparisons were made between the CNC truth data sets used in the simulations and the manually-generated CNC analyses derived from the synthetic images created for each candidate sensor model. The VIIRS sensor model selected for the baseline design was the most cost-effective model to build that provided imagery of sufficient quality to allow the human analyst to meet NPOESS threshold requirements for the manually-generated cloud data product EDRs. Attention now turns to the process used to create manually-generated CNC analysis from the synthetic VIIRS imagery.

**Deleted:** VIIRS

**Deleted:** . H

**Deleted:** d

**Deleted:** P

**Deleted:** quantitatively determined conformance of the VIIRS Imagery

**Deleted:** and

**Deleted:** with the NPOESS threshold and objective requirements.

**Deleted:** preferred

**Deleted:** and required number of VIIRS Imagery channels

**Deleted:** with the capability of constructing manually-generated cloud analyses that conformed to

### 4.3.1 Cloud Truth from Manual Interpretation of Multispectral Imagery

It is possible to create a manually-generated CNC mask of a single band or multiple bands of meteorological satellite imagery. These CNC analyses are binary cloud maps generated with special software that identifies clouds in a given spectral band by making all pixels cloudy that have values that exceed a user-defined threshold. Similarly, all pixels with values less than the threshold are cloud-free. The image typically needs to be segmented into sub-regions to delineate cloudy and cloud-free regions accurately, especially for scenes of large geographical regions or highly heterogeneous conditions, since some cloud-free land surfaces may have pixel values larger than clouds in another part of the scene. In addition, CNC analyses from multiple bands may be merged into a single, total CNC analysis. This process is illustrated in Figure 4.2.

**Deleted:** channel

**Deleted:** channels

Clouds and snow are seen of Figure 4.2(a) which shows the 0.9 μm band and Figure 4.2(b) that shows the 12.0 μm band of an AVHRR image. The scene is centered near San Francisco, CA with the Sierra Mountains seen in the lower right corner extending toward the middle of the image. The California coast and Pacific Ocean are most visible in Figure 4.2(a) although much of the coast is obscured by clouds. Lake Tahoe is clearly visible in this image at the north end of the Sierra Mountain range just to the right of the center of the image.

(a) 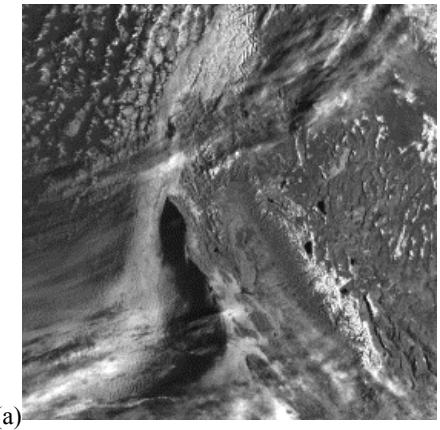

(b) 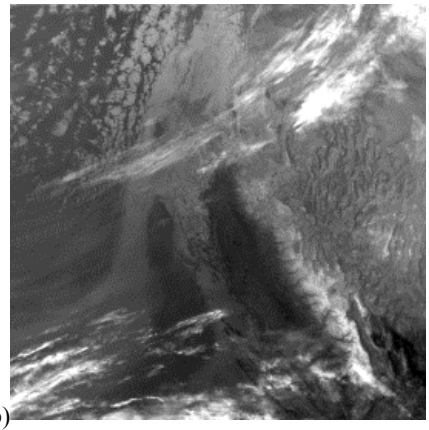

Figure 4.2. Clouds and snow are bright in AVHRR imagery channel 2 (0.9 μm) at Panel (a) and channel 5 (12.0 μm) at Panel (b) of a NOAA-12 scene collected on March 19, 1996 (Hutchison et al, 1997).

Deleted: C

Deleted: C

Using the principles discussed in Section 3.1, a CNC analysis is manually constructed for sub-regions within the scene where the contrast is sufficiently large between clouds and cloud-free backgrounds. For example, the maximum contrast occurs between clouds and both vegetated and ocean surfaces is large in the 0.6 μm AVHRR band (channel 1). Thus, an analyst can use data in this spectral band, along with the software mentioned above, to manually adjust a threshold to classify all pixels as clouds that have a reflectance higher than this threshold. A threshold of 5% reflectance causes pixels shown as red in Panel (b) of Figure 4.3 to be classified as cloudy. However, this threshold cannot be applied to the right side of either spectral band shown in Figure 4.3 since both clouds and snow have reflectances greater than 5%. Additional spectral data are needed to manually classify clouds in these sub-regions.

Deleted:

Deleted: allows

Deleted: to be maximized

Deleted: the

Deleted: in some parts of the scene

Deleted: the

Deleted: C

Deleted: Using

Deleted: band alone allows the human analyst to create a highly accurate manually-generated CNC analysis over these surfaces, as shown in

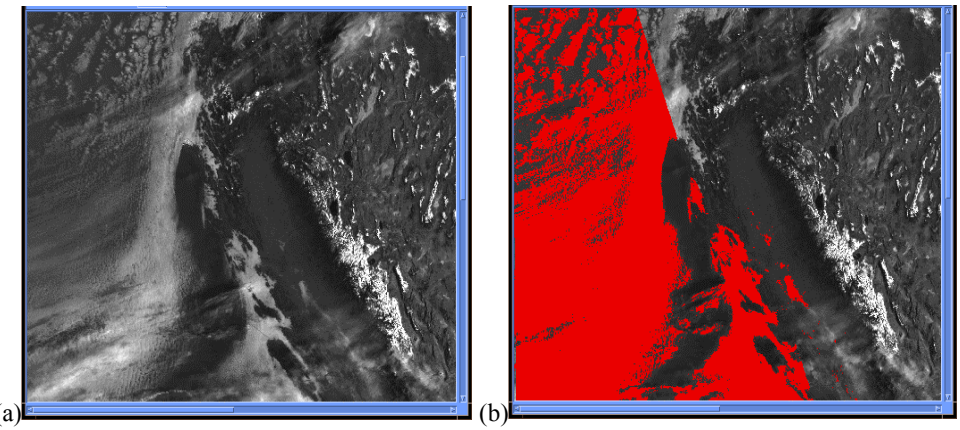

(a) (b)

Figure 4.3. Clouds seen in the 0.6 μm band (channel 1) of the AVHRR imagery in Panel (a) are contained the manually-generated cloud analysis, are shown as red, in Panel (b).

Deleted: C

Thus, prior to performing a manual analysis of the right half of the scene, the contrast between snow and clouds must be enhanced in order to differentiate between these features, since they appear very similar in the AVHRR channels 1, 2, and 5 as shown in Figure 4.2 and Figure 4.3. Prior to the launch of NOAA-15, which contains the 1.6 μm band, a methodology was developed to enhance the spectral signature of cirrus clouds and suppress the signature of snow in the daytime 3.7 μm band of AVHRR (channel 3). The procedure was applied to this scene to enhance the snow/cloud contrast. Results are shown in Figure 4.4(a) along with the manually generated cloud analyses, also shown in red for this portion of the scene in Figure 4.4(b).

Deleted: P

Deleted: C

Deleted: C

Deleted: of

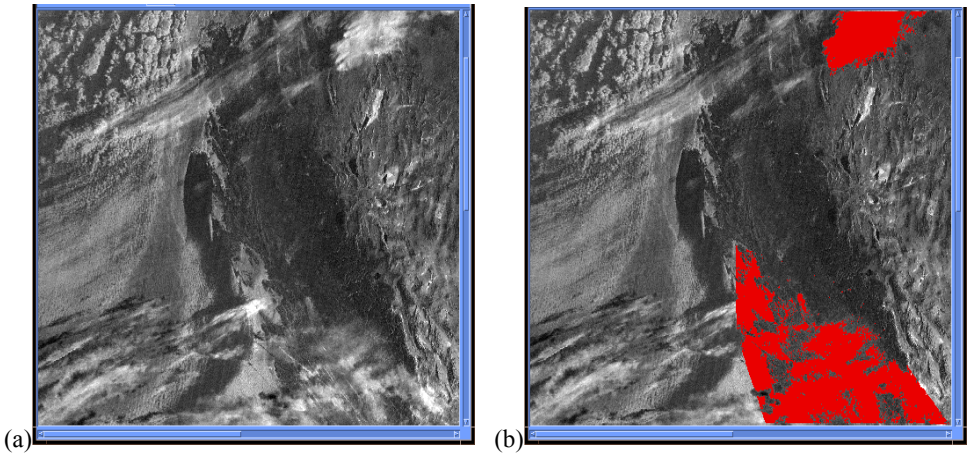


Figure 4.4. Snow now appears black in Panel (a) containing the albedo component of the 3.7 µm band (channel 3) of the AVHRR imagery while Panel (b) contains the manually-generated cloud analysis made using this image.

Deleted: C

The analysis of all cloudy pixels in the scene is constructed from the composite of the those pixels shown as red in Figure 4.3 and Figure 4.4. The total cloud analysis are those pixels shown as green in Figure 4.5. This complete manually-generated CNC analyses of all clouds in the scene is useful for determining quantitatively the performance of automated cloud detection algorithms that might be generated with data from this particular scene.

Deleted: total CNC

Deleted: for

Deleted: CNC analyses

Deleted: . These results are shown

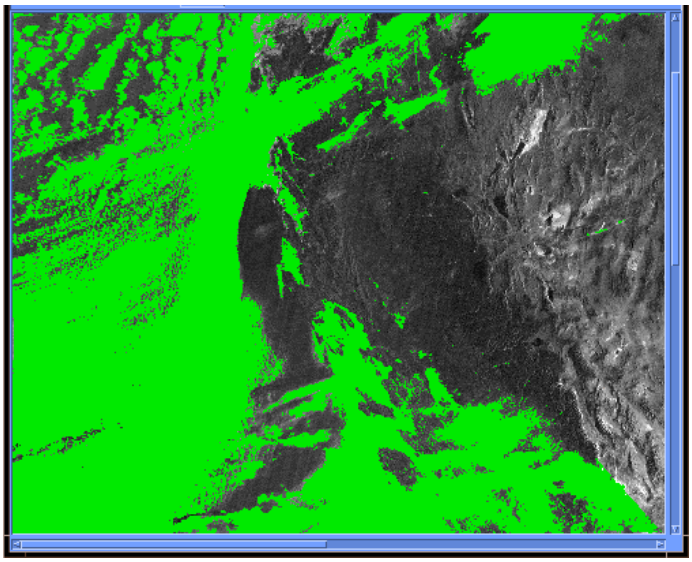

Figure 4.5. Example of a total CNC analysis created by merging CNC analyses from individual spectral bands shown in Figure 4.3 and Figure 4.4 into a single CNC analysis.

### 4.3.2 Cloud Truth in Simulated Imagery

Deleted: Synthetic Scenes for Sensor

Deleted: ions

Deleted:

Manually-generated CNC masks can also be created from simulated VIIRS imagery to optimize sensor design parameters and their effects upon image quality. The process is illustrated in Figure 4.6 and Figure 4.7. This procedure starts by defining a synthetic background, as shown in Figure 4.6(a). This particular synthetic background contains a large region of ocean surface (darkest) selected to represent the Earth's surface since it is 75% water. Next, surface regions composed of sand (next darkest), snow (large area of light), and vegetated land (small island surrounded by ocean) are added in an attempt to simulate global conditions. Synthetic clouds are the final addition to the scene and are shown as white in Figure 4.6(b). In this particular case, large regions of water clouds are added to the simulation. Atmospheric models are then added to the scene to create the complete synthetic scene before the simulated VIIRS image is generated. The process of simulating VIIRS imagery was completed with PACEOS, which is an acronym for Performance and Analysis Capabilities for Earth Observing Systems. PACEOS has been partially described in the literature (Hutchison et al., 1999).

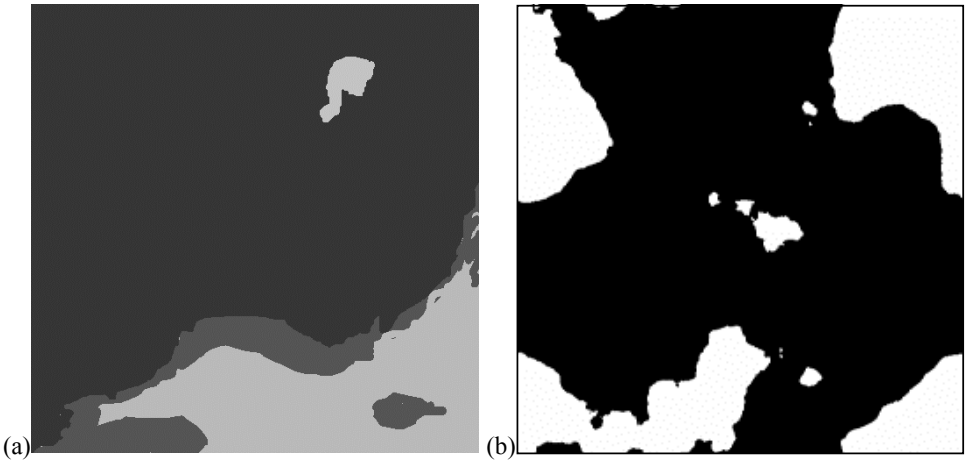


Figure 4.6. Synthetic background shown in Panel (a) are used with cloud mask, shown in Panel (b) to generate synthetic VIIRS imagery.

Any combination of CNC masks and synthetic backgrounds can be used to simulate VIIRS synthetic scenes. A cirrus cloud is shown in Figure 4.7. Once the simulated VIIRS imagery is generated (left panel in Figure 4.7), a manually-generated cloud mask can be created from this synthetic imagery as discussed above. The manually-generated cloud mask of the simulated VIIRS 12.0 μm imagery is shown in the top panel of Figure 4.7. Comparisons between the manually-generated cloud mask and the "truth" cloud mask used as input into the simulation, seen in the bottom panel of Figure 4.7, allow the performance of the manually-generated cloud mask to be quantified and the impact of sensor designs on image quality to be quantified. Differences between these two CNC analyses, shown in the right panel of Figure 4.7, are highly useful to identify problems and recommend solution to the instrument design.

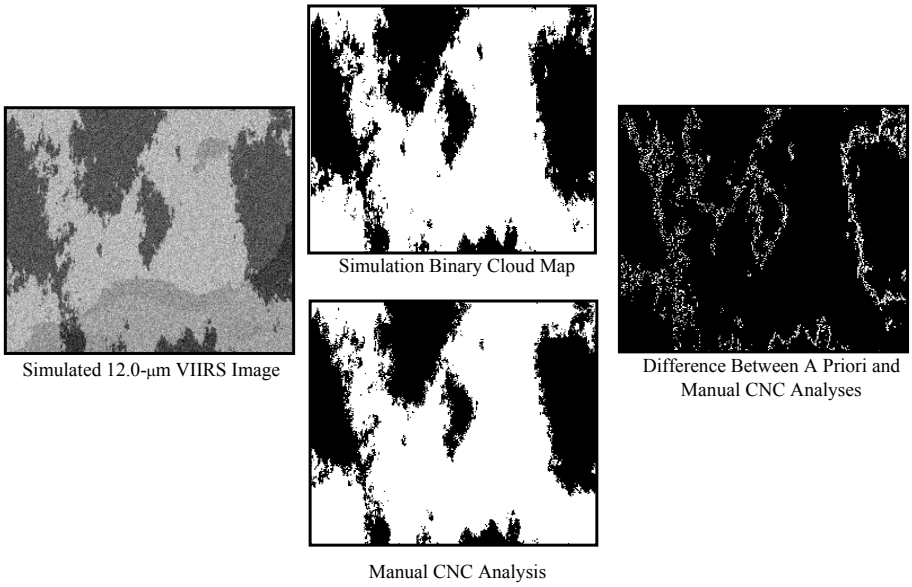


Figure 4.7. Synthetic 12.0 μm VIIRS image, manual and synthetic cloud masks, and difference fields show locations of inaccuracies in manually-generated cloud data product.

The pixel-level CNC masks, both truth and manually generated, can be summarized to any analysis resolution, e.g. for NPOESS this analysis size is referred to as the horizontal cell size (HCS) as shown in Table 4.1. Results of measurement uncertainty for the manually-generated CNC mask, compared to the ground truth CNC mask, are shown in Table 4.1 as a function of horizontal cell size. The results show that image quality produced by this particular VIIRS sensor model allowed the NPOESS Imagery EDR threshold requirements (3x3 pixels in horizontal cell size shown in "green") and objective requirements (2x2 pixels in horizontal cell size shown in "blue") for manually-generated cloud data products (measurement uncertainty not to exceed 0.1 as shown in Table 4.1) to be satisfied. It is clear from Table 4.1 that measurement uncertainty improves as horizontal cell size increases since values in these binary fields are either completely right or completely wrong.

**Deleted:** errors

**Deleted:** accurate

**Deleted:** inaccurate

Table 4.1. Comparisons of manually-generated cloud mask and simulation binary cloud mask for synthetic VIIRS imagery shown in Figure 4.7.

| HCS | NUMBER OF HCS PIXELS IN SIMULATONS | | | BI-MODAL | UNCERTAINTY |
|---|---|---|---|---|---|
| (2 x 2 pixels) | Total | Clear | Overcast | (Percent) | (Fraction) |
| Truth | 16,129 | 10,363 | 4677 | 93.25 | n/a |
| Analysis | 16,129 | 10,124 | 4969 | 93.58 | 0.099 |
| (3 x 3 pixels) | | | | | |
| Truth | 7140 | 4417 | 1890 | 88.33 | n/a |
| Analysis | 7140 | 4364 | 2010 | 89.27 | 0.078 |
| (4 x 4 pixels) | | | | | |
| Truth | 3969 | 2389 | 967 | 84.56 | n/a |
| Analysis | 3969 | 2373 | 1049 | 86.22 | 0.069 |
| (8 x 8 pixels) | | | | | |
| Truth | 961 | 528 | 170 | 72.63 | n/a |
| Analysis | 961 | 529 | 194 | 75.23 | 0.050 |
| (25 x 25 pixels | | | | | |
| Truth | 100 | 40 | 3 | 43.00 | n/a |
| Analysis | 100 | 40 | 6 | 46.00 | 0.032 |

In summary, pixel-by-pixel comparisons between the "truth" and "manually-generated" CNC analyses are used to quantitatively determine conformance of the VIIRS Imagery and sensor model with NPOESS Threshold and Objective requirements. The preferred VIIRS sensor model and required number of VIIRS Imagery bands incorporates the most cost-effective sensor model that provides the human analyst with the capability of constructing manually-generated cloud analyses that satisfy NPOESS requirements. While the process of making manually-generated cloud data products is straightforward and simplistic, it is emphasized that sufficient contrast must exist between the cloud fields and surrounding backgrounds to allow these products to be created. Therefore, attention now turns to the methodology used to select both the VIIRS Imagery bands and the sensor model for each band in order to ensure sufficient contrast is present in global imagery to differentiate between clouds and a variety of backgrounds.

**Deleted:** d

## 4.4 DERIVATION OF SENSING REQUIREMENTS FROM ANALYSIS REQUIREMENTS

**Deleted:** TRANLATION

**Deleted:** TO SENSING REQUIREMENTS

Attention now turns to an examination of the phenomenology that must be evaluated in order to select VIIRS bandpasses needed to perform manually-generated cloud analyses within the performance requirements of the NPOESS system. This process leads directly to the formulation of VIIRS bandpass sets for both Imagery and Imagery Assist bands.

In Section 4.1, it was shown that the capability to observe clouds in infrared imagery is enhanced under the following conditions:

- significant temperature contrasts exist between the cloud and the surrounding background which have very similar emissivities in one infrared band,

**Deleted:** channel

- a cloud and its surrounding background may have the same temperature but significantly different emissivities in one spectral band, or
- atmospheric transmissivity is markedly different in one band which masks the signature of the cloud from the background.

Furthermore, it was concluded that the ability of a human to detect a cloud manually in visible and near-infrared imagery and distinguish it from the surrounding background is enhanced by using one or more spectral bands where differences in the cloud and surface reflectivities are significant:

- by exploiting strong contrasts between the cloud reflectivity and its surrounding background,
- by viewing features in one band in which atmospheric transmissivity is markedly different such that the surface feature is masked by the atmosphere but the cloud is not.

A powerful method to differentiate between clouds and their surrounding cloud-free backgrounds exploits two or more bands simultaneously to examine changes in the spectral signature of either the cloud or its background. If only two spectral bands are used, this technique is commonly referred to as bi-spectral imagery analysis. Bi-spectral methods that use arithmetic manipulation, e.g. addition, subtraction, division etc., of multiple digital images have proved to be very powerful for the manual and automated detection of clouds as well as the identification of various surface backgrounds. When different bands are assigned to guns of a color monitor, differences in spectral signatures are evident by their colors. More on bi-spectral and color composite methods will be provided later in Chapter 6.

**Deleted:** channels

**Deleted:** channels

Shown in Figure 4.8 to Figure 4.11 are the phenomenological data needed to begin the VIIRS bandpass selection process. These figures contain spectral signatures of cloud particles and various backgrounds along with the solar illumination at the top of the atmosphere and the atmospheric transmission for a mid-latitude summer profile, as described by Anderson et al. (1986). Together, the figures cover the 0.3 - 12.0 μm region of the solar and terrestrial spectral. All data were generated with the MODTRAN radiative transfer model (Berk et al., 1989). The key to the figures is as follows: indices of refraction for water and ice are shown by solid and dashed turquoise lines respectively, reflectivities of cloud-free surfaces are: (a) green for vegetated land, (b) dark blue for ocean, (c) snow is white, and (d) bare soil is yellow. Top of the atmosphere solar illumination is shown in gold while atmospheric transmission is the highly irregular black line that depicts absorption by atmospheric gases and scattering by aerosols. VIIRS bandpass selections are shown as blue that extend to the top of each figure.

It can be seen in Figure 4.8 to Figure 4.11 that the VIIRS Imagery channels are generally located in regions where atmosphere attenuation is relatively small and does not change significantly with height. These regions are known as "atmospheric windows." There are several atmospheric windows in the region between 0.3 and 12.0 μm. The most

**Deleted:**

commonly known windows are the 0.5 - 0.9 μm, 3-5 μm, and 8-12 μm windows. Others include two near-IR (1.5 - 1.7 μm and 2.1 - 2.3 μm) windows. While the 3-5 μm range is typically referred to as an atmospheric window, absorption spectra in Figure 4.10 clearly show the window is most clean (highest atmospheric transmission) between 3.5 - 4.0 μm. Strong absorption occurs near 4.2 - 4.5 μm due primarily to gaseous carbon dioxide and water vapor. In fact, almost no energy emitted in this wavelength interval by a cloud-free surface on the Earth would arrive at the VIIRS sensor. Imagers necessarily operate in spectral regions where the atmosphere absorption tends to be minimal.

The International Geosphere-Biosphere Program (IGBP) recognizes 17 categories of land cover. Figure 4.8 to Figure 4.11 show the spectral reflectivities for the key land surface classes found on the Earth, i.e. ocean, vegetated land, bare soil, and snow.

To illustrate the value of these data, consider Figure 4.8 and note the differences in the spectral responses for snow, vegetated land, and bare soil in the 0.5 - 0.9 μm region. The reflectivity of vegetated land is less than 10% at 0.5 μm, increases slightly to just over 10% at 0.55 μm and reaches a minimum of ~ 0.5% between 0.65 and 0.7 μm. On the other hand, the reflectivity of bare soil has its minimum at 0.4 μm and increases steadily to nearly 40% at 1.0 μm, while snow has a much higher reflectivity across the entire wavelength interval, i.e. over 90% from 0.3 - 0.8 μm, tailing to ~ 73% at 1.0 μm. At the same time, the index of refraction for water droplets and ice particles are initially small and increase constantly across the region. These curves suggest the following:

- Cloud-free, snow-covered surfaces can be differentiated from cloud-free vegetated surfaces and bare soil surfaces by comparing responses in two bands centered near 0.65 μm and 0.86 μm. This is possible since the reflectivity of snow decreases in these two bands while the reflectivity of vegetated land increases as does the reflectivity of bare soil. One might assume that absolute albedo alone would be adequate to make these distinctions; however, that is not the case. Problems result from the need to know the angular distribution of energy of each surface type. Typically, surfaces are assumed to be lambertian, i.e. they act as isotropic scatterers. But this is not the case in reality. By examining the ratio between two bands, the absolute albedo is not important.

- A more powerful method to identify snow can be seen by examining its spectral signature in the 1.6 μm region in contrast to its value in the 0.65 μm region. The reflectivity of snow has a minimum near 1.5 μm; unfortunately, atmospheric transmission is also a minimum at 1.4 μm but begins to increase rapidly near 1.5 μm. At wavelengths slightly shorter than 1.6 μm, the reflectivity of snow is very low while the atmospheric transmission is very high, e.g. over 90 percent. Therefore, the ratio of signatures in the 1.6 μm and 0.65 μm bands is positive proof of the presence of snow since this ratio approaches zero for snow, but is much greater than unity for vegetated and bare soils. Thus, the power of bi-spectral methods is demonstrated for positive feature identification. These differences in the spectral signatures of clouds and various backgrounds will be examined in Chapters 5 and fully exploited using color composites in Chapter 6.

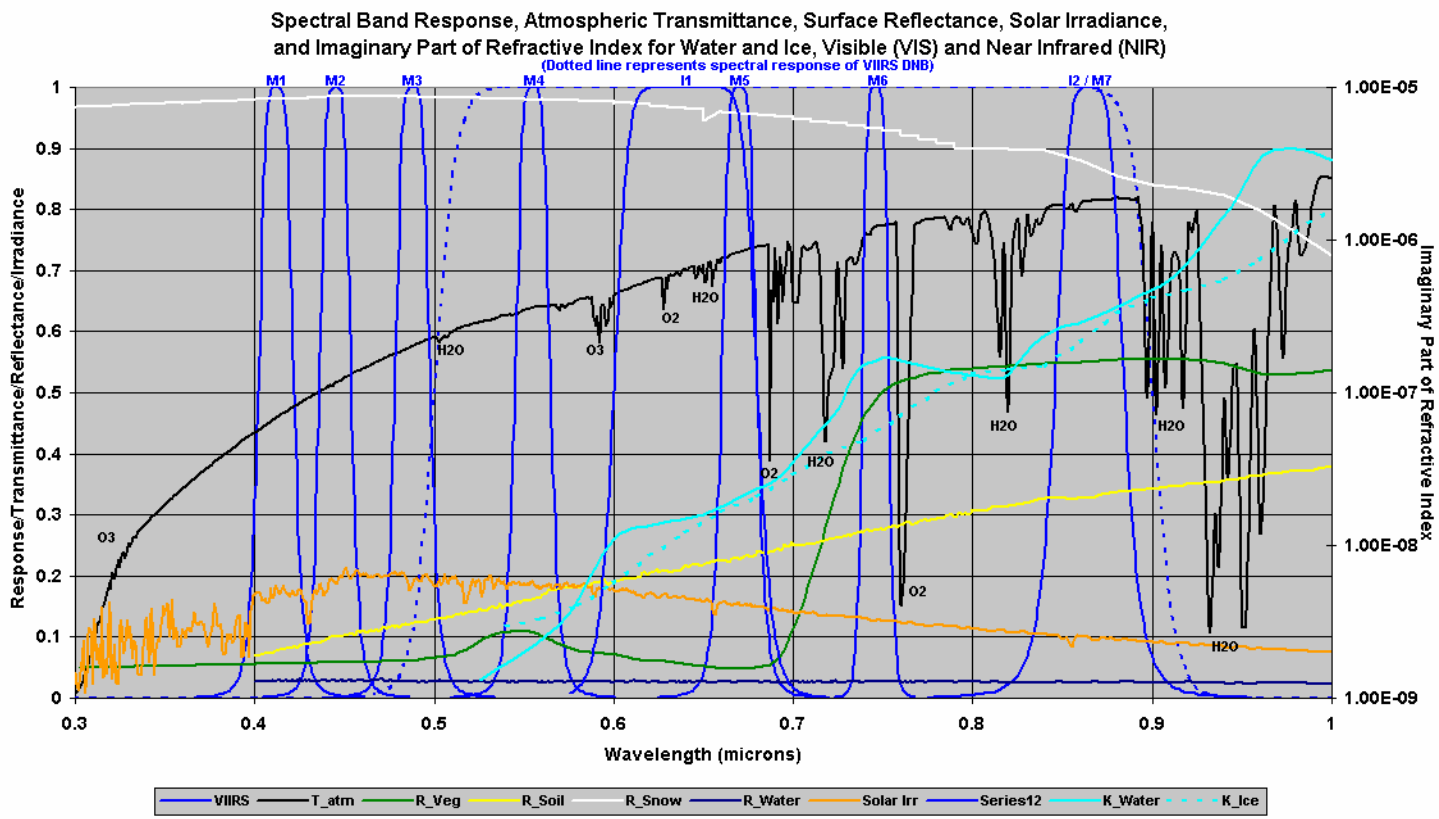


Figure 4.8. Spectral signatures of cloud particles and surface backgrounds in 0.3 - 1.0 micron range. (Key: Reflectivities: vegetated land = green, ocean = dark blue, snow = white, bare soil or sand = yellow., solar illumination = gold and atmospheric transmission = black. VIIRS bands blue, solid turquoise = index of refraction for water droplets, and dashed turquiose = index of refraction for ice.)

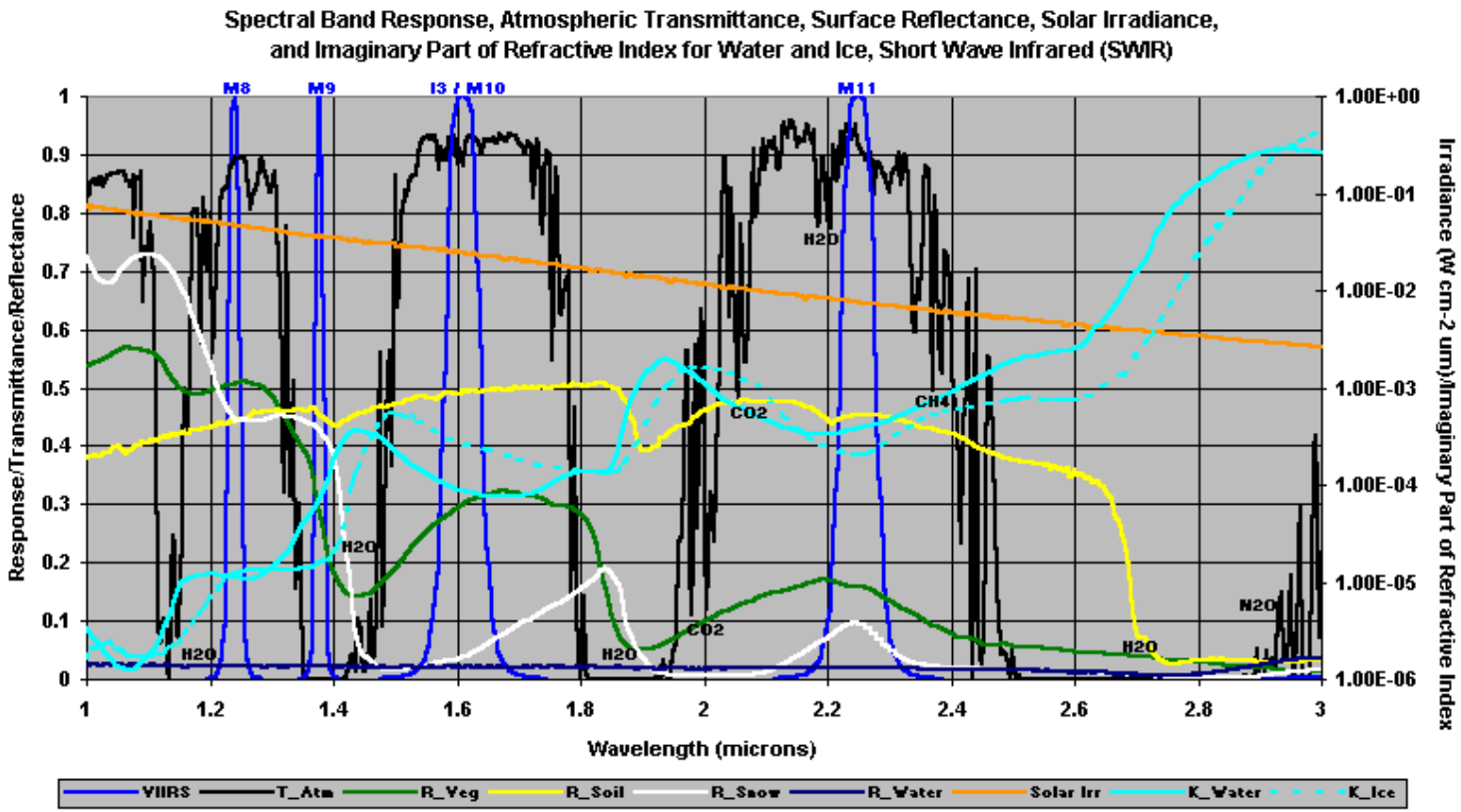


Figure 4.9. Spectral signatures of cloud particles and surface backgrounds in 1.0 - 3.0 micron range. (Key: Reflectivities of, vegetated land = green, ocean = dark blue, snow = white, bare soil or sand = yellow. Solar illumination = gold and atmospheric transmission = black. VIIRS bands are shown in lighter blue solid turquoise = index of refraction for water droplets, and dashed turquiose = index of refraction for ice.)

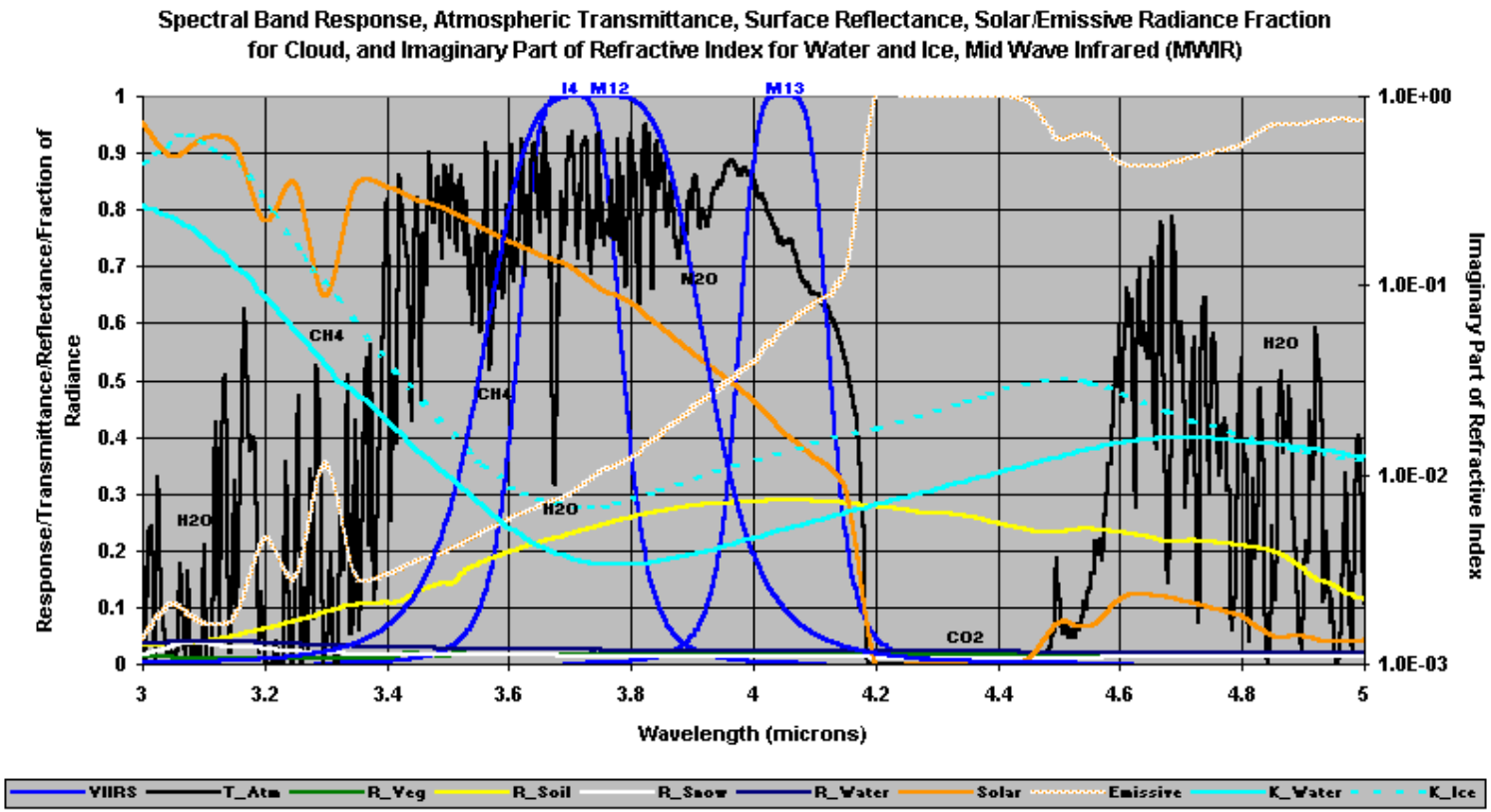


Figure 4.10. Spectral signatures of cloud particles and surface backgrounds in 3.0 - 5.0 micron range. (Key: Reflectivities of, vegetated land = green, ocean = dark blue, snow = white, bare soil or sand = yellow. Solar illumination = gold and atmospheric transmission = black. VIIRS bands are shown in lighter blue solid turquoise = index of refraction for water droplets, and dashed turquiose = index of refraction for ice.)

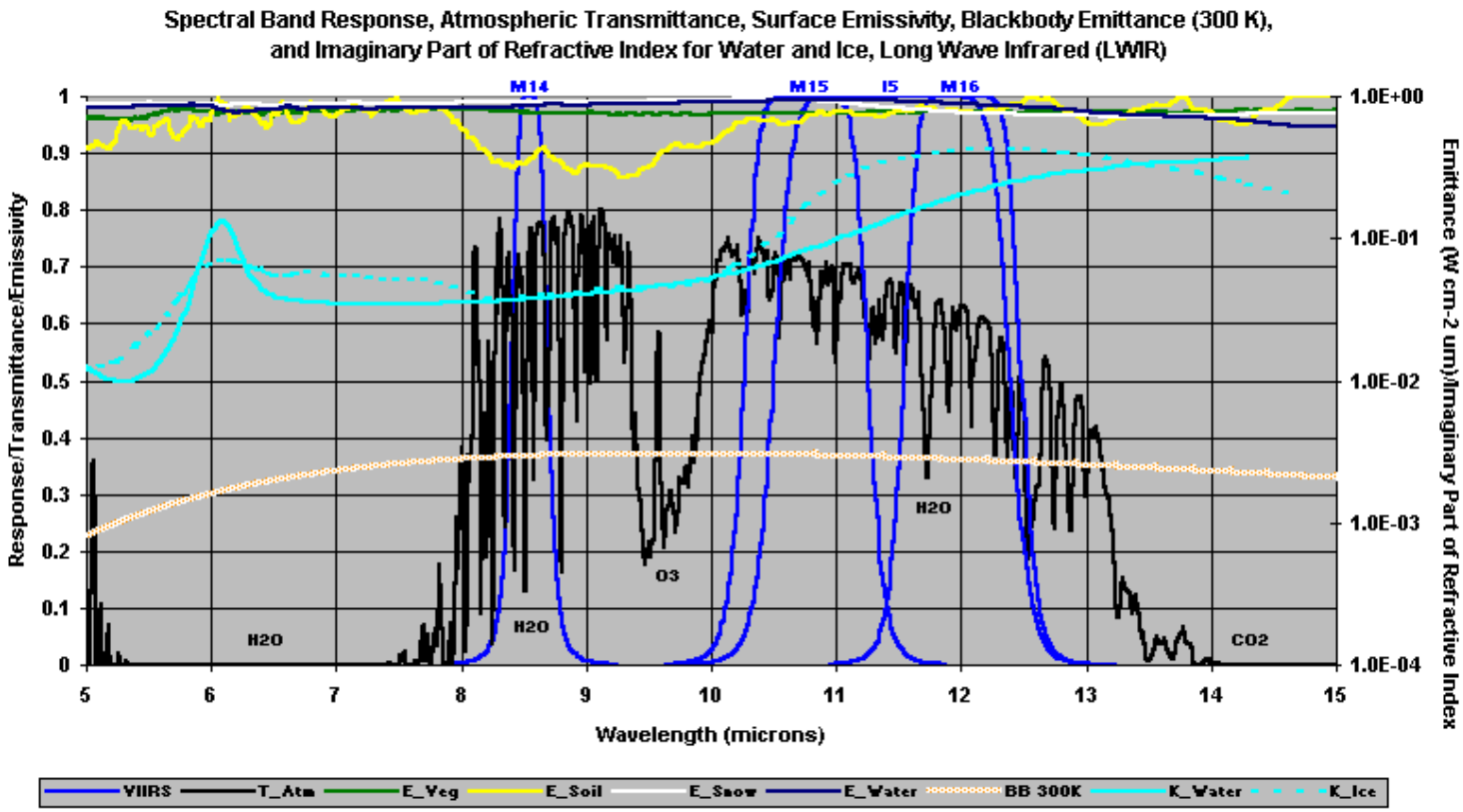


Figure 4.11. Spectral signatures of cloud particles and surface backgrounds in 5.0.- 15.0 micron range. (Key: Reflectivities of, vegetated land = green, ocean = dark blue, snow = white, bare soil or sand = yellow. Solar illumination = gold and atmospheric transmission = black. VIIRS bands are shown in lighter blue solid turquoise = index of refraction for water droplets, and dashed turquiose = index of refraction for ice.)

Based upon the preceding logic, an analysis of sensing requirements was completed to identify the minimum number of imagery channels needed to satisfy NPOESS threshold requirements for the manually-generated cloud data product EDR. Results of this analysis are shown in Table 4.2 for the imagery channels centered at 0.64, 3.7 and 12.0 µm. Two additional VIIRS imagery channels are included due to requirements established by other EDRs. They are the explicit requirement for nighttime visible imagery band and the derived requirement for a 1.6 µm band needed for the snow cover/depth EDR.

Table 4.2. VIIRS imagery channels needed to satisfy each NPOESS VIIRS requirement for manually-generated cloud cover and cloud type EDRs.

| NPOESS Attribute | Threshold Requirements | VIIRS Objectives | Comments |
|---|---|---|---|
| Cloud Detection (Measurement Uncertainty) | 0.1 for horizontal cell size 3x3 | 0.1 horizontal cell size 2x2 | Satisfies Objectives for worst case scenario using 3 imagery channels with bandpasses centered near 0.64, 3.7, and 12.0 µm |
| Cloud Typing (Probability of being Correct) | 85% for Clear, Ci, St, Cu, | 90% for all 17 cloud types | Requires spectral difference in 3.7 and 12.0 µm bands to distinguish between nighttime stratus and cirrus |
| VIIRS Capability | To Satisfy Thresholds | Toward Meeting Objective | Explanation |
| Clear from cloudy or obscured | 0.088 detection (horizontal cell size 3x3) for cirrus as a worst case | 0.099 (horizontal cell size 2x2) for cirrus as a worst case | objective satisfied for worst case scenario using 3 Imagery channels with bandpasses centered near 0.64, 3.7, and 12.0 µm |
| Cirrus | 100% typing compared to water clouds | | objective satisfied using 12.0µm and 3.7 µm band temperature differences to distinguish cirrus from stratus |
| Stratus | 100% typing compared to cirrus clouds | | 3.7 µm band needed both to detect nighttime stratus and distinguish it from cirrus |
| Cumulus | 100% typing compared to other clouds based on shape | | use 0.64 µm band over most surface along with 3.7 µm band for detection over sand (i.e. thermal component) and 3.7 µm albedo over snow-covered regions along with texture |
| Obscured/Not Cloudy | 0.1 detection accuracy for optical depth ≥ 0.07 in 0.64 | | dark pixel method using 12.0 µm band for thresholds, additional use of 0.4 µm band for detection over bright (desert) backgrounds |

Deleted: I
Deleted: I
Deleted: I
Deleted: channel
Deleted: I
Deleted: Bands N
Deleted: S
Deleted: E
Deleted: R
Deleted: M
Deleted: G
Deleted: C
Deleted: C
Deleted: C
Deleted: T
Deleted: I
Deleted: )
Deleted: channels
Deleted: )
Deleted: channel
Deleted: channel
Deleted: channel
Deleted: channel
Deleted: channel
Deleted: channel

| | | | |
|---|---|---|---|
| | μm region | | |

The VIIRS sensor design includes a total of 22 spectral bands needed to satisfy all EDR requirements shown in Section 3.1. This design includes five high resolution imagery bands which are designated as "I" bands and 17 moderate resolution bands which are designated as "M" bands in Table 4.3. As previously noted, moderate resolution bands have a more coarse spatial resolution but a much higher signal-to-noise ratio than imagery resolution bands. In several cases, both imagery and moderate resolution bands were needed to satisfy all VIIRS requirements, e.g. 0.865, 1.6, and 3.7 μm bands. Both imagery and moderate resolution bands are available for use in the creation of the manually-generated cloud data product EDRs. A detailed discussion of each VIIRS band is provided in Chapter 5 along with sample imagery to emphasize the features that can be positively identified with each band. In Chapter 6, color composites are shown of the imagery resolution bands. Also in Chapter 6 the value of using Imagery and Imagery-Assist bands together is demonstrated using color composites to quickly detect and type clouds, which is necessary to support the quality control of automated cloud analyses or create manually-generated cloud data product EDRs. From Table 4.3 it can be seen that data in the 1.61 μm bandpass must be collected at high and moderate resolution to support different EDRs. The high resolution data was demonstrated as essential to meet the snow depth portion of the snow cover EDR while the higher signal to noise requirement for moderate resolution data was needed for the cloud optical properties EDR as discussed in Chapter 8. A similar situation holds for the 11 μm bandpass. The I4 channel was needed for manually-generated cloud data while the M15 channel was required for the sea surface temperature EDR.

**Deleted:** channels

**Deleted:** channels

**Deleted:** C

**Deleted:** C

Table 4.3. VIIRS Imagery and Imagery Assist Band Selected to Satisfy NPOESS Requirements.

| Channel Number | VIIRS Designator | Central Wavelength $\lambda_C$ (μm) | Bandwidth $\Delta\lambda$ (μm) | Horizontal Sampling Interval at nadir (km) | Horizontal Sampling Interval at 55.8° (km) |
|---|---|---|---|---|---|
| 1 | DNB | 0.7 | 0.4 | 0.742 | 0.742 |
| 2 | M1 | 0.412 | 0.02 | 0.742 | 1.6 |
| 3 | M2 | 0.445 | 0.018 | 0.742 | 1.6 |
| 4 | M3 | 0.488 | 0.020 | 0.742 | 1.6 |
| 5 | M4 | 0.555 | 0.020 | 0.742 | 1.6 |
| 6 | I1 | 0.640 | 0.080 | 0.371 | 0.8 |
| 7 | M5 | 0.672 | 0.020 | 0.742 | 1.6 |
| 8 | M6 | 0.746 | 0.015 | 0.742 | 1.6 |
| 9 | I2 | 0.865 | 0.039 | 0.371 | 0.8 |
| 10 | M7 | 0.865 | 0.039 | 0.742 | 1.6 |
| 11 | M8 | 1.240 | 0.020 | 0.742 | 1.6 |
| 12 | M9 | 1.378 | 0.015 | 0.742 | 1.6 |
| 13 | I3 | 1.610 | 0.060 | 0.371 | 0.8 |
| 14 | M10 | 1.610 | 0.060 | 0.742 | 1.6 |
| 15 | M11 | 2.250 | 0.050 | 0.742 | 1.6 |
| 16 | I4 | 3.740 | 0.380 | 0.371 | 0.8 |
| 17 | M12 | 3.700 | 0.180 | 0.742 | 1.6 |
| 18 | M13 | 4.050 | 0.155 | 0.742 | 1.6 |

| | | | | | |
|---|---|---|---|---|---|
| 19 | M14 | 8.550 | 0.300 | 0.742 | 1.6 |
| 20 | M15 | 10.763 | 1.000 | 0.742 | 1.6 |
| 21 | I5 | 11.450 | 1.900 | 0.371 | 0.8 |
| 22 | M16 | 12.013 | 0.950 | 0.742 | 1.6 |

## 4.5 OVERVIEW OF VIIRS HARDWARE DESIGN

Data in this section was taken largely from Document Number PRF PS154640-101A, CAGE Code 11323, Visible/Infrared Imager/Radiometer Suite (VIIRS) Sensor Performance Specification, (Raytheon Santa Barbara Remote Sensing, 2002). While this material is not part of the analysis of the VIIRS Manually-Generated Imagery EDR. it is provided to give the interested reader a more complete description of the VIIRS sensor. It is emphasized that this data represents design specifications. Final VIIRS performance may be different that shown below.

Formatted: Font color: Auto

### 4.5.1 VIIRS Sensor Overview

Figure 4.12 shows a block diagram of the VIIRS sensor. The VIIRS optical configuration consists of an afocal, three mirror anastigmat telescope and fold mirror packaged in a rotating telescope subassembly, a rotating half-angle mirror and fixed fold mirror to further direct the scene energy into an aft optics subassembly, consisting of a four mirror anastigmat imager, two dichroics capable of providing spectral separation into three distinct optical paths, and back end optics, which include fold mirrors, dewar windows, out-of-band blocking filters and spectral bandpass filters.

Formatted: Font color: Auto

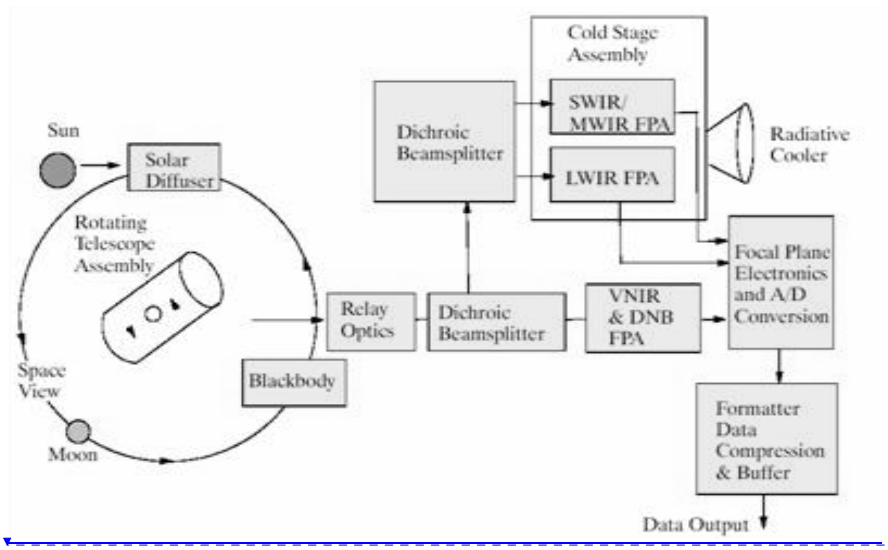


Figure 4.12 VIIRS Sensor Block Diagram (Kramer, 2002).

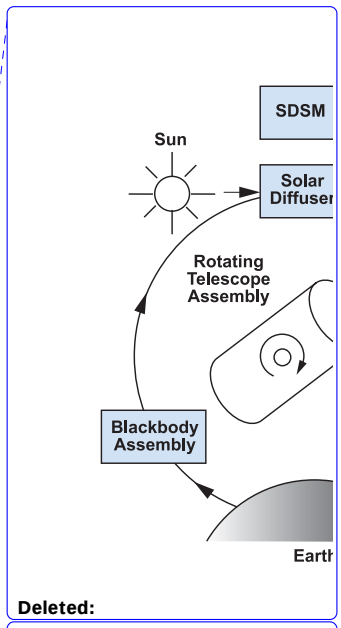


Deleted:

Formatted: Font color: Auto

The rotating telescope provides for the collection of scene spectral radiance and calibration data for VIIRS channels with characteristics as shown in Table 4.3. The band wavelength types are also referred to herein as Visible (VIS), Near Infrared (NIR), Short-Wave Infrared (SWIR), Mid-Wave Infrared (MWIR), and Long-Wave Infrared (LWIR). The Day/Night Band (DNB) and all bands with a horizontal spatial resolution (HSR) of 371 m are classified as imaging resolution bands; all other bands have an HSR of 750 m and are referred to as moderate resolution or radiometry bands. VIIRS uses three focal plane assemblies (FPAs) to detect spectral radiances. Bands M1-M7, I1, and I2 use the

VISNIR FPA; bands M8-M13, I3, and I4 use the S/MWIR FPA; and bands M14-M16, and I5 use the LWIR FPA. The DNB uses a separate FPA.

Deleted: VIS/NIR

Deleted: includes the DNB

The VIIRS sensor is equipped with a Blackbody and a Solar Diffuser to provide radiometric calibration. The Blackbody is the prime calibration source for the MWIR and LWIR bands while the Solar Diffuser provides calibration of the VIS, NIR, and SWIR bands. Two additional calibration sources used for VIIRS are views of deep space and occasional views of the moon. A solar diffuser stability monitor (SDSM) is also included to track the performance of the solar diffuser.

Formatted: Font color: Auto

VIIRS was designed to meet NPOESS requirements when flown in a near circular, sun-synchronous, near-polar orbit at a nominal 833 km altitude, in a 98.7 degree inclination, an orbital period of 101.6 minutes, β-angle (angle between the orbit normal and the solar vector) range of zero to ninety degrees, and with no sunlight on the cold space side of the spacecraft. Nominal orbits include 1330, 1730, and 2130 (ascending) nodal crossing times. The VIIRS sensor observes the Earth's surface in the cross-track direction about nadir on an NPOESS platform. It has an optical system with a cross-track spatial scan capability that scans to 56 degrees on either side of nadir to produce contiguous (i.e. non-underlapping) coverage at the equator. The spectral radiance and calibration data collected by VIIRS are transmitted as Raw Data Records (RDRs). VIIRS algorithms are applied to the RDRs to produce Sensor Data Records (SDRs) and ultimately the Environmental Data Records (EDRs).

Figure 4.13 shows the VIIRS design and heritage. VIIRS is essentially a combination of SeaWiFS foreoptics and an all-reflective modification of MODIS/THEMIS aft-optics.

Formatted: Font color: Auto

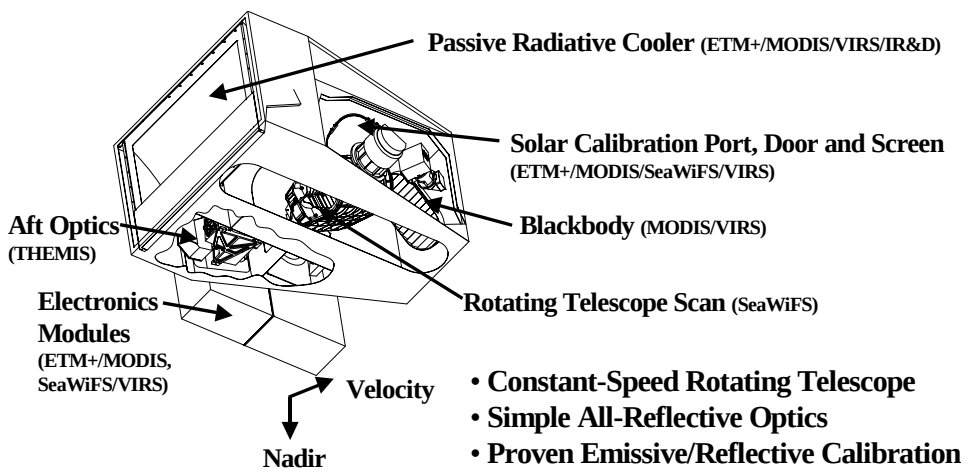


Figure 4.13 Summary of VIIRS design concepts and heritage (Byerly et al., 2000).

Formatted: Font color: Auto

The NPOESS requirement for VIIRS SRD placed explicit requirements on horizontal spatial resolution (HSR) for the Imagery EDR, as shown in Chapter 3. Specifically, these requirements stated that the HSR of bands used to meet the Imagery EDR requirements must be no greater than 400 m at nadir and 800 m at the edge of the scan. These

Formatted: Font color: Auto

requirements led to the development of a unique scanning approach which optimizes both spatial resolution and signal to noise ratio (SNR) across the scan. The concept is summarized in Figure 4.14 for the imagery resolution bands. The VIIRS detectors are rectangular, with the smaller dimension along the scan. At nadir, three detector footprints are aggregated to form a single VIIRS "pixel." Moving along the scan and away from nadir, the detector footprints become larger both along track and along scan, due to geometric effects and the curvature of the Earth and obviously these effects become much larger toward edge of scan. At 31.59 degrees in scan angle, the aggregation scheme is changed from 3:1 to 2:1. A similar switch from 2:1 to 1:1 aggregation occurs at 44.68 degrees. Consequently, the VIIRS scan exhibits a pixel growth factor of only 2 both along track and along scan, similar to the DMSP OLS, as compared with a growth factor of 6 along scan as is present in AVHRR and MODIS data. This scanning approach allows VIIRS to provide imagery at 800-m resolution or finer globally, with 375-m resolution at nadir. Additionally, MTF performance is extremely sharp (0.5 at Nyquist) due to these imagery requirements and the "sliver" detector design.

Formatted: Font color: Auto

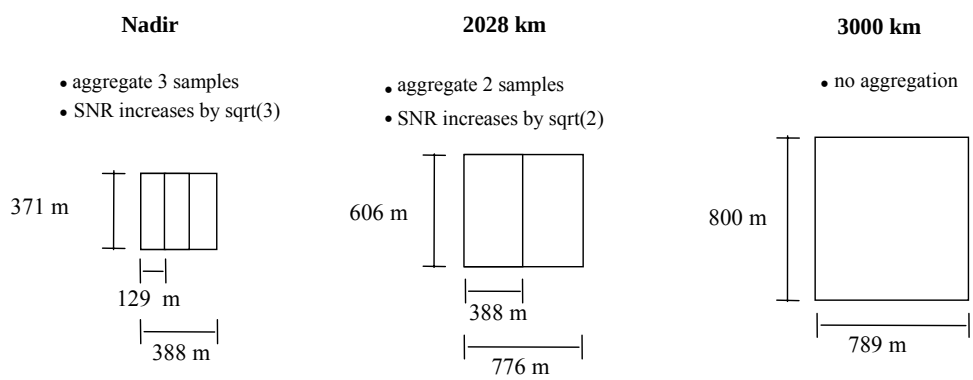


Figure 4.14 VIIRS detector footprint aggregation scheme for building Imagery "pixels".

Formatted: Font color: Auto

Figure 4.15 shows the Horizontal Sampling Interval (HSI) that results from the combined VIIRS scan characteristics and aggregation scheme to further illustrate the benefits of this aggregation scheme for horizontal spatial resolution. More precise definitions of technical terms, e.g. HSI, and HSR, are provided below in Section 4.5.2.

Formatted: Font color: Auto

Formatted: Font color: Auto

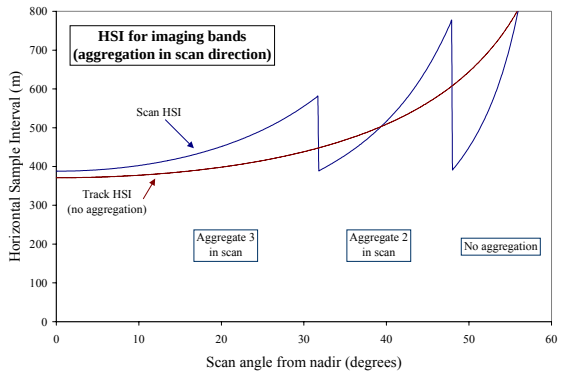


Figure 4.15 Horizontal Sampling Interval (HSI) for imagery bands (aggregation in scan direction).

Formatted: Font color: Auto

Even though the aggregation scheme greatly reduces the growth in HSI across the scan, there is still growth by a factor of 2 resulting in a residual "bow tie" effect. An additional reduction in the bow tie is achieved by deleting 4 of the 32 detectors from the output data stream for the middle (Aggregate 2) part of the scan and 8 of the 32 detectors for the edge (No aggregation) part of the scan. Figure 4.16 illustrates the resultant additional bow tie deletion.

Formatted: Font color: Auto

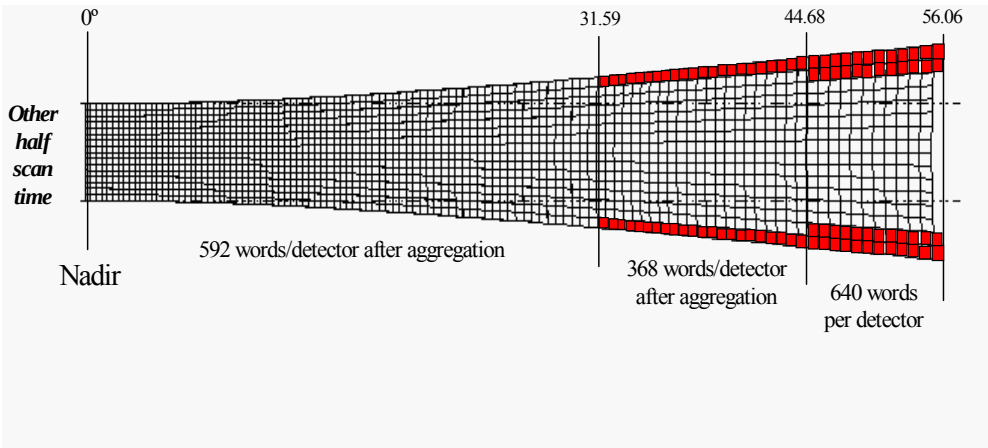


Figure 4.16 VIIRS aggregation and bow tie pixel reduction.

Formatted: Font color: Auto

### 4.5.2 Detailed VIIRS Design Capabilities

A brief overview of added VIIRS design capabilities is provided for the interested reader. Again, it is emphasized that the following information represents design specification, not system performance. The latter will be determined with the launch of the first VIIRS sensor on the NASA NPP mission.

#### 4.5.2.1 VIIRS Spectral Design Requirements

The VIIRS spectral bands are expected to meet the specifications listed in Table 4.4, as defined in Figure 4.17. The VIIRS Sensor spectral response is characterized with a wavelength uncertainty less than or equal to the values specified in the Characterization Uncertainty (nm). Bandwidth refers to the wavelength interval between the lower and upper band edges. This is also referred to as the Full Width Half Maximum (FWHM) response. Out-of-band (OOB) integration limits of the two wavelengths ($\lambda_{lower\ OOB}$ and $\lambda_{upper\ OOB}$) are used to define the out-of-band response regions. Integrated out-of-band response is the ratio of the integral of the response in the out-of-band regions to the integral of the response within the extended bandpass when viewing a source simulating the sum of a diffusely reflected 5800K blackbody (to represent 100% earth albedo) and a 300K blackbody, both of which are extended sources. This ratio includes the sum of the upper and lower out-of-band response regions

Formatted: Font color: Auto

Deleted:

Formatted: Font color: Auto

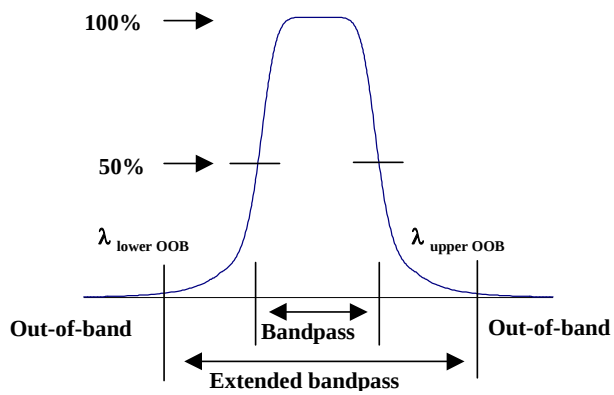


Figure 4.17 Depiction of sensor optical performance parameters.

Formatted: Font color: Auto

Table 4.4 VIIRS Spectral band optical requirements

Formatted: Font color: Auto

| Band | Center Wave-length (nm) | Tolerance on Center Wave-length (± nm) | Bandwidth (nm) | Tolerance on Bandwidth (± nm) | OOB Integration Limits (lower, upper) (nm) | Maximum Integrated OOB Response (%) | Character-ization Uncertainty (nm) |
|---|---|---|---|---|---|---|---|

| | | | | | | | |
|---|---|---|---|---|---|---|---|
| M1 | 412 | 2 | 20 | 2 | 376, 444 | 1.0 | 1 |
| M2 | 445 | 3 | 18 | 2 | 417, 473 | 1.0 | 1 |
| M3 | 488 | 4 | 20 | 3 | 455, 521 | 0.7 | 1 |
| M4 | 555 | 4 | 20 | 3 | 523, 589 | 0.7 | 1 |
| M5 | 672 | 5 | 20 | 3 | 638, 706 | 0.7 | 1 |
| M6 | 746 | 2 | 15 | 2 | 721, 771 | 0.8 | 1 |
| M7 | 865 | 8 | 39 | 5 | 801, 929 | 0.7 | 1.3 |
| M8 | 1240 | 5 | 20 | 4 | 1205, 1275 | 0.8 | 1 |
| M9 | 1378 | 4 | 15 | 3 | 1351, 1405 | 1.0 | 1 |
| M10 | 1610 | 14 | 60 | 9 | 1509, 1709 | 0.7 | 2.3 |
| M11 | 2250 | 13 | 50 | 6 | 2167, 2333 | 1.0 | 1.9 |
| M12 | 3700 | 32 | 180 | 20 | 3410, 3990 | 1.1 | 3.7 |
| M13 | 4050 | 34 | 155 | 20 | 3790, 4310 | 1.3 | 3 |
| M14 | 8550 | 70 | 300 | 40 | 8050, 9050 | 0.9 | 11 |
| M15 | 10763 | 112 | 1000 | 100 | 9700, 11740 | 0.4 | 10.8 |
| M16 | 12013 | 88 | 950 | 50 | 11060, 13050 | 0.4 | 6 |
| DNB | 700 | 14 | 400 | 20 | 470, 960 | 0.1 | 1 |
| I1 | 640 | 6 | 80 | 6 | 565, 715 | 0.5 | 1 |
| I2 | 865 | 8 | 39 | 5 | 802, 928 | 0.7 | 1.3 |
| I3 | 1610 | 14 | 60 | 9 | 1509, 1709 | 0.7 | 2.3 |
| I4 | 3740 | 40 | 380 | 30 | 3340, 4140 | 0.5 | 3.7 |
| I5 | 11450 | 100 | 1900 | 100 | 9900, 12900 | 0.4 | 20 |

#### 4.5.2.2 VIIRS Spatial Capabilities

For bands that have field stops related to each detector element (M8-M16 and I3-5), the Geometric Instantaneous Field-of-View (GIFOV) is the instantaneous geometric projection of the field stop onto the earth's surface. For bands without field stops for each individual detector element (M1-M7, I1 and I2), the GIFOV is the instantaneous geometric projection of the detector element onto the earth's surface. As specified here, the quantity GIFOV does not include the effects of integration drag, optical blur, or aggregation.

A two-dimensional sensor spatial response can be formed by convolving the optical blur (diffraction and aberrations) with the field stop geometry (or the detector geometry for the VIS/NIR bands). The optically blurred Instantaneous Field-of-View (IFOV), where IFOV is the detector field stop width divided by the effective focal length, is defined as the angular separation between the 50% response points in each of the two orthogonal directions. The IFOV does not include the blur associated with scanning or the effect of aggregation.

For each VIIRS band, the IFOV is specified in Table 4.5 For the moderate resolution bands and the DNB imaging band, the IFOV will not differ from the value shown in this table by more than ± 5% in either dimension. Except for the DNB band, the IFOV the imaging bands will not differ from the value shown in Table 4.5 by more than ± 2% in either dimension.

**Deleted:** channels

**Formatted:** Font color: Auto

**Formatted:** Font color: Auto

The IFOV for the DNB is produced by aggregating multiple sub-pixel detectors. The detector for the DNB consists of a Charge-coupled Device (CCD) with an array of

detector elements. Each of these elements has a IFOV much smaller than the values specified in Table 4.5. Signals from several of these "sub-pixel" detector elements are combined to generate the equivalent of a larger detector having the IFOV shown. This aggregation varies during the scan to create essentially constant IFOV (considering all aggregated sub-pixel detectors and the geometric effect of Time Delay Integration (TDI) and Horizontal Sampling Interval (HSI)) throughout the scan.

Formatted: Font color: Auto

Table 4.5 Optically blurred IFOV requirements.

Formatted: Font color: Auto

Formatted: Font: Not Bold

Formatted: Font: Not Bold

| Band | Center Wavelength (nm) | $IFOV_{Track}$ milliradians | $IFOV_{Scan}$ milliradians | Optically blurred GIFOV at Nadir [1] | |
|---|---|---|---|---|---|
| | | | | Track (km) | Scan (km) |
| M1 | 412 | 0.890 | 0.382 | 0.742 | 0.318 |
| M2 | 445 | 0.890 | 0.382 | 0.742 | 0.318 |
| M3 | 488 | 0.890 | 0.382 | 0.742 | 0.318 |
| M4 | 555 | 0.890 | 0.382 | 0.742 | 0.318 |
| M5 | 672 | 0.890 | 0.382 | 0.742 | 0.318 |
| M6 | 746 | 0.890 | 0.382 | 0.742 | 0.318 |
| M7 | 865 | 0.890 | 0.382 | 0.742 | 0.318 |
| M8 | 1240 | 0.890 | 0.382 | 0.742 | 0.318 |
| M9 | 1378 | 0.890 | 0.382 | 0.742 | 0.318 |
| M10 | 1610 | 0.890 | 0.382 | 0.742 | 0.318 |
| M11 | 2250 | 0.890 | 0.382 | 0.742 | 0.318 |
| M12 | 3700 | 0.890 | 0.379 | 0.742 | 0.316 |
| M13 | 4050 | 0.890 | 0.379 | 0.742 | 0.316 |
| M14 | 8550 | 0.890 | 0.362 | 0.742 | 0.302 |
| M15 | 10763 | 0.890 | 0.362 | 0.742 | 0.302 |
| M16 | 12013 | 0.890 | 0.364 | 0.742 | 0.303 |
| DNB | 700 | 0.890 | 0.890 | 0.742 | 0.742 |
| I1 | 640 | 0.445 | 0.114 | 0.371 | 0.095 |
| I2 | 865 | 0.445 | 0.114 | 0.371 | 0.095 |
| I3 | 1610 | 0.445 | 0.108 | 0.371 | 0.090 |
| I4 | 3740 | 0.445 | 0.109 | 0.371 | 0.091 |
| I5 | 11450 | 0.445 | 0.102 | 0.371 | 0.085 |

#### 4.5.2.3 VIIRS Horizontal Sampling Interval

##### 4.5.2.3.1 Modulation Transfer Function

The sensor Line Spread Function (LSF) in the along-track (cross track) direction is defined as the response to a line slit test pattern oriented in the cross-track (along-track) direction. The Modulation Transfer Function (MTF) in the along-track (cross-track) direction is defined as the magnitude of the normalized Fourier transform of the sensor LSF in the along-track (cross track) direction. The MTF is a function of spatial frequency, and it is equal to one at the origin by virtue of the normalization condition on the LSF. As used here, MTF includes contributions from diffraction, optical aberrations, detector field-of-view, integration drag, and aggregation. Additionally, charge transfer efficiency is a significant contributor to MTF for the Day Night Band (DNB).

The Nyquist frequency is determined for each band and has a spatial period equal to two HSIs on the ground. The Nyquist frequency is given by:

$$f_{nyquist} = \left( \frac{1}{2 * HSI} \right) \qquad (4.11)$$

The MTF of the VIIRS moderate resolution bands will be equal to or exceed the values specified in Table 4.6 and apply to both the along-track and cross-track directions.

Formatted: Font color: Auto

Table 4.6 Moderate resolution band MTF requirements

Formatted: Font color: Auto

| Fraction of Nyquist Frequency | Modulation Transfer Function |
|---|---|
| 0.00 | 1.0 |
| 0.25 | 0.9 |
| 0.50 | 0.7 |
| 0.75 | 0.5 |
| 1.00 | 0.3 |

4.5.2.3.2 Horizontal Spatial Resolution

The Horizontal Spatial Resolution (HSR) is the distance on the earth's surface, both in-track and cross-track, corresponding to one-half the spatial wavelength at which the sensor MTF of an object with a sinusoidal distribution of radiance has dropped to 0.5. In other words, HSR is defined via the function:

$$MTF\left( \frac{1}{2 * HSR} \right) = 0.5 \qquad (4.12)$$

Except for the DNB, VIIRS imaging bands will achieve an HSR of ≤ 0.4 km at nadir and ≤ 0.8 km worst case throughout the scan and the HSR requirements will be met for every detector in each of the imaging bands. The DNB will have an HSR less than 0.800 km in both the track and cross-track direction throughout the scan.

Deleted: B

Deleted: D

4.5.2.3.3 The Horizontal Sampling Interval (HSI)

Deleted: 2

The Horizontal Sampling Interval is defined as the distance, as measured on the ground, between adjacent samples reported by the VIIRS sensor. In the scan direction, the HSI can be calculated from the time interval between samples, the angular velocity of the scan, the cross-track aggregation factor, the scan angle relative to nadir, and the altitude of the satellite above the earth. In the track direction, the HSI is determined by the angular field stop spacing and the satellite altitude.

Bands that use a single and multiple gains are shown in Table 4.11. In bands that use a single gain, the VIIRS sensor will aggregate data in the cross-track direction to produce the value for a particular HSI, as shown in Table 4.7. With the exception of the DNB, the VIIRS sensor will not aggregate data in any band that uses multiple gain states.

Formatted: Font color: Auto

Formatted: Font color: Auto

Deleted: S

The HSI for the single gain moderate resolution bands will be as shown in Figure 4.18 while HSI for single gain imaging bands was shown in Figure 4.15. In addition, for the single-gain moderate resolution bands, the HSI in the track and HSI in scan directions will be within 5% of the values listed in Table 4.8.

Formatted: Font color: Auto

Formatted: Font color: Auto

Formatted: Font color: Auto

Table 4.7. Cross-track aggregation factors.

Formatted: Font color: Auto

| Scan angle ($\phi$) | Number of values to aggregate |
|---|---|
| $\lvert\phi\rvert < 31.59°$ | 3 |
| $31.59° < \lvert\phi\rvert < 44.82°$ | 2 |
| $\lvert\phi\rvert > 44.82°$ | 1 |

Table 4.8. HSI requirements for single-gain moderate resolution bands.

Formatted: Font color: Auto

| Scan angle (degrees) | $HSI_{track}$ (km) | $HSI_{scan}$ (km) |
|---|---|---|
| 0 | 0.742 | 0.776 |
| 10 | 0.755 | 0.805 |
| 20 | 0.797 | 0.903 |
| 30 | 0.876 | 1.111 |
| 40 | 1.018 | 1.033 |
| 50 | 1.289 | 0.899 |
| 55.84 | 1.600 | 1.579 |

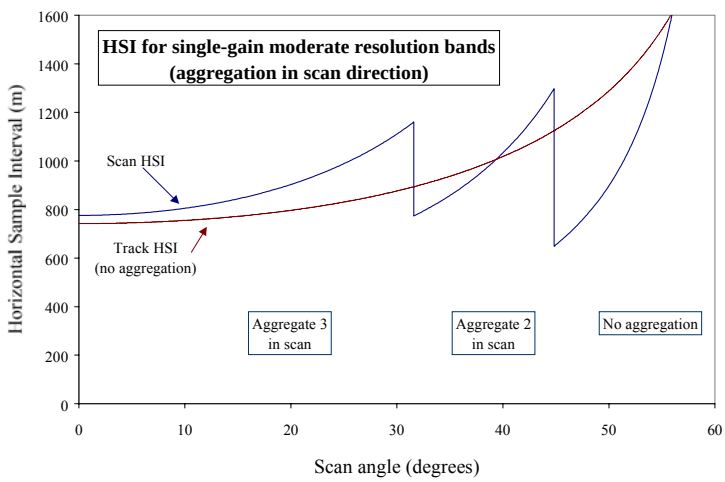


Figure 4.18 HSI for single-gain moderate resolution bands

Formatted: Font color: Auto

The HSI for the dual-gain moderate resolution bands will be as shown in Figure 4.19. The HSI in the track and in scan directions will be within 5% of the values shown in Table 4.9. However, at this time, it is believed that the HSI for archived dual-gain bands will be the same as shown in Figure 4.18.

Formatted: Font color: Auto

Formatted: Font color: Auto

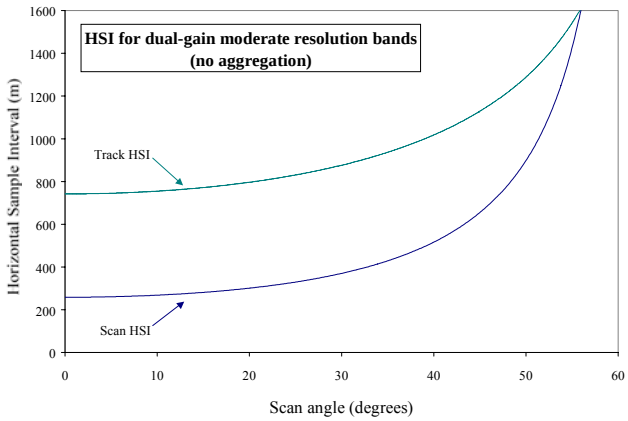


Figure 4.19 HSI for dual-gain moderate resolution bands.

Table 4.9 HSI requirements for dual-gain moderate resolution bands.

| **Scan angle (degrees)** | $HSI_{track}$ **(km)** | $HSI_{scan}$ **(km)** |
|---|---|---|
| 0 | 0.742 | 0.259 |
| 10 | 0.755 | 0.268 |
| 20 | 0.797 | 0.301 |
| 30 | 0.876 | 0.370 |
| 40 | 1.018 | 0.516 |
| 50 | 1.289 | 0.899 |
| 55.84 | 1.600 | 1.579 |

Again, the HSI for the imaging bands will be as was shown in Figure 4.15. For all imaging bands except the DNB, the HSI in the track and in scan directions will be within 5% of the values listed in Table 4.10. **F**or the DNB, the HSI in the track and scan directions will be within 5% of 742m throughout the scan.

Table 4.10 HSI requirements for imaging bands

| Scan angle (degrees) | $HSI_{track}$ (km) | $HSI_{scan}$ (km) |
|---|---|---|
| 0 | 0.371 | 0.388 |
| 10 | 0.378 | 0.403 |
| 20 | 0.398 | 0.452 |
| 30 | 0.438 | 0.555 |
| 40 | 0.509 | 0.516 |
| 50 | 0.644 | 0.449 |
| 55.84 | 0.800 | 0.789 |

#### 4.5.2.4 VIIRS Dynamic Range Capability

The dynamic range of the VIIRS reflective and emissive bands is shown in Tables 4.17 and 4.18.

Table 4.11 Dynamic range requirements for VIIRS sensor reflective bands.

**Formatted:** Font color: Auto
**Formatted:** Font color: Auto
**Formatted:** Font: Times, 11 pt
**Formatted:** Font color: Auto
**Formatted:** Font color: Auto
**Formatted:** Font color: Auto
**Formatted:** Font: Times, 11 pt, Not Bold
**Formatted:** Font: Times, 11 pt
**Formatted:** Font: Times, 11 pt
**Formatted:** Font: Times, 11 pt, Not Bold
**Formatted:** Font: Times, 11 pt, Not Bold
**Formatted:** Font color: Auto
**Formatted:** Font color: Auto
**Formatted:** Font color: Auto

| | | | Single Gain | | Dual Gain | | | |
|---|---|---|---|---|---|---|---|---|
| | | | | | High Gain | | Low Gain | |
| **Band** | **Center Wavelength (nm)** | **Gain Type** | **Lmin** | **Lmax** | **Lmin** | **Lmax** | **Lmin** | **Lmax** |
| M1 | 412 | Dual | - | - | 30 | 135 | 135 | 615 |
| M2 | 445 | Dual | - | - | 26 | 127 | 127 | 687 |
| M3 | 488 | Dual | - | - | 22 | 107 | 107 | 702 |
| M4 | 555 | Dual | - | - | 12 | 78 | 78 | 667 |
| M5 | 672 | Dual | - | - | 8.6 | 59 | 59 | 651 |
| M6 | 746 | Single | 5.3 | 41.0 | - | - | - | - |
| M7 | 865 | Dual | - | - | 3.4 | 29 | 29 | 349 |
| M8 | 1240 | Single | 3.5 | 95.0 | - | - | - | - |
| M9 | 1378 | Single | 0.6 | 41.0 | - | - | - | - |
| M10 | 1610 | Single | 1.2 | 72.5 | - | - | - | - |
| M11 | 2250 | Single | 0.12 | 31.8 | - | - | - | - |
| DNB | 700 | Multiple | 6.67E-5 | 500.0 [1] | - | | | |
| I1 | 640 | Single | 5 | 718 | - | - | - | - |
| I2 | 865 | Single | 10.3 | 349 | - | - | - | - |
| I3 | 1610 | Single | 1.2 | 56.7 | - | - | - | - |

Table 4.12 Dynamic range requirements for VIIRS sensor emissive bands.

| | | | Single Gain | | Dual Gain | | | |
|---|---|---|---|---|---|---|---|---|
| | | | | | High Gain | | Low Gain | |
| Band | Center Wavelength (nm) | Gain Type | Tmin | Tmax | Tmin | Tmax | Tmin | Tmax |
| M12 | 3700 | Single | 230 | 353 | - | - | - | - |
| M13 | 4050 | Dual | - | - | 230 | 343 | 343 | 634 |
| M14 | 8550 | Single | 190 | 336 | - | - | - | - |
| M15 | 10763 | Single | 190 | 343 | - | - | - | - |
| M16 | 12013 | Single | 190 | 340 | - | - | - | - |
| I4 | 3740 | Single | 210 | 353 | - | - | - | - |
| I5 | 11450 | Single | 190 | 340 | - | - | - | - |

#### 4.5.2.5 VIIRS Sensitivity Capability

The sensitivity of VIIRS reflective bands and emissive bands is shown in Tables 4.19 and 4.20. Note that several bands employ dual gain.

Table 4.13 Sensitivity requirements for VIIRS Sensor reflective bands.

**Formatted:** Font: 11 pt
**Formatted:** Font: 11 pt, Bold
**Formatted:** Font: 11 pt
**Formatted:** Font: 11 pt, Bold
**Formatted:** Font: 11 pt
**Formatted:** Font: 11 pt
**Formatted:** Font: 11 pt, Bold
**Formatted:** Font: 11 pt, Bold
**Formatted:** Font: 11 pt
**Formatted:** Font color: Auto
**Formatted:** Font: 11 pt, Not Bold
**Formatted:** Font: 11 pt
**Formatted:** Font: 11 pt, Not Bold
**Formatted:** Font: 11 pt
**Formatted:** Font: 11 pt, Not Bold
**Formatted:** Font: 11 pt, Not Bold
**Formatted:** Font: 11 pt
**Formatted:** Font: 11 pt
**Formatted:** Font: 11 pt, Not Bold
**Formatted:** Font color: Auto
**Formatted:** Font color: Auto
**Formatted:** Font color: Auto

| Band | Center Wavelength (nm) | Gain Type | Single Gain Range Ltyp | Single Gain Range SNR | Dual Gain Range High gain Ltyp | Dual Gain Range High gain SNR | Dual Gain Range Low gain Ltyp | Dual Gain Range Low gain SNR |
|---|---|---|---|---|---|---|---|---|
| M1 | 412 | Dual | - | - | 44.9 | 352 | 155 | 316 |
| M2 | 445 | Dual | - | - | 40 | 380 | 146 | 409 |
| M3 | 488 | Dual | - | - | 32 | 416 | 123 | 414 |
| M4 | 555 | Dual | - | - | 21 | 362 | 90 | 315 |
| M5 | 672 | Dual | - | - | 10 | 242 | 68 | 360 |
| M6 | 746 | Single | 9.6 | 199 | - | - | - | - |
| M7 | 865 | Dual | - | - | 6.4 | 215 | 33.4 | 340 |
| M8 | 1240 | Single | 5.4 | 101 | - | - | - | - |
| M9 | 1378 | Single | 6 | 83 | - | - | - | - |
| M10 | 1610 | Single | 7.3 | 342 | - | - | - | - |
| M11 | 2250 | Single | 0.12 | 10 | - | - | - | - |
| I1 | 640 | Single | 22 | 119 | - | - | - | - |
| I2 | 865 | Single | 25 | 150 | - | - | - | - |
| I3 | 1610 | Single | 7.3 | 6 | - | - | - | - |

Formatted: Font: 11 pt
Formatted: Font: 11 pt, Not Bold
Formatted: Font: 11 pt, Not Bold
Formatted: Font: 11 pt
Formatted: Font: 11 pt, Not Bold

Table 4.14 Sensitivity requirements for VIIRS Sensor emissive bands.

| Band | Center Wavelength (nm) | Gain Type | Single Gain Range Ttyp | Single Gain Range NEdT | Dual Gain Range High gain Ttyp | Dual Gain Range High gain NEdT | Dual Gain Range Low gain Ttyp | Dual Gain Range Low gain NEdT |
|---|---|---|---|---|---|---|---|---|
| M12 | 3700 | Single | 270 | 0.396 | - | - | - | - |
| M13 | 4050 | Dual | - | - | 300 | 0.107 | 380 | 0.423 |
| M14 | 8550 | Single | 270 | 0.091 | - | - | - | - |
| M15 | 10763 | Single | 300 | 0.070 | - | - | - | - |
| M16 | 12013 | Single | 300 | 0.072 | - | - | - | - |
| I4 | 3740 | Single | 270 | 2.500 | - | - | - | - |
| I5 | 11450 | Single | 210 | 1.500 | - | - | - | - |

Formatted: Font color: Auto
Formatted: Font: 11 pt
Formatted: Font: Times, 11 pt, Not Bold
Formatted: Font: Times, 11 pt, Not Bold
Formatted: Font: 11 pt
Formatted: Font: Times, 11 pt, Not Bold

#### 4.5.2.6 VIIRS Sensor Polarization Sensitivity

Several VIIRS bands have polarization requirements as shown in Table 4.15. The polarization sensitivity (or polarization factor) (PF) is defined as:

Formatted: Font color: Auto

$$PF = (I_{max} - I_{min})/(I_{max} + I_{min}) \qquad (4.13)$$

Where:

$I_{max}$ = maximum measured radiance for linearly polarized source radiance for which the plane of polarization contains the line of sight and has any orientation about the line of sight.

$I_{min}$ = minimum measured radiance for linearly polarized source radiance for which the plane of polarization contains the line of sight and has any orientation about the line of sight.

Table 4.15 Polarization sensitivity requirements.

Formatted: Font color: Auto

| Band | Center Wavelength (μm) | Maximum Polarization Sensitivity |
|---|---|---|
| M1 | 0.412 | 3% |
| M2 | 0.445 | 2.5% |
| M3 | 0.488 | 2.5% |
| M4 | 0.555 | 2.5% |
| I1 | 0.640 | 2.5% |
| M5 | 0.672 | 2.5% |
| M6 | 0.746 | 2.5% |
| I2 | 0.865 | 3% |
| M7 | 0.865 | 3% |

Deleted: 8

4.5.2.7 Detector Performance

The noise of the VIIRS VIS and NIR detectors, including photon noise, when operated at Sensor ambient temperature will be less than the noise equivalent photon flux (NEΦ) listed in Table 4.16. Additionally, the noise of the VIIRS SWIR, MWIR, and LWIR detectors, including photon noise, when operated at a temperature of 80K will be less than the noise equivalent photon flux (NEΦ). Finally, the detector and readout design for Bands M1-M16, DNB, and I1-I5 will be in accordance to Table 4.16 while the PV HgCdTe detector RoA will be as indicated in the table or as necessary to meet the NEI requirement.

Formatted: Font color: Auto

Formatted: Font color: Auto

.

Table 4.16 VIIRS Detector NEΦ Requirements

| Band | Detector Type | Readout Type | TDI | Center Wavelength (nm) | Φ (ph cm-2 sec-1) | Min RoAohm-cm$^2$ | NEΦ (ph cm-2 sec-1) |
|---|---|---|---|---|---|---|---|
| M1 | Silicon | CTIA, Dual Gain | 1 | 412 | 1.10E+12 | - | 2.51E+09 |
| M2 | Silicon | CTIA, Dual Gain | 1 | 445 | 1.61E+12 | - | 3.81E+09 |
| M3 | Silicon | CTIA, Dual Gain | 1 | 488 | 1.92E+12 | - | 4.91E+09 |
| M4 | Silicon | CTIA, Dual Gain | 1 | 555 | 1.54E+12 | - | 4.78E+09 |
| M5 | Silicon | CTIA, Dual Gain | 1 | 672 | 9.02E+11 | - | 2.93E+09 |
| M6 | Silicon | CTIA | 1 | 746 | 6.72E+11 | - | 2.71E+09 |
| M7 | Silicon | CTIA, Dual Gain | 1 | 865 | 1.42E+12 | - | 5.26E+09 |
| M8 | PV HgCdTe | CTIA | 1 | 1240 | 4.30E+12 | 6E+6 | 4.69E+10 |
| M9 | PV HgCdTe | CTIA | 1 | 1378 | 4.53E+12 | 6E+6 | 4.39E+10 |
| M10 | PV HgCdTe | CTIA | 1 | 1610 | 2.06E+12 | 6E+6 | 1.01E+11 |
| M11 | PV HgCdTe | CTIA | 1 | 2250 | 5.92E+11 | 6E+6 | 4.16E+10 |
| M12 | PV HgCdTe | CTIA | 1 | 3700 | 2.41E+13 | 6E+6 | 6.06E+10 |
| M13 | PV HgCdTe | CTIA, Dual Gain | 1 | 4050 | 7.00E+13 | 6E+6 | 1.02E+11 |
| M14 | PV HgCdTe | CTIA | 1 | 8550 | 2.94E+15 | 31 | 1.14E+12 |
| M15 | PV HgCdTe | CTIA | 1 | 10763 | 1.26E+16 | 31 | 4.33E+12 |
| M16 | PV HgCdTe | CTIA | 2 | 12013 | 1.25E+16 | 2.5 | 7.15E+12 |
| DNB | CCD | None | 1-250 | 700 | - | - | - |
| I1 | Silicon | CTIA | 1 | 640 | 7.75E+12 | - | 4.34E+10 |
| I2 | Silicon | CTIA | 1 | 865 | 5.56E+12 | - | 2.85E+10 |
| I3 | PV HgCdTe | CTIA | 1 | 1610 | 6.90E+12 | 6E+6 | 9.26E+11 |
| I4 | PV HgCdTe | CTIA | 1 | 3740 | 1.23E+13 | 6E+6 | 1.85E+11 |
| I5 | PV HgCdTe | CTIA | 1 | 11450 | 3.61E+15 | 2.5 | 8.35E+12 |

**Formatted:** Font color: Auto

**Formatted:** Font: Times, 11 pt

**Formatted:** Font: 11 pt

The number of detectors and earth view samples per detector for the VIIRS sensor are shown in Table 4.17. The integration times for the VIIRS bands are defined to meet the IFOV requirements.

Formatted: Font color: Auto

Table 4.17 Bands and detectors defined

Formatted: Font color: Auto

Formatted: Font: 11 pt, Not Bold

| Band | Number of Detectors | Number of Earth View Samples | Sample Time (μs) | Integration Time (μs) |
|---|---|---|---|---|
| M1 | 16 | 6,298 | 88.26 | 78.45 |
| M2 | 16 | 6,298 | 88.26 | 78.45 |
| M3 | 16 | 6,298 | 88.26 | 78.45 |
| M4 | 16 | 6,298 | 88.26 | 78.45 |
| M5 | 16 | 6,298 | 88.26 | 78.45 |
| M6 | 16 | 6,298 | 88.26 | 78.45 |
| M7 | 16 | 6,298 | 88.26 | 76.00 |
| M8 | 16 | 6,298 | 88.26 | 76.00 |
| M9 | 16 | 6,298 | 88.26 | 76.00 |
| M10 | 16 | 6,298 | 88.26 | 76.00 |
| M11 | 16 | 6,298 | 88.26 | 76.00 |
| M12 | 16 | 6,298 | 88.26 | 76.00 |
| M13 | 16 | 6,298 | 88.26 | 76.00 |
| M14 | 16 | 6,298 | 88.26 | 78.45 |
| M15 | 16 | 6,298 | 88.26 | 78.45 |
| M16 | 16 | 6,298 | 88.26 | 78.45 |
| DNB | 16 (Effective) | 4055 | 42.2 – 253.3 | 42.2 – 253.3 |
| I1 | 32 | 12,596 | 44.13 | 34.32 |
| I2 | 32 | 12,596 | 44.13 | 34.32 |
| I3 | 32 | 12,596 | 44.13 | 31.87 |
| I4 | 32 | 12,596 | 44.13 | 31.87 |
| I5 | 32 | 12,596 | 44.13 | 22.06 |

Deleted: 9

#### 4.5.2.8 Band to Band Registration or Co-registraton

Co-registration of spectral bands is measured by the displacement of corresponding pixels in two different bands from their ideal relative location. Two pixels are "corresponding" if their footprints should ideally coincide or if the footprint of one should ideally lie within a specific region of the footprint of the other. If co-registration is specified by a single value, this value is the upper bound on the magnitude of the displacement of the locations of corresponding pixels in any direction.

VIIRS has several requirements for band-to-band registration. First, given an unaggregated pixel for which the HSR in the track direction need not equal the HSR in the scan direction, we define

- Track misregistration (Δtrack) --- the linear separation between centroids of track-direction Line Spread Functions (LSFs) for corresponding pixels from different bands, written as a fraction of the specified HSR in the track direction.

- Scan misregistration (Δscan) --- the linear separation in the scan direction between centroids of scan-direction LSFs for corresponding pixels from different bands, written as a fraction of the specified HSR in the scan direction.

Band to band registration requirements have been established to meet the requirements of the most stringent EDRs that use difference band combinations. Thus, different requirements exist for some imaging, radiometry, and combinations of each. These requires are as follows:

- All of the Imaging Bands I1, I2, I3, I4 and I5 will be co-registered so that for any pair the product of (1-Δtrack) and (1-Δscan) is greater than 0.8. The intent of this design is to ensure that for these two bands, which are essential for the NDVI product, the over-lapping area of corresponding pixels is greater than 80% of the pixel area. The pixel area is taken to be that of the rectangular region with track and scan dimensions of HSR track and HSR scan.
- Moderate-resolution Bands M9, M12, M13, M14, M15, and M16 will be co-registered so that for any pair the product of (1-Δtrack) and (1-Δscan) is greater than 0.8.
- Moderate-resolution Bands M5 and M7 are co-registered so that the product of (1-Δtrack) and (1-Δscan) is greater than 0.8.
- Moderate-resolution Bands M3, M5, and M11 are co-registered so that for any pair the product of (1-Δtrack) and (1-Δscan) is greater than 0.7.
- All other spectral band pairs shall be co-registered so that for any pair the product of (1-Δtrack) and (1-Δscan) is greater than 0.64.

There is also a requirement for registration of imaging-resolution bands with moderate-resolution bands. The imaging-resolution pixels are approximately one half as large as the moderate-resolution pixels. The VIIRS design uses the fact that imaging pixels can be added (2 in track by 2 in scan) to overlay a moderate-resolution pixel. This feature is referred to as "nesting" of the imaging-resolution bands with the moderate-resolution bands. In this case, it is intended that in each direction the LSF corresponding to the sum of two imaging-resolution samples be registered with the LSF of an unaggregated moderate-resolution pixel.

For the purposes of specifying registration, the aggregated imaging LSFs is defined as the average of two track LSFs in track and the average of two scan LSFs in scan. In track, the centroid of an aggregated imaging LSF shall coincide with the centroid of a corresponding moderate-resolution pixel to within 20%, one-sigma of the specified HSR in the track direction. In scan, the centroid of an aggregated imaging LSF shall coincide with the centroid of a corresponding moderate-resolution pixel to within 20%, one-sigma of the specified of the HSR in the scan direction. In the event that the aggregated imaging pixel and the unaggregated moderate-resolution pixel have different HSRs, the co-registration requirements above shall use the larger HSR.

**Formatted:** Left

### 4.5.2.9 VIIRS Calibration

Deleted: 10

Calibration is the process of translating VIIRS RDRs (or digital data) into SDRs which are first expressed in terms of radiance (or energy) which can also be converted into reflectance for solar bands or equivalent blackbody brightness temperatures (EBBTs) for IR bands.

The capability to accurate calibrate sensor data is critical to all NPOESS products, since EDRs are typically generated from band reflectance and EBBTs values. Relative calibration between specific VIIRS bands is needed to create EDRs for the operational user community. For example, the VIIRS Cloud Mask product uses multiple bi-spectral cloud detection tests to classify pixels as cloud-free or cloud contaminated. Thus, data must be accurately calibration between bands. However, climate studies examine potential changes in the atmosphere-Earth system using observations over decadal time scales made with multiple sensors. Thus, it becomes essential that VIIRS also satisfy absolute radiometric calibration standards to allow inter-sensor comparisons that are required for climate-change studies. The VIIRS sensor requirements for absolute and relative calibration have been established and are provided next.

Deleted: channel

Deleted: channel

Deleted: but

Deleted: these

#### 4.5.2.9.1 VIIRS Absolute Radiometric Calibration – Uniform Scene

Formatted: Left

Deleted: 10

Thus, the absolute radiometric calibration uncertainty for spectral data collected by the VIIRS sensor will satisfy the following requirements when viewing a uniform scene:

- The VIIRS Sensor radiometric calibration shall be traceable to National Institute of Standards and Technology (NIST) standards.
- The VIIRS Sensor calibration uncertainty and stability requirements shall apply to all VIIRS sensor scan angles.
- For any VIIRS Sensor band that uses dual gain states, both gains shall be calibrated.
- For the bands specified as moderate resolution and reflective, given a uniform scene of typical spectral radiance (Ltyp) as specified in Table 4.13, the calibration uncertainty of the spectral reflectance shall be less than 2%.
- For the bands specified as imaging and reflective, given a uniform scene of typical spectral radiance (Ltyp) as specified in Table 4.13 the calibration uncertainty of the spectral reflectance shall be less than 2%.
- For the bands specified as moderate resolution and emissive, the absolute radiometric calibration uncertainty of spectral radiance for uniform scenes will be less than the percentages shown in Table 4.18 for five scene temperatures.
- For the bands specified as imaging and emissive, given a uniform scene of brightness temperature of 267K, the calibration uncertainty of spectral radiance shall be as specified in Table 4.19.

Formatted: Font color: Auto

Formatted: Font color: Auto

Formatted: Font color: Auto

Formatted: Font color: Auto

All radiance levels referred to in these requirements are to be top-of-the-atmosphere radiances.

The VIIRS sensor radiometric calibration uncertainty includes the errors due to calibrator temperature, calibrator emissivity, response versus scan angle, band center wavelength, optical and electronic crosstalk, ghosting, and out-of-band spectral response.

Table 4.18 Absolute radiometric calibration uncertainty of spectral radiance for moderate resolution emissive bands.

| Band | λc (μm) | Scene Temperature | | | | |
|---|---|---|---|---|---|---|
| | | 190K | 230K | 270K | 310K | 340K |
| M12 | 3.7 | N/A | 7.0% | 0.7% | 0.7% | 0.7% |
| M13 | 4.05 | N/A | 5.7% | 0.7% | 0.7% | 0.7% |
| M14 | 8.55 | 12.3% | 2.4% | 0.6% | 0.4% | 0.5% |
| M15 | 10.763 | 2.1% | 0.6% | 0.4% | 0.4% | 0.4% |
| M16 | 12.013 | 1.6% | 0.6% | 0.4% | 0.4% | 0.4% |

Formatted: Font color: Auto
Formatted: Font: 11 pt, Not Bold
Formatted: Font: 11 pt, Not Bold
Formatted: Font: 11 pt

Table 4.19 Radiometric calibration uncertainty for imaging emissive bands.

| Band | Center Wavelength (nm) | Calibration Uncertainty |
|---|---|---|
| I4 | 3740 | 5.0% |
| I5 | 11450 | 2.5% |

Formatted: Font color: Auto

### 4.5.2.9.2 VIIRS Relative Radiometric Calibration – Uniform Scene

Formatted: Left
Deleted: 10

The calibrated output of all channels within a band will be matched to the band mean output within the specified band NEdL / NEdT (1-σ) when viewing a uniform scene. The matching condition shall be met between radiance levels from Lmin to 0.9 Lmax. The matching condition for the DNB is to be defined (TBD) in the future, but will be met between radiance levels of one-half the maximum radiance for the high gain state and 0.9 times the maximum radiance for the low gain state.

- The VIIRS sensor response will be characterized with an uncertainty better than 0.1% for the MWIR and LWIR bands.
- The VIIRS Sensor response shall be characterized with an uncertainty better than 0.3% for the VIS, NIR, and SWIR bands.
- For the Day/Night band, the radiometric calibration uncertainty of the effective, in-band radiance ($Wm^{-2}sr^{-1}$), for a uniform scene shall be as specified in Table 4.20.

Formatted: Font color: Auto

Table 4.20 Radiometric calibration uncertainty for Day/Night Band

| Gain State | Calibration Uncertainty | Radiance level at which calibration uncertainty is to be evaluated |
|---|---|---|
| Low | 5%10% | One-half of maximum radiance for low gain state<br>Minimum radiance for low gain state |
| Medium | 10%30% | Maximum radiance for medium gain state<br>Minimum radiance for medium gain state |
| High | 30%100% | Maximum radiance for high gain state<br>Minimum radiance for High gain state |

Formatted: Font color: Auto

### 4.5.2.9.3 VIIRS Relative Radiometric Calibration – Structure Scene

Formatted: Left
Deleted: 10

Additional absolute radiometric calibration uncertainty requirements are established for structured scenes that contain a bright target, which is defined as a source of maximum radiance (excluding fires) which has an angular extent of 12 milliradians in-track by 12 milliradians cross-track located anywhere within a scene of uniform typical radiance.

- For each band, except M13 and M15, the maximum radiance (or maximum temperature) can be found in Table 4.11 and Table 4.12.
- For M13 and M15, both of which are used to support the fire EDR, the maximum temperature for the structured scene requirement will be 335K.
- The structured scene requirement places a limit on the amount of energy scattered onto a detector from a bright target a specified angular distance away. Given angular distances to a bright target as specified in TABLE 20, the amount of scattered radiance, as a fraction of typical scene radiance, shall be less than the values in Table 4.21.
- For the DNB, the radiance of the bright target shall be half the maximum radiance for the DNB low gain state, and the response of a detector 6 milliradians away shall be not more than the response of that detector to a radiance 0.002 times the bright target radiance.

Formatted: Font color: Auto

Formatted: Font color: Auto

Formatted: Font color: Auto

Table 4.21 Structured Scene requirements.

Formatted: Font color: Auto

Formatted: Font: Times, 11 pt

| Band | Center Wavelength (nm) | Angular separation from bright target (milliradian) | Maximum allowed ratio of scattered radiance to typical radiance |
|---|---|---|---|
| M1 | 412 | 6 | 0.01 |
| M2 | 445 | 6 | 0.01 |
| M3 | 488 | 6 | 0.01 |
| M4 | 555 | 6 | 0.01 |
| M5 | 672 | 12 | 0.02 |
| M6 | 746 | 12 | 0.02 |
| M7 | 865 | 12 | 0.02 |
| M8 | 1240 | 6 | 0.01 |
| M9 | 1378 | N/A | N/A |
| M10 | 1610 | N/A | N/A |
| M11 | 2250 | 6 | 0.01 |
| M12 | 3700 | 3 | 0.001 |
| M13 | 4050 | 3 | 0.001 |
| M14 | 8550 | N/A | N/A |
| M15 | 10763 | 3 | 0.001 |
| M16 | 12013 | 3 | 0.001 |
| DNB | 700 | N/A | N/A |
| I1 | 640 | 6 | 0.01 |
| I2 | 865 | 6 | 0.01 |
| I3 | 1610 | 6 | 0.01 |
| I4 | 3740 | N/A | N/A |
| I5 | 11450 | N/A | N/A |

# CHAPTER 5

# PRINCIPLES IN IMAGE INTERPRETATION

## 5.1. INTRODUCTION

In this chapter, basic and more advanced concepts are discussed that deal with the manual interpretation of meteorological satellite data in general and MODIS/VIIRS imagery in particular. In Chapter 3, the surface energy from a cloud-free atmosphere arriving at the aperture of the satellite sensor was given in Equation 4.2 for terrestrial radiation and Equation 4.4 for solar radiation. In Chapter 4, the path was described that takes top of the atmosphere radiation into the VIIRS sensor optics through the digitizer and downlinked to the ground processing segments where RDRs are converted into calibrated SDRs. In this section, information is provided on the energy sources observed by the VIIRS sensor and the implications of interpretation on each band.

Figure 5.1 shows the normalized emission spectra for three blackbodies emitting at 6000K, 770K, and 300K. These temperatures are typical of the Sun's photosphere, a forest fire, and a global average of the Earth's surface respectively. The figure helps to illustrate the characteristics of blackbody radiation:

(1) The wavelength of the maximum emission becomes smaller as the blackbody temperature becomes larger. *Knowledge of source emission spectra helps users to determine which MODIS/VIIRS bands provide the "best" information on phenomena under investigation.* The maximum emission at the Sun's photosphere is ~ 0.5 μm but is ~ 10 μm for the Earth's surface. Forest fires typically burn at 700 K and have their maximum emission in the 3-5 μm region.

(2) The shape of each blackbody radiation curve shown in Figure 5.1 is described by Planck's Law and can be calculated using Equation 5.1. Planck's Law relates blackbody energy of monochromatic intensity ($B_\lambda$) to the absolute temperature (T in degrees Kelvin) of the object and the wavelength ($\lambda$) of the emission, where c and k are the velocity of light and the Boltzmann constant respectively.

Deleted: K

$$B_\lambda(T) = 2hc^2 / \{ \lambda^5 [\exp(hc/k\lambda T) - 1]\} \qquad (5.1)$$

Deleted: K

(3) The total radiant energy (F) of a blackbody can be derived by integrating the Planck function $B_\lambda(T)$ over the entire wavelength domain. This energy is proportional to the fourth power of the absolute temperature according to the Stefan-Boltzmann Law where $\sigma$ is the Stefan-Boltzmann constant.

$$F = \sigma T^4 \qquad (5.2)$$

(4) Finally, the wavelength of the maximum intensity ($\lambda_m$) for blackbody radiation is inversely proportional to the absolute temperature, according to Wien's Displacement Law.

$$\lambda_m = a / T \quad (5.3)$$

where a = 0.2897 cm K

- Spectral signatures of features collected at wavelengths greater than about 5 µm are unchanged during daytime and nighttime conditions.
- Spectral bands that collect energy at wavelengths shorter than 3 µm receive an insignificant amount of radiation from the Earth and generate a negligible signal in nighttime imagery. The VIIRS Day-Night Band (DNB), which is the successor to the low-light imaging capability of the DMSP OLS sensor, has special amplifiers to detect lunar illuminated surfaces.
- The 3-5 µm region receives energy from both reflected radiation from the Sun and emitted radiation from the Earth-atmosphere system. Therefore, signatures in this spectral range are complex and may change dramatically between daytime and nighttime conditions. Detailed information on this band is provided in Section 5.2.4.

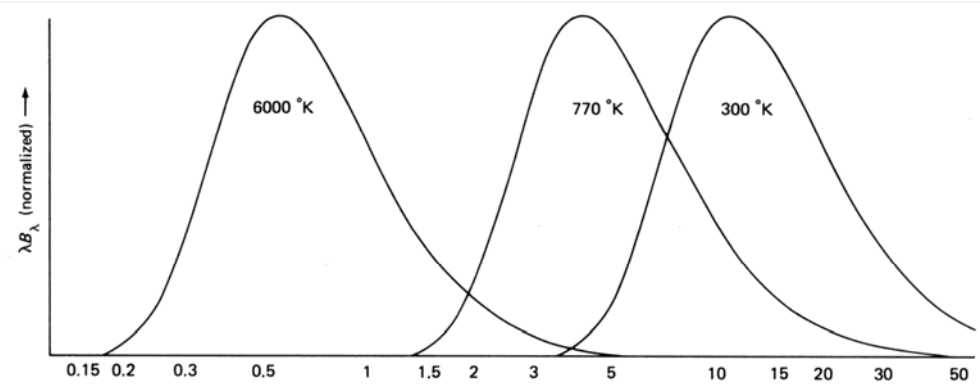


Figure 5.1. Normalized distribution of emission spectra for three blackbodies with absolute temperatures of 6000 K (Sun), 770 K (forest fires), and 300 K (Earth's surface) shows primary energy sources for each of the VIIRS spectral bands (Scorer, 1990).

The calibration process describes the conversion of the output signal from an imager, for a given spectral band, to the satellite received radiance, in that band, in absolute units, $Wm^{-2}$. Calibration is critical to the accurate interpretation of imagery. For a thermal infrared band this may be expressed as a brightness temperature, which is the equivalent blackbody temperature of the radiation received at the satellite. It is important to realize that the brightness temperature is not the same as the temperature of the target surface, whether that target is cloud or is on the Earth's surface, i.e. in a cloud-free area. The term brightness temperature refers to the temperature required to produce the energy recorded by the sensor for a surface with unity emissivity. If two target surface features in a satellite image had identical temperatures but different emissivities, the brightness temperature would be lower for the feature with the lower emissivity, as shown in Equation (4.2) or as approximated in Equation (4.3), if the observations were made through exactly the same atmosphere. In addition, if two features had identical temperatures and emissivities but were viewed through two different atmospheres, the

brightness temperature of the feature viewed through the most transmissive atmosphere would be higher.

At microwave wavelengths, Planck's Law shown in Equation (5.1) can be simplified to.

$$B_\nu(T) = (2k\nu^2 / c^2)T \qquad (5.4)$$

Deleted: K

This expression, known as the Rayleigh-Jeans Law, states that energy emitted at microwave wavelengths is linearly proportional to temperature. If, for the moment, we neglect the atmospheric effects, then for microwave radiation the relation between the temperature, $T$, of a surface and its brightness temperature, $T_B$, is quite simple:

$$\varepsilon B_\nu(T) = \varepsilon(2k\nu^2 / c^2)T = (2k\nu^2 / c^2)T_B \qquad (5.5)$$

Deleted: K

Deleted: K

therefore

$$T_B = \varepsilon T \qquad (5.6)$$

Or the temperature of a surface is $T_B / \varepsilon$. In reality, to determine the temperature of the surface we start with the brightness temperature, which is the equivalent black body temperature of the satellite-received radiation, and we have to determine the equivalent black body temperature of the radiation leaving the surface and then we can use Equation (5.6) to find the surface temperature. For thermal infrared radiation equation (5.4) does not apply and the relation between $T$ and $T_B$ is more complicated, namely

$$\varepsilon B_\lambda(T) = B_\lambda(T_B) \qquad (5.7)$$

where the full expressions for $B_\lambda(T)$ and $B_\lambda(T_B)$ must be used.

In addition, because meteorological satellites "look" toward the Earth, energy collected at wavelengths shorter than infrared wavelengths must be reflected from the Earth back toward the satellite sensor. There are two sources of energy to reflect to the sensor, solar and lunar. Only the VIIRS DNB channel is capable of collecting sufficient lunar energy to create a useful image.

From the calibration coefficients for these bands one can determine the satellite-received radiance. However, this is not what is important in cloud studies because its value will depend on the intensity of the solar illumination at the top of the atmosphere. Top of the atmosphere radiation depends on latitude, time of day, and season all of which comprise the relative orientations of the incident sunlight, the surface normal and the direction of observation of the target area by the satellite-flown instrument. What is important, therefore, is to eliminate these effects by converting the satellite-received radiance into the reflectivity of the target, i.e. its albedo. The reason for this is that the reflectivity, or albedo, is a characteristic of the physical properties of the cloud (or ground surface) and is unaffected by variations in the solar illumination. The use of albedo or reflectance for observations illuminated by the Sun (or Moon) eliminates variations in these observations that result from satellite position with respect to the local normal at the Earth's surface, the Sun or the Moon and the sensor scan geometry

Deleted: moon

For example, assume that identical water clouds are observed at three locations:

1) at the satellite subpoint, over the equator, at the summer equinox, and with the Sun directly overhead

2) at the satellite subpoint, over 40 degrees south latitude, at the summer equinox, and with the sun directly overhead

3) at 40 degrees south latitude at the summer equinox at the satellite subpoint with the sun setting on the horizon.

Clearly the total solar energy reflected from the cloud to the sensor is greatest for the first case, where the Sun is nearly overhead, and continues to decrease for case 2 and even more for case 3. However, the microphysical properties or characteristics of the cloud have not changed in these three instances, only the characteristics of the observation. Therefore, it becomes necessary to compensate for variations in the meteorological satellite observations that are due solely to external factors. This correction is made in the solar regions by dividing the energy incident upon the sensor by the energy available at the top of the atmosphere, at the local normal to the Earth's surface viewed by the sensor. The actual energy observed by the sensor is divided by the solar energy ($F_o$) in the VIIRS band multiplied by (1) the ratio of the mean Earth-Sun distance to the actual distance between the Sun and Earth and (2) the cosine of the solar zenith angle (SZA), i.e. the angle between the Sun's direct rays and the local normal to the Earth's surface,. Thus, the actual top of the atmosphere solar energy is also a function of the local normal of latitude ($\alpha$), solar inclination ($\delta$), and solar hour angle ($\eta$) as described in Equation (5.8):

$$F = F_o S(d_m/d)^2 \, \mathrm{Cos}(SZA) \qquad (5.8)$$

$$\text{Where } \mathrm{Cos}\,(SZA) = [\, \sin\alpha \sin\delta + \cos\alpha \cos\delta \cos\eta] \qquad (5.9)$$

Once the energy recorded at the VIIRS sensor is divided by the top of the atmosphere solar energy, as defined by Equation (5.8), an identical cloud observed in the three situations previously described will be exactly the same.

## 5.2. VIIRS IMAGERY DATA

A detailed discussion is now presented on the spectral content of each VIIRS band. The format followed is (1) an analysis of phenomenology of the bandpass, based upon theoretical calculations, and (2) examples of the signatures in actual sensor data. A summary is provided in Table 5.1 of the bandpasses in the previous instruments flown on operational and research satellites that most closely approximate VIIRS imagery channels and radiometry channels within the imagery bandpasses.

Table 5.1. Bandpasses of Instruments that Approximate VIIRS Imagery Resolution Bands.

Deleted: s

Deleted: S

Deleted:

Deleted:

Deleted:

Deleted: channel

| Band | VIIRS ChannelDesignator | Central Wavelength (µm) | Bandwidth (µm) | Satellite System and Channel | Wavelength Interval (µm) |
|---|---|---|---|---|---|
| 1 | DNB | 0.7 | 0.4 | DMSP/OLSL | 0.58 - 0.98 |
| 6 | I1 | 0.640 | 0.080 | MODIS 1 | 0.620-0.670 |
| 9 | I2 | 0.865 | 0.039 | MODIS 2 | 0.841-0.876 |
| 13 | I3/M10 | 1.61 | 0.06 | AVHRR 3A | 1.628-1.652 |
| 16 | I4/M12 | 3.74 | 0.38 | AVHRR 3B | 3.55-3.93 |
| 21 | I5/M15 | 11.45 | 1.9 | DMSP/OLST | 10.4 – 12.7 |

**Deleted:** (µm)

**Deleted:** ¶

**Deleted:** (µm)

### 5.2.1. VIIRS Imagery Band I1 (0.64 ± 0.040 μm)

#### 5.2.1.1. Theoretical Basis for Band Interpretation

As shown in Figure 4.8, the VIIRS I1 band is contained within an atmospheric window with ~ 30% attenuation, resulting primarily from molecular scattering and to a lesser degree from absorption by ozone, oxygen and water vapor. Approximately 70% of the top of the atmosphere solar energy in this band arrives at the Earth's surface when water vapor concentrations are typical of a mid-latitude winter profile (Anderson et al., 1986). Energy in these relatively short wavelengths is scattered according to Rayleigh theory, which means approximately equal amounts of energy are scattered in the forward and backward direction. The net effect of Rayleigh scattering on VIIRS imagery is that the albedo or reflectance of pixels slowly increases as VIIRS scans from nadir to the edge of the scan. Thus, in cloud-free conditions, over a relatively homogeneous, poorly reflective surface, such as the ocean, the albedo in the I1 Imager Band may increase from ~ 2-3 percent at nadir and as much as 7-percent at the edge of the scan. While such effects are insignificant for manual cloud analyses, they may be important in other applications.

**Deleted:** ing

**Deleted:** I

Noted in Figure 4.8 are the signatures for snow, vegetated land, bare soil, and ocean surfaces. The reflectivity of snow in this band is very high and appears very bright in the band while the reflectances of the ocean surfaces and vegetated land are very low and they appear very dark. Bare soil has a moderate albedo of approximately 20 percent which should make it appear less bright than snow and much brighter than vegetated land and water regions.

Water clouds (e.g. stratus, cumulus, etc.) appear bright in this band because they typically have large particle "number concentrations." Since the reflective power of a cloud is defined by its ability to scatter, known as its scattering coefficient, and the particle drop size distribution and number concentration, these clouds are highly reflective. In terms of scattering efficiency, this means *water clouds have a relatively large optical thickness, even if their geometric thickness is relatively small*. Typical droplet concentrations for water clouds range between 100-500 $cm^{-3}$ (Liou, 1992). On the other hand, cirrus clouds appear less bright at this wavelength because the optical depth of ice clouds is much smaller for a given geometric thickness due to their larger particle size and smaller number concentrations. Typical number concentrations for cirrus clouds are in the 0.01 - 0.1 $cm^{-3}$ range (Liou, 1992). In terms of scattering efficiency, this means *ice clouds have a relatively small optical thickness, even if their geometric thickness is relatively large*. Consequently, water clouds are typically very bright in this band while ice clouds may be only barely visible to the human analyst.

#### 5.2.1.2. Representative Imagery of the VIIRS I1 Band (0.640 ± 0.040 μm)

Manual detection of clouds in this band is based upon the concepts outlined in Section 4.1 that emphasized the importance of maximizing the contrast between clouds and the background. Manual cloud classification with the VIIRS I1 band emphasizes (1) texture, (2) spatial resolution of cloud elements, and (3) shadows which may be cast from clouds high in the atmosphere onto lower level clouds.

A manual interpretation of features contained in the VIIRS I1 band is demonstrated using the AVHRR channel 1 imagery shown in Figure 5.2. This image was collected by NOAA-12 at about 7:05 AM local (1505 GMT) on March 19, 1996. Shown in the imagery is an area that extends approximately 1000 km in the north-south direction from near Portland, Oregon to Los Angeles, California and 1000 km in the east-west direction from the border of Utah and Nevada to the 130 degree west meridian. The large, San Joaquin Valley of California runs from the upper center to the bottom right of the image. The scene contains over a million AVHRR pixels with a nominal resolution of 1.1 km at nadir.

**Deleted:** C

**Deleted:** 20

An extensive area of highly reflective water clouds is evident over much of the left half of the image. These clouds are stratiform in the lower half and cumuliform toward the upper-left corner. Long, narrow cloud streaks, common with cirrus clouds, are seen in the middle-left to upper right corner of the scene and shadows from these cirrus clouds are cast upon lower-level water clouds. The presence of a frontal system is suggested along the region where the cirrus is present and the lower-level water clouds change from stratiform to cumuliform. An extensive cloud-free, snow-covered region can be identified by the dendritic pattern seen in the right half of the scene, especially in the mountainous terrain contained in most of the lower right quadrant. However, it is very difficult to distinguish between land and water surfaces since the reflectivity of both are very low ( < 10%), as shown in Figure 19. A careful inspection does allow Lake Tahoe to be identified since it is neatly outlined by snow. Additionally, the arid regions of Nevada (far right hand side) which have a reflectivity greater than 20% are more pronounced than regions of the highly vegetated San Joaquin Valley, which have reflectivities less than 10%. Cirrus clouds are present in the bottom fifth of the scene, again identified by their smooth, wispy texture over the San Joaquin Valley and shadows cast upon lower-level water clouds toward the bottom-left corner of the scene.

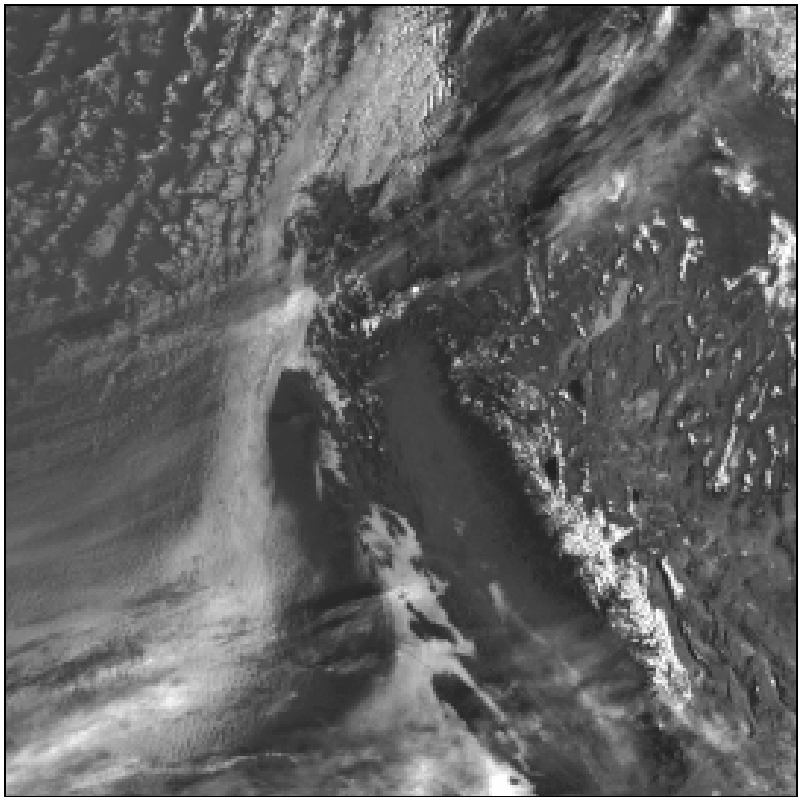

Figure 5.2. Signatures of clouds and land surfaces typical of those present in the VIIRS I1 band are seen in the NOAA-12 AVHRR channel 1 imagery collected near San Francisco, CA on February 19, 1996 (Hutchison et al., 1997(a)).

### 5.2.2. VIIRS I2 Band (0.865 ± 0.020 μm)

#### 5.2.2.1. Theoretical Basis for Band Interpretation

As shown in Figure 4.8, the VIIRS I2 band is contained within an atmospheric window with less attenuation than that of the I1 band. This higher transmission results from a reduction in molecular scattering by the atmosphere because the longer wavelength is affected less by Rayleigh or molecular scattering. Also, notice that the I2 band contains no significant water vapor absorption bands which further increases transmission in the bandpass. Energy at wavelengths in the VIIRS I2 band is reduced by Mie scattering events, e.g. by water vapor and aerosol particles, however, these particles make up only a small portion of the atmosphere in contrast to the molecular atmosphere which impacts the I1 band. Therefore, over 80% of the top of the atmosphere solar energy in this band arrives at the Earth's surface. Another significant difference between the I1 and I2 band is the increased reflectivity of vegetated land, compared to bare soil. The reflectivity of bare soil is greater than vegetated land in the I1 channel but the reverse is true in the I2 channel. The reflectivity of water clouds has also increased between the I2 and I1 bands, while the reflectivity of water surfaces remains very low as it was in the I1 band. Finally, the I2 band is designed to be more narrow than the earlier AVHRR channel 2. Narrowing the band from the 0.3 μm AVHRR bandpass to a 0.039 μm VIIRS bandpass reduces variations that are due solely to water vapor absorption. For example, one strong water vapor absorption band complex at ~ 0.83 μm was contained in the AVHRR channel 2 imagery but is outside the VIIRS I2 bandpass. The reduction in the VIIRS bandpass has little effect on cloud signatures since these features reflect very large amounts of energy to the sensor. However, narrowing the AVHRR band to the VIIRS 0.039 μm bandwidth significantly reduces global variations in the signatures of many lower reflectivity surfaces that would have changed due solely to variations in atmospheric water vapor content as the NPOESS satellite orbits the Earth. For example, VIIRS imagery will provide more accurate analysis of NDVI than is possible with AVHRR data since the VIIRS bands will manifest smaller day-to-day variations that arise from changes in the composition of the atmosphere.

**Deleted:** wa

**Deleted:** C

**Deleted:** C

**Deleted:** has no effect on

**Deleted:** channel

**Deleted:** VIIRS

**Deleted:** channels

### 5.2.2.2. Representative Imagery of the VIIRS I2 Band (0.865 ± 0.020 μm)

A manual interpretation of features contained in the VIIRS I2 band is demonstrated using the AVHRR channel 2 imagery shown in Figure 5.3. This image is of the same scene shown in Figure 5.2. The most striking difference between Figure 5.2 and Figure 5.3 is the ability to clearly see fine details in the land structure of the latter where little was evident in the former, since the reflectivity of vegetated land is nearly 60% in the VIIRS I2 band but less than 10% in the I1 band. Thus, the I2 band is highly useful for detecting land-sea boundaries, e.g. even the Sacramento River's basin is visible in this figure as it extends down the middle of the San Joaquin Valley just west of Lake Tahoe. Signatures of water clouds are similar in both the VIIRS I1 and I2 bands, although the I1 band is more useful for creating manually-generated cloud/no cloud masks since the contrast between clouds and their surrounding backgrounds is greater in the I1 band than in the I2 band.

Deleted: C

Deleted: channel

Deleted: ,

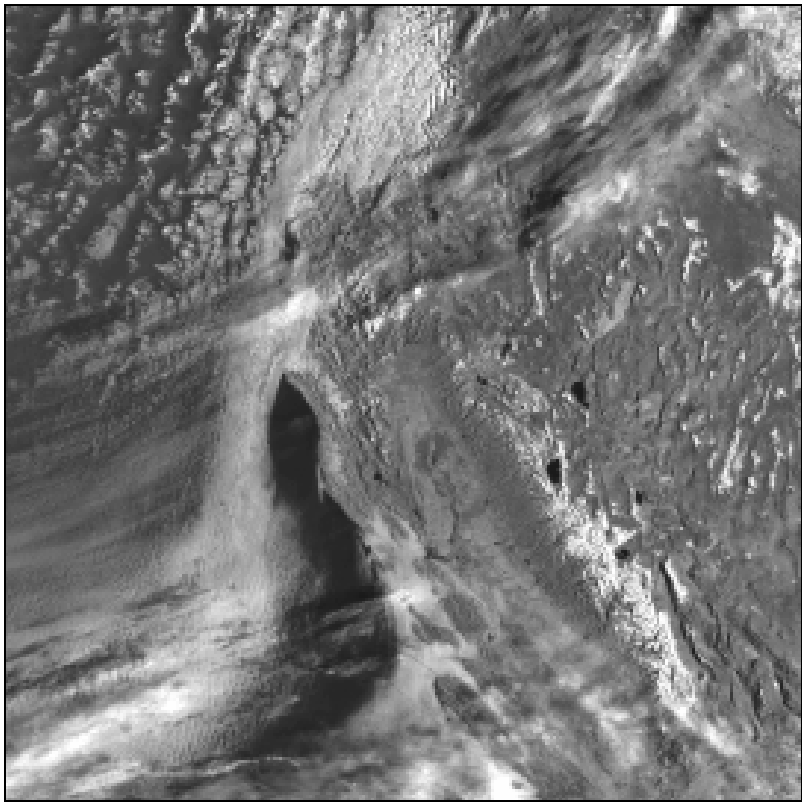

Figure 5.3. Signatures of clouds and land surfaces typical of those present in the VIIRS I2 band are seen in the NOAA-12 AVHRR channel 1 imagery collected near San Francisco, CA on February 19, 1996 (Hutchison et al., 1997(a)).

Figure 5.4 contains SeaWiFS data collected in the very narrow 0.845 – 0.885 μm band planned for the VIIRS I2 band. This scene was collected on July 13, 2001 over the Gulf of California. Notice the sharp contrast between water and land boundaries. In addition, variations in surface vegetation can be seen, especially around the Salton Sea in the upper left portion of the image. Comparisons between these data and those contained in the VIIRS 0.412, 0.488, and 0.555 μm bands show the effects of surface reflectivity upon these imagery contents.

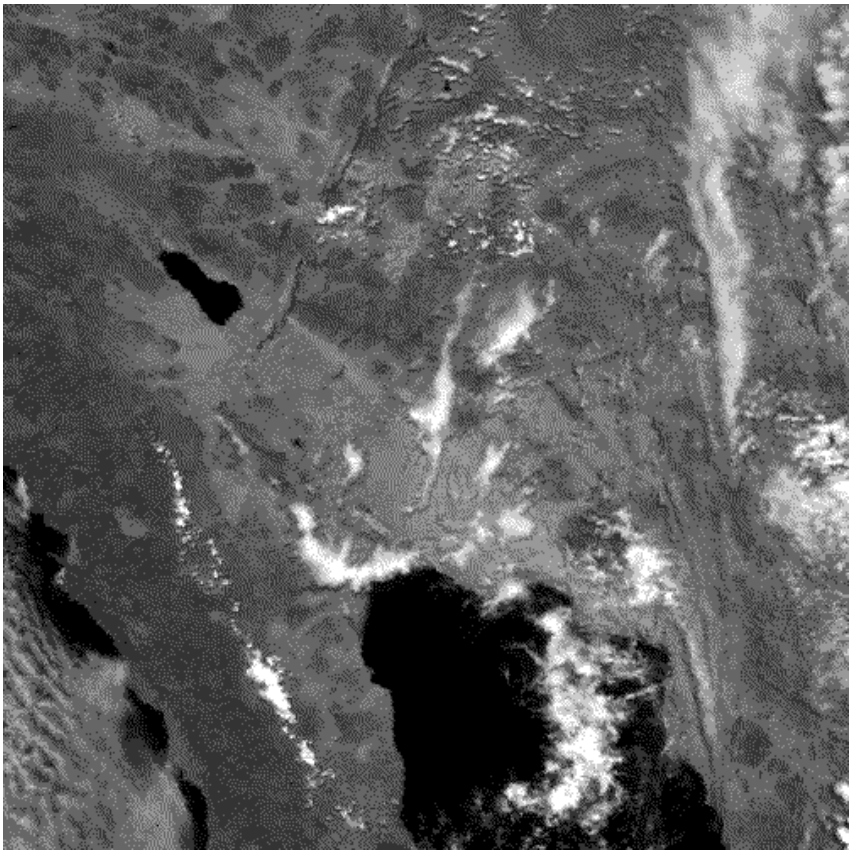

Figure 5.4. Signatures of clouds and land surfaces typical of those present in the VIIRS I2 band are seen in the SeaWiFS data collected over Southwestern US on July 13, 2001.

**Deleted:** as also shown in Figure 5.23

### 5.2.3. VIIRS I3 and M10 Bands (1.61 ± 0.03 μm)

#### 5.2.3.1. Theoretical Basis for Band Interpretation

The VIIRS I3 and M10 bands are contained within a relatively clean atmospheric window with a transmission over 90 percent. Attenuation in this band comes from the wings of water vapor absorption lines that extend into the bandpass; however, attenuation does not reach 10% in the band even in relatively humid atmospheric conditions. From Figure 4.9 it is seen that atmospheric transmission is nearly zero at 1.4 μm but rapidly increases to its maximum at about 1.58 μm where it remains until about 1.75 μm. Therefore, the region from 1.58-1.75 μm is useful for a VIIRS band.

Deleted: channel

The 1.61 μm band is most valuable for the interpretation of snow-covered surfaces due to the large differences in reflectivity between snow and other features in this band. For example, the reflectivity of snow is seen in Figure 4.9 to reach a minimum at about 1.5 μm and remain very small through 1.58 μm at which point it begins to slowly increase and reaches approximately 5% at 1.64 μm. On the other hand, the reflectance of bare soil, vegetated soil, and water clouds are significantly larger, e.g. 30-50 percent. Therefore, the contrast between snow and these features is strong in the 1.61 μm band making the I3 band very useful to confirm the presence of snow when used in conjunction with the I2 band where only the signature of snow changes significantly.

#### 5.2.3.2. Representative Imagery of the VIIRS I3/M10 Band (1.61 ± 0.03 μm)

The 1.61 μm band was first carried in space by the DMSP sensor in the late 1970s based upon the theoretical work of Valovcin (1978). A sensor known as the Snow Cloud Discriminator was first flown on DMSP spacecraft in the late 1970s; however, data in the 1.61 μm band were not routinely collected until NASA launched the Thematic Mapper (TM) sensor in the early 1980s onboard the Landsat Earth Resources Satellite series. NOAA launched the first operational 1.6 μm band (i.e. channel 3A or the albedo channel) on the TIROS NOAA-13 system in 1999, although due to technical reasons the NOAA satellites could only downlink either channel 3A or channel 3B (3.7 μm band) at any given time. Thus, there is a wealth of research and operational sensor data available to demonstrate the phenomenology described above. For convenience, data from the Thematic Mapper are shown in Figure 5.5 along with the 0.64 μm imagery typical of VIIRS channel I1.

Deleted: channel

Deleted: channel

Deleted: channel

Deleted: C

Deleted: C

Deleted: C

Deleted: C

Snow is readily identified in Figure 5.5 by comparing features in the 0.645 and 1.61 μm bands. Snow appears very bright in the shorter wavelength imagery and completely black in the 1.61 μm imagery. At the same time, clouds are relatively bright in both bands. Note also, the vegetation surrounding the lake region is much brighter at 1.61 μm than at 0.64 μm. From Figure 4.9 it is seen that the reflectivity of vegetated land is about 30 percent at 1.61 μm while its reflectivity is only about 5 percent in the I1 Band as seen

Deleted: channels

Deleted: wa

in Figure 4.8. All features in Figure 5.5 are in good agreement with information shown in Figure 4.8 and Figure 4.9.

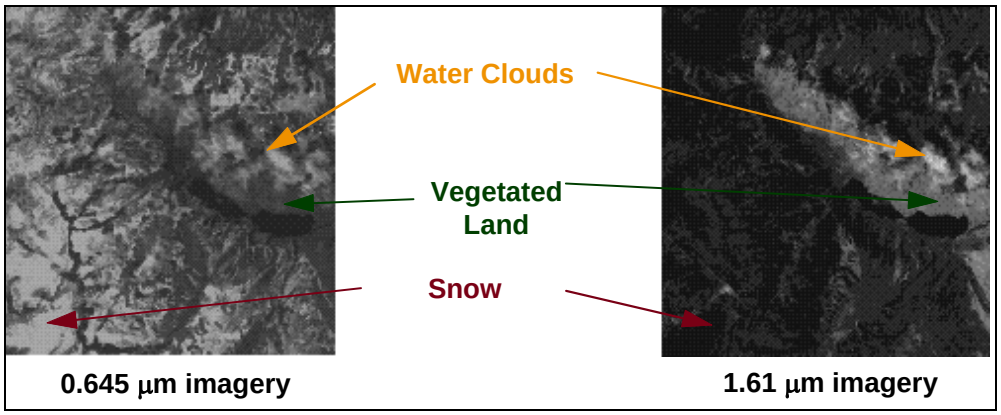


Figure 5.5. Thematic mapper data collected over the Sierra Nevada mountains show the value of 1.61 μm imagery for differentiating between water clouds (bright in both bands) and snow (black in only the 1.61 μm image).

### 5.2.4. VIIRS I4 Band 3.74 ( ± 0.19 μm) and M12 Band 3.7 ( ± 0.09 μm)

#### 5.2.4.1. Theoretical Basis for Band Interpretation

Due to the complexity of signatures within it, perhaps more information has been published in the literature about the 3.7 μm band than any other spectral band carried by meteorological satellites. Certainly, more space is allocated to 3.7 μm band in this text than any other VIIRS band. The band was originally called AVHRR channel 3 on early TIROS spacecraft but became known as channel 3B with the launch of the NOAA-13 satellite that carried the first 1.6 μm band. During the NPOESS era, the band becomes the VIIRS I4 Imagery Band with a bandpass of 3.55-3.93 μm, very similar to the original AVHRR channel 3. Highlights of information published in the literature on this bandpass are summarized in this section.

**Deleted:** channel

**Deleted:** channel

The 3.7 μm band was made a VIIRS Imagery band (channel I4) to satisfy threshold requirements for the VIIRS manually-generated cloud type EDR, i.e. the VIIRS I4 band is essential to distinguish manually between stratus and cirrus clouds in nighttime data. Information collected in the I4 bandpass is also needed at much higher signal-to-noise performance for the retrieval of other NPOESS EDRs, such as sea surface temperature – a NPOESS key EDR. Therefore, it was also necessary to include the 3.7 μm bandpass as a separate (M12) moderate resolution band since the required signal-to-noise could only be achieved at a lower spatial resolution. The M12 moderate resolution (imagery assist) band has a narrower bandpass (3.61-3.79 μm) than the I4 band to reduce the effects of global variations in atmospheric attenuation due primarily to water vapor as shown in Figure 4.10.

**Deleted:** channel

**Deleted:** band

**Deleted:** B

**Deleted:** B

Interpretation of signatures in the I4 band (3.55-3.93 μm) is more difficult than most VIIRS bands since it, as well as moderate resolution bands M12 and M13, may contain energy from two sources: the Sun and the Earth. This is seen by close inspection of Figure 5.1, which shows the normalized distribution of emission spectra for blackbodies with temperatures of 6000 K (sun) and 300 K (Earth's surface). These curves overlap in the 3-5 μm region. From Figure 4.10, it is seen that solar irradiance falls off sharply at wavelengths longer than about 4.2 μm, which correlates with an extremity of the M13 bandpass. Even though interpretation of 3.7 μm imagery may be complicated, the wealth of information that can be extracted from this band ensures it will remain most valuable throughout the foreseeable future.

**Deleted:** channels

**Deleted:** m

**Deleted:** channel

The 3.7 μm bandpass was first flown on the NOAA series of satellites to improve sea surface temperature retrievals through better atmospheric correction of attenuation caused by water vapor. Observations in two spectral bands in which water vapor attenuation was sufficiently different allowed the amount of water vapor to be estimated based upon the brightness temperature difference in the bands, assuming a priori knowledge of ocean emissivity (Anding and Kauth, 1970, 1972). It was concluded that SST retrievals with an accuracy of 1K would be possible using observations made in multiple infrared (McMillin, 1971). Soon thereafter, all AVHRR satellites also carried the long-wave, split window bands known as AVHRR channel 4 and channel 5. The relationship between total atmospheric water vapor and attenuation in AVHRR IR bands is shown in Figure 5.6. In the VIIRS sensor, the corresponding channels are I4, M15, and M16. For the M12 band, attenuation due to water vapor absorption is less than that shown in Figure 5.6.

**Deleted:** channels

**Deleted:** channels

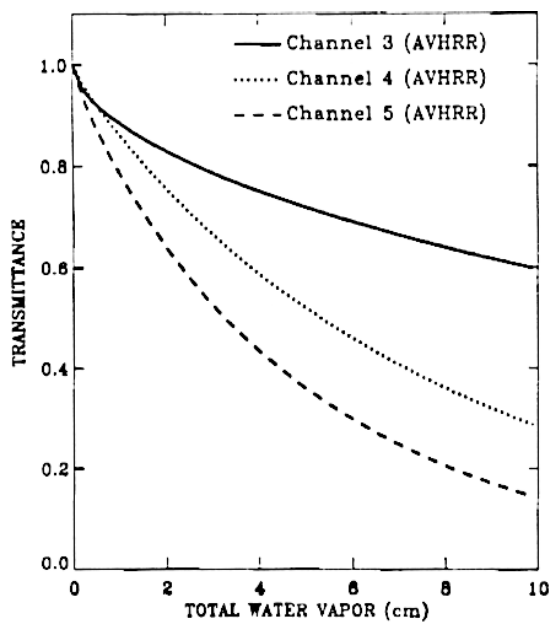


Figure 5.6. Atmospheric attenuation in AVHRR 3.7, 10.8, and 11.8 μm bands as a function of total atmospheric water vapor (Hutchison et al., 1995).

**Deleted:** IR channels

While the feasibility of retrieving improved SST fields was demonstrated soon after the launch of the AVHRR, there remained the challenge of detecting cloud contaminated pixels and removing them from the SST analyses. In particular, identifying stratus in nighttime imagery and thin cirrus in both daytime and nighttime imagery was problematic. Prior to the launch of the AVHRR, even the most sophisticated automated

cloud classification schemes, such as the RTNEPH Model developed by the United States Air Force (USAF) Weather Agency (AFWA), had difficulty detecting these clouds due to the relatively small thermal contrasts that could exist between them and their cloud-free surroundings. Therefore, significant effort was expended to correct bad analyses by highly trained satellite meteorologists who performed quality control of the automated cloud analyses by manually comparing them against high-resolution satellite imagery collected by the Operational Linescan System (OLS) flown by the Defense Meteorological Satellite Program (DMSP). The OLS collected imagery at 0.65 km resolution with a near-constant cross scan resolution and carried a photo-amplification capability that allowed visible imagery to be collected at night under conditions of at least one-quarter lunar illumination. This nighttime visible sensor is the forerunner to the VIIRS Daytime/Nighttime Visible (DNB) imagery channel (c.f. Section 5.2.6). However, the positive identification of nighttime stratus clouds by human analysts continued to be very difficult.

Deleted: I

The automated detection of clouds, especially nighttime stratus and thin cirrus clouds, was greatly enhanced using the multiple spectral bands carried by AVHRR. Bell and Wong (1981) demonstrated that the contrast between nighttime stratus and ocean surfaces was greatly enhanced in the brightness temperature difference field which is created by subtracting the AVHRR 3.7 μm brightness temperatures from the AVHRR 11.0 μm brightness temperatures, i.e. ($T_{11.0}$ - $T_{3.7}$). The increased contrast resulted from differences in emissivity of stratus clouds at these two wavelengths, not in the blackbody temperatures of the cloud and surrounding background. Stratus clouds have an emissivity of about 0.8 at 3.7 μm but nearly 1.0 at 11.0 μm. Based upon Equation 4.3, this difference in emissivity results in a nearly 20 percent difference in the energy measured in these two bands. Thus, brightness temperatures of stratus in the 3.7 μm band are as much as 4 K colder than in the 11.0 μm band.

The impact of undetected cirrus clouds on SST analyses is more critical than stratus due to the colder radiating temperatures and variations in transmissivity of these clouds. Inoue (1985) demonstrated that the contrast between cirrus and its surroundings could be greatly enhanced by looking at the feature $T_{11.0}$ - $T_{12.0}$ in a composite of two AVHRR images. Saunders and Kriebel (1988) summarized and extended the work of numerous earlier investigations in a new formalism that exploits bi-spectral methods for improved cloud masking for SST analyses. From this point forward, multispectral analyses became the fundamental technology used in the meteorological analysis of remotely-sensed satellite data. More recently, the increased value of using a bi-spectral test based upon the 3.7 μm and 12.0 μm bands was demonstrated to further improve the capability for automated thin cirrus detection (Hutchison et al., 1995; Stowe et al., 1991).

Deleted: channels

Snow-cloud discrimination became another very useful application for the 3.7 μm imagery. As seen in Figure4.10, the reflectivity of snow is nearly zero in the 3.7 μm band. In fact, its reflectivity is even smaller in the I4 band than it is in the 1.6 μm region. Therefore, it was believed that accurate snow maps could be generated from daytime AVHRR channel 3 data if the thermal or terrestrial radiation in the observed radiance could be isolated and removed from the solar component. Initial attempts proved successful in differentiating between snow and water clouds; however, the presence of cirrus (ice) clouds was problematic (Allen et al., 1990). Subsequently, a different

Deleted:

Deleted: 26

approach was taken to segregate the thermal and solar components of the 3.7 μm band for snow and cloud detection by producing the channel 3.7 μm albedo image (Hutchison et al., 1997a). Note that we refer to this derived image as the channel 3.7a so as not to confuse it with the AVHRR 3.7A channel, which is collects data in the 1.6 μm bamd. This new approach simultaneously enhanced the signature of thin cirrus clouds and suppressed the signature of snow making it possible (1) to differentiate water clouds from snow, (2) to differentiate snow from ice (cirrus) clouds, and (3) to differentiate water clouds from thin cirrus clouds, although some ambiguity exists for cirrus clouds with larger optical depths (Hutchison et al., 1997b). If fact, the procedure even allowed snow to be manually classified in the presence of overcast thin cirrus clouds using only signatures in the solar bands rather than thermal infrared bands (Hutchison and Locke, 1997).

Numerous additional applications have been developed for data collected in the 3.7 μm band, including (1) forest fire detection and (2) retrievals of cloud optical depth and cloud effective particle size to name a few. In addition, other phenomenology effects on 3.7 μm signatures have been described in the reference materials (Scorer, 1990, Chapter 5, Cracknell 1997, Chapter 6).

**Deleted:** currently the AVHRR

**Deleted:** channel

**Deleted:** channels

**Deleted:** longwave

**Deleted:** channels

**Deleted:** with

**Deleted:** channel

### 5.2.4.2. Representative Imagery of VIIRS I4 Band (3.74 ± 0.19 μm)

The phenomenology contained in the 3.7 μm band is now demonstrated with sample imagery. By convention, data collected in the 3.7 μm band is described in terms of brightness temperature since albedo is meaningless unless the emitted thermal radiances is removed from the signature. In general, warmer surface temperatures produce more energy at the sensor than colder temperatures. Digital data generated by the sensor associates larger amounts of energy with higher digital values and smaller amounts of energy with lower digital data. In visible and near-infrared bands, the highest digital values are conventionally represented as white and the lowest digital values appear as dark or black. Thus in visible and near-infrared band images the clouds, which are bright, appear white. Since most satellite analysts prefer to see "white" clouds, thermal infrared data are typically displayed in the inverted mode, i.e. colder temperatures, with lower digital values, appear brighter than warmer temperatures, with higher digital values. This is the opposite way from the way that the visible and near-infrared data are displayed Thus, warmer radiating surfaces appear darker in inverted IR imagery because they produce higher energy levels at the sensor. Conversely, colder radiating temperatures produce smaller energy levels at the sensor and appear brighter in imagery displayed in the inverted mode.

**Deleted:** channel
**Deleted:** channel
**Deleted:** imagery
**Deleted:** .
**Deleted:** t

Confusion can arise in the display of 3.7 μm imagery because the total radiance consists of a thermal emission and a solar reflection terms. Unlike the normal situation with shorter wavelength radiation (visible and near-infrared) in which the amount of energy scattered by water clouds increases with particle size, in the 3.7 μm band, the energy scattered by water clouds increases as the particle size decreases. Therefore, solar radiation in the 3.7 μm band is totally absorbed by large ice particles and cumuliform water clouds (Scorer, 1990). On the other hand, solar energy scattered to the sensor increases for stratiform clouds that have smaller droplet sizes. Thus, low-level (warm) stratiform clouds appear most bright and high-level (cold) ice clouds appear most dark when 3.7 μm imagery is displayed in the inverted mode. Detailed discussions follow on the signatures in the 3.7 μm band.

**Deleted:** channel

#### 5.2.4.2.1. Sun Glint and the Absence of Sky Light

There is a 'blip' in the curve of the refractive index of water that overlaps the VIIRS I4 band of wavelengths. This blip has the effect of producing a very strong reflected beam when radiation in the 3.7 μm imagery band impinges on a water surface, including oceans and inland lakes. (Scorer, 1990) No similar effect is indicated with ice. The reflection can be so bright at low angles of incidence, such as occur towards the eastern horizon for the early morning satellite or the western horizon of the afternoon satellite, that it may be possible to saturate most radiometers. No detail is available in the area of such strong sun glint unless the sea is quite rough. Conversely, when the sea is rough in an area of very bright glint, it is darkened.

**Deleted:**

In the region of sun glint on the surface of the sea, the sun appears as a very bright source of 3.7 μm radiation in an otherwise very dark sky, much as it appears on the moon due to

**Deleted:** sea

an absence of sky light. Thus, illumination in the band results from direct sunshine and shadow areas are very dark. Evidence of the absence of skylight is seen in very sharp boundaries on the dark shadows that cirrus projects onto layers of lower clouds (Scorer, 1990). The terminator (which is the boundary of direct sunshine) is very difficult to identify in the 3.7 μm band because the thermal emission from the surface and clouds is comparable with the weak sunshine in such areas. For example, it is easy to view clouds and some shadows in the I2 band for an area deep into regions where the Sun has not yet risen or has long since set due to illumination from the atmosphere above the cloud. But in the 3.7μm band, no such shadows are seen and as clouds are located further toward the nighttime areas, only the sun-facing edges of progressively higher clouds show any illumination. The lack of skylight coupled with simultaneous emission of thermal energy creates imagery that appears completely different from that seen in any other band (Scorer, 1990). Examples are shown from the early morning NOAA AVHRR scene contained in Figure 5.7. These data show an extensive area of sun glint surrounding Florida with the terminator located near the left-bottom corner of the scene.

Deleted: ,

Deleted: than

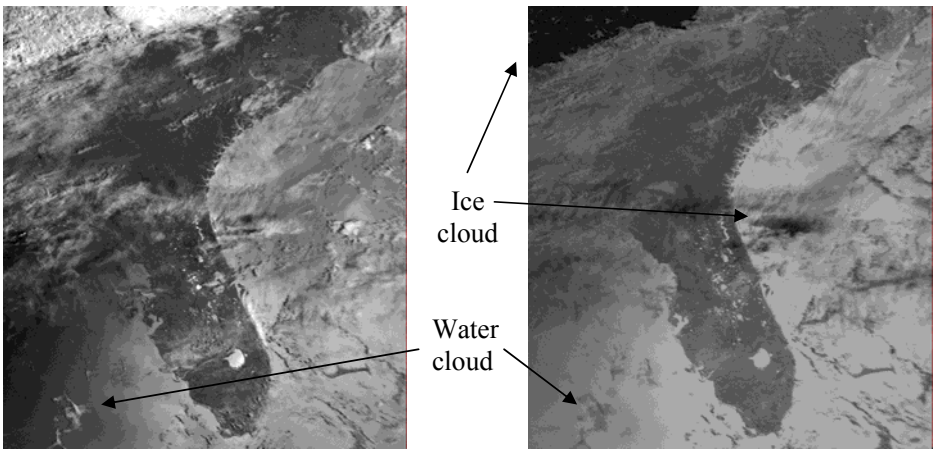


0.845 μm band 3.74 μm band

Figure 5.7. Sun glint in AVHRR channel 2 and channel 3 bands of NOAA-15 mission over southeastern United States.

Deleted: Sunglint

Deleted: C

Deleted: C

Notice in Figure 5.7 that land and cloud-free ocean features appear similar in both AVHRR channels 2 (0.845 μm band) and 3 (3.7 μm band). Water surfaces appear very bright with sun glint occurring on most of these surfaces. However, clouds appear very different in these two spectral bands. Dense clouds in the upper left-corner appear very bright in the channel 2 imagery but black in channel 3. Also, note that in the channel 2 imagery shadows are cast from the high clouds upon lower clouds just east of Cape Canaveral but no shadows are seen in channel 3 owing to the absence of skylight. This region simply appears black due to the strong absorption by large particles in this region of thunderstorms. At the same time, cumulus "streets" running in a north-south direction over land west of the Cape appear bright in both bands while similar clouds in the lower left-corner of the image are more bright toward the center in channel 2 but more dark toward the center in channel 3. In channel 2, the thickest part of the cloud produces the brightest signature because this part of the cloud is most highly reflective to the source of

Deleted: C

Deleted: C

Deleted: Channel

Deleted: sunglint

Deleted: C

Deleted: C

Deleted: C

Deleted: C

Deleted: C

Deleted: C

Deleted: C

radiation which is the direct rays of the Sun. In channel 3, the thickest part of the cloud is most dark because these particles strongly absorb solar radiation and in this case, in the absence of skylight, the source of radiation is the reflected solar energy from the ocean's surface. Thus, the centers of the clouds must attenuate solar energy more strongly than the edges in order for the centers to appear more dark and the edges more bright.

Deleted: C

The combined effects of the absence of skylight and presence of sun glint in 3.7 µm satellite imagery are summarized as follows. Together these effects make clouds appear as though the human were viewing the clouds in direct sunlight from the Earth's surface (Scorer, 1990). The thickest part of a water cloud appears darkest because less energy from below penetrates them. The thinner parts of a water cloud appear brighter because the sun's energy reflected from the ocean surface is transmitted through them. Cirrus clouds, however, appear black because these large particles strongly absorb energy in the 3.7 µm band whether its source is sky radiation from above or reflected solar energy from the ocean below.

Deleted: sunglint

Deleted: most

#### 5.2.4.2.2. Nighttime Stratus Clouds

As noted earlier, the accurate detection and typing of nighttime stratus requires the use of data in the 3.7 µm spectral band. Before data were available from the 3.7 µm region, nighttime stratus was difficult to detect using the thermal infrared 10-12 µm bands because the Earth's surface temperature is often nearly identical to the cloud top temperature. The contrast between nighttime stratus and the ocean surface temperature is greatly enhanced in the 3.7 µm band due to differences in emissivities between stratus clouds and the ocean surface. As noted in Equation 4.3, there are three primary factors that determine the amount of IR radiation arriving at the VIIRS sensor: emissivity of the surface, blackbody temperature of the surface, and transmission of the atmosphere across the bandpass. Thus a difference of 20 percent in emissivity between the cloud-free surface skin temperature (1.0) and the stratus cloud (0.8) results in as much as 4 K difference in brightness temperature between these features when viewed in the 3.7 µm band.

Deleted:

Deleted: channel

The NEΔT performance estimate for VIIRS band I4 is 0.92 K for a source brightness temperature of 270 K. Thus, we expect the difference in emissivity between the stratus cloud and the cloud-free ocean surface to be sufficient to allow the clouds to be detected and identified in the VIIRS I4 band. This is demonstrated in the AVHRR imagery shown in Figure 5.8.

Figure 5.8 contains an extensive area of stratus that is routinely found off the coast of San Francisco, especially during the summer. In the right panel is shown data collected in the longer wavelength IR band typically available on most instruments, even before the launch of AVHRR. This particular image contains AVHRR channel 4 which is centered near 11.0 μm. Brightness temperatures of water surfaces are shown for Lake Tahoe at 18.6 $^{0}$C since the ocean was completely cloudy. The stratus temperature is 11.0 $^{0}$C in the same band. On the other hand, the brightness temperature in the 3.7 μm band is 1.1 K warmer for cloud-free Lake Tahoe but 5.4 K colder for the stratus cloud. Since Lake Tahoe is rather high in the Sierra Nevada mountains, atmospheric attenuation due to water vapor (shown in Figure 5.6) causes the 1.1 K difference in brightness temperatures between these bands while the variation in surface emissivity causes the 5.4 K difference in these bands in the stratus cloud brightness temperatures. Certainly, the difference between brightness temperatures for stratus is explained primarily by the difference in emissivity of the stratus at these two wavelengths. The leading edge of the stratus cloud is clearly seen extending into the San Joaquin Valley in the 3.7 μm imagery while the same edge is not distinct in the 11.0 μm band.

**Deleted:** the long wavelength

**Deleted:** channel

**Deleted:** C

**Deleted:** n

**Deleted:** channel

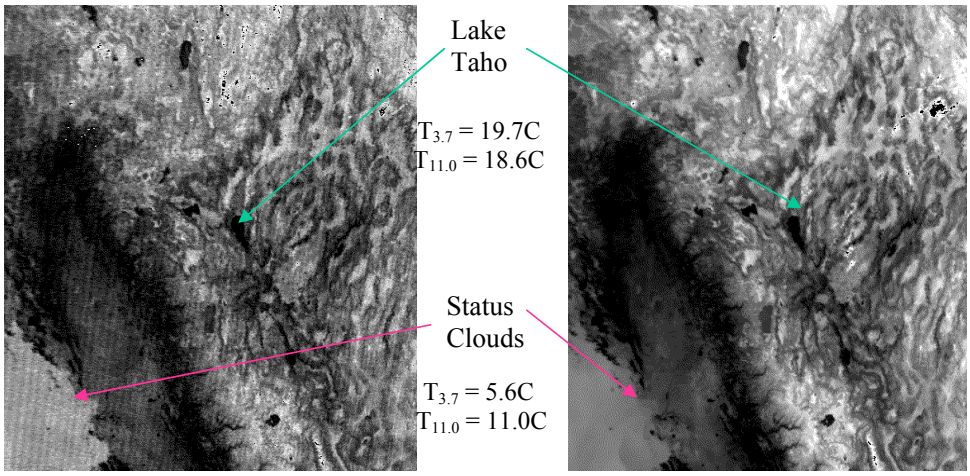


3.74 μm band 11.0 μm band

Figure 5.8. Stratus over San Francisco Bay and coastal California in nighttime 3.7 μm and 11 μm imagery collected by NOAA-14.

#### 5.2.4.2.3 Snow/Cloud Discrimination

Figure 5.9 demonstrates the challenge of differentiating between snow and clouds in AVHRR imagery using only bandpasses similar to the VIIRS I1 and I5 channels. The scene is from NOAA-14 collected at 2:20 PM PST [2220 GMT] on December 18, 1996. It covers the same area described in Figure 5.2. The three images are from AVHRR channels 1, 3, and 5, which are similar to VIIRS I1 band at 0.64 μm, I4 band at 3.74 μm, and I5 band at 11.5 μm. An extensive area of stratus is seen in the San Joaquin Valley, in the center of the 0.64 μm band, nearly parallel to the snow-covered Sierra-Nevada Mountains. In the 3.75 μm band, ice clouds appear white along with snow while thicker [colder] cirrus appears brighter in the 12.0 μm band. It is apparent from these images that the spectral signatures of cirrus clouds and snow are similar in all the AVHRR channels and differ only in relative strength. Thus, while the dendritic pattern in channel 1 makes snow along the mountains relatively easy to recognize, other snow-covered areas are difficult to identify with certainty.

Deleted: channel

Deleted: C

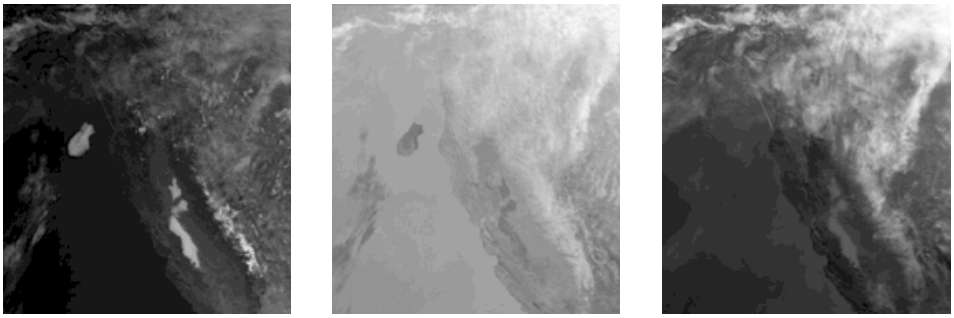

**0.64 μm** **3.7 μm** **12.0 μm**

Figure 5.9. Channels 1,3, and 5 of NOAA-12 imagery collected at about 7:05 AM PST on March 19, 1996 over western United States and Pacific coastal regions.

The solar and thermal components of the I4 band can be segregated into two distinct images that are highly useful for several applications, including snow-cloud discrimination and cloud top phase classification, as discussed in the next section. The former is most valuable for differentiation between snow and ice clouds. It is also useful for detecting water clouds and snow in the absence of 1.6 μm data, which could result from VIIRS sensor degradation. Analysis of cloud phase is useful for the vertical placement of clouds in the atmosphere, since ice clouds are typically higher in the atmosphere than water clouds. A brief overview of the procedure used to create two spectral bands is provided next.

The 3.7 μm daytime albedo (reflectance) image, i.e. channel 3a, can be created by modifying the observed VIIRS radiances for thermal emissions and converting the resultant values into albedo as follows. First, the 12.0 μm brightness temperature of each pixel is calculated, using Equation 4.3, by inverting the Planck function, shown in

Equation (5.1), after the top of the atmosphere radiance is divided by the atmospheric transmission. Atmospheric transmission is taken from the curves shown in Figure 5.6 using a priori knowledge of total water vapor, e.g. from conventional weather data or a numerical forecast model. Next, the thermal emission in the 3.7 μm band is calculated using the Planck function for the skin temperature of each pixel and attenuated to space. The calculated radiance in the 3.7 μm band is then subtracted from the measured radiance in the 3.7 μm band, leaving a useful approximation to the reflected solar energy component in the 3.7 μm band. This energy is converted to albedo by dividing by the fractional solar radiance at the top of the atmosphere for each pixel, as shown in Equations (5.8) and (5.9). The resultant albedos or reflectances values have been called the "derived" channel 3a image. (Again, note that the derived 3.7 μm albedo image should not to be confused with the 1.6 μm band designed as channel 3A in the TIROS series satellites.)

**Deleted:** C

While the procedure used to separate the thermal and solar components of 3.7 μm radiation provides only an estimate of the albedo in each pixel, the derived 3.7 μm albedo channel has proved to be adequate for creating manual and automated snow masks in complex scenes. (Inaccuracies in knowledge of cloud top temperatures, especially of thin cirrus clouds, and the assumption that surface emissivity does not vary between the two bands makes this a gross correction.) The reason only an estimate of the actual solar component is valuable can be seen by examining Figure 4.9 and Figure 4.10 which show that the reflectivity of snow in the 3.7 μm region is actually smaller than in the 1.61 μm band. Figure 4.10 shows that the reflectance of snow in the 3.7 μm band is extremely small, especially when compared to the 0.64 μm band for example, which means that an approximate measure of the 3.7 μm albedo can be useful for identifying surfaces that are snow-covered.

**Deleted:** channel

Figure 5.10 shows the 3.7 μm imagery and derive 3.7 μm albedo component of the scene contained in Figure 5.9. Notice that in the "albedo" image, snow covered regions of the Sierra Nevada mountains are dark, indicative of very low reflectance values. Also note that the long, narrow stratus cloud in the San Joaquin Valley of California has been changed from dark in the 3.7 μm image, which indicates a warm cloud, to bright in the derived albedo image, indicating high reflectivity. Finally, notice that the thin cirrus clouds present over much of the image in the 12.0 μm band, shown in Figure 5.9, are more visible in the albedo image shown in Figure 5.10. Thin cirrus is more pronounced in the 3.7 μm albedo image because it is essentially a 3.7 μm minus 12.0 μm brightness temperature difference field, which is known to enhance the signature of cirrus clouds. Thus, the derived 3.7 μm imagery is useful for snow detection and cirrus cloud classification.

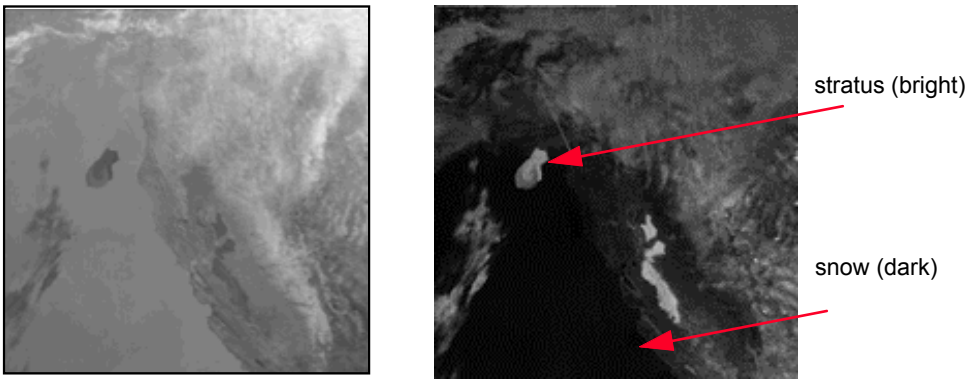


3.7 μm imagery

3.7 (albedo)μm
"derived" channel

Figure 5.10. NOAA-12 scene collected at about 7:05 AM local PST (1505 GMT) on March 19, 1996 over western United States and Pacific coastal regions (Hutchison and Locke, 1997).

#### 5.2.4.2.4 Application of 3.7 μm Imagery for Cloud Top Phase Classifications

As previously seen, the derived channel 3a imagery provides valuable information for the discrimination of clouds and snow covered surfaces. In addition, these data are useful for the determination of cloud top phase, since thin cirrus clouds in the albedo component of this band are enhanced while water clouds signatures are not. However, care must be taken when attempting to determine cloud top phase due to ambiguities in the spectral signature of ice clouds.

Examples of cloud phase signatures are seen in Figure 5.11(a), (b), (c), and (d) which contain daytime AVHRR channels 1, 3, 5, and derived channel 3a respectively and show two large areas of highly reflective, cold clouds surrounded by lower-level clouds in a NOAA-12 scene collected at 7:58 AM (1558 GMT) on March 12, 1996. The location of these data are the same as those in the previous section.

Deleted: C

Deleted: C

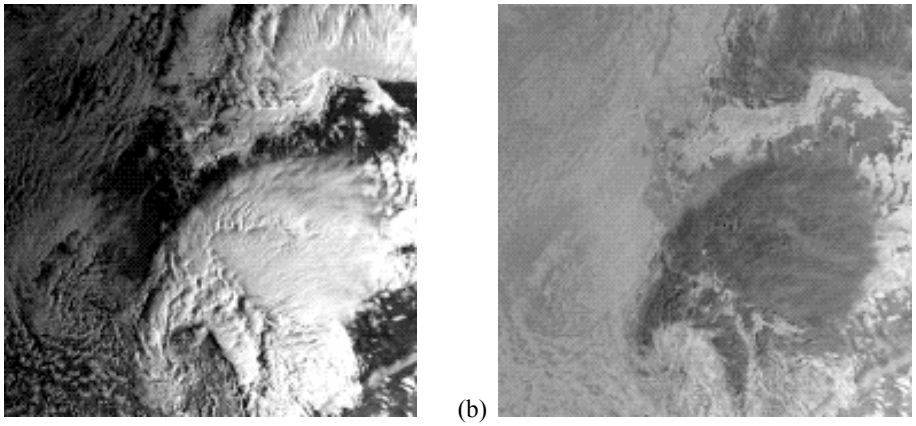

(a) (b)

(a) Two highly reflective cloud patterns are seen in AVHRR channel 1, and (b) many of the cloud tops are glaciated as seen in channel 3. Numerous water clouds are also present

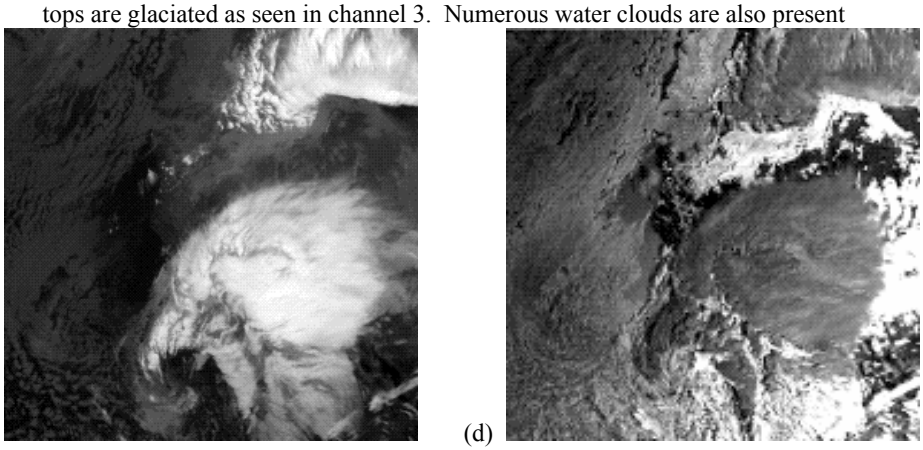

(c) (d)

(c) The coldest clouds approach -55C in channel 5 and (d) appear very dark in the derived channel 3a, while thin cirrus clouds in the lower right corner appear much brighter in channel 3a.

Figure 5.11. NOAA-12 scene collected at about 7:58 AM local (1558 GMT) on March 12, 1996 over western United States and Pacific coastal regions (Hutchison et al., 1997(b)).

Data in both AVHRR channel 3 and the derived channel 3a images show a large, comma-shaped system that has glaciated tops evidenced by very dark signatures where cloud top temperatures are observed to be as low as –53 $^{0}$C in channel 5. (Water droplets become glaciated in a vacuum at –40 $^{0}$C according to the theory of homogeneous nucleation. Water droplets may freeze at warmer temperatures due to nucleation particles in the atmosphere but all droplets become ice at temperatures of –40 $^{0}$C or less.) In addition,

Deleted: -

Deleted: T

Deleted: H

Deleted: N

many cloud elements surrounding the coma-shaped cloud pattern appear to be water clouds (bright in channel 3 and much warmer in channel 5).

However, the spectral signatures of ice clouds can be ambiguous when both thick and thin cirrus appear in the same scene. This is illustrated in Figure 5.12(a) and Figure 5.12(b) which magnifies the lower-right corner of channel 5, shown in Figure 5.11(c), and the derived channel 3a, in Figure 5.11(d), respectively. In Figure 5.12(b), glaciated cloud tops are present at point (a) where the channel 3a signatures appear black. However, clouds in the vicinity of (b) appear very bright which suggests the possibility that these cloud tops are composed of liquid water. Upon examining the shadows that these clouds cast onto the adjacent high, cold clouds, seen in Figure 5.11(a), it becomes apparent that the clouds at point (b) are actually high clouds, i.e. thin cirrus. Thus, the cloud top phase of pixels between points (a) and (b) is ambiguous, since cloud emissivity transitions from larger to smaller values as indicated by the cloud signatures changing from dark to light in Figure 5.12(b).

Deleted: C

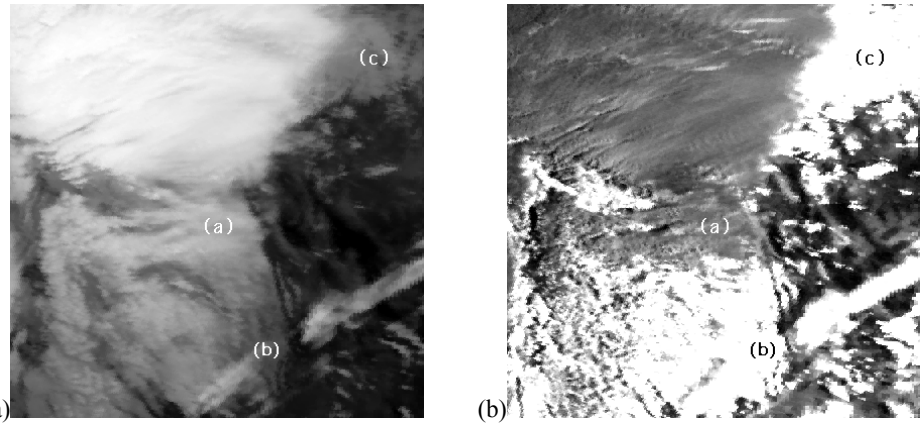


(a) (b)

Figure 5.12. Ambiguities in spectral signatures can impact a-priori cloud top phase analyses of this NOAA-12 AVHRR scene collected at 1558 GMT on March 12, 1996. Zooming in on the lower-right quadrant of channel 5, (a), and channel 3A, (b), shows the difficulty in manually classifying cirrus since ice appearance changes as optical thickness decreases from (a) to (b) (Hutchison et al, 1997).

Ambiguity is also seen in cloud signatures along the right side of the scene in the brightest part of channel 3a, shown at point (c) in Figure 5.12(b). With the Sun near the horizon, energy reflected off water clouds overwhelms the normal poorly reflective signature of the ice in channels 3 and 3A, which makes the cirrus transparent in these data. In addition, the signature of these very thin cirrus clouds over the lower-level water clouds is not distinct in channel 5, at point (c) in Figure 5.12(a). Thus, it is difficult to determine precisely the edge of the thin cirrus shield in any of these AVHRR channels.

Deleted: of

Theoretical calculations demonstrate the reason for the variations observed in the AVHRR 3.7 μm albedo channel for ice clouds. Figure 5.13 shows simulated nighttime 3.7 μm minus 12.0 μm brightness temperature differences for cirrus clouds having a temperature of 236 K, versus optical thickness for ice particles of different sizes in a mid-latitude summer atmosphere. (Recall that the 3.7 μm albedo signature is in fact identical to the $T_{3.7}$-$T_{11.0}$ field.) The results show that the $T_{3.7}$-$T_{11.0}$ feature approaches a maximum of about 20 K at a small optical thickness of about unity. However, the brightness temperature difference field changes dramatically as optical depth increase or decreases. Cirrus optical depths generally fall within the 0.05 – 10 range. Figure 5.14 shows results from additional nighttime simulations of the $T_{3.7}$-$T_{11.0}$ feature versus AVHRR channel 4 brightness temperature for a cirrus cloud with a 10 km base and variable channel 3 emissivities (thickness') in a sub-Arctic winter atmosphere. These data show that the $T_{3.7}$-$T_{11.0}$ feature remains rather large even in a relatively cold, dry atmosphere. Both panels confirm that the $T_{3.7}$-$T_{11.0}$ feature starts small but increases as the emissivity or optical thickness of the thin cirrus cloud increases then drops rapidly as the cloud becomes more optically thick and its radiative characteristics approach that of a blackbody. Thus, it is this thermal signature feature against the poorly reflective snow background that makes the presence of the very thin cirrus clouds readily detectable in the channel 3a image but it is the potential for large variations in the brightness temperature difference field that can make the classification of cirrus clouds difficult.

Deleted: C

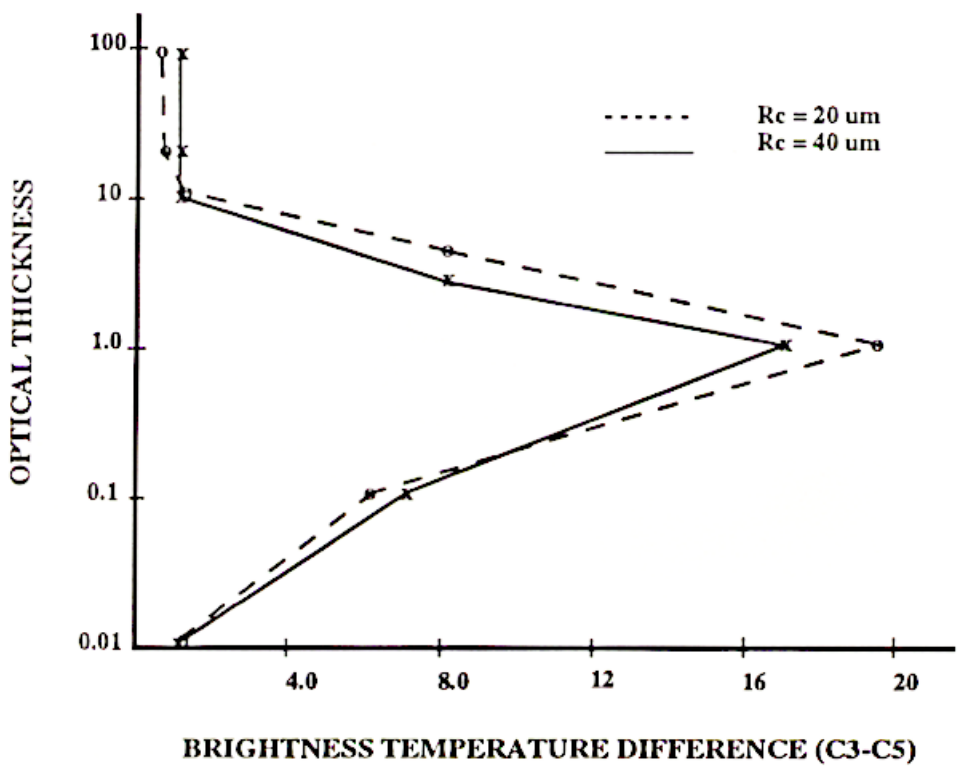

Figure 5.13. Simulated AVHRR ($T_{3.7}$-$T_{11.0}$) brightness temperature difference versus optical thickness of cirrus in mid-latitude winter atmosphere with cloud temperature of 236 K and radii of 20 and 40 microns (Hutchison et al., 1997).

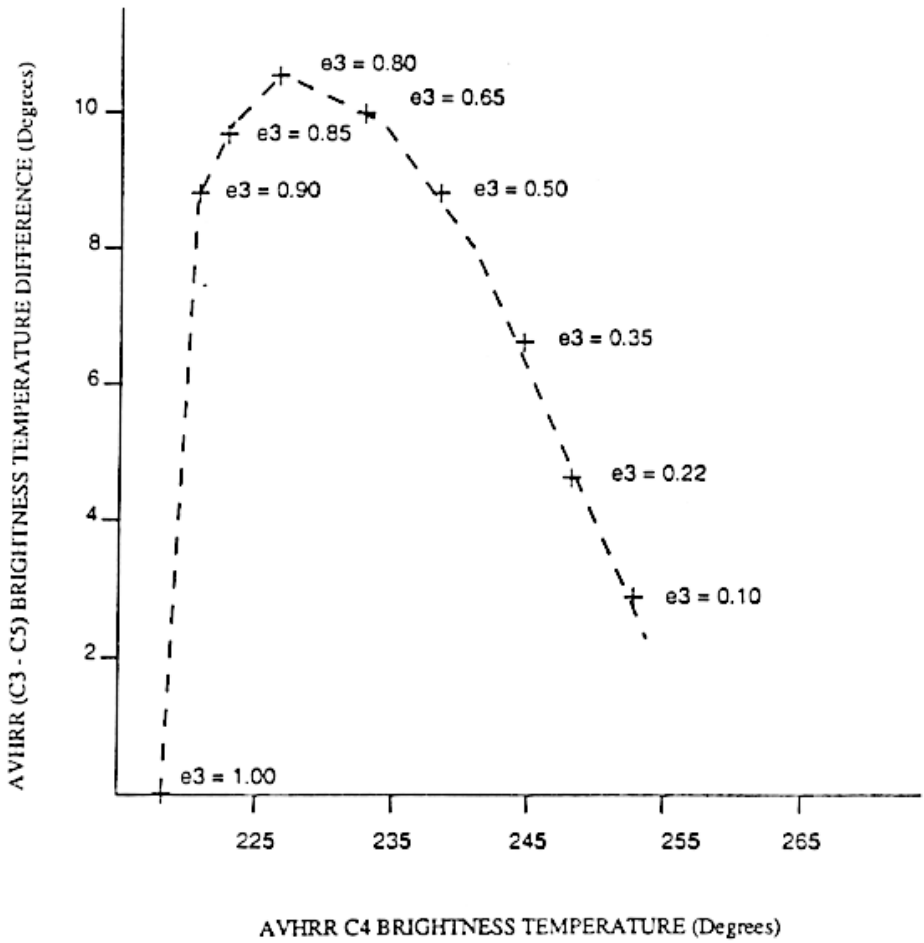


Figure5.14. Simulated AVHRR (channel 3 minus channel 5) brightness temperature difference versus channel 4 temperature for cirrus of variable emissivity (e) at 10 km in sub-arctic winter atmosphere (Hutchison et al., 1997).

#### 5.2.4.2.5 Forest Fires

Forest fires burn at great intensity with temperatures in the 500-1000K range which means their wavelength of maximum emission occurs in the 3-5 µm region as shown in Figure 5.1. Therefore, these fires are readily observed in the 3.7 µm spectral bandpass. Figure 5.15 and Figure 5.16 contain several examples of forest fires in NOAA-12 imagery collected at 2319 GMT on May 11, 2000.

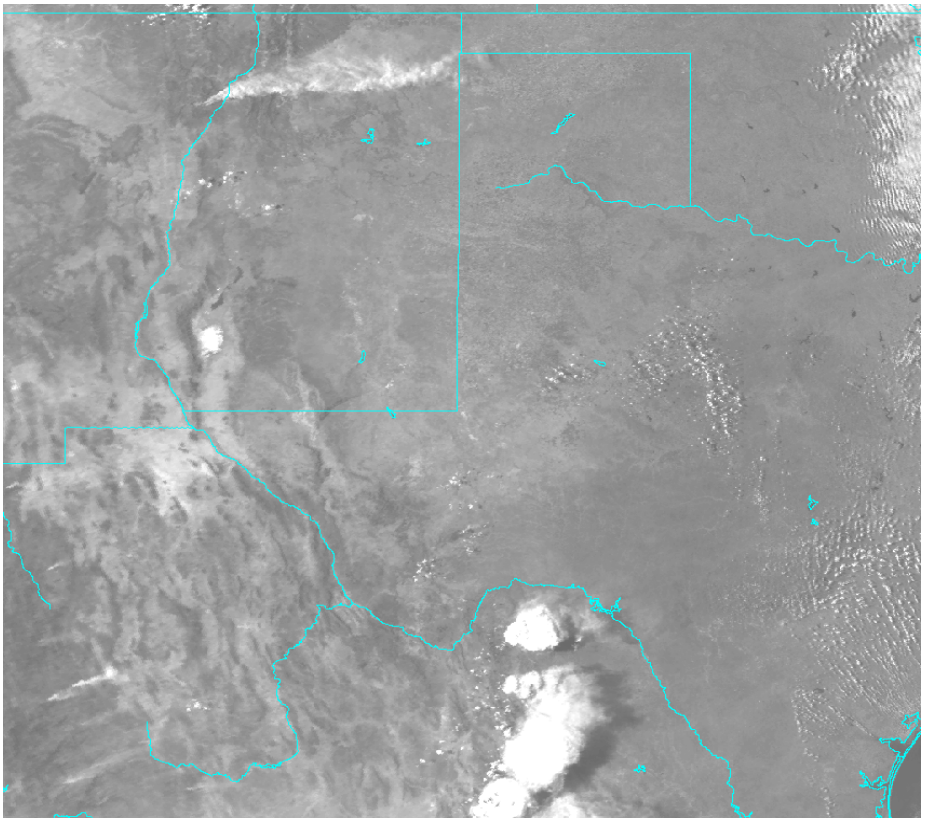

Figure 5.15. Smoke plumes from several forest fires (including the one near Los Alamos, New Mexico) are evident in channel 2 of the NOAA-12 AVHRR scene collected at 2319 GMT on May 11, 2000.

Deleted: C

Most evident in Figure 5.15 are the thunderstorms just south of the Rio Grande River near Big Bend National Park in Texas. Next, a large plume of smoke is seen originating from an apparent point source near Los Alamos, New Mexico. The US news services carried extensive coverage of this fire since it was intentionally set alight by the US Forestry Service to clear brush as a means of reducing the risk of fires during a particularly dry period in the southwestern US due to several years of drought conditions. Less obvious are several plumes in the mountains of Mexico, seen in the lower-left corner of the scene.

The 3.7 µm band is particularly valuable for detecting "hot spots", that appear black in Figure 5.16, in the early stages of the forest fire evolutionary cycle. In particular, these data can be used to identify potential forest fires before they become sufficiently large to generate a smoke plume that is visible in the shorter wavelength bands, as shown above in Figure 5.15.

Deleted: channel

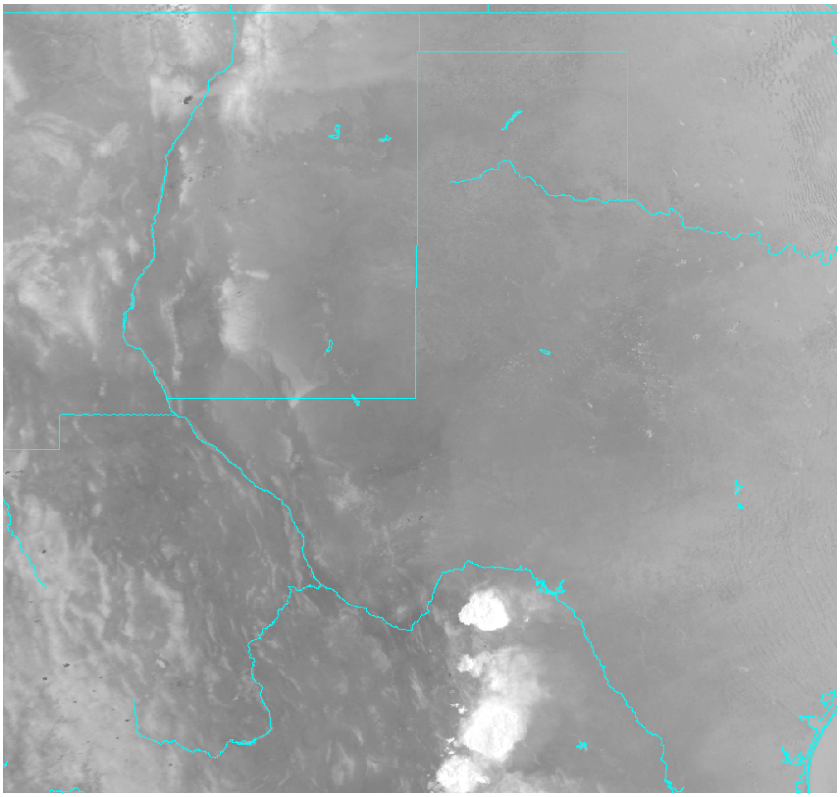

Figure 5.16. Hot spots in the forest fires are evident in channel 3 of the NOAA-12 AVHRR scene collected at 2319 GMT on May 11, 2000. Several in the mountains of Mexico show no plumes.

Deleted: C

The hot spot associated with the fire near Los Alamos, New Mexico is clearly visible as a large black spot in the 3.7 µm imagery shown in Figure 5.16. In addition, 4-5 smaller hot spots can be seen in the mountains of Mexico and upon careful inspection, two other black spots are seen north and west of the most northern thunderstorm. These two hot spots are associated with a forest fire that burned for several days in the Glass Mountains of West Texas. While the Cerro Grande fire at Los Alamos received national attention, the Cook Ranch fires went unnoticed by most. However, this particular fire ultimately scorched more than 47,000 acres of timber and came dangerously close to natural gas wells near Odessa, Texas. More insight into the value of 3.7 µm imagery for detecting forest fires is found in the VIIRS Active Fires ATBD *[Y3252]*.

## 5.2.5. VIIRS I5 Band (11.45 ± 0.95 μm)

### 5.2.5.1. Theoretical Basis for Band Interpretation

The VIIRS I5 imagery channel has a heritage in both the AVHRR channel 4 and channel 5 infrared bands. It has a broad bandpass that contains the combined information of the M15 and M16 moderate resolution bands but at the VIIRS Imagery resolution of 371 m at nadir. For those more familiar with DMSP, the VIIRS I5 imagery could be considered very similar to an enhanced DMSP OLS thermal fine band. Additionally, VIIRS M15 and M16 bands are very similar to AVHRR channels 4 and 5. Spectral signatures in these bands are shown in Figure 4.11.

While the I5 channel is useful for manual detection of cloud with temperature much colder than the radiating surface, such as cirrus, it is also critical for the manual analysis of the cloud types defined in Section 3.3. Many of the requirements for manually-generated cloud types are based simply upon cloud height, e.g. stratus versus altostratus, stratocumulus versus altocumulus. A deficiency is that actual cloud type classifications were created from surface observations that refer to the altitudes of cloud bases, while satellite observations refer to cloud top heights.

Therefore, a primary goal of manual cloud typing is to identify accurately the cloud top height for the quality control process described in Section 3.4. The VIIRS I5 band is unique for this task since the emissivity of water droplets, bare soil, and vegetated soil are more close to unity in the VIIRS I5 channel, as seen in Figure 4.11, than in any other spectral bandpass. Since emissivity is nearly unity for many features, brightness temperature can be readily correlated with skin temperature after correcting for atmospheric attenuation due to water vapor concentration along the line-of-sight between the feature and the VIIRS sensor. (Cirrus clouds are the exception since the emissivity of cirrus continues to be highly variable in this and all VIIRS bands.) As shown in Figure 4.11 above and Figure 5.6, atmospheric transmittance in the I5 Imagery band is reduced substantially by water vapor absorption. Water vapor above the cloud top absorbs some of the energy emitted by the cloud and re-radiates energy at a lower temperature, due to the lapse rate in the atmosphere, i.e. temperature generally decreases with increases in altitude throughout the troposphere. Thus, the VIIRS sensor receives less energy from a cloud in a humid atmosphere than it would from a cloud in a drier atmosphere. If uncorrected, the effect of this atmospheric attenuation would result in the cloud top height being estimated higher than its actual location in the atmosphere.

Attenuation of energy by atmospheric water vapor in the I5 Imagery Band is relatively small for dry atmospheric conditions so that brightness temperatures are usually only about 1-2 $^{0}$C colder than actual cloud top temperatures. In more humid conditions, brightness temperatures may be 3-6 degrees C colder that actual cloud top temperatures. Assuming a psuedo-adiabatic lapse rate of ~6 $^{0}$C/km, estimates of cloud top heights would be in error by at most about 500–1000 m if no correction is made for atmospheric water vapor. With corrections, these errors should be no more that several hundred meters for water clouds. Cloud top temperatures from the VIIRS I5 band, used in

**Deleted:** I

**Deleted:** C

**Deleted:** C

**Deleted:** C

**Deleted:** The main difference between VIIRS I5 and DMSP OLS data is that the VIIRS data are highly calibrated and radiometrically accurate while OLS data are not well calibrated, e.g. more typical of infrared photographs.

**Deleted:** C

**Deleted:** ¶

**Deleted:** band

**Deleted:** channel

**Deleted:** B

**Deleted:** degrees

**Deleted:** 1

conjunction with atmospheric profile information from another NPOESS sensor or NWP products, readily support the classification of both low and mid-level water clouds and differences between them. Differentiation between classes within these groups, e.g. stratiform and cumuliform, is based upon cloud texture and is best done with the added use of visible imagery.

Alternatively, it is possible to differentiate between cloud top heights (low versus middle for example) by examining differences in brightness temperatures between each cloud top. For example, assuming the brightness temperature differences between two groups is 18 degrees C, the difference in cloud tops between these clouds would be approximately 3 km again assuming a pseudo-adiabatic lapse rate. Using the same technique, the height of the cloud could be compared to the cloud-free surrounding surface to estimate cloud top height above the ground since the emissivity of many surfaces is unity in the I5 band. Even this simplistic methodology supports the manual classification of water cloud types.

While cirrus clouds are readily detected and manually typed in the VIIRS I5 band, it becomes more of a challenge to manually identify the altitude of these clouds. Cirrus clouds can vary in altitude greatly depending upon where they occur across the globe. Since they are generally present near the tropopause, they may be found at very low altitudes in the high latitude regions or at much higher altitudes in the mid-latitude regions and the tropics. If precise information is needed on cirrus cloud top height, it may not be possible to obtain it with the simplistic method described above. Most cirrus clouds are optically-thin which means that these clouds normally allow some energy emitted from lower-levels of the atmosphere to pass unattenuated to space, unlike water clouds that are near blackbodies in this part of the spectrum. In other words, the emissivity of cirrus is highly variable as shown in Section 5.2.4.2.4. Some energy emitted at lower levels passes unattenuated through cirrus clouds which can result in VIIRS I5 brightness temperatures being as much as 30 degrees C warmer than the actual cloud top temperatures. Techniques similar to those used to estimate water cloud tops could easily be in error by 5 km or more if used to analyze the tops of optically-thin cirrus clouds. Thus, if accurate cloud top heights of cirrus clouds are needed, they should be taken from the VIIRS automated Cloud Top Height EDR which uses a multi-channel retrieval algorithm to retrieve cloud top height, emissivity, and cloud top temperature simultaneously.

Most cloud types listed previously can be manually classified with VIIRS imagery resolution bands 1-5, with several exceptions. First, nimbostratus cannot be classified from imagery alone since the presence of rain distinguishes this cloud from other clouds such as altostratus. Use of ancillary data, e.g. rain mask from microwave imagery, could support the distinction between these cloud types. Also, altocumulus constallanus may be difficult to identify since the distinguishing feature of these clouds is typically of a scale much smaller than VIIRS imagery.

### 5.2.5.2. Representative Imagery of the VIIRS I5 Band (11.45 ± 0.95 μm)

Attention now turns to a demonstration on the use of the imagery in the 12.0 μm band for cloud detection and cloud typing. Figure 5.17 contains daytime visible and IR imagery of clouds over Texas on April 4, 2001 at 1600 GMT. Extensive areas of water clouds are seen over the eastern half of Texas in the visible imagery while a large amount of cirrus is seen over the western half of the state in the IR imagery. The fact that these cirrus clouds are not readily seen in the visible data demonstrates that they are optically-thin clouds.

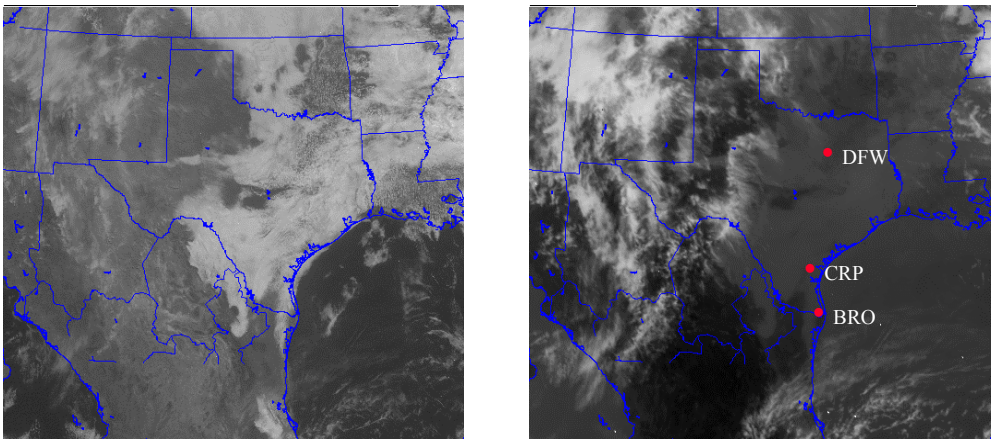


**GOES-E Visible Imagery 4/4/01, 1600 GMT** **GOES-E Infrared Imagery 4/4/01, 1600 GMT**

Figure 5.17. GOES-East visible and IR imagery of Texas on April 4, 2001 at 1600 GMT show extensive water clouds over the eastern and thin cirrus clouds over western Texas.

In an attempt to determine cloud top temperatures that are needed to define cloud types, additional images of this area were analyzed along with coincident radiosonde observations valid at 1200 GMT earlier in the morning. The coincident NOAA-14 AVHRR channel 4 imagery shown in Figure 5.18 has a data time of 1127 GMT on April 4th along with brightness temperatures of various cloud tops associated with radiosonde stations. Figure 5.19 shows the radiosonde observation and thermodynamic plot of these data for Corpus Christi (CRP), TX.

Deleted: C

The radiosonde observation for Corpus Christi shows a rapid decrease in the humidity and simultaneous increase in temperature that marks the cloud top height. From the mandatory and significant levels of data reported in the radiosonde, it is possible to identify accurately the cloud top height and cloud top temperature. In this case, the radiosonde observation reveals the cloud top temperature to be 19.6 $^{0}$C and the cloud top height to be 615 meters

An examination of the NOAA-14 12.0 μm infrared imagery collected at 1127 GMT shows the clouds over Corpus Christi have a brightness temperature of 19.3 $^0$C which is just 0.3 $^0$C colder than the temperature measured by the radiosonde. This relatively small difference is due to the absorption of energy by water vapor above the cloud and re-emissions by these gases at a lower temperature. In this case, the atmosphere is relatively dry - if more water vapor were present in the atmosphere, the AVHRR channel 4 brightness temperature would be lower and this difference larger. Several small cloud-free regions over the ocean have brightness temperatures of 21.5 $^0$C. Thus, from the 12.0 μm satellite imagery alone, the manually-generated cloud top height is estimated to be (21.5-19.3)/(6 $^0$C/km) = 367 m. The error in cloud top height is slightly greater than 200 m. Based upon the cloud's texture and altitude, it is classified as a stratus cloud.

Deleted: t

Deleted: C

Deleted: 1

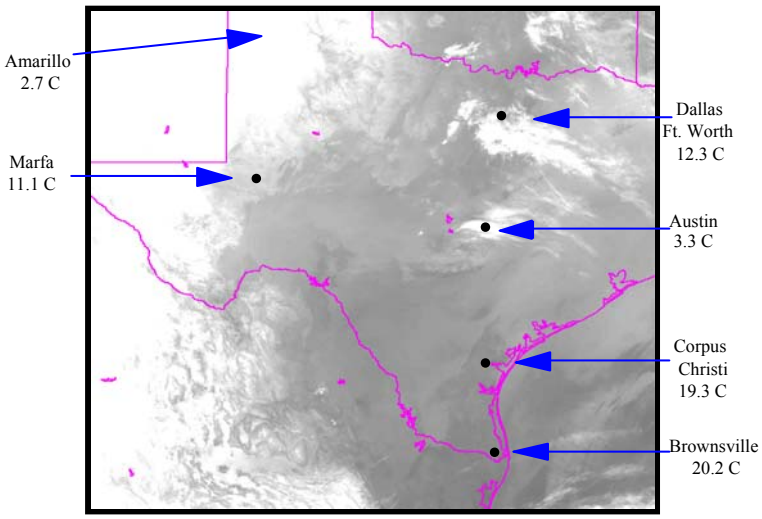


Figure 5.18. Brightness temperatures in AVHRR channel 4 imagery of various clouds located over Texas at 1127 GMT on April 4, 2001.

| | | | | | | | | |
|---|---|---|---|---|---|---|---|---|
| 1 | 12924 | 72251 | 27.77 | -97.50 | | 14 | 1103 | |
| 2 | 200 | 1741 | 500 | 74 | | 7 | 3 | |
| 3 | | CRP | | | 99999 | | kt | |
| 9 | 10100 | 14 | 216 | 204 | 130 | | 7 | |
| 4 | 10000 | 102 | 218 | 207 | 140 | | 10 | |
| 6 | 9767 | 304 | 99999 | 99999 | 170 | | 18 | |
| 6 | 9427 | 609 | 99999 | 99999 | 185 | | 23 | |
| 5 | 9420 | 615 | 196 | 183 | 99999 | | 99999 | |
| 4 | 9250 | 778 | 204 | 171 | 185 | | 27 | |
| 6 | 9105 | 914 | 99999 | 99999 | 185 | | 29 | |
| 5 | 8940 | 1071 | 212 | 152 | 99999 | | 99999 | |
| 6 | 8788 | 1219 | 99999 | 99999 | 190 | | 30 | |
| 5 | 8780 | 1227 | 226 | 96 | 99999 | | 99999 | |
| 4 | 8500 | 1512 | 214 | 44 | 200 | | 24 | |
| 6 | 8193 | 1828 | 99999 | 99999 | 200 | | 21 | |
| 5 | 7930 | 2108 | 208 | -22 | 99999 | | 99999 | |

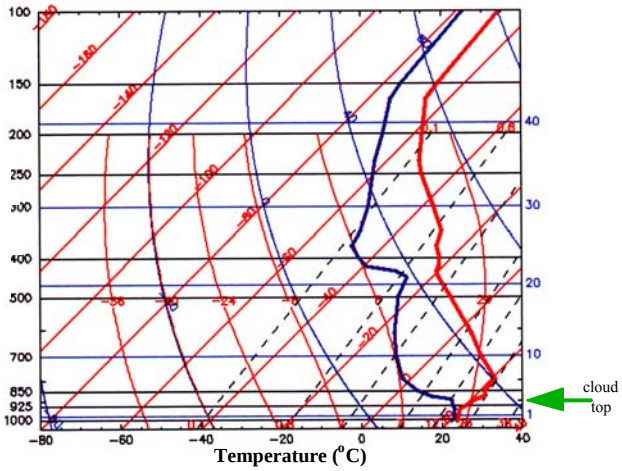


Figure 5.19. Radiosonde for Corpus Christi, Texas at 1200 UTC on April 4, 2001 along with thermodynamic (SkewT-LogP) chart of these data show cloud top temperature of 19.6 $^{0}$C.

This simplistic approach for the manual classification of cloud and estimation of cloud top height does not work well in the presence of optically-thin cirrus. While it is apparent that cirrus clouds extend over the Dallas/Ft.Worth (DFW) region, it is difficult to estimate the height of these clouds from 12.0 μm imagery. For example, the brightness temperature in Figure 5.18 for Dallas/Ft.Worth is 12.3 C. A correlation of this height to the DFW radiosonde would suggest cloud top heights of 740 mb which is approximately 8,000 feet for this atmosphere. Clearly these clouds are much higher - probably 25,000 feet or more. Unfortunately, it is often not possible to detect cirrus clouds in radiosonde observations. Thus, 12.0 μm imagery cannot be used to estimate cloud top heights of optically-thin cirrus clouds because these clouds allow lower-level energy to pass unattenuated to space so cloud top temperatures appear much higher than they are in reality. Thus causes cloud top heights to be placed too low in the atmosphere if one is using only the VIIRS I5 Imagery band.

## 5.2.6. VIIRS Day Night Band (DNB)

### 5.2.6.1. Theoretical Basis for Band Interpretation

The VIIRS Daytime/Nighttime Visible Imagery band (also called the Day Night Band, or DNB) has a heritage in the DMSP/OLS L channel, and indeed will be the operational successor to the OLS. The main purpose of the band is to provide low light visible imagery at the terminator and for lunar illuminated nighttime scenes. The spectral response of the DNB has been designed to operate efficiently under lunar illumination conditions, as shown in Figure 5.20.

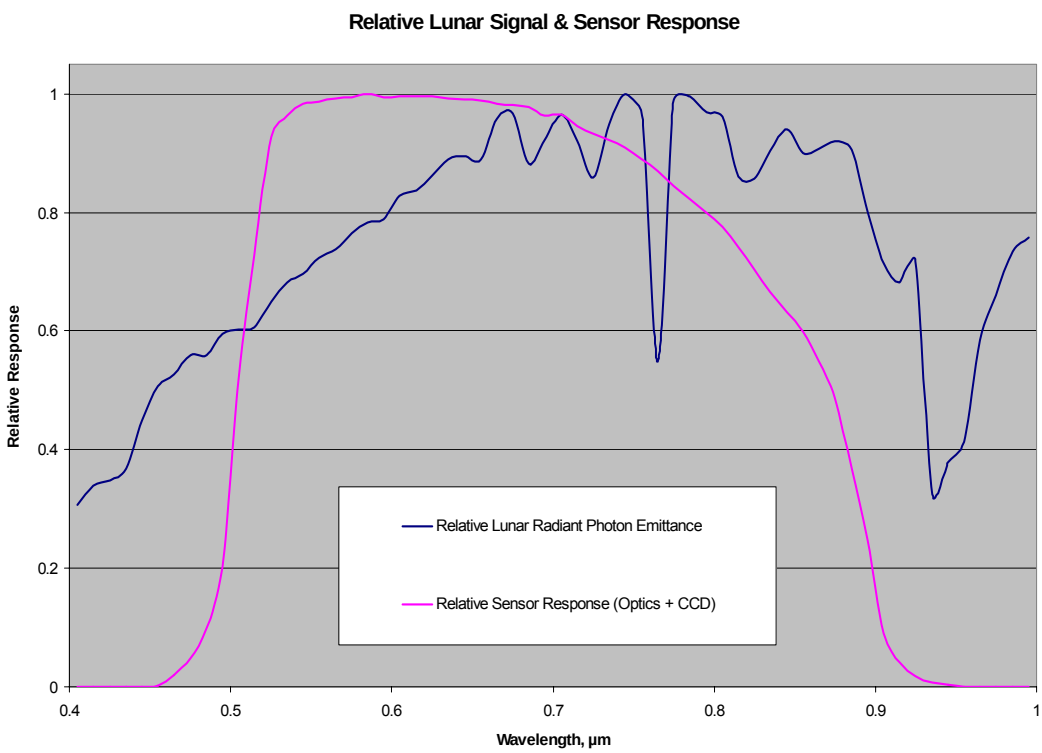


Figure 5.20. Spectral Response of the Daytime/Nighttime Visible Imagery band, compared with the lunar signal.

The spectral response of the DNB is designed to decline sharply at 0.5 µm, as can be seen in Figure 5.20. The purpose of the short-wave cut-off is to reduce contamination by atmospheric path radiance, which is more pronounced at shorter wave lengths. The design is compatible with OLS heritage.

The DNB measurement range will provide useful cloud imagery under quarter Moon illumination. Signal to noise ratio performance at night will vary with lunar phase, lunar elevation angle, and scan angle. An example for quarter moon phase is shown in Figure 5.21.

Deleted: (c.f. Table 3)

Deleted: moon

Deleted: signal

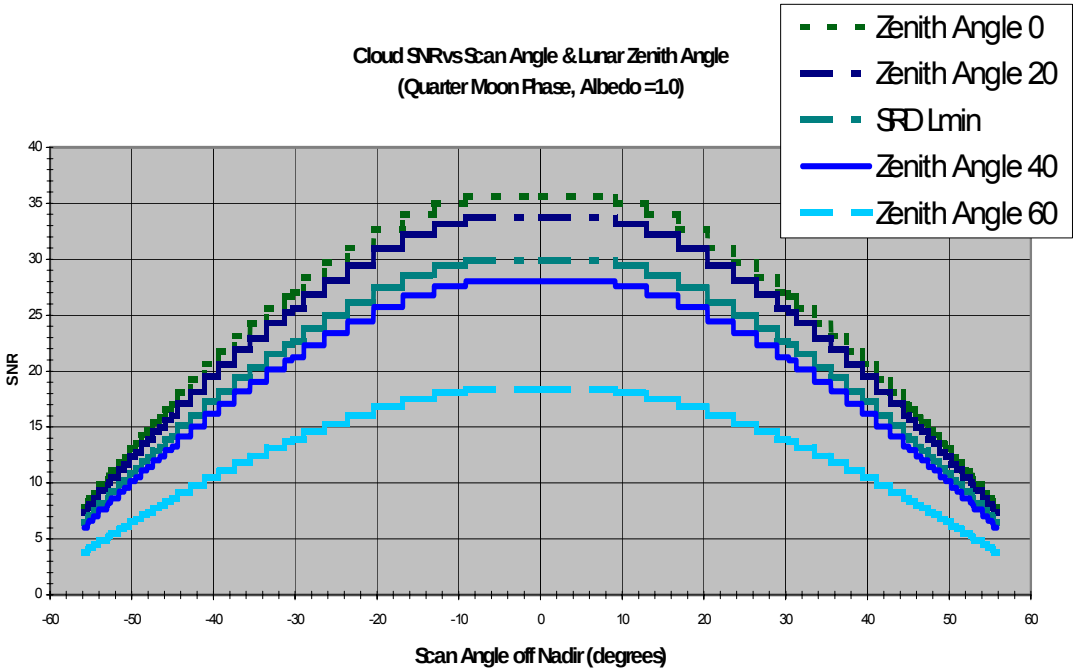


Figure 5.21. Signal to noise ratio Performance of the Daytime/Nighttime Visible Imagery under quarter-moon illumination conditions, as a function of scan angle.

The top two curves and bottom two curves represent lunar zenith angles of 0, 20, 40, and 60 degrees respectively. The middle curve corresponds to the minimum measurement range of $4 \times 10^{-9}$ $Wcm^{-2}$ $sr^{-1}$. A signal to noise ratio greater than 10 is achieved at the minimum radiance for almost the entire scan. A signal to noise ratio as high as 30 is achieved at the minimum radiance for a nadir view.

Deleted: /

Deleted: /

The characteristics of DNB imagery are similar to those of the I1 imagery band. Reflectivity from clouds and snow is very high, while vegetated land is noticeably darker, and ocean surfaces are very dark. Manual detection of clouds is based on the reflectivity contrast between clouds and darker surfaces, though snow/cloud discrimination is more challenging. As with the I1 band, manual cloud classification with the VIIRS DNB emphasizes (1) texture, (2) spatial resolution of cloud elements, and (3) shadows which may be cast from clouds high in the atmosphere onto lower level clouds.

### 5.2.6.2 Representative Imagery of the VIIRS DNB (0.7 ± 0.2 μm)

An example of DNB terminator imagery can be seen in Figure 5.22.

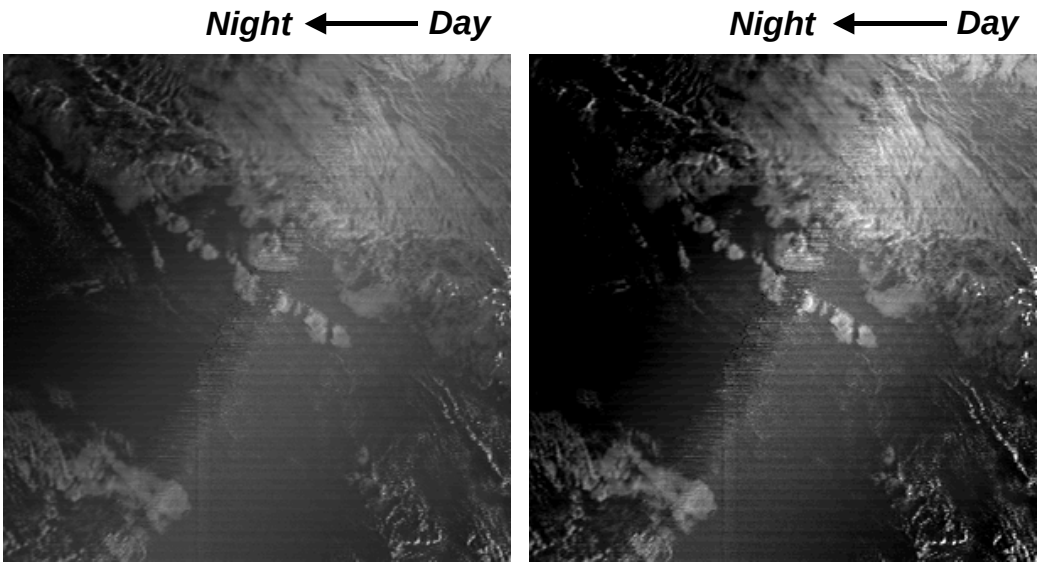


Figure 5.22 – F13 OLS Visible (HRD) image for the first terminator crossing of the July 20, 2001 1131 UT orbit.

The image in Figure 5.22 displays 300 scan lines for a scan angle range of 24 – 47 degrees . The daytime/nighttime sides are indicated. The full dynamic range is displayed in the left hand image. The right hand image is contrast-enhanced to highlight the terminator crossing effects (e.g., path radiance from atmospheric scattering). Figure 5.22 demonstrates how well the OLS on board gain management algorithm works, as the source radiance has a dynamic range over the scene greater than six orders of magnitude. The VIIRS baseline algorithm for NCC Imagery is designed to capture the on board OLS gain management algorithm within the data processing architecture of the VIIRS Ground Segment which will make the VIIRS DNB performance comparable to that of OLS.

**Deleted:** 0
**Deleted:** 0
**Deleted:** LEFT
**Deleted:** RIGHT
**Deleted:** Our
**Deleted:** We therefore expect
**Deleted:** to be
**Deleted:** the

In Figure 5.22, clouds are bright and the underlying surface is dark, allowing for cloud detection. Cloud classification can be made from the texture and shadowing structure evident in the imagery. The figure also illustrates the difficulty in snow/cloud discrimination with visible band imagery. The bright features in the lower right section of the image are distinguishable as snow, because the section is cloud-free, allowing the analyst to observe the terrain structure of the bright/dark contrast. It is probable that snow is present in the upper left section of the image, but this is more difficult to determine, as the section contains clouds.

## 5.3. VIIRS IMAGERY ASSIST DATA

Characteristics for the VIIRS moderate resolution bands are shown in Table 5.2 along with characteristics of existing systems. These VIIRS bands are known officially as Radiometry Bands and were included in the VIIRS design to satisfy most of the EDR requirements shown in Section 3.1. In some cases, these bands are also useful for manual cloud detection and cloud typing and thus we refer to them as image assist bands. Image assist bands are not essential to meet NPOESS threshold requirements for manually-generated cloud data products but may be used to advance system performance toward objective levels, as discussed in Section 3.3. In this section we discuss the use of imagery assist bands with imagery bands to further improve the manually-generated cloud cover and cloud type data products.

**Deleted:** hannel c

**Deleted:** band

**Deleted:** in VIIRS Imagery EDR

Table 5.2. Bandpasses of Sensors that Closely Approximate VIIRS Moderate Resolution Bands.

| Band | VIIRS Channel | Central Wavelength (μm) | Bandwidth (μm) | Satellite System and Channel | Wavelength Interval (μm) |
|---|---|---|---|---|---|
| 2 | M1 | 0.412 | 0.02 | MODIS 8 | 0.405-0.420 |
| 3 | M2 | 0.445 | 0.018 | MODIS 9 | 0.438-0.448 |
| 4 | M3 | 0.488 | 0.02 | MODIS 10 | 0.483-0.493 |
| 5 | M4 | 0.555 | 0.02 | MODIS 12 | 0.546-0.556 |
| 7 | M5 | 0.672 | 0.02 | MODIS 13 | 0.662-0.672 |
| 8 | M6 | 0.746 | 0.015 | MODIS 15 | 0.743-.0753 |
| 10 | M7 | 0.865 | 0.039 | MODIS 2 | 0.841-0.876 |
| 11 | M8 | 1.24 | 0.02 | MODIS 5 | 1.230-1.250 |
| 12 | M9 | 1.378 | 0.015 | AVIRIS | 1.370-1.380 |
| 14 | M10 | 1.61 | 0.06 | MODIS 6 | 1.628-1.652 |
| 15 | M11 | 2.25 | 0.05 | MODIS 7 | 2.105-2.155 |
| 17 | M12 | 3.7 | 0.18 | MODIS 20 | 3.660-3.840 |
| 18 | M13 | 4.05 | 0.155 | MODIS 21 | 3.929-3.989 |
| 18 | M13 | 4.05 | 0.155 | MODIS 22 | 4.020-4.080 |
| 19 | M14 | 8.55 | 0.3 | MODIS 29 | 8.400-8.700 |
| 20 | M15 | 10.763 | 1 | MODIS 32 | 11.77-12.27 |
| 22 | M16 | 12.013 | 0.95 | MODIS 32 | 11.77-12.27 |

**Deleted:** □

### 5.3.1. VIIRS M1 – M4 Bands (0.412 ± 0.010 μm, 0.445 ± 0.009 μm, 0.488 ± 0.010 μm, 0.555 ± 0.010 μm)

#### 5.3.1.1. Theoretical Basis for Band Interpretation

The spectral signatures of the Earth's atmosphere and key surface backgrounds in the VIIRS M1 – M4 bands are shown in Figure 4.8. The bands are considered here as a set since the signatures shown in the figure change little with each band center. The figure shows that the available solar irradiance is large in these bands since the wavelength of maximum emission for the Sun with its 6000K blackbody surface temperature is near 0.5 μm. In addition, it is seen that the reflectivity of snow is very large, at > 95%, while atmospheric transmission is relatively low, averaging about about 50%.

The large attenuation of solar energy is primarily due to Rayleigh (or molecular) scattering while the wings of some ozone absorption lines extend into the shorter wavelengths. Rayleigh scattering results from the interaction of the very short wavelengths of solar radiation with the molecular structure of the atmosphere, consisting primarily of the permanent gases (those with constant mixing ratios) which are oxygen and nitrogen, along with variable constituents (gases with mixing ratios that vary within the vertical) such as water vapor. The reduction in solar illumination due to molecular scattering causes unprocessed M1 data to appear bright and washed out, even over surfaces that have a low (< 10 percent) reflectivity such as bare soil and vegetated land. In fact, Rayleigh scattering has the effect of turning on a uniformly bright light in a scene being photographed. This brightness can be corrected in several ways: (1) the contrast of the entire scene can be reduced at the loss of scene content since all features are uniformly darkened, (2) pixel radiances can be corrected for Rayleigh scattering which is a function of atmospheric path length or sensor scan angle, and (3) composite images can be formed with other bandpasses which do not experience the effects of Rayleigh scattering. The second and third methods tend to preserve the information content of surfaces and allow information to be extracted over desert surfaces.

The VIIRS M1-M4 bands were justified to provide information on the chlorophyll content of the ocean's surface, as previously demonstrated with SeaWiFS and MODIS sensors. The reflectivity of chlorophyll is strong in these VIIRS bands; unfortunately the retrieval of chlorophyll is complicated by the strong reduction in the signal arriving at the spacecraft. Since 90% of chlorophyll's spectral signature is lost by this atmospheric attenuation, both SeaWiFS and MODIS create a product called water leaving radiances which provides useful estimates of ocean surface radiances. Recall that all other VIIRS data previously examined were referenced against the top of the atmosphere.

The M1 band is very useful for distinguishing between lower-level water clouds and backgrounds in semi-arid regions of the world. At 0.412 μm, bare soil has a reflectivity of about 5 percent, as shown in Figure 4.8, while the reflectivity of water clouds and snow are much larger. The reflectivity of bare soil increases constantly across the VIIRS M1 – I2 spectral region and reaches a maximum of about 35 percent at 0.865 μm. Little change is seen in the reflective characteristics of water clouds and snow across the same spectral region. Therefore, the M1 band can be used as an *"Imagery Assist Band"* with

VIIRS imagery bands in the manual detection of clouds over arid regions such as the Middle East. If for some reason the M1 band is not available, data from the M2, M3, or M4 band can be used in its stead but with a decreasing level of value since the reflectivity of bare soil increases from about 5 – 15 percent over 0.4 – 0.6 μm range. In addition, the VIIRS M1 band is also useful for the manual detection of volcanic aerosols over semi-arid surfaces. Finally, the water leaving radiance product is considered a useful data set for scene interpretation over the ocean surfaces to examine near-coastal effects.

#### 5.3.1.2. Representative Imagery of the VIIRS M1 Band (0.412 ± 0.05 μm)

Figure 5.23 shows sample M1 and M3 data collected by the SeaWiFS sensor for a scene over the southwestern US at 1954 GMT on July 13, 2001. The scene contains a large layer of stratocumulus in the left-bottom corner, to the left of Baja California. The Altar Desert is located in the middle of the scene, and the Gulf of California at the bottom center of the image. Note that some land features are slightly more evident in the 0.488 μm, M3 band, in the right panel, than in the 0.412 μm, M1 band at left. Clouds appear bright and the ocean appears equally dark in both spectral bands.

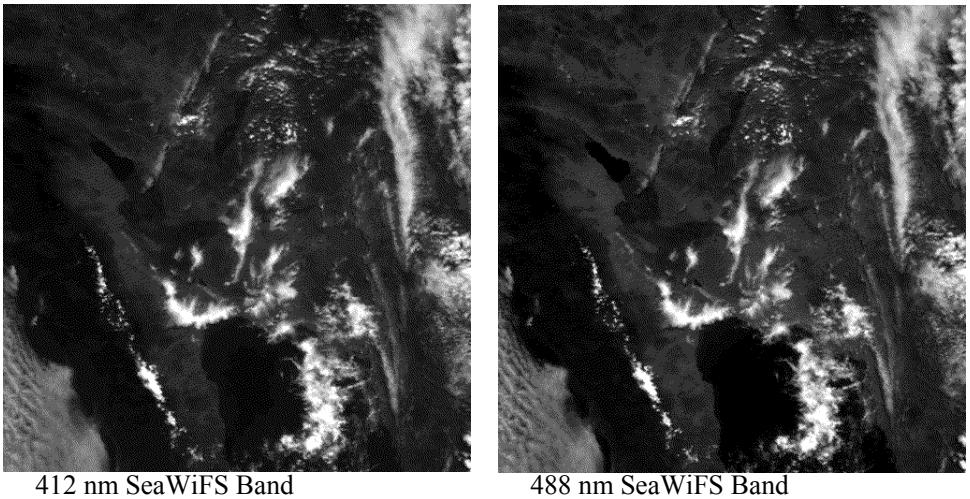

412 nm SeaWiFS Band 488 nm SeaWiFS Band

Figure 5.23. SeaWifs data from the 0.412 μm and 0.488 μm bandpasses are shown for the western US and northern Mexico on July 13, 2001 at 1954 GMT.

For convenience, in Figure 5.24, SeaWiFS images of VIIRS M4 and M6 bands are included for the same scene shown in Figure 5.23. These data contain no additional information that is particularly useful for manual cloud analyses. It is evident, however, that the surface reflectivity of bare soil, which covers much of the scene, increases with wavelength. The contrast between clouds and surface features is least at 765 nm and greatest at 0.412 μm. The 0.845 μm band for this scene was shown earlier in Figure 5.4. These changes in surface reflectivity properties are exploited in the color composites shown in Chapter 6. In addition, the value of the 0.412 μm band for cloud detection over desert has recently been demonstrated quantitatively with automated cloud detection algorithms (Hutchison and Jackson, 2003).

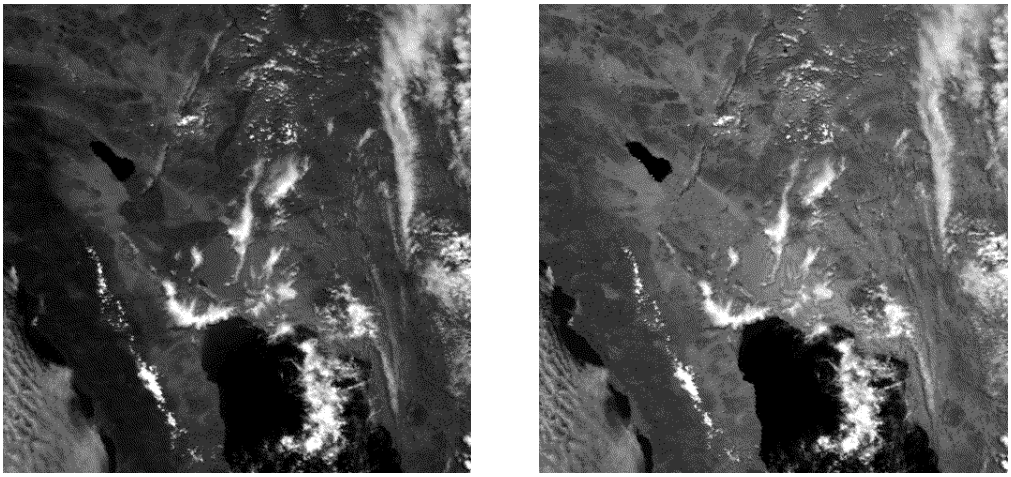

Figure 5.24. SeaWiFS data in the 0.555 μm and 0.765 μm bands are shown for the scene over the western US and northern Mexico on July 13, 2001 at 1954 GMT.

## 5.3.2. VIIRS M9 Band (1.378 ± 0.0075 μm)

### 5.3.2.1. Theoretical Basis for Band Interpretation

The VIIRS M9 channel has a very narrow bandpass centered on a very strong, but also narrow, water vapor absorption band, as seen in Figure 4.9. Its primary value for manually-generated cloud analysis is for the detection of thin cirrus clouds, especially over land surfaces, in daytime VIIRS data. Solar irradiance remains large, although it is decreasing with increasing wavelengths. Notice that atmospheric attenuation increases sharply outside the narrow VIIRS M9 band.

Since the concentration of water vapor generally has its maximum in the lower atmosphere and decreases markedly with altitude, incident solar energy in this spectral band is strongly attenuated once prior to reaching the Earth's surface and a second time after being reflected back toward space, under cloud-free atmospheric conditions. Simulations, based upon LOWTRAN (Berk et al., 1989) using a sub-Arctic summer atmospheric profile (Anderson et al., 1986), predict that only 20 percent of the solar energy would arrive at satellite altitude if reflected by a perfect reflector, i.e. 100% albedo or reflectance, located at an altitude of 6 km, as shown in Figure 5.25. Even less energy will arrive at the VIIRS sensor from reflection by clouds. This percentage of energy reflected decreases markedly as the perfect reflector is lowered toward the surface. No reflected energy reaches the satellite when the reflector is on a surface at sea level (Gao et al., 1993).

The reflectances of most surfaces are not 100% but generally less than 50% as shown in Figure 4.9. For example, the reflectivities in the VIIRS M9 bandpass of snow, bare soil, and vegetated soil, are all under 50 percent. Thus, these surfaces should not be visible in the M9 band, in effect these surface features are “perfectly black” in this spectral band.

**Deleted:** this value

On the other hand, cirrus clouds exist at levels where water vapor concentrations are typically many orders of magnitude less than at the Earth’s surface. Therefore, solar energy is scattered from cirrus clouds before it reaches the more humid levels of the atmosphere. Similarly, middle-level water clouds may be seen in M9 data since these clouds reside at altitudes where the water vapor is much less than at the surface but they are highly reflective. Lower-level water clouds may or may not be seen in the VIIRS M9 band, depending upon the concentration of water vapor between the tops of these clouds and the VIIRS sensor. Thus, data collected in the VIIRS M9 band are valuable for the detection of both high-level ice clouds and mid-level and lower-level water clouds. In addition, these data can be used to differentiate between mid-level and lower-level water clouds.

Thus, the M9 spectral band should be extremely useful for scene interpretation since surface features are generally masked in these data. The result is a high probability of detecting very thin cirrus clouds even in the presence of more highly reflective, low-level water clouds. However, in extreme elevations, the possibility exists for energy reflected from snow covered surfaces to arrive at the VIIRS sensor. Therefore, it is important that the 1.378 μm data be used in conjunction with 1.6 μm or 3.7 μm albedo imagery.

Finally, it is noted that the bandwidth of VIIRS M9 is 15 nm, half the width of MODIS channel 26. The narrower VIIRS bandwidth will reduce the risk that side lobes in the spectral response will allow leakage of surface signals to contaminate the cirrus signal.

Deleted: C

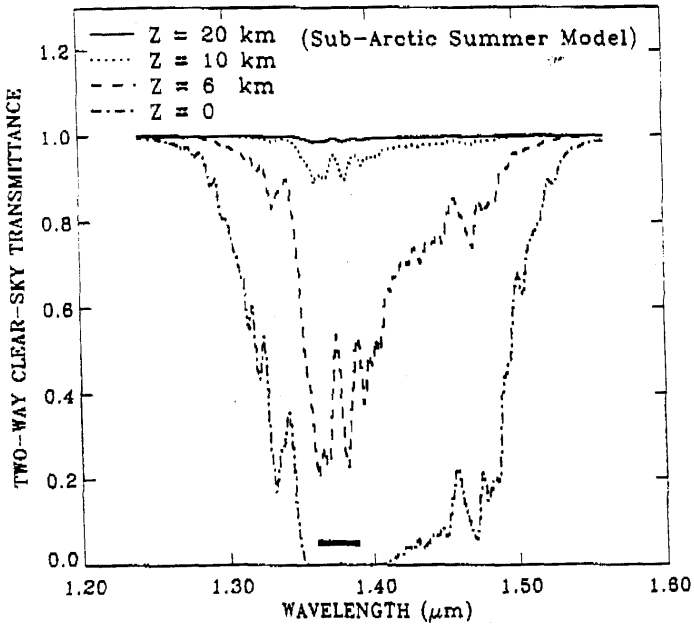


Figure 5.25. The two-way clear-sky transmittances for energy arriving at satellite altitude in the 1.38 μm region for a perfect reflector located at different altitudes. Calculations based upon sub-Arctic summer atmosphere and LOWTRAN. (Gao et al., 1993).

### 5.3.2.2. Representative Imagery of the VIIRS M9 Band (1.378 ± 0.075 μm)

The imagery shown in this section was collected by the Airborne Visible/Infrared Imaging Spectrometer (AVIRIS) sensor. Imagery collected by the very similar 1.88 μm band of the MODIS Airborne Simulator (MAS) is shown in Chapter 6. The AVIRIS sensor consists of four spectrometers that cover the 0.4-2.5 μm range providing data in 224 spectral bands. Each band is 10 nanometers wide and the bands are interleaved by line (Goetz et al., 1985; Vane 1987). The resolution of a typical AVIRIS pixel is about 20 meters, for data collected by aircraft flying at a nominal altitude of 20 km. Both the MAS and AVIRIS sensors were flown on NASA's ER-2 aircraft. AVIRIS data are archived at the Jet Propulsion Laboratory.

Two scenes of AVIRIS data are shown in Figure 5.26 and Figure 5.27, each with different surface characteristics. The first scene selected was collected over Coffeyville, Kansas at 1923 GMT on December 5, 1991 and represents a case of moderate surface reflectivity. The second scene was recorded over the Gulf of Mexico area at 1543 GMT earlier on December 5, 1991 and represents the case of low surface reflectivity. Figure 5.26 shows the 0.64 μm and 1.38 μm imagery collected over the Coffeyville, Kansas region as part of the First ISCCP Regional Experiment (FIRE) IFO. Notice that surface features clearly visible in the 0.645 μm band cannot be seen in the 1.38 μm image. Also, no cloud cover is evident in the shorter wavelength data; however, cirrus is obviously present in the upper left and right corners in the 1.38 μm image. In this case, it is more difficult to determine whether the signatures in the remaining 1.38 μm pixels were due to thin cirrus or sensor noise. Similar difficulties were not present with the next generation of AVIRIS sensors.

Deleted: ¶

Deleted:

0.645 μm AVIRIS Channel

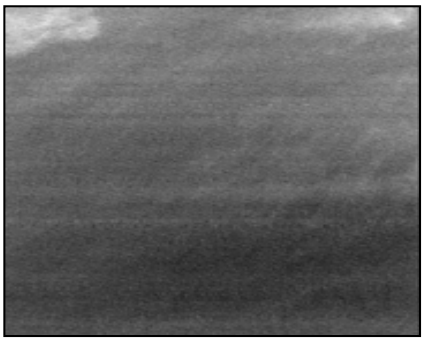

1.378 μm AVIRIS Channel

Figure 5.26. AVIRIS imagery for VIIRS I2 and M9 channels over Coffeville, Kansas shows value of masking surface features for manual interpretation of thin cirrus.

Deleted: s

The second scene shown in Figure 5.27 was recorded over the Gulf of Mexico area. Lower-level water clouds and some cirrus are evident in the 0.64 μm AVIRIS imagery. However, only the cirrus are seen in the 1.38 μm spectral band. The signature of the low-level water clouds is suppressed in the 1.38 μm band because there is sufficient water vapor present above the water cloud top to absorb the energy reflected from it. Therefore, the 1.38 μm band provides the analyst with the unique capability to identify multiple cloud layers in single pixels of imagery.

Deleted:

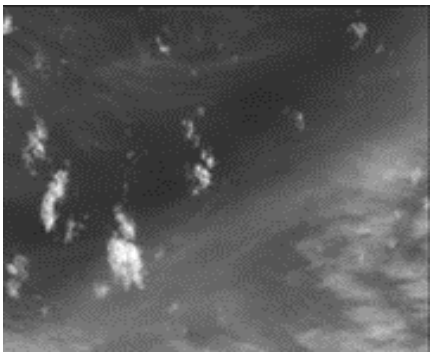

0.645 μm AVIRIS Channel

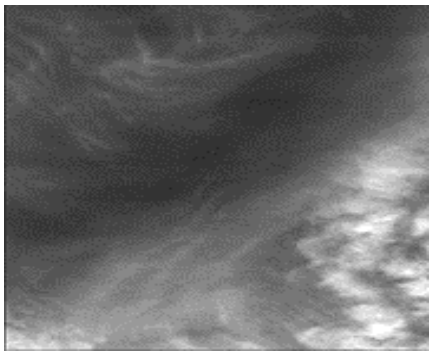

1.378 μm AVIRIS Channel

Figure 5.27. AVIRIS imagery for VIIRS I1 and M9 channels over Texas Gulf Coast reveals that low-level water clouds are masked in 1.38 μm imagery.

# Chapter 6

# MULTICOLOR COMPOSITES OF MULTISPECTRAL IMAGERY

## 6.1. INTRODUCTION

Image enhancement techniques can facilitate the simultaneous interpretation of many cloud and background signatures in multiple bands of meteorological satellite imagery. In Chapter 5, background information was provided on the sources of radiation observed by the VIIRS sensor and on the interpretation of these observations in each VIIRS band. Individual signatures found in a given band can be viewed with those of additional bands using color imagery composites. These composites speed the process of manual image interpretation and decrease ambiguities in the signatures found in any single image by viewing the signatures in multiple bands simultaneously. In this chapter, sample color composites are provided to extract specific types of information from different features contained in multiple scenes. Before looking at examples of false color composites, background information is provided on the concept of creating and using color composites for image interpretation.

Deleted: ly

Color composites are highly valuable for visualizing differences in spectral signatures of numerous features simultaneously in multispectral satellite imagery. A color composite is created when one band is viewed in either the red, blue, and green gun of a color CRT and one or more different bands are placed in the remaining guns. Assume that one of three different spectral bands is placed in the red gun, another is in the blue gun and yet another is in the green gun of the CRT. A feature in the scene will appear reddish, greenish, bluish, or some combination of these colors when its signature is more distinct in one or two of the bands than it is in the third. If little or no difference exists in the spectral signature of a feature in all bands, the feature will appear black, white, or another shade of gray. The variations in gray-shade depend upon whether the brightness temperature of the feature is cold or hot in infrared bands or whether they reflect solar radiation strongly or weakly in the visible and near-IR bands.

Deleted: imagery channel

Deleted: channels

Deleted: is

Deleted: channels

Deleted: channels

Deleted: channels

The concept of constructing color composites is demonstrated with the scene over California previously shown in Figure 4.2, Figure 5.2, and Figure 5.3. In Figure 6.1, the 0.865 μm band is assigned to the green gun of the CRT while the 0.64 μm band is assigned to the red and blue guns.

This particular band assignment makes a very popular color composite for monitoring vegetation health since densely vegetated regions appear green while poorly vegetated surfaces appear a shade of gray. The greenish hue in the color composite occurs because the reflectivity of vegetated surfaces is very low in the 0.6-0.7 μm region then increases markedly with wavelengths between 0.7 – 0.75 μm where it becomes nearly constant through 1.0 μm, as was shown in Figure 4.8. On the other hand, the reflectivity of bare soil increases slowly over the same spectral region. In the 0.64 μm band, the reflectivity of bare soil is slightly larger than that of vegetated surfaces but the situation is reversed at 0.865 μm. Thus, the mountains and highly agricultural regions of California are brilliant green while the desert regions, in the lower right corner of the scene, have a grayish hue

Deleted: is useful to

Deleted: map

Deleted: s

because the signature of bare soil is nearly the same in both bands. Clouds and the snow covered surfaces in the Sierra Mountains are a (bright) shade of gray in the color composite because the reflectivities of these features are very similar and high in each band. The cloud-free areas of the ocean have a dark, purple hue since the albedos in both bands are low but Rayleigh scattering produces a slightly higher albedo in the shorter wavelength band.

Deleted: cha

Deleted: nnels

Deleted: y

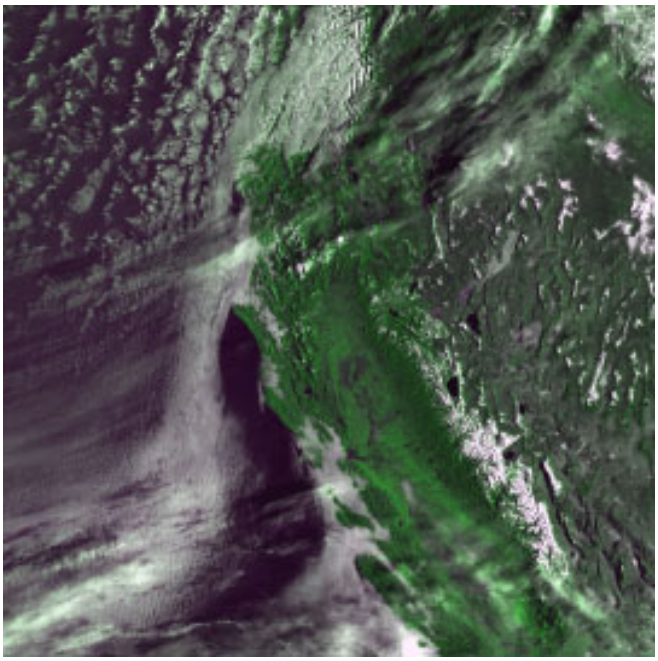

Figure 6.1. Color composite to emphasize vegetated land surfaces created by assigning 0.64 μm band assigned to red and green guns of CRT and 0.865 μm albedo band assigned to blue gun.

Several color composites may be needed to accurately interpret all features in any given scene. For example, using Figure 6.1 it remains difficult to distinguish between snow and water clouds; therefore, additional spectral data must be used to resolve these ambiguities. Additionally, color composites can be created to emphasize variations in brightness temperatures as well as reflectivities. At least one IR band, consisting of brightness temperatures, is needed to obtain information on relative cloud top heights. The 12.0 μm band is most valuable for this purpose.

Deleted: channel

It is the focus of this chapter to present a variety of color composites that can be used to interpret the contents of features contained in multispectral imagery collected by the NPOESS VIIRS sensor. Background information obtained from the creation of these color composites should provide the knowledge necessary to create additional composites for unique mission applications.

## 6.2. COLOR COMPOSITES OF (0.64μm, 0.865μm, AND 12.0 μm) SURFACE VEGETATION AND CLOUD CLASSIFICATIONS

Color composites that contain at least one infrared band provide valuable information on feature temperatures that are useful for cloud classification. Figure 6.2 contains the same scene shown in Figure 4.2, Figure 5.2, Figure 5.3, and Figure 6.1. This color composite contains the 0.64 μm (visible) band assigned to the red gun, the 0.865 μm (near-infrared) band to the green gun, and the 12.0 μm infrared band assigned to the blue gun. The infrared band is displayed in the inverted mode, i.e. warmer is darker and colder is brighter. The major difference between the color composites shown in Figure 6.1 and Figure 6.2 is that the latter provides information on cloud top temperatures and relative heights in addition to the same information on vegetation and land/water boundaries found in the earlier figure.

**Deleted:** channel

**Deleted:** channel

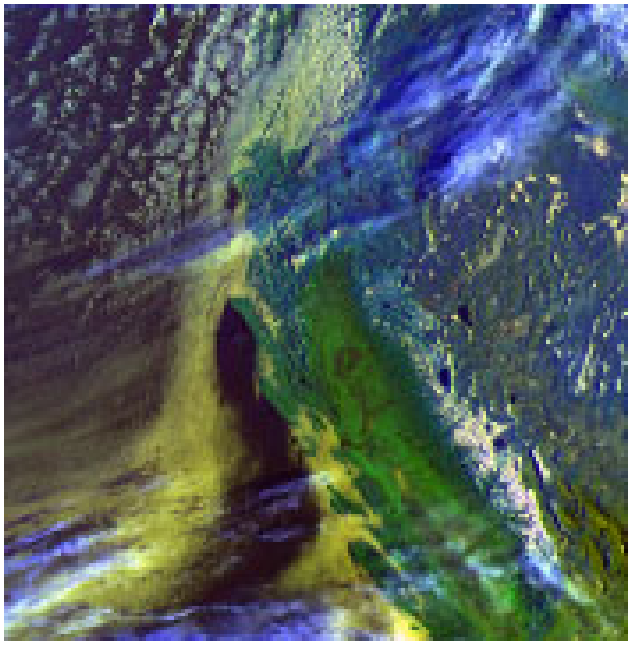

Figure 6.2. Placing the 12.0 μm band in the blue gun of Figure 6.1 provides valuable data on cloud top temperatures needed for cloud typing. Warm, low level water clouds appear yellow while colder ice clouds are blue.

**Deleted:** channel

In Figure 6.2, distinction is readily made between low-level water clouds, seen as yellow, and the much colder ice clouds, which appear blue. The yellowish hue of the water clouds results from nearly equal contributions from the red and green guns of the CRT since water clouds are highly reflective and bright in both bands. On the other hand, the contribution from the blue gun is 50% less, since these water clouds are relatively warm and thus provide much less energy to the blue gun.

**Deleted:** e

Thin cirrus appears blue in Figure 6.2 because this gun has more than twice the contribution of either the red or green guns. Cirrus contributes much more to the blue gun of the CRT, when displayed in the inverted mode, since these clouds are very cold in the AVHRR thermal infrared band but have low albedos in both the visible and near-infrared bands. Regions of dense or optically thick cirrus appear less blue, e.g. bright shade of gray, because thick cirrus cloud elements can be very cold and highly reflective so the contributions in all guns of the CRT are similar.

**Deleted:** channel

**Deleted:** channels

The color composite shows that the cumuliform clouds in the upper left-corner have temperatures that are warmer than the (blue) cirrus but colder than the (yellow) stratus. Thus, these clouds probably occur in the middle-levels of the atmosphere but may also be lower-level clouds in a much colder air mass than found in the bottom left corner of the scene. Thus, it is important to compare cloud top temperatures in the far-infrared band with adjacent cloud-free temperatures to determine approximate cloud top height.

Finally, land regions in the right part of the scene have a bluish hue because the land is relatively cold and sparsely vegetated, especially near snow fields. Analyses show that these regions have most energy in the blue gun and slightly more energy in the green gun than in the red gun. Thus, the land must be sparsely vegetated.

It is emphasized that the inclusion of the 12.0 μm band into a color composite provides valuable information on cloud top temperatures which is most valuable for manual cloud classifications. In Figure 6.2, the following clouds have been identified:

(d) Stratus – yellow
(e) Stratocumulus - yellow
(f) Thin cirrus – blue
(g) Thick cirrus – white
(h) Altostratus – greenish
(i) Altocumulus - greenish

Snow along the Sierra Nevada mountain range remains white because it is highly reflective in the solar bands and very cold in the thermal bands. White means there is no unique spectral signature for snow in this color composite. While the presence of snow is inferred by the dendritic pattern in the mountain regions, additional spectral data might be needed to positively confirm the presence of snow in another scene, based solely upon its signature in a color composite. For example, additional spectral data are essential to identify snow in non-mountainous regions where scene interpretation might be complicated by the presence of other relatively cold features, including supercooled clouds.

## 6.3 COLOR COMPOSITES (3.7 μm ALBEDO, 0.865μm, 12.0 μm) FOR SNOW DETECTION

Snow appears white in the color composites shown in Figure 6.1 and Figure 6.2 because it is highly reflective in both the 0.64 μm and 0.865 μm bands and cold in the 12.0 μm band. Thus equal contributions are received from snow by each gun in the CRT. While snow covered regions were readily identified by the dendritic patterns in the moutainous regions of these earlier scenes, it becomes more difficult to identify in less rugged terrain without the use of specific imagery where snow has a unique spectral signature. In this section, another VIIRS band is examined, where the spectral signature of snow is very different from those shown previously. Thus use of this band allows snow to be positively identified in any sunlit terrain. The color composite is shown in Figure 6.3 below.

Deleted: than

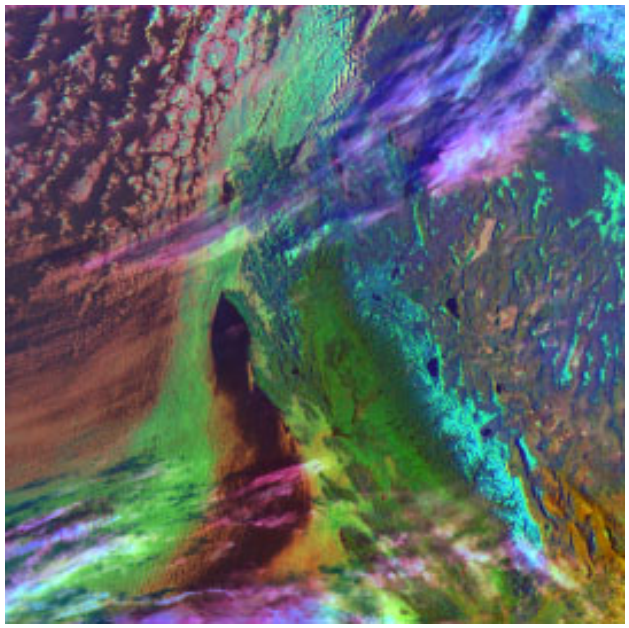

Figure 6.3. Replacing the band in the red gun of Figure 6.2 with the AVHRR 3.7 albedo channel allows snow to be differentiated from lower-level water clouds, thin cirrus, and thicker cirrus while maintaining information on cloud top temperatures and vegetated land surfaces (red = 3.7 μm albedo, green = 0.865 μm, blue = 12.0 μm).

Snow appears turquoise in Figure 6.3 because it is highly reflective in the 0.865 μm band and very poorly reflective in the derived AVHRR 3.7 μm (albedo) channel while relatively cold temperature exists in the 12.0 μm band. Turquoise results from the absence of red in the CRT display. Thus, an extensive area of snow is readily seen along the entire Sierra Nevada Mountain Range. Smaller regions of snow are seen east and north of these mountains, over Nevada, Utah, and Idaho. In addition, snow is confirmed in this color image in the mountains just north of the San Joaquin Valley. Specially, Mt Shasta can vaguely be seen through the thin cirrus clouds. In this composite, snow and

thin cirrus are readily differentiated because the signatures of cirrus clouds have a purplish hue, demonstrating strong signatures in the red and blue guns. It should be noted that use of the 1.6 μm VIIRS band in place of the 3.7 μm albedo band will produce the same signature for snow; however, the signature of thin cirrus is less dramatic in the 1.6 μm band since the 3.7 μm band enhances the signature of thin cirrus while the 1.6 μm band suppresses it. The phenomenology for the enhanced signature of thin cirrus in the 3.7 μm band was discussed in Section 5.2.4.2.3.

**Deleted:** channel

**Deleted:** channel

**Deleted:** channel

The intensity of the turquoise color is related to the combined effects from the green gun and blue guns in the CRT. The contribution in the green gun is generally large, assuming daytime imagery. There is a minimum expected contribution from the blue gun since surface (skin) temperatures of snow-covered areas must be at least freezing. In some regions, surface temperatures may be significantly colder. For example, brightness temperatures in the Sierra Mountains are considerably colder than those seen in the large snow regions on the very right edge of the scene. However, the turquoise appears similar for both regions.

Finally, note that the "streets" of snow east of the Sierra Nevada Mountains are surrounded by a blue tint. The bluish hue demonstrates a region of very cold air, which is associated with both the altitude of these "smaller" mountains and the airmass over them. In the lower-right corner, the color becomes orange due to the surface being very warm over the Death Valley Desert of California. The snow-covered region just north of Death Valley and east of the Sierra Mountains is readily identified as the White Mountains. The topography of these mountains frequently results in severe, mountain-wave turbulence under proper meteorological conditions with rotor clouds occasionally reported in weather observations issued from Bishop, California.

## 6.4. COLOR COMPOSITES OF (0.64 μm, 0.64μm, 3.7μm ALBEDO) SNOW MAPPING THROUGH THIN CIRRUS CLOUDS

For some applications, it might be useful to determine the presence of snow in cloud-covered conditions, especially when the clouds are optically thin or semi-transparent in the visible part of the solar spectrum. In this section, a methodology is shown to identify snow even if cirrus completely envelops the region. The color composite shown in Figure 6.4 uses the scene first described in Figure 5.9 and Figure 5.10.

The color composite shown in Figure 6.4 was created by assigning the 0.64 μm band to both the red and green guns of the CRT and the 3.7 μm albedo band to the blue gun. Snow appears yellow in this composite and can be seen even through the cirrus clouds. Inspection of the 12.0 μm band in Figure 5.9 reveals overcast cirrus across much of the upper right portion of this region.

**Deleted:** channel

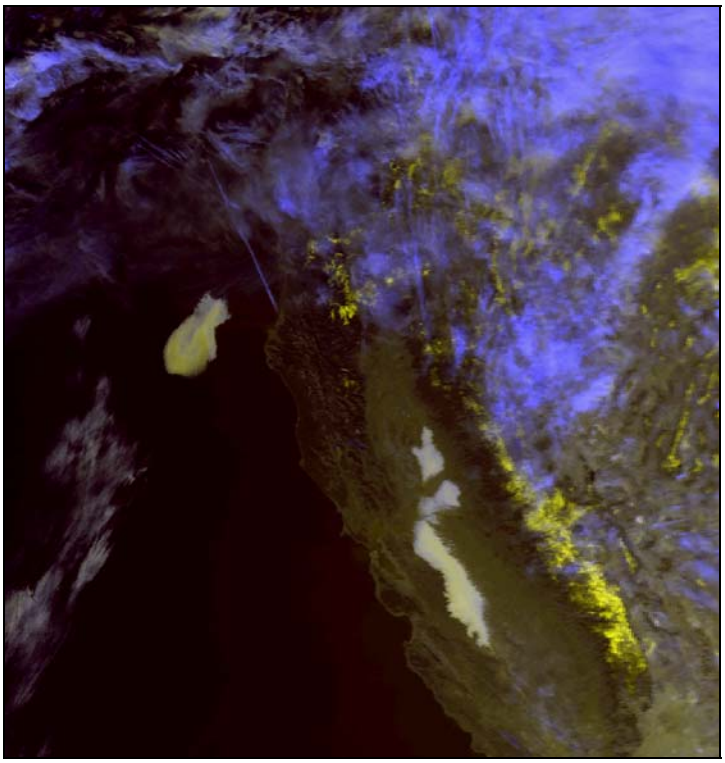

Figure 6.4. Color composite red = 0.64 μm band, green = 0.64 μm band, blue = 3.7 μm albedo band) for the manual detection and mapping of snow through cirrus cloudy conditions (Hutchison and Locke, 1997).

The yellowish hue of snow in this color composite results from nearly equal contributions coming from the red and green guns and the absence of any significant contribution in the blue gun. Thin cirrus has a bluish hue since the signature of optically-thin cirrus is enhanced in the 3.7 μm albedo image but much less evident in the 0.64 μm band. Thus, snow can be seen through overcast cirrus clouds since the reflectance of snow is much stronger in the band in which the thin cirrus is not readily seen, i.e. the 0.64 μm band. Therefore, it is possible to map snow through thin cirrus clouds.

**Deleted:** channel

It is noteworthy to mention that the 3.7 μm albedo band cannot be interchanged with the 1.6 μm band for this application. While both the 3.7 μm albedo band and the 1.6 μm band can be used interchangeably to distinguish between water clouds and snow, the 3.7 μm albedo band is more useful for mapping snow through thin cirrus clouds. As noted in Chapter 5, the signature of thin cirrus is simultaneous enhanced while the snow is suppressed in the derived 3.7 μm albedo band. The signature of thin cirrus is enhanced in this band because the methodology used to create it makes the image very similar to a 3.7 – 12.0 μm brightness temperature difference field. Thus, it is the thermal signature of the thin cirrus that is enhanced in the 3.7 μm albedo band. There is no thermal (terrestrial) energy in the 1.6 μm band.

Finally, the signature of snow and water clouds can be very similar in this color composite as seen by the yellowish hue of the stratus clouds located in the San Joaquin Valley and off the California coast. An additional color composite that uses the 1.6 μm band is essential to avoid any confusion between water clouds and snow-covered surfaces.

**Deleted:** channel

## 6.5. COLOR COMPOSITES OF (0.412 μm, 0.865 μm, AND 0.64 μm) CLOUDS OVER ARID REGIONS

The color composite shown in Figure 6.5 was generated using SeaWiFS data collected over the Southwestern US on July 13, 2001. The scene contains a large layer of stratocumulus in the left-bottom corner, to the left of Baja California. The Altar Desert is located in the middle of the scene, and the Gulf of California at the bottom center of the image. Gray-scale images and descriptions of these data are at Figure 5.4 and Figure 5.24.

This color composite was created by assigning the 412 nm or 0.412 μm (M1) band to the red gun, the 0.865 μm (I2) band to the green gun and the 0.64 μm (I1) band to the blue gun. Densely vegetated regions appear green in the composite image, while bare soil, sand, and very sparely vegetated regions appear turquoise, due to the strong contributions of green and blue channels but the absence of red, as discussed in Section 6.3. The 0.412 μm band was identified as an Imagery Assist band in the VIIRS design since albedos over desert have a minimum in this VIIRS bandpass. Therefore, water clouds, when present in desert regions, appear as bright shade of gray (or white) since they strongly reflect energy in each of the bandpasses. Thus, this composite assists in the differentiation between obscurations cause by clouds and perhaps blowing sand in arid environments.

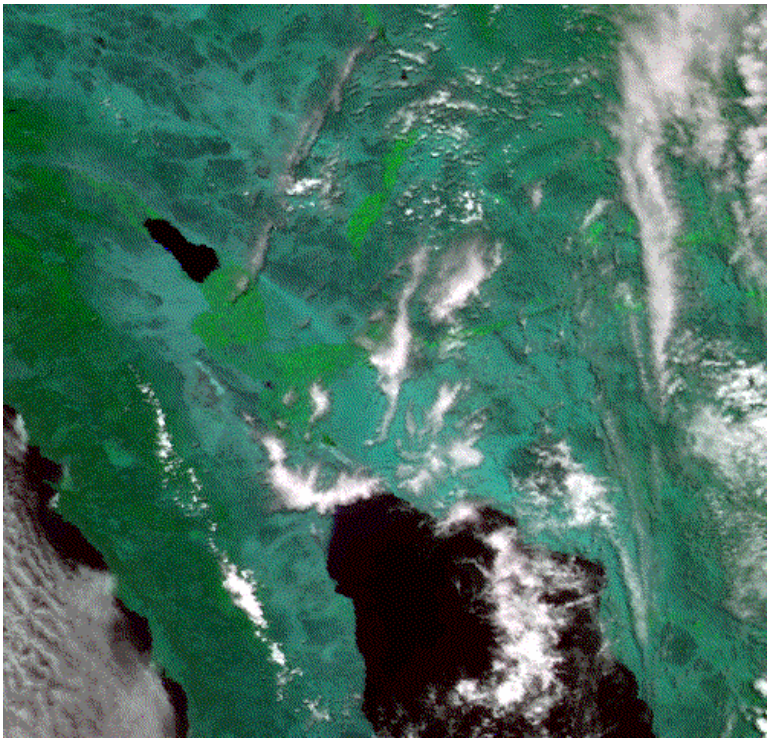

Figure 6.5. Composite image (red = 0.412 μm, green = 0.865 μm, blue = 0.64 μm) for the detection clouds over highly reflective, arid or semi-arid regions.

The strong separation between bare soil (turquoise) and vegetated (green) regions results from the cross-over in reflectivities for these surfaces between 0.64 and 0.865 μm. As seen in Figure 4.8, the reflectivity of bare soil is about 20 percent at the shorter wavelength while that for vegetated land is only 5 percent. At 0.865 μm, the reflectivity for vegetated regions is about 55 percent while that for bare soil is now around 35 percent. In addition, both surface types reflect energy very poorly at 0.412 μm. Therefore, bare vegetated regions contribute mostly in the 0.865 μm band (placed in the green gun of the CRT), while bare soil contributes nearly equally to the green and blue guns. Neither bare soil nor vegetated regions contribute to the red gun. Clouds appear white since they are highly reflective in all bands. The ocean is dark since it does not reflect significant energy in any of the three bands.

Deleted: O

The fact that VIIRS imagery resolution bands have a spatial resolution of 371 m while the imagery assist band has a spatial resolution of 742 m is of little consequence on this or any color composite. However, it is necessary to perform pixel replication on the 0.412 μm band to make all channels have the same number of pixels in the scene. With pixel replication limited to 2:1, no distortion appeared in any of the color composites.

# Chapter 7

# CASE STUDIES IN THE USE OF MULTICOLOR COMPOSITES FOR SCENE INTERPRETATION

## 7.1 OVERVIEW

The principles established in Chapters 5 and 6 will be more fully demonstrated, in Sections 7.2 and 7.3, through the systematic interpretation of MODIS Airborne Simulation (MAS) data collected by NASA's ER-2 aircraft. The MAS sensor collects data in 50 spectral bands between 0.55 and 14.2 μm with a nominal 50 m horizontal spatial resolution across the 37 km swath width when the ER-2 is flown at an altitude of 20 km (King et al., 1996). Thus, MAS collects data in most MODIS and VIIRS bandpasses, except those used primarily for ocean color. Thus, color composites that utilize the 0.412 μm band, as demonstrated in Figure 6.5, cannot be constructed with data from the MAS instrument.

It should be noted that both MODIS and VIIRS have a bandpass at 1.378 μm while its MAS counterpart is in the 1.88 μm channel. Inspection of Figure 4.9 shows that the key atmosphere and land surfaces characteristics are similar in these two bands. While the reflectivities of vegetated land and snow are smaller in the 1.88 μm band than in the 1.378 μm band, additional solar radiation present at the shorter wavelength (seen by inspection of Figure 5.1) supports higher signal-to-noise potential for the shorter wavelength band. Additionally, atmospheric attenuation by water vapor is sufficiently strong in both bands to mask surface reflections in most cases; however, the wider water vapor absorption continuum in the 1.88 μm band reduces the potential for errors in filter bandpasses to impact the utility of the band. As previously noted, the MODIS 30 nm bandpass allows energy from the wings of the strong water vapor absorption line to be collected by the sensor thereby reducing its value for masking surface features in the imagery without special processing of these data.

In the discussion that follows, key spectral bands used to create manually-generated cloud analyses are presented as gray-scale images. These data have been scaled from 32-bit integers, which are collected by the MAS sensor, to 16-bit integers using ENVI, a commercial software package by IDL. Since typical MAS data sets contain 716 pixels across and more than 5000 scan lines, the data were next converted to 8-bit images using Adobe Photoshop, as shown in Figure 7.1, while maintaining a density of approximately 275 pixels $cm^{-1}$. This procedure allows more detailed analyses of the scenes using color composites created from the 8-bit imagery, as shown in Figure 7.2. The color composites are segmented and enlarged, compared to gray-scale images, to reveal more clearly the richness of the features contained within these data sets. Below each image is a table that lists features that (a) can be confirmed, (b) are suspected, or (c) remain ambiguous in each of the color composites. Upon reviewing this chapter, it becomes clear that no single color composite provides sufficient information to analyze all features in most scenes. It is hoped that these images will provide valuable insights into the variety of composites that can be created to suit individual applications.

**Deleted:** (1"x 8")

**Deleted:** 00

**Deleted:** per

**Deleted:** inch

## 7.2 MAS DATA OVER ALASKA

Shown in Figure 7.1 are sample images from 5671 scan lines of MAS data collected over the North Slope of Alaska at approximately 2000 GMT on June 7, 1995. The geographical range for the nadir pixels was 67.88 – 69.51 $^{0}$N and 148.05 – 148.71 $^{0}$W. These data were collected during Flight Track #01 as part of the Arctic Radiation Measurement in Column: Atmosphere-Surface (ARMCAS) campaign. The data were collected specifically to demonstrate the ability to detect and differentiate between clouds, ice, and snow. ARMCAS data can be obtained from the Distributed Active Archive Center (DAAC) at NASA Goddard Space Flight Center (GSFC).

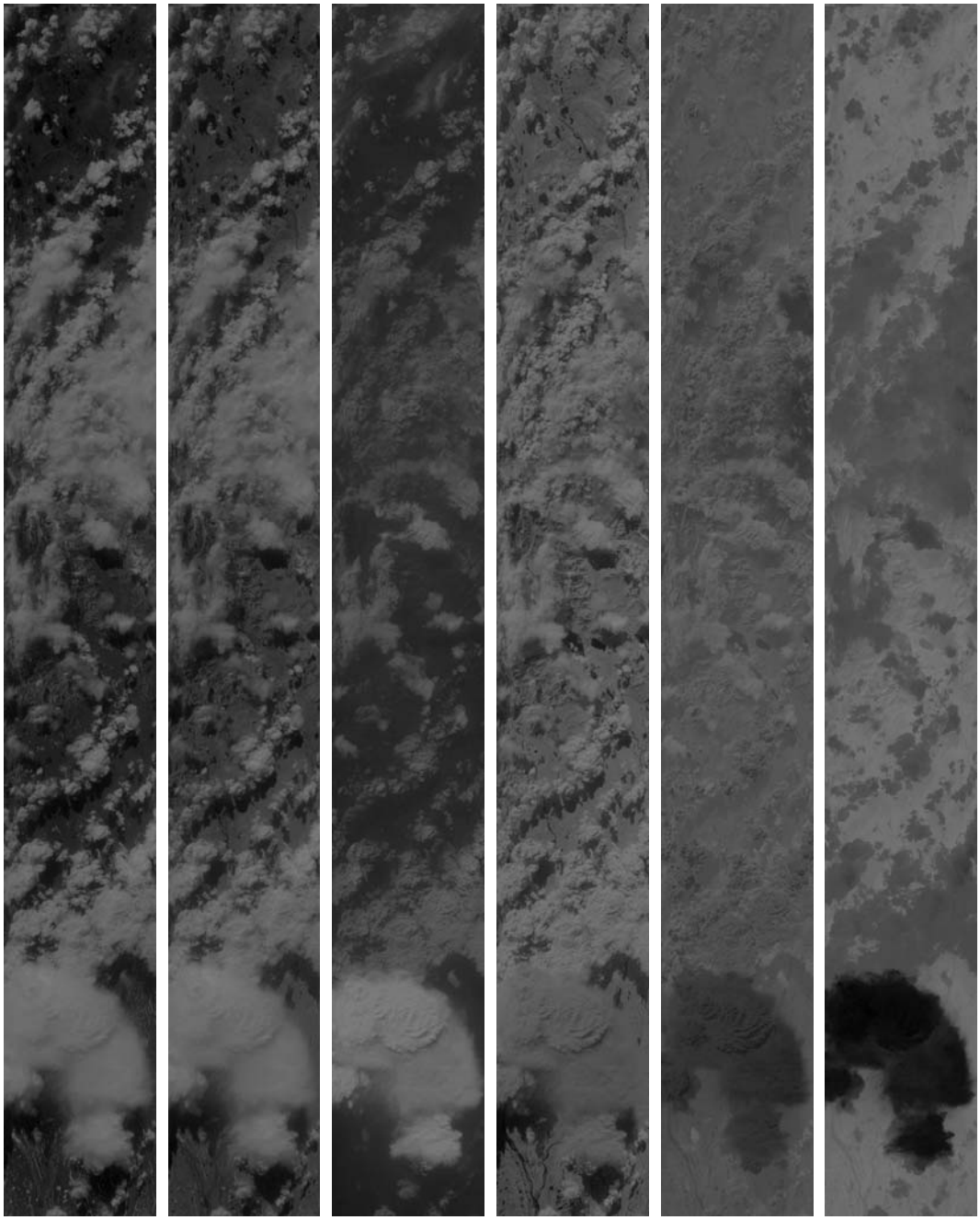

0.645 µm 0.865 µm 1.88 µm 1.61 µm 3.74 µm 11.45 µm

Figure 7.1. Gray-scale MAS imagery collected over the north slope of Alaska during Flight Track #01 on June 7, 1995. Data shown are those MODIS and VIIRS bands needed to interpret cloud and surface features in the scene.

**Deleted:** channels

## COLOR COMPOSITE #1: IDENTIFICATION OF VEGETATED SURFACES

Vegetated regions can be positively identified using the color composite shown in Figure 6.1, where the 0.865 μm band is in the green gun of the CRT and the 0.645 μm band is in both the red and blue guns. Results, shown in Figure 7.2, demonstrate that much of the scene is densely vegetated, as seen by a deep green hue in the color composite. Clouds appear white since they reflect equally in both bands while a pinkish hue is associated with features that are more strongly reflective in the shorter wavelength band. A list of features that can be identified in this composite is given in Table 7.1. Additional composites are needed to confirm the presence of features not uniquely identifiable in this image.

**Deleted:** channels

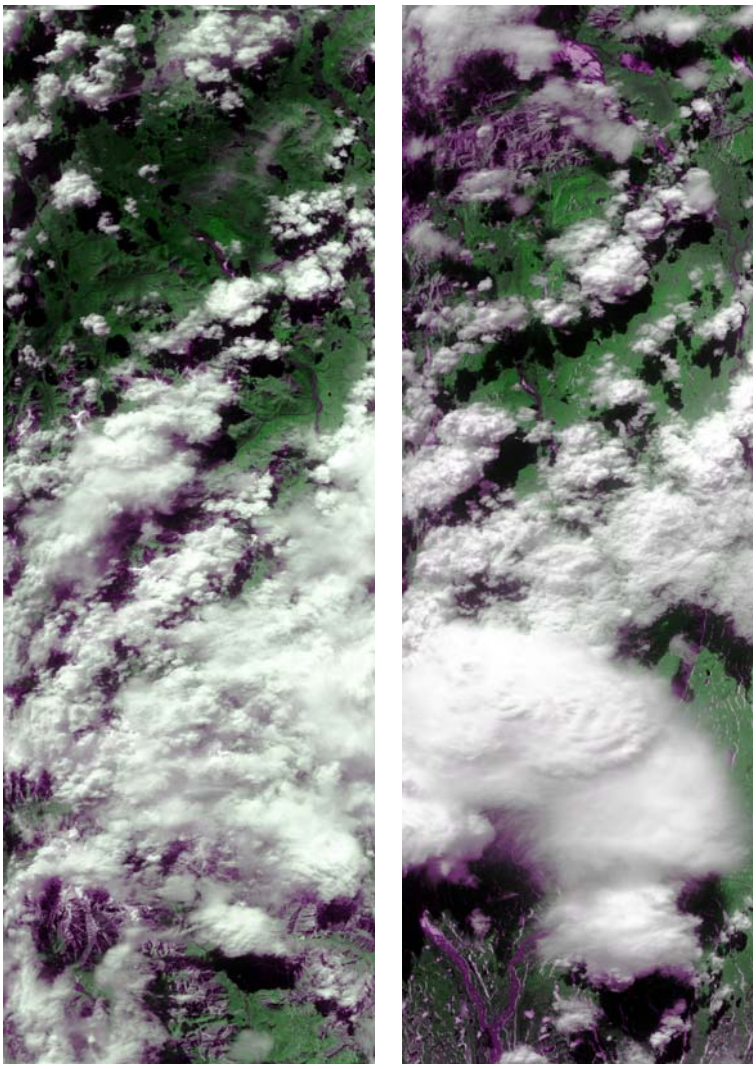

Figure 7.2. Color composite (red = 0.645μm, green = 0.845 μm, blue = 0.645 μm) shows most of the surface is (green) highly vegetated.

Table 7.1. Feature Detection and Identification Based Upon Interpretation of Figure 7.1.

| Feature | Location (Panel and Position, e.g. Left Panel, middle section) | Signature Confirmed, Suspected, or Ambiguous | Comments |
|---|---|---|---|
| Vegetated land | Left and Right Panels, Top to Bottom | Confirmed | Densely vegetated land surfaces confirmed in this composite by dark-green color |
| Sparsely vegetated land | Not present | Not applicable | Would appear shade of gray since sparsely vegetated surface reflect in both bands |
| Water clouds | Left and Right Panels, Top to Bottom | Ambiguous | Water clouds evident but cannot be distinguished from snow fields using only these two bands |
| Ice Clouds | Left and Right Panels, Top to Bottom | Suspected | Ice clouds apparent in several regions by smooth texture of clouds but cloud top phase cannot be confirmed |
| Frozen Water Surfaces | Right Panel, Top to Bottom | Suspected | Frozen surfaces apparent by purple hue, versus dark gray-shade for unfrozen water, and shapes which conform to lakes and rivers. Cannot distinguish frozen rivers from snow. |

## COLOR COMPOSITE #2: IDENTIFICATION OF SNOW AND ICE FEATURES

Regions that contain snow, ice, and potentially glaciated cloud tops can be identified with the addition of the 1.61 μm band in the color composite shown in Figure 7.3. Snow and frozen water surfaces appear yellowish in this image since they are highly reflective in the 0.645 and 0.865 μm bands but reflect poorly in the 1.61 μm band. Water clouds are highly reflective in each of these bands and appear white while clouds with glaciated tops have a yellowish hue and in some case a smooth texture, typical of cirrus. Many cloud-free surfaces appear blue-green since they are highly reflective in both the 0.865 and 1.61 μm bands (Hutchison, 1999). A list of features that can be identified in this composite is given in Table 7.2.

Deleted: channel

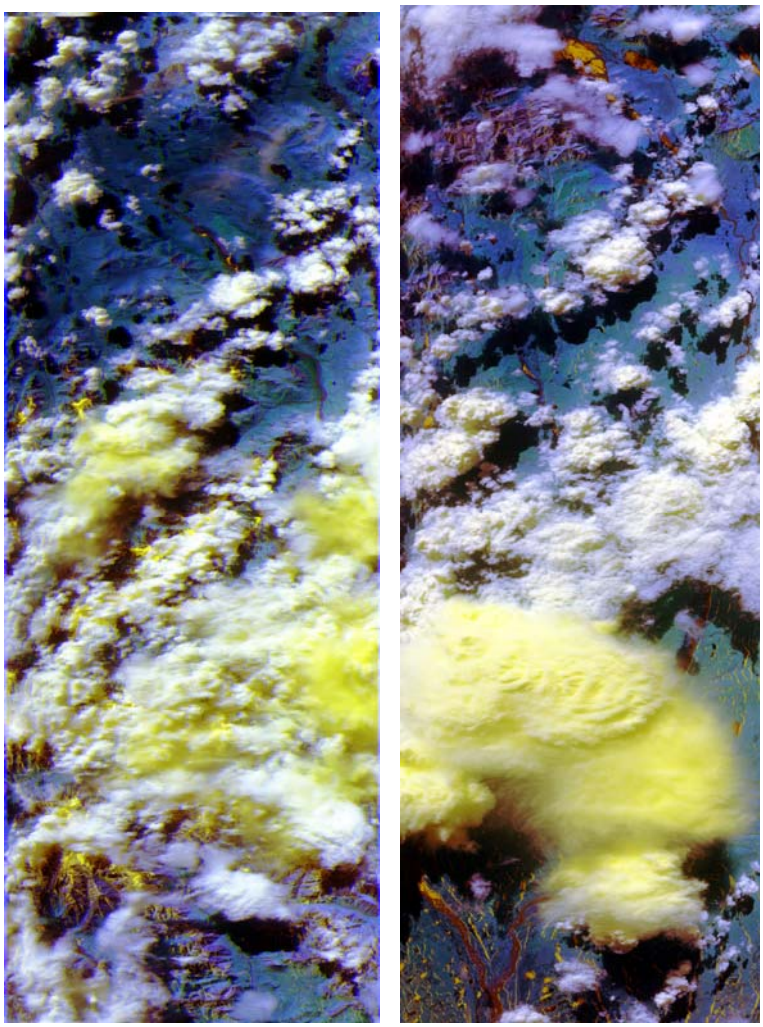

Figure 7.3. Color composite (red = 0.645μm, green = 0.845 μm, blue = 1.61 μm) shows snow, ice, and glaciated clouds as yellow. Notice the smooth texture associated with cirrus clouds.

Table 7.2. Feature Detection and Identification Based Upon Interpretation of Figure 7.3.

| Feature | Location (Panel and Position, e.g. Left Panel, middle section) | Signature Confirmed, Suspected, or Ambiguous | Comments |
|---|---|---|---|
| Vegetated land | Left and Right Panels, Top to Bottom | Suspected | Both densely and sparsely vegetated land surfaces appear blue since both are highly reflective in the 0.845 μm and 1.61 μm bands |
| Sparsely vegetated land | Not present | Not applicable | Would have bluish hue since sparsely vegetated surfaces reflect most strongly in the longest wavelength and least in the shortest wavelength |
| Water clouds | Left and Right Panels, Top to Bottom | Suspected | Water clouds appear white and can be distinguished from ice and snow fields (yellowish). Thin cirrus may also appear white, especially if over sparsely vegetated surfaces where reflectivity of the 1.61 μm band is large and overwhelms the reduced reflectivity of ice crystals |
| Ice Clouds | Left and Right Panels, Top to Bottom | Confirmed | Ice clouds apparent in several regions by yellow appearance and smooth texture. Some thin cirrus may be erroneously classified as water clouds as discussed above |
| Frozen Water Surfaces | Right Panel, Top to Bottom | Confirmed | Frozen surfaces apparent by yellow hue, versus dark gray-shade for unfrozen water, and shapes which conform to lakes and rivers. May not be able to distinguish frozen rivers from snow. |

**Deleted:** channel

## COLOR COMPOSITE #3: CLOUD TYPE CLASSIFICATION – PART I

Figure 7.4 is a robust composite for multi-feature image analyses and demonstrates the value of VIIRS imagery for cloud classifications using the 0.645 μm in the red gun, 1.88 (1.378) μm band in the green gun, and the 11.45 μm band in the blue gun of the CRT. A list of features that can be identified in this composite is given in Table 7.3.

Starting with the top of the left panel, regions of very thin cirrus are shown in green while towering cumulus appear white. The green appearance results from a strong contribution from the green gun and negligible contributions from the red and blue guns. The strong response in the green gun occurs because the clouds occur high in the atmosphere, above the water vapor regions near the Earth's surface. The poor responses in the blue and red guns occur because thin cirrus is optically thin in the 11.45 μm band, which allows energy from the relatively warm surface to pass unattenuated to the sensor, and cirrus reflects poorly in the 0.645 μm band respectively. Thus thin cirrus produces its strongest contribution to the green gun of this color composite. On the other hand, thicker (whitish) clouds are seen embedded within the areas of cirrus. These thicker clouds are towering cumulus cells, which are both highly reflective, producing a strong response in the red gun, and relatively cold, producing a strong response in the blue gun for IR data displayed in the inverted mode. Towering cumulus are readily differentiated from lower-level clouds by the strong contributions from the green gun which does not exist with lower-level water clouds in the 1.378 μm band. Thus, towering cumulus clouds appear white in this composite. (It is worth noting that the distinction between towering cumulus and lower-level cumulus fields is less evident with MODIS data collected by Terra and Aqua due to the large bandwidth of the 1.378 μm band which allows energy from the lower-level clouds to reach the sensor. This oversight has been corrected in the design of VIIRS.)

**Deleted:** channel

**Deleted:** i

**Deleted:** channel

Moving toward the middle and lower section of the left panel, the dramatic differences become evident between optically thick water clouds and towering cumulus clouds in this composite image. Lower level water clouds appear pinkish because the red gun of the CRT receives significantly more energy than the green and blue guns. The strong red gun contribution occurs because water clouds reflect strongly in the 0.645 μm band. Responses in the green and blue guns decrease as cloud top heights become lower since less reflected energy arrives at the sensor from the 1.378 (1.88) μm band assigned to the green gun and the cloud top temperature in the 11.45 μm band become warmer. Some water clouds in these regions have a turquoise appearance indicative of lower energy contributions in the red gun of the CRT. In some instances, this turquoise color results from shadows from higher clouds that reduce the reflected energy received by the sensor from lower-level water clouds. Shadows are often seen in high resolution imagery and can be observed most easily in the gray-scale images shown in Figure 7.1. A large shadow is shown on the lower side of the large towering cumulus seen at the bottom of the image in the left panel.

Turning to the right panel of Figure 7.3, the most dominant feature seen is the large thunderstorm located near the bottom of the image. It is evident that this is an active thunderstorm since the texture of the cumuliform cell is seen above the cirrus outflow from the storm, i.e. the storm has an "overshooting top" characteristic of an active, severe

thunderstorm. In addition, notice that the cirrus associated with this cloud system is white, which means that the cirrus is thick, i.e. cold in the IR band and highly reflective in the solar bands. The turquoise hue along the right edge of the large cirrus region results from a decrease in the red gun and indicates that the cirrus becomes optically thinner along this border. Variations in humidity can also be seen in this composite by examining cloud free features. A purplish hue at the bottom of this panel indicates highly reflective and more humid regions while the greenish-brown clour along the right side of the panel shows drier areas that allow surface contributions to be recorded in the 1.88 μm band.

**Deleted:** d

**Deleted:** Regions of

**Deleted:** d

**Deleted:** regions

**Deleted:** very

**Deleted:** y

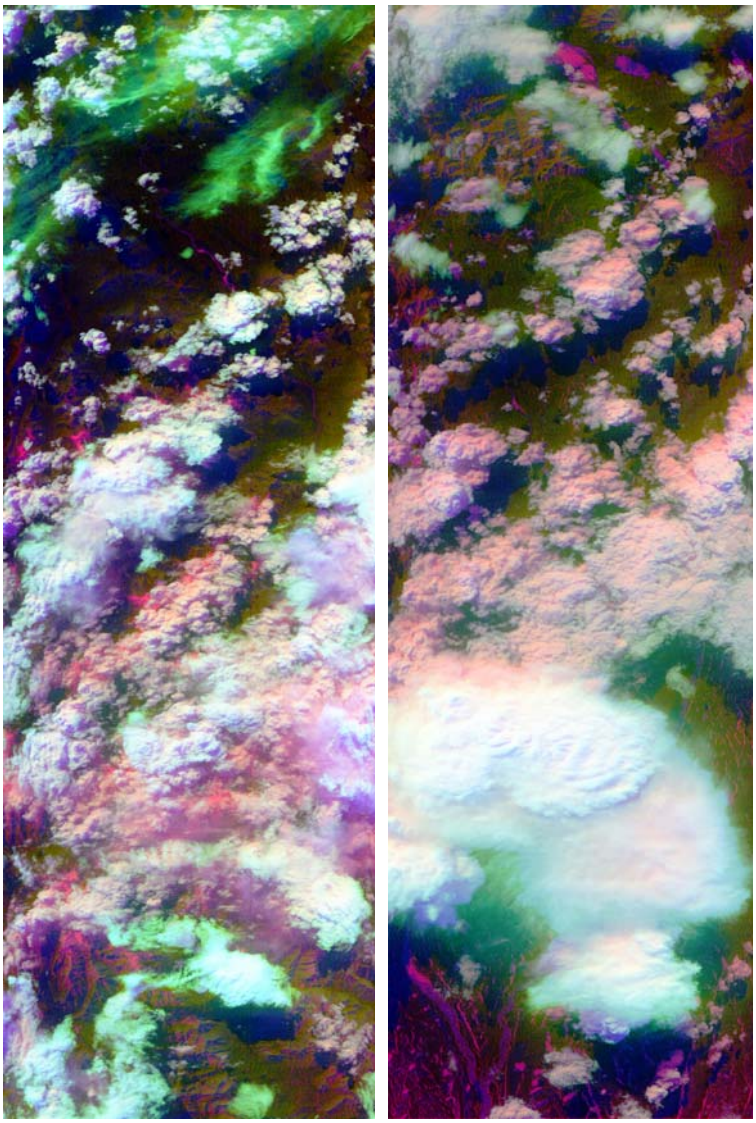

Figure 7.4. Color composite (red = 0.645 μm, green = 1.88 μm, blue = 11.45 μm) provides valuable information for cloud type, surface, and atmospheric moisture classifications.

Table 7.3. Feature Detection and Identification Based Upon Interpretation of Figure 7.4.

| Feature | Location (Panel and Position, e.g. Left Panel, middle section) | Signature Confirmed, Suspected, or Ambiguous | Comments |
|---|---|---|---|
| Vegetated land | Left and Right Panels, Top to Bottom | Suspected | Densely vegetated land surfaces appear dark, possibly with blue tint depending upon surface temperatures. |
| Sparsely vegetated land | Not present | Not applicable | Sparsely vegetated surfaces have a reddish hue, possibly taking on a purplish color if surface temperatures are low |
| Water clouds | Left and Right Panels, Top to Bottom | Confirmed | Lower-level water clouds are reddish due to strong reflectivity in 0.645 μm band, relatively warm cloud top temperatures in the 11.45 μm band, and poor reflectivity in the 1.88 μm band caused by atmospheric absorption above the cloud top.<br><br>Middle-level water clouds have a bluish-gray hue due to strong reflectivity in solar bands and lower cloud top temperatures. |
| Ice Clouds | Left and Right Panels, Top to Bottom | Confirmed | Optically-thin cirrus clouds have a greenish hue which arises from the signature in the 1.88 μm band, where low-level surface features are masked.<br><br>Optically-thick cirrus clouds appear a shade of gray (white) since they are highly reflective in both solar bands and relatively cold |
| Frozen Water Surfaces | Right Panel, Top to Bottom | Confirmed | Frozen surfaces apparent by reddish hue, due to higher reflectivity in 0.645 μm band and lower surface temperatures. May be difficult to detect compared to other composites, e.g. Figure 7.3. |

## COLOR COMPOSITE #4: CLOUD TYPE CLASSIFICATION – PART II

Figure 7.5 demonstrates the subtle variations possible for using VIIRS imagery for cloud classification. In this case, the 0.645 μm band is placed in the red gun, 0.865 μm band in the green gun, and the 11.45 μm band in the blue gun of the CRT. This combination is aimed at differentiating between cloud top heights of optically-thick (water) clouds. Optically thick clouds, e.g. water clouds, are highly reflective and appear yellowish in this composite, in the absence of a strong blue component. Thus, low level water clouds are nicely contrasted against vegetated surfaces as seen in both panels of this figure. As the clouds become higher, and colder, the color gradually shifts from yellow to grayish and becomes white when the clouds are both highly reflective in the solar bands and cold in the IR band. A list of features identified with this composite is given in Table 7.4.

**Deleted:** channels

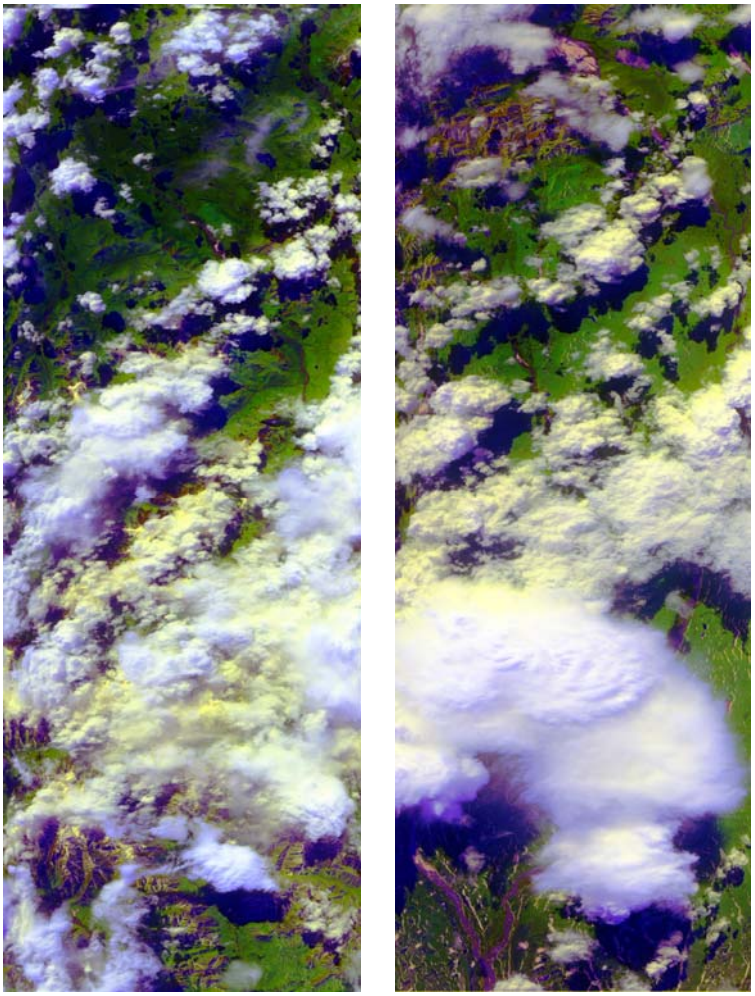

Figure 7.5. Color composite (red = 0.645 μm, green = 0.865 μm, blue = 11.45 μm) provides useful information on surface features and cloud top temperatures and heights.

Table 7.4. Feature Detection and Identification Based Upon Interpretation of Figure 7.5.

| Feature | Location (Panel and Position, e.g. Left Panel, middle section) | Signature Confirmed, Suspected, or Ambiguous | Comments |
|---|---|---|---|
| Vegetated land | Left and Right Panels, Top to Bottom | Suspected | Densely vegetated land surfaces appear dark with greenish hue, possible mixed with blue tint, depending upon surface temperatures. Sparsely vegetated surfaces appear brighter due to stronger reflectivities in solar bands |
| Sparsely vegetated land | Not present | Not applicable | Would appear grayish if surfaces are warm to blue if surface temperatures are cold |
| Water clouds | Left and Right Panels, Top to Bottom | Confirmed | Lower-level water clouds appear reddish due to strong reflectivity in shorter solar band and relatively warm cloud top temperatures. |
| Ice Clouds | Left and Right Panels, Top to Bottom | Confirmed | Ice clouds apparent in several regions by blue-greenish hue which arises from low reflectivity in 1.61 μm band and lower temperatures in 11.45 m band |
| Frozen Water Surfaces | Right Panel, Top to Bottom | Confirmed | Frozen surfaces apparent by reddish hue, due to higher reflectivity in 0.645 μm and lower surface temperatures. May be difficult to detect compared to other composites, e.g. Figure 7.3. |

## 7.3 MAS SUCCESS DATA COLLECTED OVER COLORADO

Deleted: E

Shown in Figure 7.6 are sample images from 5678 scan lines of MAS data collected over the mountains west of Denver, Colorado at approximately 2100 GMT on May 2, 1996. The geographic range for the nadir pixels was 39.91 – 39.66 $^{0}$N and 107.51 – 105.25 $^{0}$W. These data were collected during Flight Track #24 as part of the Subsonic Aircraft Contrail and Cloud Effects – Special Study (SUCCESS) campaign. The data were collected specifically to investigate the effects of subsonic aircraft on high-level clouds and atmospheric chemistry to improve our knowledge of the radiative properties of cirrus clouds and contrails and their impact on the Earth's radiation budget. SUCCESS data can also be obtained from the NASA GSFC DAAC.

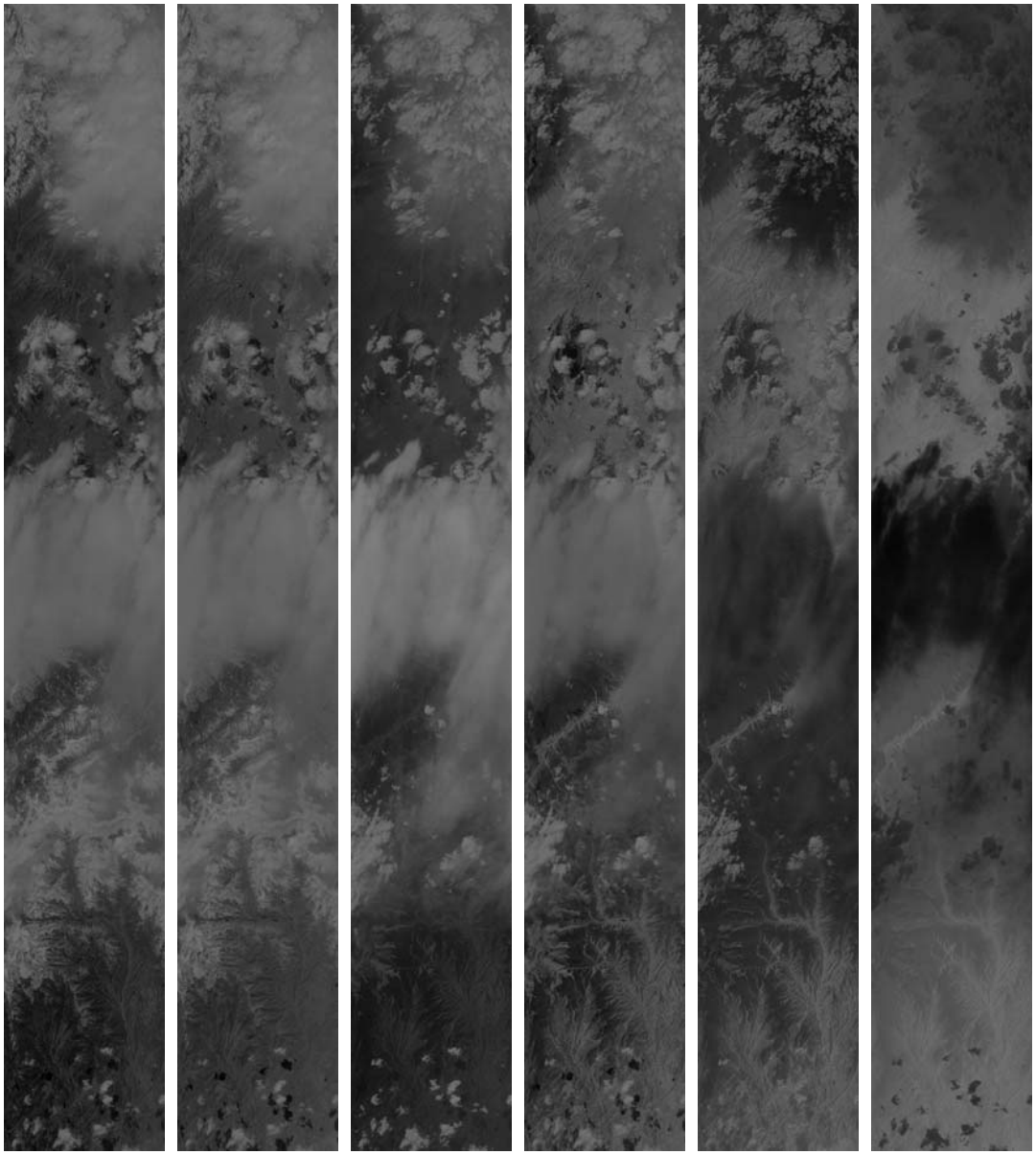

0.645 µm 0.865 µm 1.88 µm 1.61 µm 3.74 µm 11.45 µm

Figure 7.6. Gray-scale imagery collected over Colorado during Flight Track #26 of the MODIS Airborne Simulator on July 5, 1995. Data shown are those MODIS and VIIRS bands needed to interpret features in the scene.

**Deleted:** channels

## COLOR COMPOSITE #1: IDENTIFICATION OF VEGETATED SURFACES

Interpretation of this MAS data over Colorado follows the example shown in Section 7.2. Vegetated regions are confirmed using the color composite shown in Figure 7.7, where the 0.865 μm band is in the green gun of the CRT and the 0.645 μm band is in both the red and blue guns. This scene contains small densely vegetated areas, which appear as deep green. Clouds, snow, and sparsely vegetated regions appear as a lighter shade of gray. A list of features that can be identified in this composite is given in Table 7.5. Additional composites are needed to confirm features not uniquely identifiable in this image.

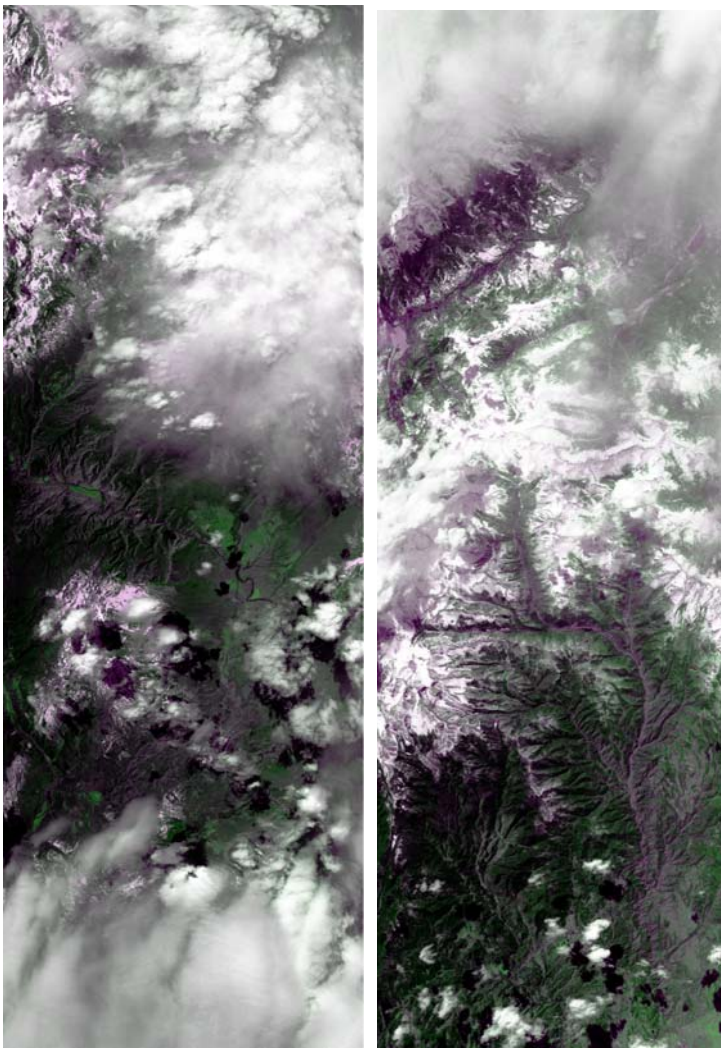

Figure 7.7. Color composite (red = 0.645μm, green = 0.845 μm, blue = 0.645 μm) shows most of the surface is not (green) highly vegetated.

Table 7.5. Feature Detection and Identification Based Upon Interpretation of Figure 7.7.

| Feature | Location (Panel and Position, e.g. Left Panel, middle section) | Signature Confirmed, Suspected, or Ambiguous | Comments |
|---|---|---|---|
| Vegetated land | Left and Right Panels, Top to Bottom | Confirmed | Densely vegetated land surfaces confirmed in this composite by dark-green color |
| Sparsely vegetated land | Center of left and right panels | Suspected | Cannot distinguish sparsely vegetated surfaces from snow and some cloud fields |
| Water clouds | Left and Right Panels, Top to Bottom | Ambiguous | Water clouds evident but cannot be distinguished from snow fields, especially in right panel |
| Ice Clouds | Left and Right Panels, Top to Bottom | Suspected | Ice clouds apparent in several regions by smooth texture of clouds but difficult to distinguish from snow, especially in right panel |
| Frozen Water Surfaces | Right Panel, Top to Bottom | Ambiguous | Some frozen surfaces have a purplish hue, versus dark gray-shade for unfrozen water, but cannot distinguish frozen rivers from snow or frozen surfaces from clouds. |

## COLOR COMPOSITE #2: IDENTIFICATION OF SNOW AND ICE FEATURES

As previously shown in Figure 7.3, regions that contain snow, ice, and possibly glaciated cloud tops can be readily identified with the addition of the 1.61 μm band in the color composite shown in Figure 7.8. Frozen surfaces appear yellow in this image while many cloud-free surfaces appear blue. Optically thick clouds (water and cirrus) remain white but optically thin clouds with glaciated tops have a yellowish hue. The features that are identifiable in this composite are given in Table 7.6.

**Deleted:** channel

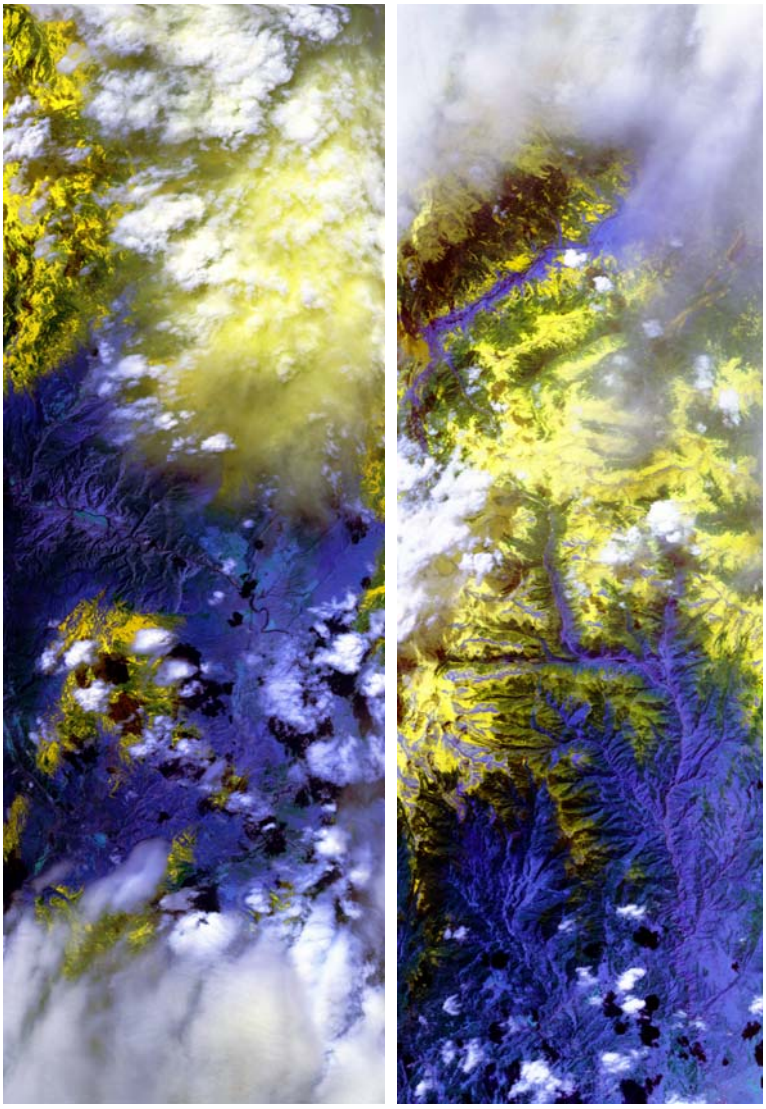

Figure 7.8. Color composite (red = 0.645μm, green = 0.845 μm, blue = 1.61 μm) shows snow, ice, and glaciated (optically-thin) clouds as yellow. Thicker clouds remain white.

Table 7.6. Feature Detection and Identification Based Upon Interpretation of Figure 7.8.

| Feature | Location (Panel and Position, e.g. Left Panel, middle section) | Signature Confirmed, Suspected, or Ambiguous | Comments |
|---|---|---|---|
| Vegetated land | Left and Right Panels, Top to Bottom | Suspected | Both densely and sparsely vegetated land surfaces appear blue since both are highly reflective in the green and blue guns |
| Sparsely vegetated land | Center of left and right panels | Suspected | Has a bluish hue since reflectivity increases with wavelength in this composite |
| Water clouds | Left and Right Panels, Top to Bottom | Suspected | Water clouds appear white and can be distinguished from ice and snow fields (yellowish). Thin cirrus may also appear white, especially if over sparsely vegetated surfaces where the reflectivity of the 1.61 μm band is large and overwhelms the reduced reflectivity of ice crystals |
| Ice Clouds | Left and Right Panels, Top to Bottom | Confirmed | Ice clouds apparent in several regions by yellow appearance and smooth texture. Some thin cirrus may be erroneously classified as water clouds as discussed above |
| Frozen Water Surfaces | Right Panel, Top to Bottom | Confirmed | Frozen surfaces apparent by yellow hue, versus dark gray-shade for unfrozen water, and shapes which conform to lakes and rivers. May not be able to distinguish frozen rivers from snow. |

**Deleted:** channel

## Color Composite #3: CLOUD TYPE CLASSIFICATION – PART I

Figure 7.9 is again used for multi-feature image analyses including cloud type classification. The composite is made by placing the 0.645 μm in the red gun, 1.88 (1.378) μm band in the green gun, and the 11.45 μm band in the blue gun of the CRT as shown earlier in Figure 7.4. A list of features that can be identified in this composite is given in Table 7.7.

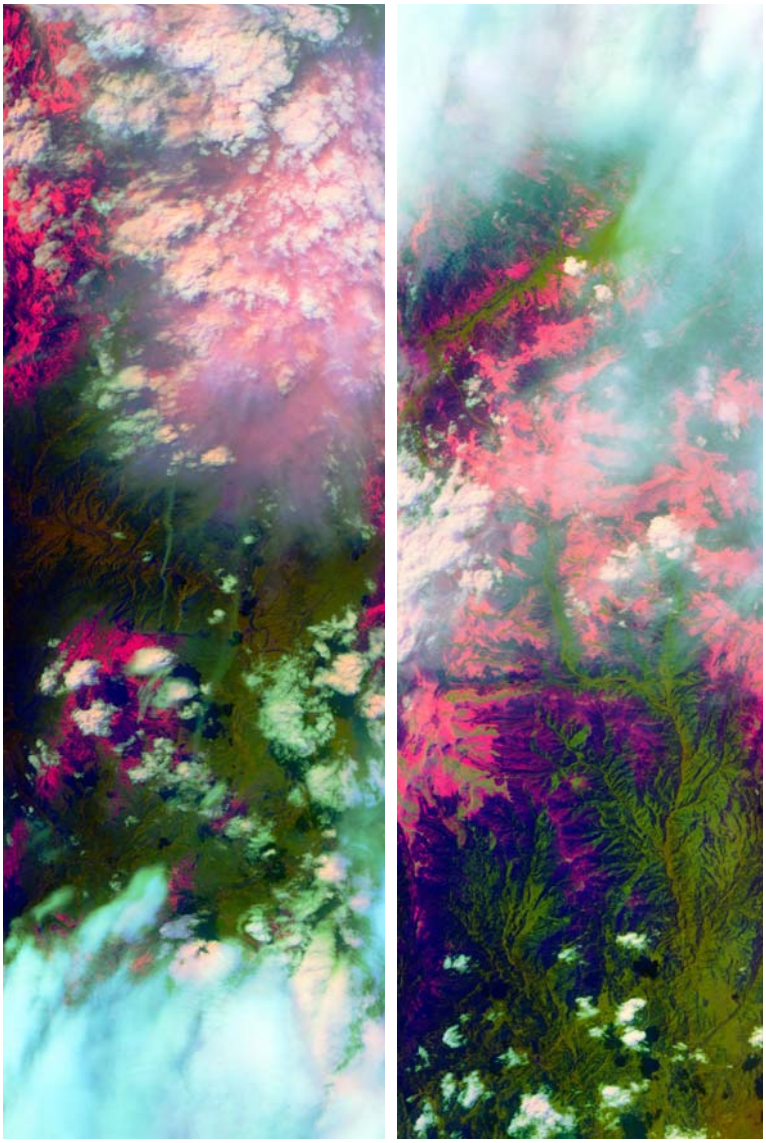

Figure 7.9. Color composite (red = 0.645 μm, green = 1.88 μm, blue = 11.45 μm) provides information on cloud type, surface, and atmospheric moisture classifications.

In the top left corner of the left panel through the lower right panel, snow covered surfaces continue to appear red-purplish in the color composite since the contributions to the composite are primarily from the 0.645 μm band with secondary contributions from the 11.45 μm band. The 1.88 μm band provides no contribution.

Deleted: channel

On the other hand, optically-thin cirrus no longer appears green in this composite, as it did in Figure 7.4. In Figure 7.9, cirrus appears bluish to gray, which reflects colder temperatures in the 11.45 μm band in this image. The grayish hue results from nearly equal contributions for both solar and IR bands, since these clouds are highly reflective and quite cold. The bluish hue in the top half of the right panel suggests colder surface temperatures or more dense cirrus, though still optically-thin, than present in the top left panel of Figure 7.4. Clearly, surface temperatures are causing the bluish hue in the middle-right panel, where snow can be seen through the thin cirrus clouds, but multi-layered clouds cause the bluish hue at the top of this same panel. In the top of the left panel, some clouds have rose-colored hue and become bluish. The rose color occurs when the primary contribution is from the red gun and becomes increasingly more gray as the contribution increases in the green gun. The deeper reddish clouds must be lower-level clouds compared to the more blue-gray colored clouds. Therefore, it is possible to differentiate between lower-level and middle-level clouds. Additionally, this image provides information on the presence of both single and multi-layered cloud conditions when cirrus is present.

Evidence of the low atmospheric humidity is also seen in this color composite. In the middle-left and lower-right panels, the greenish hue indicates a primary contribution from the green gun with a secondary contribution from the red gun. The strong signature in the green gun suggests very low-levels of water vapor in the atmosphere since the surface can be seen in the 1.88 μm band. Of course, shadows of clouds cause variations in cloud-free surfaces of this composite. Shadows are readily seen to the right of the cumuliform clouds near the middle of the left panel and near the bottom of the right panel.

Deleted: are

Deleted: channel

Table 7.7. Feature Detection and Identification Based Upon Interpretation of Figure 7.9.

| Feature | Location (Panel and Position, e.g. Left Panel, middle section) | Signature Confirmed, Suspected, or Ambiguous | Comments |
|---|---|---|---|
| Vegetated land | Middle of Left Panel and Lower Half of Right Panels | Confirmed | Densely vegetated land surfaces appear dark with greenish hue, possibly mixed with blue tint, depending upon surface temperatures. Sparsely vegetated surfaces appear brighter due to stronger reflectivities in the solar bands |
| Sparsely vegetated land | Center of left and right panels | Suspected | Features appear reddish to purple if surface temperatures are sufficiently cold |
| Water clouds | Left and Right Panels, Top to Bottom | Confirmed | Lower-level water clouds are reddish due to strong reflectivity in 0.645 μm band, relatively warm cloud top temperatures in 11.45 μm, and lower reflectivity in 1.88 μm band, even if relatively dry atmosphere.<br><br>Middle-level water clouds have a pinkish-bluish-gray (white) hue due to strong reflectivity in the solar bands and lower cloud top temperatures. |
| Ice Clouds | Left and Right Panels, Top to Bottom | Confirmed | Optically-thin cirrus clouds have a bluish hue which arises from the signature in the 1.88 and 11.45 μm bands, when low-level surface features are not fully masked.<br><br>Optically-thick cirrus clouds appear a shade of gray (white) since they are highly reflective in both solar bands and relatively cold |
| Frozen Water and Snow Surfaces | Left Panel, Top to Middle along left half of scene, Right Panl, middles of scene | Confirmed | Frozen surfaces apparent by reddish hue, due to higher reflectivity in 0.645 μm and lower surface temperatures. |

## Color Composite #4: CLOUD TYPE CLASSIFICATION – PART II

The final color composite for routine analyses is shown in Figure 7.10. The 0.645 μm band is placed in the red gun, 0.865 μm band in the green gun, and the 11.45 μm band in the blue gun of the CRT to help differentiate between cloud top heights of optically-thick (water and cirrus) clouds as discussed in Figure 7.5. Notice that in this image, the water and optically-thick cirrus (i.e. cold clouds) appear white while all others take on a bluish hue. A list of features that can be identified in this composite is given in Table 7.8.

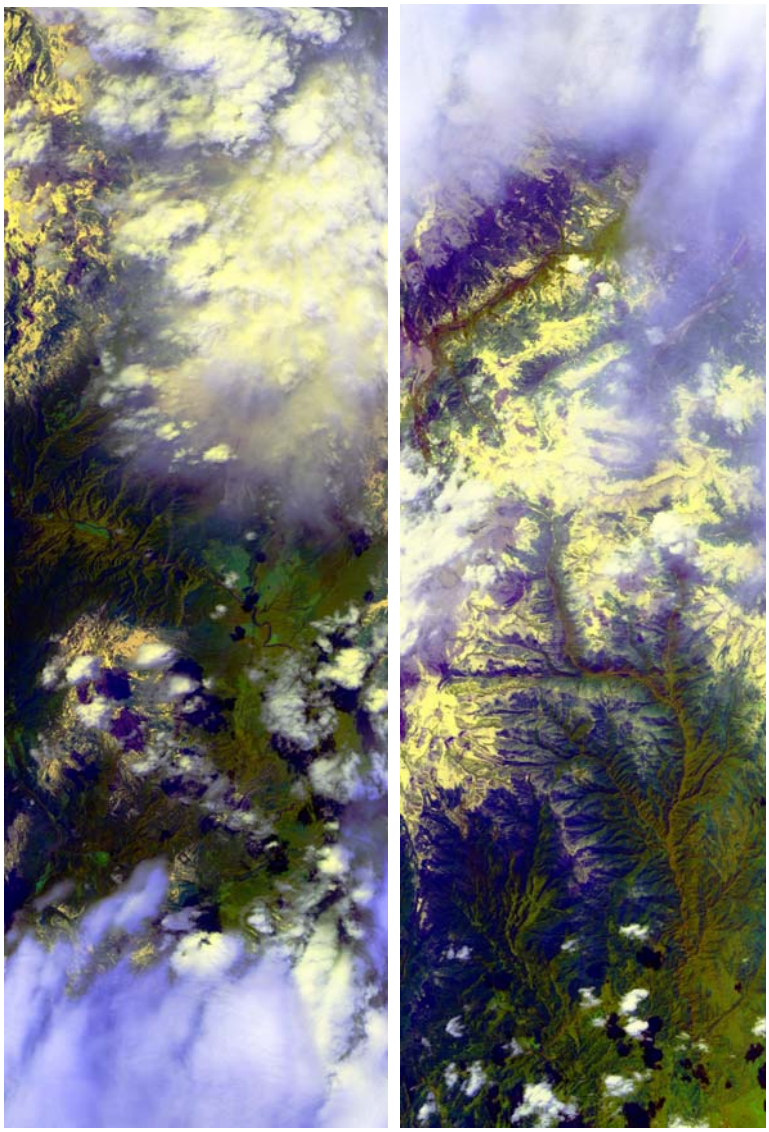

Figure 7.10. Color composite (red = 0.645 μm, green = 0.865 μm, blue = 11.45 μm) provides useful information on surface features and cloud top temperatures and heights.

Table 7.8. Feature Detection and Identification Based Upon Interpretation of Figure 7.10.

| Feature | Location (Panel and Position, e.g. Left Panel, middle section) | Signature Confirmed, Suspected, or Ambiguous | Comments |
|---|---|---|---|
| Vegetated land | Middle of Left Panel and Lower Half of Right Panels | Confirmed | Densely vegetated land surfaces appear dark with greenish hue, possibly mixed with blue tint, depending upon surface temperatures. Sparsely vegetated surfaces appear brighter due to stronger reflectivities in the solar bands |
| Sparsely vegetated land | Center of Left and Right Panels | Suspected | Surfaces appear gray if surfaces are warm to bluish if they are cold |
| Water clouds | Left and Right Panels, Top to Bottom | Ambiguous | Lower-level water clouds appear yellowish, from strong reflectivity in the shorter solar wavelengths, to gray depending upon cloud top temperatures. It may be difficult to distinguish between these clouds and snow fields in this composite |
| Ice Clouds | Left and Right Panels, Top to Bottom | Confirmed | Ice clouds apparent in several regions by bluish hue which arises from low reflectivity in solar band coupled with lower temperatures in 11.45 μm band. Texture is also important in determining the presence of ice clouds |
| Frozen Water Surfaces | Right Panel, Top to Bottom | Ambiguous | Frozen surfaces appear yellowish due to higher reflectivity in both solar bands, which also is a characteristic of water clouds. |

# Chapter 8

# AUTOMATED 3-DIMENSIONAL CLOUD ANALYSES FROM NPOESS

## 8.1 ARCHITECTURE FOR 3-DIMENSIONAL CLOUD ANALYSES

In this chapter, an overview is provided of an approach to exploit many of the cloud signatures described in previous chapters to generate automated 3-dimensional (3D) cloud analyses from multiple sensors carried on NASA EOS and NPOESS satellites, e.g. VIIRS and CMIS or MODIS and AMSU sensors. In some cases there are a variety of approaches to retrieve certain cloud properties, e.g. a pixel-level cloud/no cloud mask. In these cases, the procedures described below are based upon a variety of articles published in the refereed literature (Hutchison, 2002; Hutchison, 1999; Hutchison et al., 1997b; Hutchison and Hardy, 1995).

**Deleted:** cloud, no cloud

The architecture for 3D cloud analyses (3DCLOUDS) is shown in Figure 8.1. This architecture requires many processing functions, which will be discussed in subsequent sections, including:.

**Deleted:** the

a. Analyses of VIIRS data
    1. Automated cloud detection to generate a VIIRS cloud mask,
    2. Cloud top phase classification (ice, water, mixed phase, and multi-layers),
    3. Cloud optical properties (optical depth and effective particle size),
    4. Cloud top properties (height, pressure, and temperature), and
    5. Cloud base height.
b. Analyses of CMIS data
    1. Conversion of the VIIRS cloud mask analyses to CMIS resolution,
    2. Total Precipitable Water (TPW)
    3. Cloud liquid/ice water path (LWP or IWP)
    4. Atmospheric profiles (temperature and moisture) and
    5. Cloud base height (constrained by VIIRS cloud top temperatures).
c. Merge processes
    1. If the VIIRS cloud optical depth exceeds the measurement range, replace optical depth with CMIS LWP,
    2. Use of a rule-based system to identify best satellite cloud base report,
    3. Integrate conventional cloud base height observations with satellite observations

A 3-dimensional cloud analysis begins with the creation of an automated, pixel-level binary cloud/no cloud analysis, which becomes the basis of all additional cloud products. The approach is based upon a series of bi-spectral cloud tests first described by Saunders and Kriebel (1988). It is modified by (1) using threshold functions for the analysis of global multispectral imagery and (2) including new cloud detection tests to exploit satellite data that have become available with MODIS but were not collected by AVHRR, such as the 0.412 μm band (Hutchison and Jackson, 2003; Hutchison and Choe, 1996; Hutchison and Hardy, 1995).

**Deleted:** cloud, no cloud

Next cloud phase is determined since separate processing paths are followed for ice and water clouds to obtain other cloud parameters, i.e. from cloud optical properties, cloud top parameters, and cloud base heights. The procedure used by NASA for cloud phase is highlighted (Menzel and Stabala, 1997); however, new research suggests this approach may soon be updated with the approach described by Pavolonis and Heidinger (2004). The current NASA algorithm produces four classes of clouds: (a) ice, (b) water, (c) mixed-phase, and (d) ambiguous. However, the Pavolonis and Heidinger algorithm produces (a) ice, (b) water, (c) multilayered, and (d) mixed. The ability to identify multilayered clouds within a single pixel is important since subsequent algorithms assume a single cloud layer in each pixel. Thus, knowledge about the presence of multilayered clouds allows a quality flag to identify retrievals that may be subject to larger errors. In addition, cloud top pressures from the IR sounder can be used to resolve ambiguities in cloud phase (Hutchison et al., 1997a).

**Deleted:** an

**Deleted:** i

**Deleted:** 3

**Deleted:** i

Two approaches can be used to the cloud optical properties. One exploits solar scattering in the near IR bands during daytime while the other uses thermal emissions in the longer IR bands. The former is an approach developed by NASA (King et al., 1997) while the latter is unique to the NPOESS program (Ou et al., 2002). The approach taken by Ou et al. is examined in detail.

Once cloud optical properties are retrieved, cloud top parameters (i.e. temperature, pressure, and height) are analyzed as the final inputs needed in the retrieval of the VIIRS cloud base heights product. The approach described assumes that optically thin clouds may be present in both ice and water phase. Thus, energy from below the cloud can arrive at the sensor unattenuated. The methodology employed corrects brightness temperatures for this source of contamination to produce improved cloud top temperature analyses.

The final cloud product from VIIRS data is the cloud base height EDR (Hutchison, 2002). The approach converts the cloud optical thickness into a geometric thickness based upon the cloud type and current knowledge of microphysical properties of the cloud. However, it assumed that cloud liquid water concentration (LWC) and ice water concentration (IWC) are constant through the vertical path of the cloud, which is not correct. A method to retrieve profiles of LWC and IWC from NPOESS data remains an area of research.

**Deleted:** s

**Deleted:** Unfortunately, a

Analyses of VIIRS data are supplemented by processing in the microwave chain, including the use of LWP from microwave imagery to extend the VIIRS cloud base height product. However, over ocean surfaces, the microwave moisture sounder can also be used to retrieve an independent measure of cloud base height, at a more coarse spatial resolution (Wilheit and Hutchison, 2000). To obtain a microwave cloud base height, it is necessary first to retrieve total precipitable water which is a constraint on the retrieval of moisture profiles (Wilheit et al., 1994). Next, a temperature profile is retrieved using the iterative physical relaxation algorithm described by Rosenkranz et al (1997). These data are needed, along with the VIIRS cloud top temperature, to produce the most accurate moisture profile from the microwave moisture sounder (Wilheit and Hutchison, 1997) and finally the microwave cloud base height. Since the methodology is not germane to

**Deleted:** P

this text and a full description of these algorithms would be lengthy, the approach to retrieve cloud base heights from microwave moisture sounder data is only mentioned in passing. However, understanding the characteristics of this product is needed to integrate it with other cloud base height data sets.

Finally, a unified cloud base height product must be created to merge separate cloud base height data products retrieved from VIIRS and CMIS with surface-based weather observations. The use of all three products is especially important when multiple cloud layers are analyzed in the cloud phase product. In addition, it is important to fully exploit conventional weather observations, where available, since these measurements of cloud base heights are typically more accurate than those retrieved from a satellite alone.

Deleted:

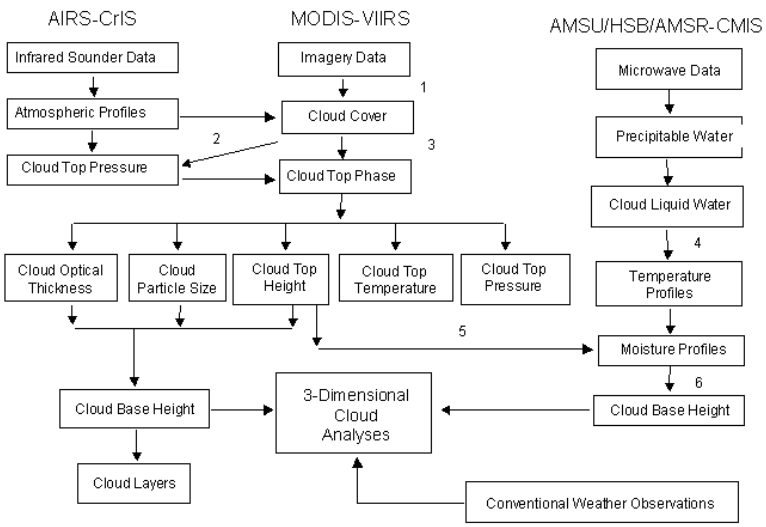


Figure 8.1 Overview of an approach to retrieving 3-dimensional cloud fields from satellite data (Hutchison, 2002).

## 8.2 AUTOMATED CLOUD DETECTION

The manual discrimination between cloudy and cloud-free pixels is readily accomplished using the principles of satellite interpretation described in Chapter 5, as demonstrated in Chapters 6 and 7. However, the task of creating automated cloud analyses is more complex since computer logic must replicate the processes that are nearly automatic for the human brain.

There are a variety of approaches that can be used to create an automated cloud mask, i.e. perform automated cloud detection. These approaches can be grouped into four broad categories which are briefly below:

a. Single channel cloud classifiers,

b. Multispectral cloud classifiers,
c. Spatial cloud classifiers, and
d. Spectral/spatial classifiers.

In this text, focus is upon the well-known multispectral cloud classifier approach described in the literature by Saunders and Kriebel (1988) which formed the theoretical basis for APOLLO or Processing scheme Over Land, Clouds, and Ocean (Kriebel et al 2003), CLAVR (CLouds from AVHRR by Stowe et al., 1999), SERCCA (Support of Environmental Requirements for Cloud Analyses and Archive by Gustafson et al., 1994), and the MODIS cloud mask algorithms (Ackerman et al., 1997; Ackerman et al., 1998; Ackerman et al., 2002). The VIIRS cloud mask algorithms follow closely the logic used with MODIS which has been modified to exploit the unique design of the VIIRS sensor including spatial tests to exploit the high resolution visible and infrared imagery bands along with spectral tests to exploit dual gain bands that will not saturate in the presence of clouds (Hutchison et al, in press).

**Deleted:** ). The precepts outlined by Saunders and Kriebel formed the basis for APOLLO (Processing scheme Over Land, Clouds, and Ocean), CLAVR (CLouds from AVHRR by Stowe et al., 1991), SERCCA (Support of Environmental Requirements for Cloud Analyses and Archive by Gustafson et al., 1994), and the MODIS (MODIS Algorithm Theoretical Basis Document by Ackerman et al., 1997) cloud detection or cloud mask algorithms.

### 8.2.1 Single Channel Cloud Detection Algorithms

Single channel cloud classifiers typically compare radiances in one IR band against a database of expected radiances, pre-calculated for cloud-free conditions. (Distinction is made here between an algorithm that uses only a single band or channel of satellite data to make a complete cloud analysis versus one cloud test that uses a single channel among many cloud tests to make the final analysis.) If the expected radiance for a pixel is less than the observed radiance by some specified amount, known as the cloud detection threshold, it is classified as cloud-contaminated. A difficulty in implementing this approach is accurately forecasting the surface brightness temperature (emissivity times skin temperature) and then attenuating this brightness temperature along the sensor viewing geometry to establish the expected radiance at the satellite. Both are non-trivial tasks but the process has been used successfully for many years. Alternatively, a solar band can be used in place of or to complement the IR band, but a priori information on the surface albedo for this band, under cloud-free conditions, is needed to exploit these data. Complications arise since the surface albedo can change for a variety of reasons, e.g. weather conditions (recent snow or droughts), seasons and/or time of day (solar illumination). The Real-time Nephanalysis Model used these principles (Hamil et al., 1992) but the model required continuous quality control by meteorologists to overcome large errors in cloud analyses, as discussed in Section 3.4.

**Deleted:** channel

**Deleted:** -channel

**Deleted:** knows

### 8.2.2 Multispectral Channel Cloud Detection Algorithms

Multi-spectral cloud classifiers became the preferred automated cloud detection algorithms after the launch of the NOAA AVHRR. Early work focused on improved detection of nighttime fog (Bell and Wong, 1981) using the 3.7 and 11.0 μm data and thin cirrus with split window data in the 11-12 μm window (Inoue, 1985). Both had been problematic for global cloud analyses models such as the RTNEPH (Hutchison and Janota, 1989). An early description of a multi-spectral cloud detection algorithm was published by Saunders and Kriebel (1988). This approach assumes that each pixel is cloud-free, then employs a series of bi-spectral cloud tests to exploit the different signatures of clouds and their surrounding backgrounds in multispectral data. If any

single cloud test detects a cloud, the pixel is changed from cloud-free to cloud contaminated. The use of bi-spectral cloud detection tests has become widely accepted in most automated cloud detection algorithms.

One possible deficiency in the Saunders and Kriebel approach to automated cloud detection stemmed more from application of their techniques rather than any inadequacy in their approach. These algorithms were designed initially for regional application and used cloud detection thresholds that were restrictive for each test. For example, the Thin Cirrus Test, that used AVHRR 10.8 and 11.8 μm bands, used thresholds that were calculated for mid-latitude maritime atmospheric conditions. Thus, the thresholds were actually "tuned" to detect clouds for a pre-selected range of atmospheric water vapor values. If the atmosphere were significantly more humid, such as in the tropics, cloud-free pixels might be classified as cloudy. Similar generalizations could be made about the nighttime fog detection test, that used AVHRR band in the 3.7 and 10.8 μm region, and the daytime bi-spectral reflectance ratio test that used AVHRR data in the 0.86 and 0.65 μm bands.

Thus the Saunders and Kriebel approach has been generalized (Hutchison and Hardy, 1995) to make it more applicable for the analysis of global imagery. The process used was to use cloud tests that employ threshold functions, where possible, rather than constant values, in an attempt to detect accurately clouds in the range of geophysical conditions where they might be found.

**Deleted:** ed

Threshold functions were developed for most cloud detection tests and those key to the analysis of global imagery are briefly highlighted. These threshold functions use solar illumination and use scattering geometry (including scattering phase function, scattering angle, and solar zenith angles) for bands that are in units of albedo and precipitable water for infrared bands that are in temperature. The key tests used include:

- Daytime bispectral-reflectance ratio (0.865/0.645 μm) cloud test: The variable threshold for this cloud detection test is shown in Figure 8.2. The test was designed to detect optically think clouds over dark surfaces in the 0.645 μm band. A justification for the approach is outlined by Hutchison and Hardy (1995). This test cannot be used for pixels with backgrounds that have the same signature of clouds in these two bands, e.g. regions of snow, deserts, and sparsely vegetated areas. A dynamic surface data base is needed for areas that experience rainy and dry seasons.

**Deleted:** the

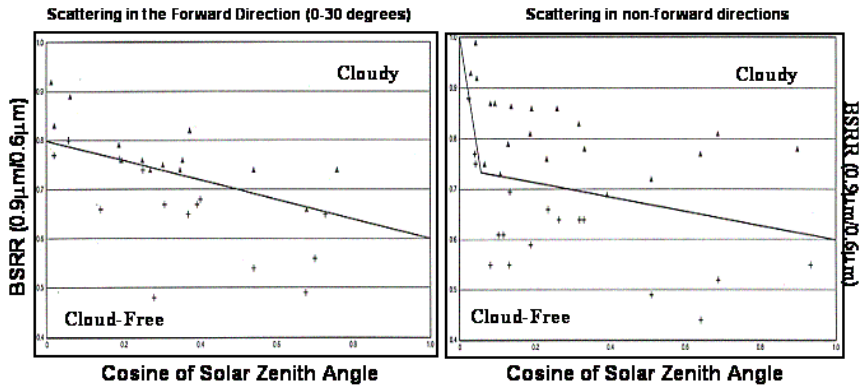


Figure 8.2 Bi-spectral reflectances ratio (BSRR) in the forward and non-forward scattering directions for optically-thick clouds (▲)and cloud–free pixels (+) over ocean surfaces as a functions of cosine solar zenith angle (from Hutchison and Hardy, 1995).

- Nighttime thin cirrus and stratus cloud tests: A similar set of thresholds, shown in Figure 8.3, were developed for nighttime detection of cirrus and stratus clouds in the 3.7 μm and 11.0 μm bands as a function of precipitable water. (Hutchison and Hardy (1995).

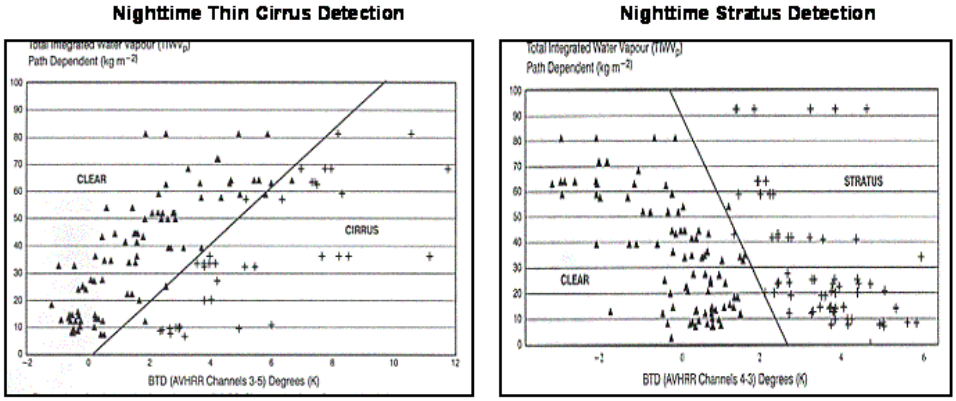


Figure 8.3 Brightness temperature differences (BTD) between nighttime 3.7 μm minus 11.0 μm for thin cirrus clouds (▲) and cloud cloud–free pixels (+) are shown in the left panel as a function of total atmospheric water content. In the right panel, 11.0 μm minus 3.7 μm BTDs are shown for stratus clouds (▲) and cloud-free (+) pixels in nighttime AVHRR imagery (from Hutchison and Hardy, 1995).

- Gross IR Test: From the panels in Figure 8.3, it is apparent that the signature of these two clouds are opposite. Thus, if both occur in a single pixel, the spectral signatures can cancel and the cloud may not be detected. However, when both of

present, the 10.8 μm temperature is much colder than the expected surface temperature. Thus, a gross IR test is used to capture clouds in these situations. For example, if the 10.8 μm temperature is more than some number, e.g. 10 degrees, colder that this surface temperature, clouds must be present. Implementation of this test might use an SST field, a forecast 850 mb temperature field, etc. (This test is similar to those used in the single channel algorithms described above.)

- Similar research has been completed to improve cloud detection under a variety of geophysical conditions. Briefly, these include:
    - Use of the 0.412 μm band for cloud detection over desert surfaces (Hutchison and Jackson, 2003). This band is proposed for use in place of the 0.865 μm band in the BSRR test above for use over semi-arid and sparsely vegetated regions but more research is needed before it can be implemented.
    - Use of the albedo component of the 3.7 μm band to suppress the signature of snow while simultaneously enhancing the signature of thin cirrus. This approach supports the detection of thin cirrus over snow fields, which may prove more difficult using the 1.6 μm band (Hutchison and Locke, 1997; Hutchison et al., 1997a).
    - Use of a variable threshold with the 1.375 μm band was demonstrated with aircraft data (Hutchison and Choe, 1996). Recently, an approach has been developed that provides greatly improved results with MODIS data (Roskovensky and Liou, 2003). This procedure will work even better with VIIRS since the bandpass of this band is reduced to 15 nm versus the 30 nm MODIS band.

It should be noted that not all cloud detection algorithms take the approach described above. The MODIS cloud mask assumes that the bi-spectral cloud detection threshold values are constant and determines the probability that a pixel is cloudy (e.g. definitely cloudy, probably cloudy, etc.) based upon how close the results of the test are to the threshold (Ackerman et al., 1998). Since this algorithm currently employs a static surface data base, the thresholds are invariant. Still other methods have been suggested to make cloud detection thresholds more dynamic or compensate for the use of single-valued thresholds. For example, Coakley and Bretherton (1984) performed a search over a group of pixels to identify the most cloud-free pixel and establish a cloud detection threshold for the rest of the pixels in the region. A variation of this method was later used at NOAA with their cloud in AVHRR (CLAVR) algorithms (Stowe et al., 1991; Stowe et al., 1999).

### 8.2.3 Spatial Cloud Classifier Algorithms

Cloud classifiers that employ spatial techniques typically compute statistics for an array of pixels and classify each pixel in the array as cloudy or cloud-free based upon the inhomogeneity in the array. For example, a 3x3 pixel array might be used and the standard deviation computed for the 11.0 μm band. If the result is sufficiently larger than some threshold, the pixels are classified as cloudy. This test is typically used only over relatively homogeneous surfaces, such as the ocean away from coastal regions.

**Deleted:** channel

Spatial cloud tests are particularly valuable for identifying pixels that are on the edge of larger cloud fields, e.g. to detect fractionally cloud-filled pixels or cloud edges (Saunders and Kreibel, 1988). Therefore, they can be used effectively with the single channel or multispectral cloud tests. For example, a spatial test is used in the NOAA cloud algorithms to ensure that no partially cloud-filled pixels are included in the sea surface temperature analyses.

Deleted: cloud

## 8.3 CLOUD TOP PHASE CLASSIFICATIONS

The retrieval of cloud top phase is the next step in the process of generating cloud base heights from VIIRS and 3D cloud fields from NASA's Aqua mission or NPOESS data. It will be seen below that cloud top phase is required to analyze all other cloud products, including cloud optical properties, cloud top parameters, and cloud base heights. It is also used to assess the accuracy of microwave cloud base heights since (1) the microwave algorithm requires an accurate cloud top temperature to retrieve a cloud base height for water clouds and (2) an accurate cloud top temperature for a water cloud cannot be determined in the presence of thin cirrus clouds. More specifically, the microwave cloud base height algorithm requires from VIIRS, fractional cloud cover within the microwave pixel to within ± 5% and a cloud top temperature of the water cloud to within about ± 3K (Wilheit and Hutchison, 2000). This limits the effective use of the microwave cloud base algorithm to only those pixels that contain water clouds but do not contain thin cirrus.

Deleted: +/-

Deleted: +/-

Deleted:

The characteristics of the cloud phase algorithm follow that created for the NASA EOS program (Menzel et al., 2002). The intention of this algorithm was to implement an infrared approach that worked under all solar illumination conditions. Originally, it was thought that a tri-spectral technique (using the 8.5, 11, and 12 μm bands) would be adequate for application to global data. (Menzel and Strabala, 1997). Strabala et al. (1994) had demonstrated that the radiances of ice clouds and water clouds tended to separate when brightness temperature differences between 8.5 μm and 11 μm, or $T_{8.5}$- $T_{11.0}$, and between 11 μm and 12 μm, or $T_{11.0}$- $T_{12.0}$, were compared. Ice clouds tended to have greater values of $T_{8.5}$- $T_{11.0}$ than $T_{11.0}$- $T_{12.0}$ whereas water clouds tended to have greater values of $T_{11.0}$- $T_{12.0}$ than $T_{8.5}$- $T_{11.0}$ values.

Deleted: s

Deleted: (Menzel and Strabala, 199

Deleted: 7

However, results obtained from operational testing of the original MODIS cloud phase algorithm caused a change from the tri-spectral approach to the use of a bi-spectral algorithm (Menzel et al., 2002). Prior to the launch of MODIS, testing of the tri-spectral algorithm was based upon MODIS Airborne Simulator (MAS) data, or with carefully selected case studies using much lower-resolution HIRS data, which was the only satellite sensor that collected data in all three IR bands. The MAS data were collected primarily in the northern hemisphere mid-latitude regions and did not include mixed phase clouds and, due to its high (50 m) spatial resolution, these data seldom included clouds at multiple levels. Both situations occur routinely in more coarse resolution MODIS data. Finally, while the tri-spectral approach performed well on case studies where ice and water clouds were at distinctively different heights, these same signatures became ambiguous when cloud top temperatures fell in the 250-270 K range. The difficulties associated with the tri-spectral test are most severe for mid-level clouds and this test performs better when clouds are either high or low.

A different approach to cloud phase classification (Hutchison 1999; Hutchison et al., 1997a) involved the development pf an algorithm that was based upon three assumptions: (1) cloud spectral signatures alone cannot be used to differentiate between ice and water clouds without some ambiguity, (2) where ambiguities exist, cloud top pressures might be useful to help resolve them, and (3) it is not desirable to put sounding bands in an imaging system, i.e. VIIRS would probably not have MODIS channels 33-36, therefore it would be desirable to use cloud top pressures retrieved from a high-resolution IR sounds like the CrIS. The architecture for the algorithm is shown in Figure 8.4.

**Deleted:** channels

The formulation of this cloud phase algorithm maintains the analysis at the resolution of the imaging sensor, identifies pixels that are definitely ice and definitely water, and resolves pixels that have ambiguous signatures with cloud top pressure obtained from the sounder. The original algorithm was limited by the spectral data supplied by the AVHRR/2 sensor and potential improvements were identified for implementation after the launch of MODIS, including the use of 1.375 μm and 8.5 μm data.

The primary objective for the cloud phase algorithm shown in Figure 8.4 was to resolve differences between low-level water clouds and thin cirrus. (It was assumed that thin cirrus detection would be improved during daytime conditions using the 1.375 mm band (Hutchison and Choe, 1996) and during nighttime conditions using the tri-spectral approach (Ackerman et al., 1990). While this is a trivial task for the interpretation by a human, as shown in the previous chapters, it is more complicated for automated algorithms since cirrus is often very thin and energy from its cloud top mingles with energy from below. Perhaps surprisingly, thin cirrus is readily distinguished from mid-level water clouds, at least in daytime imagery, due to the large (often > 20 $^{0}$C) brightness temperature differences (BTD) between 3.75 μm and 11.0 μm in cirrus signatures are much smaller, e.g. 5 K, depending upon the amount of water vapor in the atmosphere. Therefore, the use of the tri-spectral test might represent a most valuable modification to the cloud phase architecture shown in Figure 8.4.

**Deleted:**

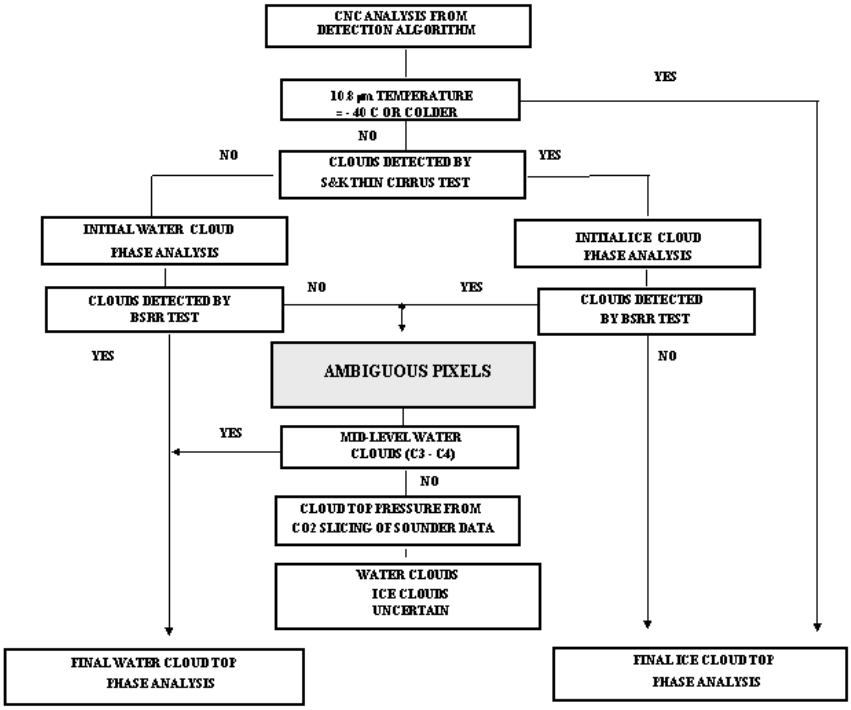


Figure 8.4 Cloud phase classification from the fusion of spectral signatures in AVHRR imagery and cloud top pressures from $CO_2$ slicing of high resolution IR sounder data. (from Hutchison et al., 1997a) S & K = Saunders and Kriebel (1988); BSRR = bispectral reflectance ratio

The current MODIS cloud phase algorithm relies upon the bi-spectral, $T_{8.5} - T_{11.0}$, test (Menzel et al., 2002). Cloud top properties (height, temperature, and effective emissivity) are generated using the $CO_2$ slicing algorithm based upon measurements in the 13-15 μm bandpasses, i.e. MODIS channels 33-36. It produces cloud type classes: water, ice, mixed phase, and ambiguous.

Deleted: ly

Unfortunately, the MODIS cloud phase classes are not the desired inputs for subsequent cloud algorithms shown in Figure 8.1. For example, all algorithms used to generate cloud optical properties make the assumption that only a single cloud layer exists in each pixel. Therefore, the preferred cloud classes are water, ice, multi-layered, and mixed phase. This algorithm has been developed and the results are exceptional (Pavolonis and Heidinger, 2004). It is similar to the architecture shown in Figure 8.4 from the perspective that it uses a series of cloud tests to evaluate clouds as a function of the spectral signatures in these bands. The only drawback is that the current algorithm is applicable only during daytime conditions. A comparison between the results from the current MODIS algorithm and the algorithm developed by Pavolonis and Heidinger is shown in Figure 8.5 and Figure 8.6. The newer algorithm classifies as multi-layered clouds those pixels classified as ambiguous by the current MODIS algorithm. In addition, the new algorithm classifies more clouds as mixed-phase as shown in Table 8.1, which compares the performance of these two algorithms as a function of latitude regions using 8-days of global MODIS imagery.

Deleted: i

Deleted: 3

Deleted: i

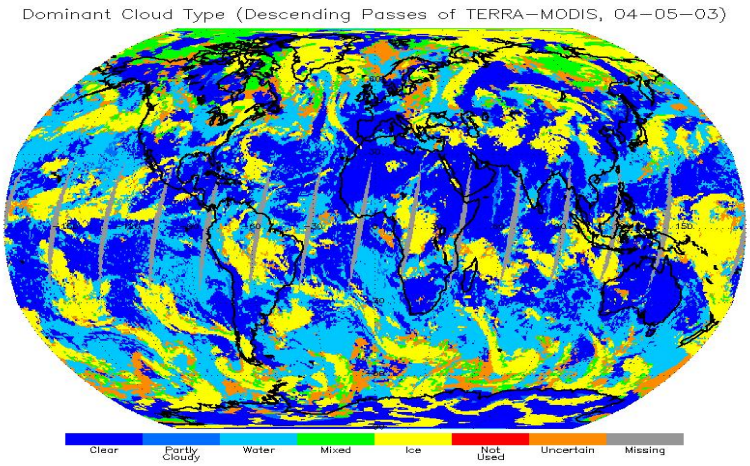


Figure 8.5 Analysis of cloud phase classes from global Terra MODIS data using current MODIS algorithm (Menzel et al., 2002).

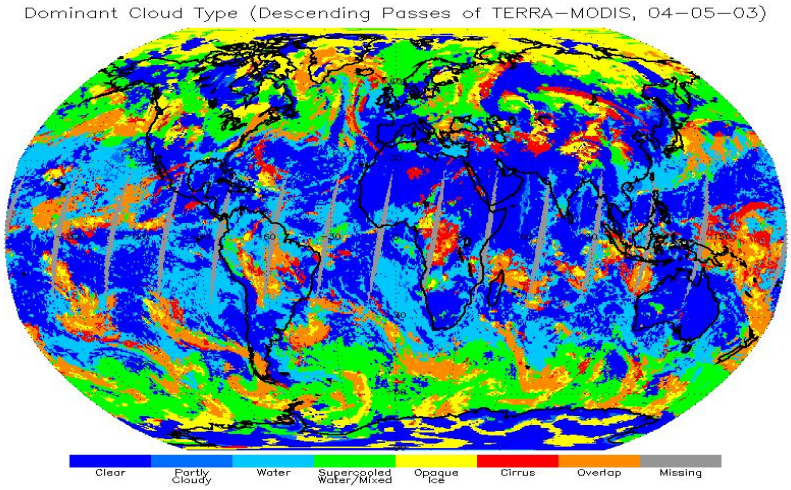


Figure 8.6 Analysis of cloud phase classes from global Terra MODIS data using Pavolonis and Heidinger algorithm (Pavolonis and Heidinger 2004).

Table 8.1 Frequency of occurrence of cloud types from current MODIS algorithms and those developed by Pavolonis and Heidinger (2004) for 8-day period.

**Deleted:** i

**Deleted:** i

**Deleted:** 3

**Deleted:** o

**Deleted:** i

**Deleted:** 3

Region 60-90 N Latitude

| Algorithm | Julian. Day | Water | Ice | Mixed | Ambig. | Multiple Layers (e.g. Overlap) |
|---|---|---|---|---|---|---|
| P&H (MODIS) | 91 | 0.2(9.5) | 66.9(42.1) | 24.4(32.9) | 0.0(15.5) | 8.5(0.0) |
| P&H(MODIS) | 92 | 0.4(10.1) | 65.9(41.4) | 24.9(32.6) | 0.0(15.9) | 8.7(0.0) |
| P&H (MODIS) | 93 | 0.4(10.0) | 63.1(43.0) | 26.3(29.4) | 0.0(17.6) | 10.1(0.0) |
| P&H (MODIS) | 94 | 0.2(9.6) | 62.9( 42.7) | 25.5(31.2) | 0.0(16.5) | 11.3(0.0) |
| P&H (MODIS) | 95 | 0.4(10.9) | 62.5(41.4) | 27.0(30.9) | 0.0(17.0) | 10.1(0.0) |
| P&H (MODIS) | 96 | 0.7(11.4) | 59.4(42.6) | 27.8(28.2) | 0.0(17.8) | 12.1(0.0) |
| P&H (MODIS) | 97 | 0.5(12.3) | 60.5(40.6) | 27.8(30.3) | 0.0(16.7) | 11.2(0.0) |
| P&H (MODIS) | 98 | 0.9(13.4) | 59.2(40.0) | 27.6(31.0) | 0.0(15.6) | 12.3(0.0) |
| 8-Day Averages | | | | | | |
| P&H(MODIS) | | 0.5 (10.9) | 62.6(41.7) | 26.4(30.8) | 0.0(16.6) | 10.6(0.0) |

Region: 30S – 30 N

| | | | | | | |
|---|---|---|---|---|---|---|
| 8-Day Averages | | | | | | |
| P&H(MODIS) | | | 57.4(48.7) | 21.4(35.8) | 5.9(2.2) | 0.0(13.2) 15.3(0.0) |

Region: 30 N(S) – 60 N(S)

| | | | | | | |
|---|---|---|---|---|---|---|
| 8-Day Averages | | | | | | |
| P&H(MODIS) | | | 23.6(45.5) | 20.7(28.1) | 36.0(9.8) | 0.0(16.6) 19.7(0.0) |

Deleted: <sp>

## 8.4 CLOUD OPTICAL (THICKNESS AND PARTICLE SIZE) PROPERTIES

The NPOESS requirement for the retrieval of cloud microphysical properties, defined as cloud optical thickness and cloud effective particle size, includes ice and water clouds during both daytime and nighttime conditions. Thus, there are four logic paths for these NPOESS products (Ou et al., 2003; Ou et al., 1995; Ou et al., 2002). On the other hand, the primary focus of the NASA EOS program was on the retrieval of these products for water clouds during daytime conditions (King et al., 1997). While NASA retrieved these optical properties for ice clouds under daytime conditions, no attempt was made to retrieve them using nighttime data.

A review of the approaches used to retrieve cloud optical properties has been completed by King (1997). The underlying principle on which most techniques are based is the fact that the reflection function of clouds at a non-absorbing band in the visible wavelength region is primarily a function of the cloud optical thickness, whereas the reflection function at a water (or ice) absorbing band in the near-IR is primarily a function of cloud particle size. In VIIRS, these bands include the 0.672 μm region as a non-absorbing band while the 1.6 and 2.25 μm bands represent absorbing bands for ice and water. Slightly different bandpasses are used in MODIS.

The retrieval of cloud optical properties begins with the assumption that cloud mask/phase algorithms have accurately identified cloud-contaminated pixels and determined cloud top phase. For VIIRS, processing then flows into one of four basic retrieval techniques that were developed: solar and infrared for both cirrus and water clouds. The solar approach follows the two-band correlation technique of Nakajima and King (1990) to retrieve the cloud optical thickness and effective particle size during daytime. The IR approach follows the two-band cirrus technique of Ou et al. (1993) to infer the cloud-top temperature and IR emissivity simultaneously. Application of the IR approach for cirrus clouds during the local daytime requires the removal of the solar component in the 3.7 μm radiances. We consider that the infrared approach for the retrieval of water cloud optical properties is less likely to yield useful results on a routine basis. Therefore, discussion of water clouds is limited to retrieval during daytime conditions.

**Deleted:** channel

**Deleted:** channel

### 8.4.1 Retrieval for Water Clouds During Daytime Conditions

The architecture for the retrieval of optical properties for water clouds is outlined in the NPOESS VIIRS Algorithm Theoretical Basis Document and shown in Figure 8.7 (Ou et al., 2002).

Additional insight into the VIIRS solar water cloud retrieval algorithm is contained in Figure 8.8. It shows that optical depth and mean effective size are retrieved from comparisons of satellite-observed reflection functions with similar calculations made using the theory of radiative transfer in plane parallel atmospheres. Results from the radiative transfer model are used to create look-up-tables which are stored in a computer library.

Entry into the look up tables begins with the sun-sensor geometric parameters, as shown in Figure 8.9 including the solar zenith angle, the sensor viewing zenith angle, the relative azimuth angle for each pixel. Information on the surface albedo can come from: (1) a histogram of cloud-free reflectances, (2) climatological data, or (3) a surface type data base, e.g. such as the surface albedo product retrieved for VIIRS cloud-free pixels. With these data inputs, the mean water droplet radius and optical depths are selected using numerical procedures that search the computer library for the simulated reflectances that best match satellite observations by minimizing the sum of the squares of the "residual" for each band. The "residual" is defined as the difference between the natural logarithms of simulated and the satellite-observed reflectances.

Deleted: channel

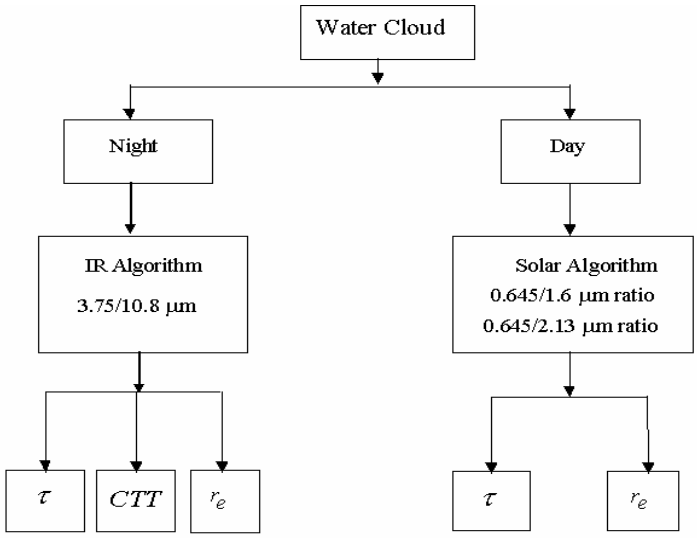


Figure 8.7. Architecture for the retrieval of water cloud microphysical properties during daytime and nighttime conditions. CTT = cloud top temperature (Ou et al., 2002)

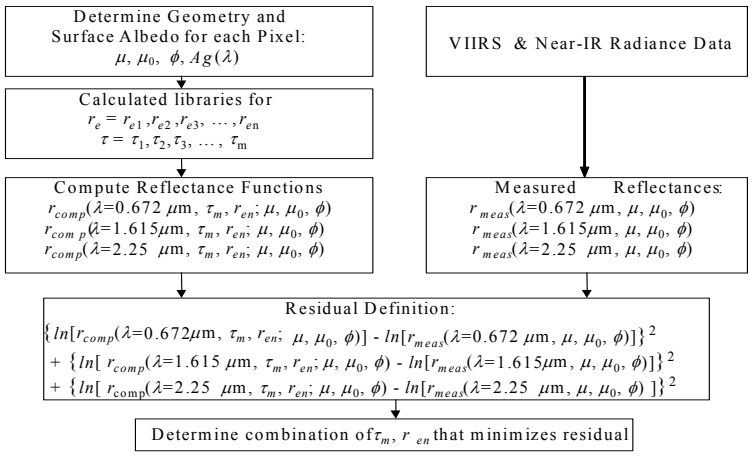

Figure 8.8. Overview of the water cloud solar retrieval algorithm. $A_g(\lambda)$ = surface albedo for wavelength $\lambda$ (Ou et al., 2002)

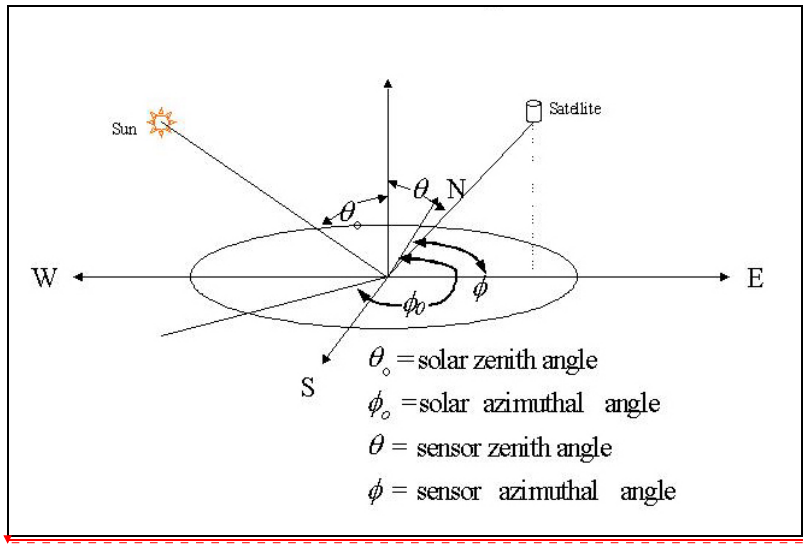


Figure 8.9. Sun satellite geometry. (Ou et al., 2002)

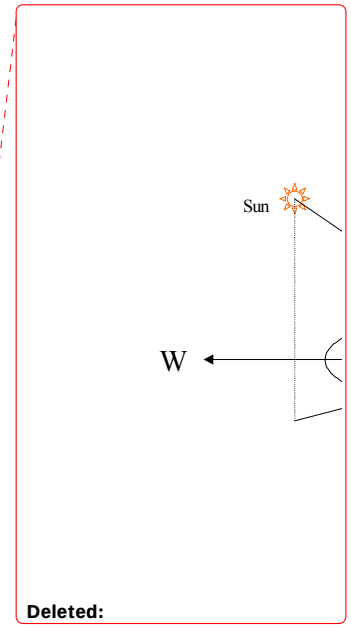


Obviously the physics in this approach to retrieval of water cloud optical properties is contained in the generation of the look up table entries. The first step in the process involves defining global geophysical conditions that become input parameters to the radiative transfer model, e.g. atmospheric profiles, sun-sensor geometries, surface properties, and cloud optical and microphysical properties. Since only top of the atmosphere radiances are needed for these look up tables, a radiative transfer model is used for computing high spectral resolution radiances using the combination of the correlated-*k* distribution method and the adding-doubling method that allows the optimum number of azimuth angles or radiation streams. For example, a given scenario might include an atmospheric profile, solar and sensor geometry, band parameters, and cloud phase, cloud-top height, and surface albedo. For each scenario, the radiative transfer model is executed over a wide range of cloud optical thickness values and cloud effective particle sizes. Results for each scenario and for each spectral band are then stored in radiance tables that are converted into reflectance functions using the solar spectral irradiance at the top of atmosphere. To simulate accurately the atmospheric scattering/absorption effects, the radiative transfer model includes reliable phase functions and single-scattering properties for non-spherical ice crystals, spherical water droplets, molecules and aerosols. Single-scattering properties include the extinction coefficient (or efficiency), the single-scattering albedo, and the asymmetry factor.

Figure 8.10 shows the results of sample calculations that demonstrate the theoretical relationship between the reflection function at 0.664 μm and (a) 1.621 μm and (b) 2.142 μm for various values of cloud optical thickness (at 0.664 μm) and cloud effective particle size for the geometry $\theta_0$ =26°, $\theta$ = 40° and $\phi$ = 42° (King et al., 1997). Data from

measurements above marine stratocumulus clouds during ASTEX are superimposed on the figure (22 June 1992).

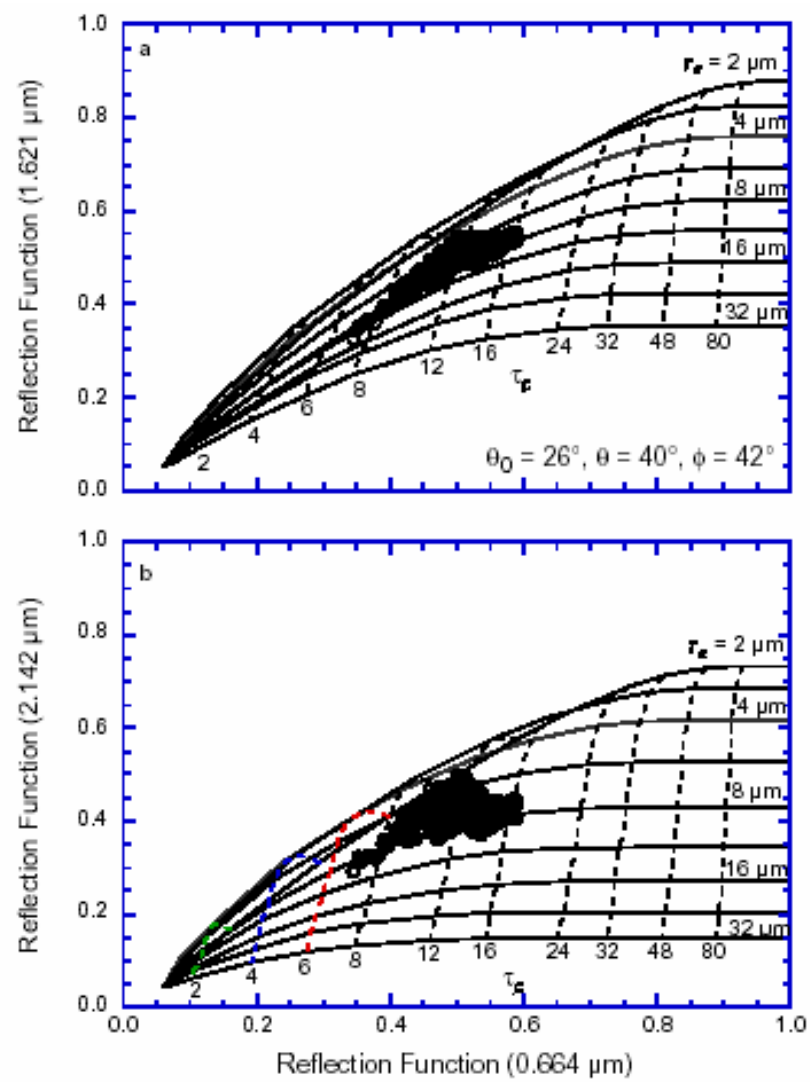


Figure 8.10. Theoretical relationship between the reflection function at 0.664 μm and (a) 1.621 μm and (b) 2.142 μm for various values of $\tau_c$ (at 0.664 μm) and $r_e$ when $\theta_0$ =26°, θ = 40° and φ = 42°. (King et al., 1997)

For the results presented in Fig. 8.10, the underlying surface was assumed to be Lambertian with surface albedo ($A_g$) = 0.06, 0.05, and 0.045 for wavelengths of 0.664, 1.621, and 2.142 μm which roughly corresponds to an ocean surface. The dashed curves in Fig. 8.10 represent the reflection functions at 0.664, 1.621 and 2.142 μm that result for specified values of the cloud optical thickness at 0.664 μm. The solid curves represent the reflection functions that result for specified values of the effective particle radius. These results show that the cloud optical thickness is largely determined by the reflection

Deleted: 503

Deleted: 503

function at a non-absorbing wavelength (0.664 μm in this case), with little dependence on particle radius. The reflection function at 2.142 μm (or 1.621 μm), by contrast, is very sensitive to cloud particle size, with the largest values of the reflection function occurring for small particle sizes. In fact, as the optical thickness increases to about 12, the sensitivity of the non-absorbing and absorbing bands to cloud optical thickness (0.664 μm) and cloud effective particle size is very nearly orthogonal. This implies that under these optically thick conditions, optical thickness and effective radius can be determined nearly independently, and thus measurement errors in one band have little impact on the cloud optical property determined primarily by the other band. The data points superimposed on the theoretical curves represent over 400 measurements obtained with the MODIS Airborne Simulator (MAS), a 50-band scanning spectrometer that was mounted in the right wing superpod of the NASA ER-2 aircraft during ASTEX (King et al., 1996). These observations were obtained as the aircraft flew over marine stratocumulus clouds in the vicinity of the Azores approximately 1000 km southwest of Lisbon, Portugal on 22 June 1992 (King et al., 1997).

**Deleted:** of Fig. 5.03

There are several assumptions involved in the theoretical development of cloud particle size and optical thickness retrievals.

- At the present time, the algorithm is valid for single-layer, liquid water, plane-parallel geometry.
- Cloudy pixels that encounter multiple-layer and horizontal inhomogeneity will not be retrieved correctly.
- Some errors are expected to be encountered in retrieved cloud effective particle radius and optical thickness when ice clouds are present.
- The upper limit of the solar zenith angle for reliable retrievals has not been determined but unsatisfactory results will occur when the solar zenith angle ($\theta_o$) > 80° due to the long slant path and limit in radiative transfer model simulations for large $\theta_o$.

**Deleted:** ~

### 8.4.2 Retrieval for Ice Clouds Microphysical Properties

The architecture for the retrieval of optical properties for ice clouds is shown in Figure 8.11. In principle, the microphysical properties of ice clouds during daytime conditions can be retrieved in a manner similar to that described for water clouds in the previous section. However, the retrieval is further complicated by two additional factors: the shape and orientation of the ice particles that occur naturally in the atmosphere. These features must be accurately described in the radiative transfer model used to generate the look up tables. In addition, cirrus clouds generally have a smaller optical depth than water clouds; therefore, it becomes necessary to use the look up table approach across the full range of requirements. Due to variability found in measurement of ice particle shapes and orientations, the accuracy of cirrus cloud optical property retrievals has greater uncertainty than for water clouds (Liou, 2002).

**Comment [kh1]:**

The retrieval of ice cloud optical properties during nighttime conditions is more feasible than for water clouds and an approach has been developed for these VIIRS products. In particular, Ou *et al*. (1993) have demonstrated a physical retrieval methodology that uses radiance data from AVHRR 3.7 μm and 10.9 μm bands to infer nighttime cirrus cloud

**Deleted:** channels

parameters, including cloud temperature, optical depth, and mean effective ice crystal size, based on the theory of radiative transfer and cloud parameterizations.

While the NPOESS program applies this nighttime (IR) approach to all cirrus clouds, during daytime and nighttime conditions as shown in Figure 8.11, we consider it to be more useful with nighttime data. The infrared retrieval approach is complementary to the solar method, since the 3.7 μm band senses a different part of the cloud from the other two near-IR bands (Ou et al., in press); however, the solar approach should be more reliable under most circumstances, except near local dawn or dusk. When the sun is low, the IR approach may perform better than the solar approach. Once cloud optical thickness and effective particle size are retrieved with solar data, equations used in the IR technique could be used to retrieve effective cloud top temperature.

Deleted:

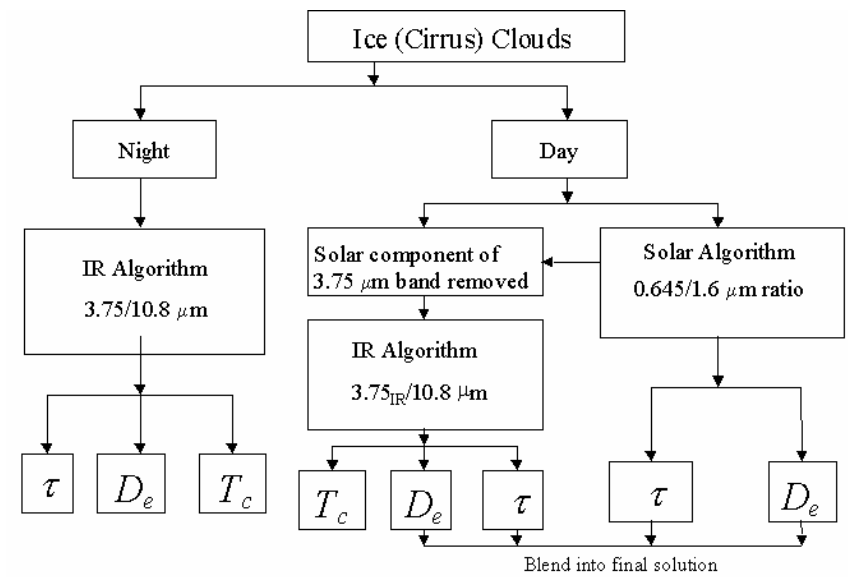


Figure 8.11. Architecture for the retrieval of ice cloud microphysical properties from VIIRS data during daytime conditions and VIIRS data during nighttime. $T_c$, and $D_e$ are cloud top temperature and ice crystal diameter (Figure 4.11 from Ou et al., 2002).

### 8.4.2.1 Retrieval of Ice Cloud Properties in Daytime Imagery

The concept behind the retrieval of cloud optical properties during daytime conditions was highlighted in the previous section. In this section, additional information is provided to demonstrate the steps involved in processing VIIRS and/or MODIS data to retrieve these parameters for ice clouds.

The daytime cloud optical properties algorithms for VIIRS reflectances follow the series of processing steps shown in Figure 8.12. The first step in the process again involves defining scenarios that will be analyzed and are based upon the range of requirements, e.g. 0-12 optical thickness values for ice clouds. These scenarios are used to define inputs for the look up tables generated by the radiative transfer model. Once the look up tables are generated, the retrieval of cloud optical properties proceeds directly from satellite measurements as describe above for water clouds.

Deleted:

Deleted:

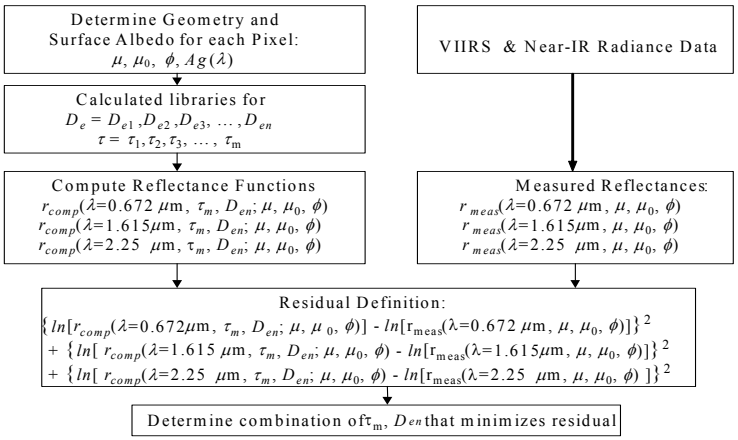


Figure 8.12 Processing sequence for retrieval of ice cloud optical properties in daytime conditions.

### 8.4.2.2 Retrieval of Ice Cloud Properties in Nighttime Imagery

An approach has been developed for the NPOESS program to retrieve ice cloud optical properties based upon the work of Ou et al. (1993). The nighttime algorithm is used to retrieve cloud top temperature, mean effective ice crystal size, and optical depth from VIIRS 3.7 μm and 10.76 μm (denoted for convenience as bands and 2) radiances.

**Deleted:** channel 1
**Deleted:** c
**Deleted:** C
**Deleted:** hannel
**Deleted:** channels
**Deleted:** channel

The top of the atmosphere radiance ($R_i$) for the 3.7 μm and 10.76 μm bands over a cirrus cloudy atmosphere is described in terms of the cirrus cloud-top temperature $T_c$ and emissivities ($\varepsilon_1$, $\varepsilon_2$) of each band as follows:

$$R_i = (1 - \varepsilon_i)\, R_{ai} + \varepsilon_i\, B_i(T_c) \qquad \text{for } i = 1, 2 \qquad (8.1)$$

where $R_{ai}$ denotes the upwelling radiance reaching the cloud base and $B_i(T_c)$ are the respective Planck functions for the cloud top temperature. The first term on the right-hand side of Equation (8.1) represents the contribution of the transmitted radiance from below the cloud while the second term is the emission contribution from the cloud. Energy due to water vapor emission above the cirrus cloud is neglected as well as the effects of cloud reflectivity; these are generally less than 3 percent of the incident radiance.

**Deleted:** is
**Deleted:** ,

To solve Equation 8.1 for $T_c$ and $\varepsilon_i$ numerically, $\varepsilon_1$ and $\varepsilon_2$ must be correlated we must express $B_1(T_c)$ in terms of $B_2(T_c)$. The clear radiances $R_{a1}$ and $R_{a2}$ must also be known. First, to express $B_1(T_c)$ in terms of $B_2(T_c)$ the Planck functions are computed at 0.1 K intervals over the range of 150-300 K while taking into account the respective band filter functions. Values in the look up table are then fitted to a third-degree polynomial based on a least-square regression technique, where the regression coefficients for AVHRR are: $a_0$ = 2.6327e-4, $a_1$ = -1.063e-4, $a_2$ = 8.2976e-6, and $a_3$ = 3.7311e-7.

**Deleted:**
**Deleted:** channel

$$B_1(Tc) = \sum a_n[B_2(T_c)]^n = f[B_2(T_c)] \quad n = 0,1,2,3 \qquad (8.2)$$

Next, the relationship between the emissivities for the two bands is evaluated. The cirrus emissivities at the 3.7 μm and 10.76 μm wavelengths may be parameterized in terms of visible optical depths τ using the form:

$$\varepsilon_i = 1 - \exp(-k_i\tau) \quad \text{for } i=1,2 \qquad (8.3)$$

The exponential term represents the effective transmissivity where the parameters $k_i$ represent the effective extinction coefficients for the two bands, accounting for multiple scattering within cirrus clouds and for the difference between visible and IR extinction coefficients. Thus the products $k_i\tau$ may be considered as the effective optical depth that would yield the same emissivity values for the nonscattering conditions at the 3.7 μm and 10.76 μm wavelengths. Eliminating τ from Equation 8.3, results in the desired relationship between $\varepsilon_1$ and $\varepsilon_2$:

$$(1-\varepsilon_1)^{1/k1} = (1-\varepsilon_2)^{1/k2} \qquad (8.4)$$

The substitution of (8.1) into (8.4) results in a nonlinear, algebraic equation with $B_2(Tc)$ as the key unknown as shown in Equation (8.5).

$$[(R_2 - B_2(T_c))/(Ra_2 - B_2(T_c))] - [(R_1 - f[B_2(T_c)])/(Ra_1 - f[B_2(T_c)])]^{k2/k1} = 0 \qquad (8.5)$$

To close the system of equations, a relationship is needed between the ratio $k_2/k_1$ which can be expressed in terms of $1/D_e$ in the form:

$$k_2 / k_1 = \sum_{n=0}^{2} b_n D_e^{-n}, \qquad (8.6)$$

where the coefficients $b_n$ are determined from a second-order least squares method using the radiance tables. On the other hand, based on a dimensional analysis, a relationship between $De$, $T_c$ and $\tau$ can be derived:

$$D_e = c\{\tau/[\Delta z(\alpha+\beta/D_e)\langle IWC\rangle]\}^{1/3}\langle D_e\rangle. \qquad (8.7)$$

where $\Delta z$ is the cloud thickness, and $\langle IWC\rangle$ and $\langle D_e\rangle$ are temperature dependent mean values of $IWC$ and $D_e$, respectively:

$$\langle IWC\rangle = \exp\{-7.6+4\exp[-0.2443\times10^{-3}(253-T_c)^{-2.445}]\} \quad \text{For } T_c < 253 \text{ K} \qquad (8.8)$$

$$\langle D_e\rangle = \sum_{n=0}^{3} c_n (T_c - 273)^n \qquad (8.9)$$

The flowchart in Figure 8.13 shows the approach to retrieve cirrus clouds optical properties using Equation (8.5).

Deleted: channels

Deleted: channels

Deleted: $_i$

Deleted:

Deleted:

Deleted: *Ice Water Content*

Deleted: )

Deleted: the

Deleted:

Deleted:

Deleted:

Deleted:

Deleted: ¶

Deleted:

Deleted:

- $Ra_1$ and $Ra_2$ (radiances at the cloud base) are accurately estimated from cloud-free radiances in each band, since atmospheric attenuation in these window bands is due primarily to water vapor and there is little of it at the level of cirrus clouds,
- $f[B_2(T_c)]$ is given in terms of $B_2(T_c)$ as shown in Equation (8.2),
- The ratio of $k_2/k_1$ is unknown and must be estimated from other data.

**Deleted:** channel

**Deleted:** channels

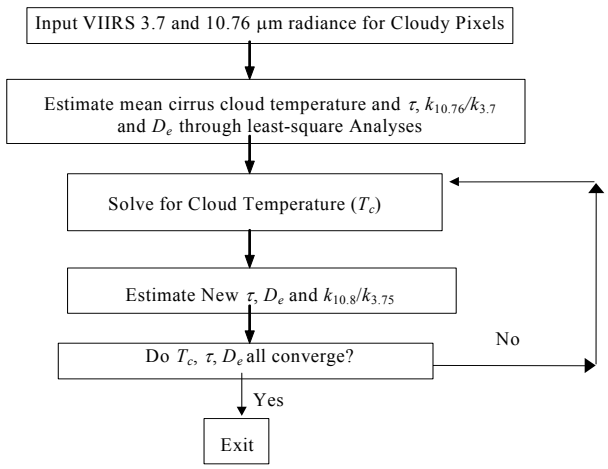


Figure 8.13 Processing sequence for retrieval of ice cloud optical properties in nighttime conditions.

The procedure is as follows:

- We first input VIIRS 3.7 μm and 10.76 μm radiance for cloudy pixels into the retrieval program
- We then estimate mean cirrus cloud temperature and $\tau$, $k_2/k_1$, and $D_e$ for a retrieval domain through an optimization analyses (See Equations 58-62 and Appendix B in VIIRS Cloud Optical Properties Algorithm Theoretical Basis Document, Ou et al 2002). These are initial guess values
- Cloud top temperature is then calculated using Equation (8.5).
- We subsequently evaluate $\tau$, $k_2/k_1$, and $D_e$ based on Equation (8.5), Equation (8.6), and Equation (8.7)
- Finally, we put $T_c$, $\tau$, and $D_e$ to a convergence test, which checks whether the ratios of successively iterated cloud parameters are smaller than prescribed threshold values. If these parametric values are not converged, we repeat steps 3 and 4. If converged, then these parametric values are the solutions.

This algorithm can be applied to daytime data after the solar component is removed from the 3.7 μm band. However, as previously noted, a better approach might be to retrieve cloud particle size and optical thickness directly from solar measurements, and then use Equation (8.5) to calculate cloud top temperature.

## 8.5 CLOUD TOP (TEMPERATURE, PRESSURE, AND HEIGHT) PARAMETERS

The retrieval of cloud top properties follows the processing of cloud optical properties and cloud top phase (Ou et al., 1995). Since ice clouds are typically semi-transparent to terrestrial radiation, effective cloud top temperature is retrieved simultaneously along with cloud optical thickness and effective particles size as shown in Figures 8.11 and Figure 8.13. The retrieval of cloud top temperatures for opaque water clouds is readily completed using the 10.76 µm brightness temperature after correcting for atmospheric attenuation, due primarily to water vapor between the cloud top and satellite sensor. Once cloud top temperatures have been retrieved, cloud top height and pressure are obtained by comparisons with a priori atmospheric profiles, e.g. from numerical models or other sensor data.

Therefore, an unresolved problem is to obtain accurate cloud top temperatures for semi-transparent (optically thin) water clouds, which are characterized by optical thickness values less than 5-6. Since cloud optical properties can be retrieved most accurately for these water clouds during daytime conditions, this becomes the focus of this discussion. As a corollary, since poor results are expected in the retrieval of cloud optical properties during nighttime conditions, as note above, the retrieval of cloud top temperature under these conditions follows the same approach used for optically thick clouds, recognizing that results will have larger errors.

In the presence of optically thin water clouds, the radiation reaching the satellite in the longwave infrared region comes from the surface, the atmosphere, and clouds in the sensor's field of view. Therefore, the retrieval of cloud top temperature is completed by removing contributions for the surface and atmosphere from satellite measurements. The problem is complicated by the fact that the amount of unattenuated surface energy arriving at the satellite is a function of the cloud optical thickness or transmissivity. Therefore, the approach recommended to retrieve cloud top temperatures employs a look up table that includes expected sateallite radiances based upon a range of cloud top temperatures, cloud optical thicknesses, surface temperatures, and atmospheric transmission that varies with cloud top height and total water content between the cloud top and the satellite. Almost any radiative transfer model should be sufficient for generating this look up table since the radiative transfer of spherical cloud drops is well known. However, errors in a priori knowledge of surface temperature and cloud effective particle size may be too large to make this approach useful or the results meaningful.

**Deleted:** values based upon an intial

The relationship between atmospheric pressure, temperature, and height enables one to determine cloud top pressure and cloud top height, if the cloud top temperature is known, or cloud top pressure and temperature, if the cloud top height is known, provided that an atmospheric temperature profile is available. Nevertheless, the cloud base heights that will subsequently be retrieved will greatly profit from this attempt to get the most accurate cloud top temperatures and heights, since the latter is a direct input into the cloud base height algorithm and it performs better for optically thin water clouds than for those that are optically thick.

**Deleted:** Top of the atmosphere radiance when the clouds are not optically thick; the relative contribution depends on the cloud thickness and effective particle size.

## 8.6 CLOUD BASE HEIGHTS

The retrieval of cloud base height solely from MODIS or VIIRS data is calculated from the difference between cloud top height and cloud thickness, as shown in Equation (8.10), where the latter is derived from cloud microphysical properties, i.e. effective particle size and optical depth. There are two algorithms that differ slightly according to cloud top phase. MODIS cloud optical properties are corrected for viewing geometry such that all measurements are for the nadir position, as shown in Figure 8.14.

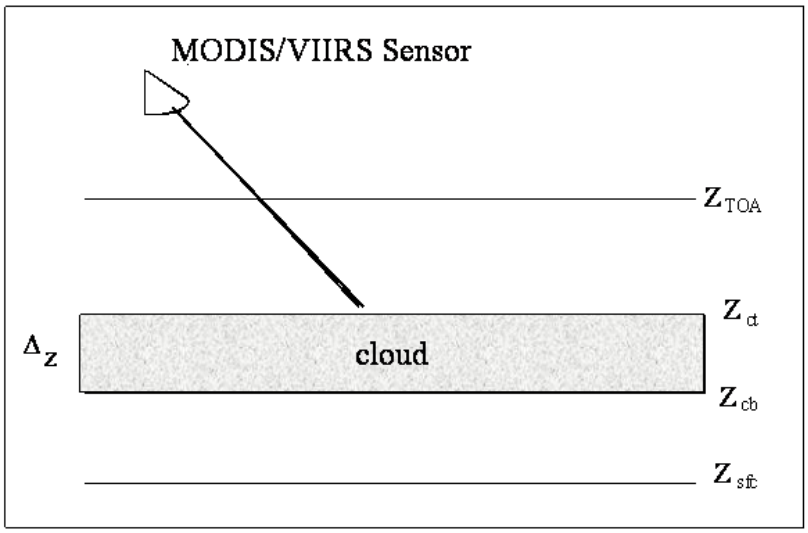


$$Z_{cb} = Z_{ct} - (\Delta Z)$$

Figure 8.14 Geometry for retrieval of cloud base height using cloud top height along with cloud optical properties the obtain cloud thickness (Hutchison, 2002).

### 8.6.1 Cloud base heights retrieved for water clouds

For water clouds, cloud thickness ($\Delta Z$) is based upon the relationship between liquid water path (LWP), in gm $m^{-2}$, and liquid water content (LWC), where liquid water content is the integration of cloud size distribution over droplet size and has units of gm $m^{-3}$. liquid water path has been related to cloud optical depth or cloud optical thickness ($\tau$) and cloud effective cloud particle size ($r_{eff}$) as shown in Equation (8.11) (Liou, 1992).

Deleted: /

Deleted: /

$$Z_{cb} = Z_{ct} - (\Delta Z) = Z_{ct} - [LWP/LWC] \quad (8.10)$$

where: LWP = Liquid water path = $[2\ \tau\ r_{eff}] / 3$ (8.11)

LWC = Liquid water content

$\tau$ = cloud optical depth

$r_{eff}$ = cloud droplet effective particle size

Measurements show the value of the liquid water content varies between about 0.20-0.45 g m$^{-3}$, as a function of cloud type. Initially, the liquid water content is assumed constant throughout the vertical extend of the cloud. This assumption becomes increasingly less reliable as clouds become more thick or precipitation begins (Slingo et al., 1982; Martin et al., 1994). Thus initial tests of this cloud base height algorithm were restricted to simpler cloud systems, e.g. relatively thin, non-precipitating stratiform cloud layers.

Deleted:

Deleted:

Deleted: /

Deleted: a

### 8.6.2 Cloud base heights retrieved for ice clouds

The form of the MODIS cloud base height algorithm for ice clouds follows that for water clouds with the exception that the relevant terms in Equation (8.10) become Ice Water Path (IWP) and Ice Water Content (IWC) as shown in Equation (8.12). The parameterization for ice water path, shown in Equation (8.13) (Liou, 1992), is a function of cloud optical depth ($\tau$), through the ice crystal size distribution, and ice crystal diameter ($D_e$=2$r_{eff}$).

$$Z_{cb} = Z_{ct} - (\Delta Z) = Z_{ct} - [IWP/IWC] \qquad (8.12)$$

$$\text{where} \quad IWP = \tau / [a+b/D_e] \qquad (8.13)$$

The regression coefficients (a) and (b) in Equation (8.13) are given by Liou (Table 5.4, 1992) with values a = - 6.656e-3; b = 3.686. The ice water content is a function of cloud top temperature and is given by:

$$\ln(IWC) = -7.6 + 4 \exp[-0.2443e\text{-}3(|T| - 20)^{2.455}] \quad \text{for } |T| > 20 \text{ deg C} \qquad (8.14)$$

Deleted:

Additionally, $D_e$ is a function of cloud top temperature as shown by Ou et. al. (1993)

$$D_e = c_0 + c_1 T + c_2 T^2 + c_3 T^3 \qquad (8.15)$$

Deleted:

where

$$c_0 = 326.3,\ c_1 = 12.42,\ c_2 = 0.197,\ c_3 = 0.0012 \qquad (8.16)$$

Deleted:

### 8.6.3 Ancillary Data and Products from Other Sensors

The expected range of cloud thickness that can be retrieved solely from MODIS data is estimated using the expected measurement ranges for optical depth and effective particle radius of each cloud type shown in Table 8.2 and solving Equation 8.10 and Equation (8.12) for $\Delta Z_{max}$.. While the MODIS program defines cloud optical depth measurement ranges of 0 - 100, there appears to be no clearly defined accuracy requirements for this product (King et al., 1997). On the other hand, the National Polar-Orbiting Operational Environmental Satellite System (NPOESS) program has established rigorous requirements in its Technical Requirements Document (TRD) for the NPOESS system (NPOESS TRD, 2001) and the Sensor Requirements Document (SRD) for the Visible/InfraRed Imager/Radiometer Suite (VIIRS). The NPOESS system requires the retrieval of cloud optical depth across the range of 0-64 for water clouds and 0-10 for ice

clouds with an accuracy of 10 percent or 0.05, whichever is greater (NPOESS TRD, 2001; NPOESS VIIRS SRD, 2000). In the absence of a similar MODIS requirement, these minimum VIIRS requirements form the basis for the following sensitivity analyses. Thus, the maximum cloud thickness for a water cloud can be estimated

Table 8.2. Predicted cloud thickness for expected optical depths, (10 for ice and 64 for water clouds) which might be retrieved from MODIS imagery.

| Cloud Type | $r_{eff}$ (μm) | LWC ($g\ m^{-3}$) | $\Delta z_{max}$(m) |
|---|---|---|---|
| Stratus I (oceans) | 3.5 | 0.24 | 622 |
| Stratus II (land) | 4.5 | 0.44 | 436 |
| Stratocumulus | 4.0 | 0.09 | 1896 |
| Altostratus | 4.5 | 0.41 | 468 |
| Cirrus | ~ 100 (= $D_e$) | ~ 0.01 (= IWC) | 3333 |

Deleted: /

Table 8.2 shows that cloud optical depth quickly reaches 64 for some water clouds, e.g. 400 - 600 m, while an optical depth of 10 represents a comparatively thick cirrus cloud, i.e. greater than 3 km. Thus, the limitation that cloud optical thickness be less than 64 for water clouds restricts the retrieval of cloud base heights to less than 1-km in geometric thickness. It is reasonable to consider the use of microwave products, such as Cloud Liquid Water (CLW) and Cloud Ice Water Path (CIWP) that are retrieved from the AMSR-E, when optical depths retrieved with MODIS exceed 64; however, the feasibility of this approach has yet to be demonstrated. The use of microwave data products with the MODIS or VIIRS cloud base height algorithms is attractive since the concept could extend the MODIS algorithm to nighttime conditions by using CLW/CIWP directly when cloud optical properties may be less accurate. The NPOESS program provides insight into the potential measurement ranges and accuracy that might be achieved for relevant microwave products that can be used in the retrieval of cloud base height with MODIS data. In the NPOESS program, the cloud liquid water product retrieved from the Conical Scanning Microwave Imager/Sounder (CMIS) has a minimum system measurement range of 0-1 mm (NPOESS TRD, 2001). This upper limit translates to a cloud liquid water of 1 $kg\ m^{-2}$ and increases $\Delta z_{max}$ to over 2,000 meters for typical water clouds shown in Table 8.2. Thus, the cloud liquid water product from the microwave imagery could provide a valuable source of additional information to extend the range of cloud thickness that might be retrieved using the MODIS/VIIRS cloud base height algorithms. These data may also allow lower-level cloud bases to be estimated in the presence of multiple layers of clouds, although spacing between cloud layers would be difficult.

Deleted: EO

Deleted: /

### 8.6.4 Integration of VIIRS, CMIS, and Conventional Cloud Base Observations

The final task in the generation of 3-dimensional cloud fields is the integration of various cloud base observations into a single, unified cloud base height product. Each observation has inherent strengths and weaknesses as shown in Table 8.3. The challenge is to create a final product that maximizes the strengths and minimizes the weaknesses of each observation to create the "best" cloud base height product from the available information.

Table 8.3 shows that the MODIS and VIIRS cloud base height algorithms may provide the best information on cirrus cloud base heights. Clearly, the microwave algorithm will provide no information. However, in the absence of cirrus clouds, the microwave approach can retrieve cloud bases for very thick clouds and multiple cloud layers within a single pixel. However, when multiple cloud layers are present, microwave data does not provide useful information on the separation between two cloud layers. On the other hand, the MODIS and VIIRS algorithms provide information only on the highest cloud layer. Finally, the microwave algorithm can be used only over ocean surfaces (Wilheit and Hutchison, 2000) while the MODIS/VIIRS algorithms can be used over any surface. Measurement uncertainties of cloud base heights from surface observations, especially those made at instrumented airports, are smaller than those associated with methods developed to retrieve them from remotely-sensed satellite data. Therefore, reliable surface observations should be integrated into the final cloud base height EDR when available, as shown in Figure 8.1.

**Deleted:** /

**Deleted:** although will not like give

**Deleted:** while

**Deleted:** /

**Deleted:** s

Table 8.3 Characteristics of cloud base height observations.

| Characteristic of Cloud Base Observations | MODIS/VIIRS Cloud Base Height Observations | Microwave Cloud Base Height Observations | Conventional (surface-based) Observations |
|---|---|---|---|
| 1. Number of layers detected | Single | Multiple (Possible) | Multiple (Possible) |
| 3. Perspective of clouds observation | Highest cloud first (ice or water) | Water cloud only | Lowest cloud first |
| 2. Applicable Backgrounds | Land and water | Water only | All conditions |
| 3. Cirrus | Detectible, if present | If present, not detectible and severely impacts water cloud retrieval | May be obscured by lower-level clouds |
| 4. Accuracy | < 1 km | 1 km | 50 m |
| 5. Coverage | Global | Oceans only | Surface observation sites only |
| 6. Cloud Thickness | Limited to relatively thin clouds, i.e. $\tau < 64$ | Applicable to thick clouds | Applicable to thick clouds |

**Deleted:** u

**Deleted:** Tau

The technological challenge of including surface observations in the NPOESS cloud base height EDR is the determination of how far to extend or spread the surface observation, i.e. how many satellite pixels can be accurately represented by a single surface observation. Similar problems have occurred with other global cloud models such as the Real-Time Nephanalysis (RTNEPH) model used for decades by the US Air Force. In this model, three processor modules are used: a satellite data analysis module (NEFSAT), a conventional data processor (CONRTN) module, and a "merge" data processing (NEFMRG) module (Hamill et al., 1992).

The general approach outlined in Figure 8.1 to integrate conventional surface weather observations with satellite-derived cloud base heights calls for the former to be spread across the maximum number of cloudy pixels using an automated cloud typing algorithm. As long as the cloud field remains homogeneous, conventional cloud base observations are given higher weights than satellite observations. However, if the satellite-derived cloud type changes, increased weight must be placed upon another surface observation or the best satellite cloud base heights observation.

Deleted: Chapter 9¶

# REFERENCES


Abel, P., Guenther, B., Galimore, R. N. and J. W. Cooper, 1993: Calibration results for NOAA-11 AVHRR channels 1 and 2 from congruent path aircraft observations, J. Atmos. and Ocean. Tech., 10, 493-508.

Abel, P., 1991: Pre-launch calibration of AVHRR reflected-solar channels, Remote Sens. Environ., **31**, 2227-229.

Ackerman, S., Strabala, K., Menzel, P., Frey, R., Moeller, C., Gumley, L., Baum, B., Seeman, S. W. and H. Zhong, 2002: Discriminating Clear-Sky from Cloud with MODIS - Algorithm Theoretical Basis Document, ATBD-MOD-06, Goddard Space Flight Center, pp 115.

Ackerman, S. Strabala, K., Menzel, P., Frey, R., Moeller, C., Gumley, L., Baum, B., Schaaf, C., and G. Riggs, 1997: Discriminating clear-sky from cloud with MODIS - Algorithm Theoretical Basis Document (MOD35), ATBD-MOD-06, Goddard Space Flight Center, pp 125.

Ackerman, S. A., Strabala, K. I., Menzel, W. P., Frey, R. A., Moeller, C. C. and L. E. Gumley, 1998: Discriminating clear sky from clouds with MODIS, J. Geophy. Res., **103**(D24), 32,141-32,156.

Ackerman, S. A., Smith, W. L., and H. E. Revercomb, 1990: The 27-28 October 1986 FIRE IFO cirrus case study: spectral properties of cirrus clouds in the 8-12 micron window, Mon. Weather Rev., **118**, 2377-2388.

Allen, R. C., Durkee, P. A., and C. H. Wash, 1990: Snow/cloud discrimination with multispectral satellite measurements, *J. Appl. Met.*, 29, 994-1004.

Anderson, G. P., Clough, S. A., Kneizys, F. X., Chetwynd, J. H., and E. P. Shettle, 1986: AFGL Atmospheric Constituent profiles (0-120 km), A. F. Geophysics Laboratory Technical Report, GL-TR-86-0110, pp. 43.

Anding, D. and R. Kauth, 1972: Reply to comment by G. A. Maul and M. Sidran, Remote Sensing Environ., 2, 171-173.

Anding, D. and R. Kauth, 1970: Estimation of sea surface temperature from space, Rem. Sens. Environ., 1, 217-220.

Arnold, C. P., 1975: Selective Reconnaissance Program of the western north Pacific, Bull. Amer. Meteo. Soc., **56**, 362-371.

Barton, I. J., 1995: Satellite-derived sea surface temperatures: Current status, J. Geophys. Res., **100**, 8777-8790.

Bell, J. J. and M. C. Wong, 1981: The near-infrared radiation received by satellites from clouds, Mon. Weath. Rev., 109, 2158.

Berk, A., Bernstein, L. S., and D. C. Robertson, 1989: MODTRAN: A Moderate Resolution Model for LOWTRAN 7, A. F. Geophysics Laboratory Technical Report, GL-TR-89-0122, pp 38.

Dickenson, L.G., Boselly, S.E., and W.W. Burgmann, 1974: "Defense Meteorological Satellite Program (DMSP) User's Guide", AWS TR-74-250, HQ Air Weather Service, Scott AFB, IL., pp 109.

Brandli, H. W., 1976: Satellite Meteorology. Air Weather Service TR-76-264, Det. 11, 2WS, Patrick AFB Florida, pp 188.

Byerly, W. P., Clement, J. E., Dorman, T., Engel, J., Julian, R., Miller, S. W., Young, J. B. and J. A. Walker, Radiometric Calibration, VIIRS Algorithm Theoretical Basis Document, Raytheon Information Technology and Scientific Services, pp. 56.

Chang A. T. C. and T. T. Wilheit 1979: Remote sensing of atmospheric water vapor, liquid water, and wind speed at the ocean surface by passive microwave techniques form the Nimbus-5 satellite, Radio Science, **14**, 793-802.

Charney, J. G., 1951: Dynamical forecasting by numerical process. *Compendium of Meteorology,* T. F. Malone, Ed., Amer. Meteor. Soc., 470–482.

Charney, J. G., Fjøertoft, R. and J. von Neumann, 1950: Numerical integration of the barotropic vorticity equation. *Tellus,* **2,** 237–254.

Che, N. and J. C. Price, 1992: Survey of radiometric calibration results and methods for visible and near infrared channels of NOAA-7, -9, and -11AVHRRs, Remote Sens. Environ., **41**, 19-27.

Coakley, J. A. and F. P. Bretherton, 1982: Cloud cover from high resolution scanner data: detecting and allowing for partially filled fields of view, J. Geophys. Res., 87(C7), 4917-4932.

Cracknell, A.P., 1997, The Advanced Very High Resolution Radiometer, Taylor and Francis, London.

Crum, T. D., 1987: AFGWC cloud forecast models, AFGWC Tech. Note 87/001, Air Force Global Weather Central, Omaha NE, 73 pp.

Dickenson, L.G., Boselly, S.E., and W.W. Burgmann, 1974: "Defense Meteorological Satellite Program (DMSP) User's Guide", AWS TR-74-250, HQ Air Weather Service, Scott AFB, IL., pp 109.

**Formatted:** Font: 12 pt

**Formatted:** title page

**Deleted:** R.

**Deleted:** Charney, J. G., 1951: Dynamical forecasting by numerical process. *Compendium of Meteorology,* T. F. Malone, Ed., Amer. Meteor. Soc., 470–482.¶
¶

Dvorak, V.F., 1973: A technique for the analysis and forecasting of tropical cyclone intensities from satellite pictures, Washington D.C., NOAA Tech. Memo. NESS 45, pp 19.

Emery, W. J., Yu, Y., Wick, G. A., Schluessel, P., and R. W. Reynolds, 1994: Correcting infrared satellite estimates of sea surface temperature for atmospheric water vapor attenuation, J. Geophys. Res., **99(C3)**, 5219-5236.

Farman, J. C., Gardiner, B. G., and J. D. Shanklin, 1985: Large losses of total ozone in Antarctica reeal seasonal $ClO_x/NO_x$ interaction, Nature, **315**, 207-208.

Fuller, J. F., 1990: Thor's Legions: Weather Support to the U.S. Air Force and Army, 1937-1987, American Meteorological Society, Historical Monograph Series, pp 443.

Fye, F. K., 1978: The AFGWC automated real-time cloud analysis model, AFGWC Tech. Note 78/002, Air Force Global Weather Central, Omaha, NE, 97 pp.

Gao, B. C. and Goetz, A. F. H., and W. J. Wiscombe, 1993: Cirrus cloud detection from Airborne Imaging Spectrometer Data using the 1.38 micron water vapor band, Journal of Geophysical Letters, **20**, 301-304.

Gesell, G., 1989: An algorithm for snow and ice detection using AVHRR data: An extension to the APOLLO software package, Int. J. Remote Sens., **10**, 897-905.

Goetz, A. F. H., Van, G., Solomon, J., and B. Rock, 1985: Imaging spectrometry for Earth remote sensing, Science, **228**, 1147-1153.

Gustafson, G. B., Isaacs, R. G., d'Entremont, R. P., Sparrow, J. M., Hamill, R. M., Johnson, D. W., Sarkisian, C. P., Peduzzi, D. C., Pearson, B. T., Jakabhazy, V. D., Belfiore, J. S., and A. S. Lisa, 1994: Support of environmental requirements for cloud analyses and archive (SERCAA): algorithm descriptions, US Air Force Phillips Laboratory Tech. Report, 94-2114, Hanscom Air Force Base, MA, pp 100.

Hamill, T. M., d'Entremont, R. P., and J. T. Bunting, 1992: A description of the Air Force Real-Time Nephanalysis Model, Weather and Forecasting, **7**, 288-306.

Hughes, F. D., 1987: Skill of medium-range forecast group. NMC Office Note 326, NWS, NOAA, U.S. Dept. of Commerce.

Hughes, N. A., 1984: Global cloud climatologies: an historical review, J. Clim. Appl. Meteor., **23**, 724-751.

Hutchison, K. D., Roskovensky, J., Jackson, J., Heidinger, A., Pavolonis, A., Frey, R., and T. Kopp (in press): Automated cloud detection and typing of data collected by the Visible Infrared Imager Radiometer Suite (VIIRS).

Hutchison, K. D. and J. M. Jackson, 2003: Cloud detection over desert regions using the 412 nanometer MODIS channel, Geoph. Res. Ltrs., **30(23)**, 2187, doi:10.1029/2003GL018446.

Deleted: xx, yyy-yyy

Hutchison, K. D., 2003: "Application of MODIS Data and Products for Air Quality Management across the State of Texas," Atmospheric Environment, **37**, 2403-2412.

Hutchison, K. D., 2002: "The Retrieval of Cloud Base Heights from MODIS and 3-Dimensional Cloud Fields from NASA's EOS Aqua Mission," International Journal of Remote Sensing. **23**, 5247-5263.

Hutchison, K. D., 1999: Application of AVHRR/3 Imagery for the Improved Detection of Thin cirrus clouds and specification of Cloud Top Phase, Journal of Atmospheric and Oceanic Technology, 16, 1885-1899.

Hutchison, K. D., Marusa, S., Henderson, J. R., Kenley, R. C., Topping, P. C., Uplinger, W. and J. Twomey, 1999: "System Design Considerations for the Retrieval of Sea Surface Temperatures during the NPOESS Era," Journal of Atmospheric and Oceanic Technology, **1**, 107-116.

Hutchison, K. D. and J. K. Locke, 1997: Snow Identification through Cirrus Cloudy Atmospheres using AVHRR Daytime Imagery, Geophysical Research Letters, 24, 1791-1794.

Hutchison, K. D., Etherton, B. J., Topping, P. C., and A. H. L. Huang, 1997a: Cloud Top Phase Determination from the Fusion of Signatures in Daytime AVHRR Imagery and HIRS Data , International Journal of Remote Sensing, 18, 3245-3262.

Hutchison, K. D., B. J. Etherton, and P. C. Topping, 1997b: Validation of Automated Cloud Top Phase Algorithms: Distinguishing Between Cirrus Clouds and Snow in A-priori Analyses of AVHRR Imagery, Optical Engineering, 36, 1727-1737.

Hutchison, K. D. and N. Choe, 1996: Application of 1.38-µm imagery for thin cirrus detection in daytime imagery collected over land surfaces, Int'l. J. Rem. Sens., **17**, 3325-3342.

Deleted:

Hutchison, K. D. and K. Hardy, 1995: Threshold functions for automated cloud analyses of global meteorological satellite imagery, *International Journal of Remote Sensing,* **16**, 3665-3680.

Hutchison, K. D., Hardy, K., and Gao, B. C., 1995: Improved Detection of Optically-Thin Cirrus Clouds in Nighttime Multispectral Meteorological Satellite Imagery using Total Integrated Water Vapor Information, Journal of Applied Meteorology, 34, 1161-1168.

Hutchison, K. D., Marusa, S., Henderson, J. R., Kenley, R. C., Topping, P. C., Uplinger, W., and J. Twomey, 1999: System Design Considerations for the Retrieval of Sea

Surface Temperatures during the NPOESS Era, Journal of Atmospheric and Oceanic Technology, 1, 107-116.

Hutchison, K., and P. Janota, 1990: Cloud Models Enhancement Project Phase II Report, The Analytic Sciences Corporation (TASC) Technical Report, TR-5773-2, August 1990.

Hutchison, K., and P. Janota, 1989: Cloud Models Enhancement Project Phase I Report, The Analytic Sciences Corporation (TASC) Technical Report, TR-5773-1, August 1989.

Inoue, T., 1985: On the temperature and effective emissivity determination of semitransparent cirrus clouds by bi-spectral measurements in the 10 micron window region, *Journal of Meteorological Society of Japan,* 63, 88-99.

Kalnay, E., and Coauthors, 1996: The NCEP/NCAR 40-Year Reanalysis Project. *Bull. Amer. Meteor. Soc.,* **77,** 437–471.

Kalnay, E., Lord, S. J., and R. D. McPherson, 1998: Maturity of Operational Numerical Weather Prediction: Medium Range, Bull. Amer. Meteo. Soc., **79**, No. 12, 2753-2769.

Key, J., D. Santek, C.S. Velden, N. Bormann, J.-N. Thepaut, L.P. Riishojgaard, Y. Zhu, and W.P. Menzel, 2003: Cloud-drift and Water Vapor Winds in the Polar Regions from MODIS, IEEE Trans. Geosci. Remote Sensing, **41**(2), 482-492.

Kidder, S. Q. and T. H. Vonder Haar, An Introduction to Satellite Meteorology, pp 466, San Diego, Academic Press.

King, M. D. and R. Greenstone, 1999: 1999 EOS Reference Handbook, NASA GSFC Publication, 361 pp

King, M. D., Tsay, S-C., Platnick, S. E., Wang, M., and K-N. Liou, , 1997: Cloud Retrieval Algorithms for MODIS: Optical Thickness, Effective Particle Radius, and Thermodynamic Phase, MODIS Algorithm Theoretical Basis Document No. ATBD-MOD-05, Version 5, pp. 83.

Kramer, H.J., 2002: Observation of the Earth and its Environment, Springer, Berlin, pp. 1510.

Keiss, R. B., and W. M. Cox, 1985: The AFGWC automated real-time cloud analysis model, US Air Force Tech. Note, 88/001, Air Force Global Weather Central, Omaha, NE, 82 pp.

King, M. D., Menzel, W. P., Grant, P. S., Myers, J. S., Arnold, G. T., Platnick, S. E., Gumley, L. E., Tsay, S-C., Moeller, C. C., Fitzerald, M., Brown, K. S., and F. G. Osterwisch, 1996: Airborne Scanning Spectrometer for Remote Sensing of Cloud,

**Deleted:** JONES … 1992 (SEE SECTION 1.3.2 AND ELSEWHERE).¶

**Deleted:** 2002

**Deleted:** pp (has this been published in the refereed literature?)

Aerosol, Water Vapor, and Surface Properties, Journal of Atmospheric and Oceanic Technology, 13, 777-794.

King, M. D. and R. Greenstone, 1999: 1999 EOS Reference Handbook, NASA Goddard Space Flight Center Publication, 361 pp

Kreibel, K. T., Gesell, G., Kaestner, M. and H. Mannstein, 2003: The cloud analysis tool APOLLO: Improvements and validations, Journal of Remote Sensing, **24**, 2389-2408.

Lameii, N., Hutchison, K. D., Crawford, M. M. and N. Khazanie, 1994: "Cloud Type Discrimination via Multispectral Textural Analysis," Optical Engineering, **33**, 1303 – 1313.

Liebe, H. J., 1985: An updated model for millimeter wave propagation in moist air, Radio Science, **20**, 1069-1089.

Liou, K-N., 2002: Introduction to Atmospheric Radiation, International Geophysics Series, 26, 2nd Edition, London, New York: Academic Press, pp 581.

Liou, K-N., 1992: Radiation and Cloud Processes in the Atmosphere, Oxford press, pp 487.

Liou, K-N., 1986: The influence of cirrus on weather and climate process: A global perspective, Mon. Wea. Rev., **114**, 1167-1199.

Liou, K-N., 1980: Introduction to Atmospheric Radiation, International Geophysics Series, 26, London, New York: Academic Press, pp 392.

London, J., 1957: A study of the atmospheric heat balance, AFCRC Tech. Repot 57-287, College of Engineering, New York University, NY.

Lorenz, E. N., 1963: Deterministic nonperiodic flow, *Journal of Atmospheric Scences*, **20,** 130–141.

Lorenz, E. N., 1965: A study of the predictability of a 28-variable atmospheric model. *Tellus,* **17,** 321–333.

Lorenz, E. N., 1969: The predictability of a flow which possesses many scales of motion. *Tellus,* **21,** 289–307.

Maul, G. A. and M. Sidran, Comment of Anding and Kauth, Remote Sensing Environ., 2, 165-169.

Martin, G. M., Johnson, D. W. and A. Spice, 1994: The measurement and parameterization of effective radius of droplets in warm stratocumulus clouds, Journal of Atmospheric Science, **51**, 1823-1842.

**Deleted:** .

**Deleted:** *os*

**Deleted:** *i*

**Deleted:** 8

**Deleted:** et al…… 994, see section 8.6.1¶

McClain, E. P., Pichel W. G., Walton, C. C., Ahmad, A., and J. Sutton, 1983: Multichannel improvements to satellite-derived global sea surface temperatures, Adv. Space Res., **2(6)**, 43-47.

McClain, E. P., Pichel, W. G., and C. C. Walton, 1985, Comparative performance of AVHRR-based multichannel sea surface temperatures, J. Geophys. Res., **90(C6)**, 11,587 - 11,601.

McMillin, L. M. and D. S. Crosby, 1984: Theory and validation of the multiple window sea surface temperature technique, J. Geophys. Res., 89(C3), 3655-3661.

McMillin, L. M., 1971: A method of determining surface temperatures from measurements of spectral radiance at two wavelengths, PhD dissertatin, Iowa State Univ., Ames.

Menzel, W. P., Baum, B. A., Strabala, K. L., and R. A. Frey, 2002: Cloud top properties and cloud phase - Algorithm Theoretical Basis Document, ATBD-MOD-04, Goddard Space Flight Center, pp 62.

Menzel, W. P. and K. L. Strabala, 1997: Cloud top properties and cloud phase - Algorithm Theoretical Basis Document, ATBD-MOD-04, Goddard Space Flight Center, pp 55.

Minnett, P. J., 1986: A numerical study of the effects of anomalous North Atlantic atmospheric conditions on the infrared measurement of sea surface temperature from space, J. Geophys. Res., **91(C7)**, 8509-8521.

Meyer, W. D., 1985: DMSP: Review of its impact, Monitoring Earth's Ocean, Land, and Atmosphere from Space – Sensors, Systems, and Applications, Progress in Astronautics and Aeronautics, AiAA, **97**, 129-149.

Nakajima, T. and M. D. King, 1990: Determination of the optical thickness and effective particle radius of clouds from reflected solar radiation measurements. Part I: Theory. *J. Atmos. Sci.*, **47**, 1878–1893.

National Polar-Orbiting Operational Environmental Satellite System (NPOESS) Technical Requirements Document (TRD), Appendix D, NPOESS System EDR Requirements, Version 6a, June, 2001, pp 86.

National Polar-Orbiting Operational Environmental Satellite System (NPOESS) Visible/Infrared Imager/Radiometer Suite (VIIRS) Sensor Requirements Document (SRD), Version 3, June, 2000, pp 91.

National Polar-Orbiting Operational Environmental Satellite System (NPOESS) Conical Scanning Microwave Imager/Sounder (CMIS) Sensor Requirements Document (SRD), Version Three, March 2001, pp 70.

**Deleted:** a

**Deleted:** t

**Deleted:** c

**Deleted:** b

**Deleted:** d

**Deleted:** Cooperative Institute for Meteorological Studies, University of Wisconsin – Madison,

**Deleted:** a

**Deleted:** t

**Deleted:** c

**Deleted:** b

**Deleted:** d

**Deleted:** Cooperative Institute for Meteorological Studies, University of Wisconsin – Madison

**Deleted:** (Get the right reference for the original ATBD).

**Deleted:** CONICAL

**Deleted:** CANNING

**Deleted:** ICROWAVE

**Deleted:** MAGER

**Deleted:** OUNDER

National Polar-Orbiting Operational Environmental Satellite System (NPOESS) Cross Track Infrared Sounder (CrIS) Sensor Requirements Document (SRD), Version Two, March 1999, pp 46.

National Polar-Orbiting Operational Environmental Satellite System (NPOESS) GPS Occultation Sensor (GPSOS) Sensor Requirements Document (SRD), Version Two, Revision b, May 2000, pp 28.

National Polar-Orbiting Operational Environmental Satellite System (NPOESS) Ozone Mapping Profiling Suite (OMPS) Sensor Requirements Document (SRD), Version Two, February 1999, pp 28.

National Polar-Orbiting Operational Environmental Satellite System (NPOESS) Space Environmental Sensor Suite (SESS) Sensor Requirements Document (SRD), Version One, June 1999, pp 44.

Ou, S-C., Liou, K-N., and Y. Chen, Inference of the vertical distribution of ice crystal sizes using MODIS multi-channel data, Geophysical Research Letters (in press).

Ou, S-C., Liou, K-N., Takano, Y., Higgins, G. J., George, A., and R. Slonaker, Cloud effective particles size and cloud optical thickness, VIIRS Algorithm Theoretical Basis Document, Ver. 5, Rev. 1: May 2002, pp 176.

Ou, S-C., Liou, K-N., Takano, Y., Higgins, G. J., George, A., and R. Slonaker, 2003: Remote sensing of cirrus cloud optical thickness and effective particle size for the National Polar-orbiting Operational Environmental Satellite System Visible/Infrared Imager Radiometer Suite: sensitivity to instrument noise and uncertainties in environmental parameters, Applied Optics, **42**, 7202-7214.

Ou, S. C., Liou, K-N., Gooch, W. M. and Y. Takano, 1993: Remote sensing of cirrus cloud parameters using advanced very-high resolution radiometer 3.7 and 10.9 micron channels, Appl. Opt., **32**, 2171-2180.

Ou, S. C., Liou K-N., Tokano, Y., Rao, N. X., Fu, Q., Heymsfield, A. J., Miloshevich, M. L., Baum, B. and S. A. Kinne, 1995: Remote sounding of cirrus cloud optical depths and ice crystal size from AVHRR: Verification using FIRE II IFO Measurements, **52**, Journal of Atmospheric Sciences, 4143-4158

Pavolonis, M. J. and A. K. Heidinger, 2004: Daytime cloud overlap detection from AVHRR and VIIRS, Journal of Applied Meteorology, 43, 762-778.

Phillips, N. A., 1990: Dispersion processes in large-scale weather. World Meteorological Organization, 700, 126 pp. [Available from World Meteorological Organization, Avenue Giuseppe-Motta, 41, CP2300, 1211 Geneva 2, Switzerland.]

Phillips, N. A., 1998: Carl-Gustaf Rossby: His times, personality, and actions. *Bull.*

**Deleted:** ROSS
**Deleted:** RACK
**Deleted:** NFRARED
**Deleted:** OUNDER
**Deleted:** CCULTATION
**Deleted:** ENSOR
**Deleted:** ZONE
**Deleted:** APPING
**Deleted:** ROFILING
**Deleted:** UITE
**Deleted:** PACE
**Deleted:** NVIRONMENTAL
**Deleted:** ENSOR
**Deleted:** UITE
**Deleted:** Pavolinis
**Deleted:** 3
**Deleted:** (citation pending)

*Amer. Meteor. Soc.,* **79,** 1097–1112.

Planet, W.G. (ed.), (1988). Data extraction and calibration of TIROS-N/NOAA radiometers. NOAA Technical Memorandum NESS 107 – Rev. 1, Oct. 1988. 130 pp.

Randall, D. A., Coakley, J. A., Fairall, C. W., Uropfli, R. A., and D. H. Lenschow, 1984: Outlook for research on subtropical maritime stratiform clouds, Bull. Americ. Meteo. Soc., **65**, 1290-1301.

Rao, C. R. and J. Chen, 1993: Calibration of the visible and near-infrared channels of the Advanced Very High Resolution Radiometer (AVHRR) after launch, Conf. on Recent Advances in Sensors, Radiometric Calibration, and Processing of Remotely Sensed Data, SPIE, **1938**, Orlando, FL.

Rao, P.K., Holmes, S.J., Anderson, R.K., Winston, J.S. and Lehr, P.E., 1990, Weather Satellites: Systems, Data and Environmental Applications (American Meteorological Society: Boston). pp. 503.

Rosenkranz, P. W., Hutchison, K. D., Hardy, K. R. and M. S. Davis, 1997: "An Assessment of the Impact of Satellite Microwave Sounder Incidence Angle and Scan Geometry on the Accuracy of Atmospheric Temperature Profile Retrievals," Journal of Atmospheric and Oceanic Technology, **14**, 488-494.

Rosenkranz, P. W., Hutchison, K. D. and K. R. Hardy, 1994: "Simulations of Temperature Retrieval Accuracy in the Middle and Lower Atmosphere using Oxygen Microwave Lines," Proceedings of the Seventh AMS Conference on Satellite Meteorology, Monterey, CA, J11-J14.

Rosovensky, J. K. and K. N. Liou, 2003, Detection of thin cirrus using a combination of 1.38 μm reflectance and window brightness temperature difference, J. Geophys, Res., **108(D18), 4570**, doi:10:1029/2002JD003346.

Rossby, C.-G., 1940: Planetary flow patterns in the atmosphere. *Quart. J. Roy. Meteor. Soc.,* **66** (Suppl.), 68–87.

Rossby, C.-G., and Coauthors, 1939: Relation between variations in the intensity of the zonal circulation of the atmosphere and the displacements of the semi-permanent centers of action. *J. Mar. Res.,* **2,** 38–55.

Rossow, W. B., Moscher, F., Kinsella, E., Arking, A., Desbois, M., Harrison, E., Minnis, O., Ruprecht, E., Seze, G., Simmer, C., and E. Smith, 1985: ISCCP cloud algorithm intercomparison, J. Clim. Appl. Meteor., **24**, 877-903.

Saunders, P. M., 1967: Aerial measurements of sea surface temperatures in the infrared, J. Geophys.. Res., 72(16), 4109-4117.

**Deleted:** Rao 2000 (section 1.3.3)¶
¶

**Deleted:** isng

**Deleted:**

**Deleted:** xxxx-yyyy

Saunders, R. W. and K. T. Kriebel, 1988: An improved method for detecting clear sky and cloudy radiances from AVHRR data, *International Journal of Remote Sensing,* 9, 123-150.

Scorer, R. S., 1990: Satellite as Microscope, Ellis Horwood Limited, pp 267.

Stewart, R. H., 1985: Methods of Satellite Oceanography, University of California Press, Berkeley, CA., pp 360.

Schluessel, P., Shin, H.-Y., and W. J. Emery, 1987: Comparison of satellite-derived sea surface temperatures with in situ skin measurements, J. Geophys. Res., **92(C3)**, 2859-2874.

Schiffer, R. A. and W. B. Rossow, 1983: The International Satellite Cloud Climatology Project (ISCCP). The first project of the World Climate Research Program, Bull. Amer. Meteor. Soc., **64**, 779-784.

Slingo, A., Nicholls, S. and J. Schmetz, 1982: Aircraft observations of marine stratocumulus during JASIN, Quarterly Journal of the Royal Meteorological Society, **108**, 833-856.

Smith W. L., Knuteson, R. O., Revercomb, H. E., Feltz, W., Howell, H. B., Menzel, W. P., Nalli, N. R., Brown, O., Minnett, P., and W. McKeown, 1996: Observations of the infrared radiative properties of the ocean - implications for the measurement of sea surface temperature via satellite remote sensing, Bull. Amer. Meteor. Soc., **77**, 41-51.

Stogryn, A., 1989a: The magnetic field dependence of brightness temperatures at frequencies near the O2 microwave absorption lines. IEEE Trans. Geosci. Remote Sens., 27, 279–289.

Stogryn, A., 1989b: Mesospheric temperature sounding with microwave radiometers. IEEE Trans. Geosci. Remote Sens., 27, 332–338. von Zahn, U., and W. Meyer, 1989: Mesopause temperatures in polar summer. J. Geophys. Res., 94, 14 647–14 651

Stewart, R. H. 1985: Methods of Satellite Oceanography, University of California Press, Los Angeles, pp 360.

Stowe, L. L., Davis, P. A., and E. P. McClain, 1999: Scientific basis and initial evaluation of the CLARVR-1 global clear cloud classification algorithm for the advanced very high resolution radiometer, J. Atmos. and Ocean. Tech., 16, 656-681.

Stowe, L. L., McClain, E.P., Carey, R., Pellegrino, P., Gutman, G. G., Davis, P., Long, C., and S. Hart, 1991: Global distribution of cloud cover derived from NOAA/AVHRR operational satellite data, Advances in Space Research, **11**, 51-54.

Stowe, L. L., 1984: Evaluation of Nimbus 7 THIR/CLE and Air Force Three-Dimensional Nephanalysis estimates of cloud amount, J. Geophys. Res., **89**, 5370-5380.

**Deleted:** ?

**Deleted:**

**Deleted:**

**Deleted:** see section 8.6.1

Strabala **K. I.**, Ackerman S. A. and W. P. Menzel, 1994 **Cloud Properties Inferred From 8-12 µm Data**,

Valovcin, F. R., 1978: Spectral radiance of snow and clouds in the near infrared spectral region, Tech. Rep. *AFGL-TR-78-0289*, 46 pp.,USAF Geophysics Lab., Bedford, MA..

Vane, G., 1987: Airborne visible/infrared imaging spectrometer (AVIRIS), *Jet Propulsion Laboratory Publication 87-38*, Jet Propulsion Laboratory, Pasadena, CA.

Visible/Infrared Imager/Radiometer Suite (VIIRS) Sensor Performance Specification, CAGE Code 11323 Raytheon Company, PRF PS154640-101A, Santa Barbara Remote Sensing, Goleta CA, 4 January 2002, pp. 195.

Walton, C. C., Brower, R. L., and T. L. Signore, 1976: Satellite-derived sea surface temperatures by multi-channel regression, Proceedings of 19th COSPAR Symposium on Meteorological Observations from Space, Philadelphia, PA.

Walton, C. C., 1988: Nonlinear multichannel algorithm for estimating sea surface temperature with AVHRR satellite data, J. Appl. Meteor., **27**, 115-124.

Warnecke, G., 1987, The visualization of the ceaseless atmosphere, in *Remote Sensing Applications in Meteorology and Climatology*, edited by R.A. Vaughan (Reidel, Dordrecht), 245 – 257.

Warnecke, G. and Zick, C, 1981, The use of cinematographic methods for the presentation of atmospheric motions as revealed by remote sensing techniques from satellites, in *Remote Sensing in Meteorology, Oceanography and Hydrology*, edited by A.P. Cracknell (Ellis Horwood, Chichester), 452 – 473.

Warnecke, G., Zick, C., Carus, B., Döring, R., Eriksson, A. and Voellger, C., 1987, Information extraction from meteorological satellite image sequences, in *Remote Sensing Applications in Meteorology and Climatology*, edited by R.A. Vaughan (Reidel, Dordrecht), 259 – 283.

Watts, P. D., Allen, M. R., and T. J. Nightingale, 1996: Wind speed effects on sea surface emission and reflection for the Along Track Scanning Radiometer, J. Atmos. and Ocean. Tech., **13**, 126-141.

Webster, F. and M. Fieux, 1984: TOGA Overview. *Large-scale oceanographic experiments and satellites*, C. Gautier and M. Fieux, Eds., D. Reidel, 17-24.

Wilheit, T. T. and K. D. Hutchison, 2000: "Retrieval of Cloud Base Heights from Passive Microwave and Cloud Top Temperature Data," IEEE Transactions on Geoscience and Remote Sensing, **38**, 1253-1259.

Wilheit, T. T. and K. D. Hutchison, 1997: "Water Vapor Profile Retrievals using Passive Microwave Data Constrained by Infrared-Based Cloud Information," International Journal of Remote Sensing, **18**, 3263-3278.

**Deleted:** et al

**Deleted:** ¶

**Deleted:** s

Wilheit, T. T., Hutchison, K. D. and K. R. Hardy, 1994: "A Water Vapor Profiling Algorithm for Advanced Environmental Monitoring Satellites," Proceedings of the Seventh AMS Conference on Satellite Meteorology, Monterey, CA, 528-531.

Wylie, D. P., Menzel, W. P. , Woolf, H. M., and K. I. Strabala, 1994: Four years of global cirrus cloud statistics using HIRS, *Journal of Climate,* **7**, 1972-1986.

Za'vody, A.M., Mutlow, C.T., and D.T. Llewellyn-Jones, 1995: A radiative transfer model for sea surface temperature retrieval for the along-track scanning radiometer, J. Geophy Res., 100(C1), 937-952.

Zick, C., 1987, Cloud motion analysis of cyclones within cold air masses, in *Remote Sensing Applications in Meteorology and Climatology*, edited by R.A. Vaughan (Reidel, Dordrecht), 285 – 300.

Page v: [1] Deleted keithh 11/27/2004 11:53:00 AM


TABLE OF CONTENTS ..... II

LIST OF TABLES ..... VIII

LIST OF FIGURES ..... XI

LIST OF FIGURES ..... XI

PREFACE ..... XX

PREFACE ..... XX

CHAPTER 1 ..... 23

INTRODUCTION ..... 23

SATELLITE METEOROLOGY ..... 23

1.1 OVERVIEW OF NUMERICAL WEATHER PREDICTION MODELING ..... 23
1.2 EVOLUTION OF OBSERVATIONAL DATA FOR NWP MODELING ..... 24
1.3 ADDITIONAL APPLICATIONS OF METEOROLOGICAL SATELLITE DATA ..... 30
*1.3.1 Sea Surface Temperature Analyses ..... 30*
*1.3.2 Climate Modeling ..... 35*
*1.3.3 Tropical Storm Monitoring ..... 37*
*1.3.4 Satellite-Derived Wind Fields ..... 39*

CHAPTER 2 ..... 42

METEOROLOGICAL SATELLITE SYSTEMS ..... 42

2.1 EVOLUTION OF SATELLITES AND SENSORS ..... 42
*2.1.1 Polar-Orbiting Environmental Satellite (POES) Systems ..... 43*
2.1.1.1 The Advanced TIROS-N (ATN) Satellite Series ..... 45
2.1.1.2 Defense Meteorological Satellite Program (DMSP) ..... 49
2.1.1.3 NASA Earth Observing System (EOS) Program ..... 52
2.1.1.4 Other Polar-Orbiting Meteorological Satellite Systems ..... 52
2.1.1.5 The Proposed Eumetsat MetOp Series ..... 52
*2.1.2 Geostationary Meteorological Satellite Systems ..... 52*
2.2 THE NATIONAL POLAR-ORBITING OPERATIONAL ENVIRONMENTAL SATELLITE SYSTEM (NPOESS) ..... 52

CHAPTER 3 ..... 52

VIIRS IMAGERY DESIGN ANALYSIS ..... 52

3.1 VIIRS EDR REQUIREMENTS OVERVIEW ..... 52
3.2 VIIRS IMAGERY REQUIREMENTS ..... 52
3.3 CLOUD APPLICATIONS-RELATED IMAGERY REQUIREMENTS ..... 52
*3.3.1 Cloud Cover ..... 52*
*3.3.2 Cloud Type ..... 52*
3.4 VALUE OF MANUALLY-GENERATED CLOUD ANALYSES ..... 52
*3.4.1 Performance Verification of Automated Cloud Models ..... 52*
*3.4.2 Quality Control of Automated Cloud Analyses ..... 52*

CHAPTER 4 ..... 52

**VIIRS IMAGERY REQUIREMENTS ANALYSIS** ..... **52**

4.1 THEORETICAL BASIS FOR MANUAL CLOUD ANALYSES ..... 52
4.2 OVERVIEW OF APPROACH TO INSTRUMENT DESIGN ..... 52
4.3 CLOUD TRUTH DATA SETS TO FLOWDOWN SENSOR REQUIREMENTS ..... 52
*4.3.1 Cloud Truth from Manual Interpretation of Multispectral Imagery* ..... *52*
*4.3.2 Cloud Truth in Synthetic Scenes for Sensor Simulations* ..... *52*
*4.4 DERIVATION OF SENSING REQUIREMENTS FROM ANALYSIS REQUIREMENTS* ..... *52*
4.5 OVERVIEW OF VIIRS HARDWARE DESIGN ..... 52
*4.5.1 VIIRS Sensor Overview* ..... *52*
*4.5.2 Detailed VIIRS Design Capabilities* ..... *52*
4.5.2.1 VIIRS Spectral Design Requirements ..... 52
4.5.2.2 VIIRS Spatial Capabilities ..... 52
4.5.2.3 VIIRS Horizontal Sampling Interval ..... 52
4.5.2.4 VIIRS Dynamic Range Capability ..... 52
4.5.2.5 VIIRS Sensitivity Capability ..... 52
4.5.2.6 VIIRS Sensor Polarization Sensitivity ..... 52
4.5.2.7 Detector Performance ..... 52
4.5.2.8 Band to Band Registration or Co-registraton ..... 52
4.5.2.9 VIIRS Calibration ..... 52
4.5.2.9.1 VIIRS Absolute Radiometric Calibration – Uniform Scene ..... 52
4.5.2.9.2 VIIRS Relative Radiometric Calibration – Uniform Scene ..... 52
4.5.2.9.3 VIIRS Relative Radiometric Calibration – Structure Scene ..... 52

**CHAPTER 5** ..... **52**

**PRINCIPLES IN IMAGE INTERPRETATION** ..... **52**

5.1. INTRODUCTION ..... 52
5.2. VIIRS IMAGERY DATA ..... 52
*5.2.1. VIIRS Imagery Band I1 (0.64 ± 0.040 μm)* ..... *52*
*5.2.2. VIIRS I2 Band (0.865 ± 0.020 μm)* ..... *52*
*5.2.3. VIIRS I3 and M10 Bands (1.61 ± 0.03 μm)* ..... *52*
*5.2.5. VIIRS I5 Band (11.45 ± 0.95 μm)* ..... *52*
*5.2.6. VIIRS Day Night Band (DNB)* ..... *52*
5.3. VIIRS IMAGERY ASSIST DATA ..... 52
*5.3.1. VIIRS M1 – M4 Bands (0.412 ± 0.010 μm, 0.445 ± 0.009 μm, 0.488 ± 0.010 μm, 0.555 ± 0.010 μm)* ..... *52*
*5.3.2. VIIRS M9 Band (1.378 ± 0.0075 μm)* ..... *52*

**CHAPTER 6** ..... **52**

**MULTICOLOR COMPOSITES OF MULTISPECTRAL IMAGERY** ..... **52**

6.1. INTRODUCTION ..... 52
6.2. COLOR COMPOSITES OF (0.64μM, 0.865μM, AND 12.0 μM) SURFACE VEGETATION AND CLOUD CLASSIFICATIONS ..... 52
6.3 COLOR COMPOSITES (3.7 μM ALBEDO, 0.865μM, 12.0 μM) FOR SNOW DETECTION ..... 52
6.4. COLOR COMPOSITES OF (0.64 μM, 0.64μM, 3.7μM ALBEDO) SNOW MAPPING THROUGH THIN CIRRUS CLOUDS ..... 52
6.5. COLOR COMPOSITES OF (0.412 μM, 0.865 μM, AND 0.64 μM) CLOUDS OVER ARID REGIONS ..... 52

**CHAPTER 7** ..... **52**

**CASE STUDIES IN THE USE OF MULTICOLOR COMPOSITES FOR SCENE INTERPRETATION** ..... **52**

7.1 OVERVIEW ..... 52
7.2 MAS DATA OVER ALASKA ..... 52
*COLOR COMPOSITE #1: IDENTIFICATION OF VEGETATED SURFACES* ..... *52*
*COLOR COMPOSITE #2: IDENTIFICATION OF SNOW AND ICE FEATURES* ..... *52*
*COLOR COMPOSITE #3: CLOUD TYPE CLASSIFICATION – PART I* ..... *52*
*COLOR COMPOSITE #4: CLOUD TYPE CLASSIFICATION – PART II* ..... *52*
7.3 MAS SUCEES DATA COLLECTED OVER COLORADO ..... 52
*COLOR COMPOSITE #1: IDENTIFICATION OF VEGETATED SURFACES* ..... *52*
*COLOR COMPOSITE #2: IDENTIFICATION OF SNOW AND ICE FEATURES* ..... *52*
*Color Composite #3: CLOUD TYPE CLASSIFICATION – PART I* ..... *52*
*Color Composite #4: CLOUD TYPE CLASSIFICATION – PART II* ..... *52*

**CHAPTER 8** ..... **52**

**AUTOMATED 3-DIMENSIONAL CLOUD ANALYSES FROM NPOESS** ..... **52**

8.1 ARCHITECTURE FOR 3-DIMENSIONAL CLOUD ANALYSES ..... 52
8.2 AUTOMATED CLOUD DETECTION ..... 52
*8.2.1 Single Channel Cloud Detection Algorithms* ..... *52*
*8.2.2 Multispectral Channel Cloud Detection Algorithms* ..... *52*
*8.2.3 Spatial Cloud Classifier Algorithms* ..... *52*
8.3 CLOUD TOP PHASE CLASSIFICATIONS ..... 52
8.4 CLOUD OPTICAL (THICKNESS AND PARTICLE SIZE) PROPERTIES ..... 52
*8.4.1 Retrieval for Water Clouds During Daytime Conditions* ..... *52*
*8.4.2 Retrieval for Ice Clouds Microphysical Properties* ..... *52*
8.4.2.1 Retrieval of Ice Cloud Properties in Daytime Imagery ..... 52
8.4.2.2 Retrieval of Ice Cloud Properties in Nighttime Imagery ..... 52
8.5 CLOUD TOP (TEMPERATURE, PRESSURE, AND HEIGHT) PARAMETERS ..... 52
8.6 CLOUD BASE HEIGHTS ..... 52
*8.6.1 Cloud base heights retrieved for water clouds* ..... *52*
*8.6.2 Cloud base heights retrieved for ice clouds* ..... *52*
*8.6.3 Ancillary Data and Products from Other Sensors* ..... *52*
*8.6.4 Integration of VIIRS, CMIS, and Conventional Cloud Base Observations* ..... *52*

**CHAPTER 9** ..... **52**

**REFERENCES** ..... **52**

**Page v: [2] Deleted** **keithh** **11/27/2004 11:53:00 AM**

**TABLE OF CONTENTS** ..... **II**

**LIST OF TABLES** ..... **VI**

**LIST OF FIGURES** ..... **VIII**

**LIST OF FIGURES** ..... **VIII**

**PREFACE** ..... **XIII**

**PREFACE** ..... **XIII**

**CHAPTER 1** ..... **16**

**INTRODUCTION** ..... **16**

**SATELLITE METEOROLOGY** ..... **16**

1.1 OVERVIEW OF NUMERICAL WEATHER PREDICTION MODELING ..... 16
1.2 EVOLUTION OF OBSERVATIONAL DATA FOR NWP MODELING ..... 17
1.3 ADDITIONAL APPLICATIONS OF METEOROLOGICAL SATELLITE DATA ..... 23
*1.3.1 Sea Surface Temperature Analyses* ..... *23*
*1.3.2 Climate Modeling* ..... *28*
*1.3.3 Tropical Storm Monitoring* ..... *30*
*1.3.4 Satellite-Derived Wind Fields* ..... *31*

**CHAPTER 2** ..... **34**

**METEOROLOGICAL SATELLITE SYSTEMS** ..... **34**

2.1 EVOLUTION OF SATELLITES AND SENSORS ..... 34
*2.1.1 Polar-Orbiting Environmental Satellite (POES) Systems* ..... *35*
2.1.1.1 The Advanced TIROS-N (ATN) Satellite Series ..... 37
2.1.1.2 Defense Meteorological Satellite Program (DMSP) ..... 41
2.1.1.3 NASA Earth Observing System (EOS) Program ..... 47
2.1.1.4 Other Polar-Orbiting Meteorological Satellite Systems ..... 52
2.1.1.5 The Proposed Eumetsat MetOp Series ..... 54
*2.1.2 Geostationary Meteorological Satellite Systems* ..... *57*
2.2 THE NATIONAL POLAR-ORBITING OPERATIONAL ENVIRONMENTAL SATELLITE SYSTEM (NPOESS) ..... 61

**CHAPTER 3** ..... **66**

**VIIRS IMAGERY DESIGN ANALYSIS** ..... **66**

3.1 VIIRS EDR REQUIREMENTS OVERVIEW ..... 66
3.2 VIIRS IMAGERY REQUIREMENTS ..... 67
3.3 CLOUD APPLICATIONS-RELATED IMAGERY REQUIREMENTS ..... 69
*3.3.1 Cloud Cover* ..... *70*
*3.3.2 Cloud Type* ..... *71*
3.4 VALUE OF MANUALLY-GENERATED CLOUD ANALYSES ..... 72
*3.4.1 Performance Verification of Automated Cloud Models* ..... *72*
*3.4.2 Quality Control of Automated Cloud Analyses* ..... *73*

**CHAPTER 4** ..... **77**

**VIIRS IMAGERY REQUIREMENTS ANALYSIS** ..... **77**

4.1 THEORETICAL BASIS FOR MANUAL CLOUD ANALYSES ..... 77
4.2 OVERVIEW OF APPROACH TO INSTRUMENT DESIGN ..... 80
4.3 CLOUD TRUTH DATA SETS TO FLOWDOWN SENSOR REQUIREMENTS ..... 83
*4.3.1 Cloud Truth from Manual Interpretation of Multispectral Imagery* ..... *84*
*4.3.2 Cloud Truth in Synthetic Scenes for Sensor Simulations* ..... *87*
*4.4 TRANLATION FROM ANALYSIS REQUIREMENTS TO SENSING REQUIREMENTS* ..... *90*
4.5 OVERVIEW OF VIIRS HARDWARE DESIGN ..... 101
*4.5.1 VIIRS Sensor Overview* ..... *101*
*4.5.2 Detailed VIIRS Design Capabilities* ..... *104*
4.5.2.1 VIIRS Spectral Design Requirements ..... 105

4.5.2.2 VIIRS Spatial Capabilities ..... 106
4.5.2.3 VIIRS Horizontal Sampling Interval ..... 107
4.5.2.4 VIIRS Dynamic Range Capability ..... 110
4.5.2.5 VIIRS Sensitivity Capability ..... 111
4.5.2.6 VIIRS Sensor Polarization Sensitivity ..... 112
4.5.2.8 Detector Performance ..... 113
4.5.2.9 Band to Band Registration or Co-registraton ..... 115
4.5.2.10 VIIRS Calibration ..... 117
4.5.2.10.1 VIIRS Absolute Radiometric Calibration – Uniform Scene ..... 117
4.5.2.10.2 VIIRS Relative Radiometric Calibration – Uniform Scene ..... 118
4.5.2.10.3 VIIRS Relative Radiometric Calibration – Structure Scene ..... 118

**CHAPTER 5 ..... 120**

**PRINCIPLES IN IMAGE INTERPRETATION ..... 120**

5.1. INTRODUCTION ..... 120
5.2. VIIRS IMAGERY DATA ..... 123
*5.2.1. VIIRS Imagery Band I1 (0.64 ± 0.040 μm) ..... 125*
*5.2.2. VIIRS I2 Band (0.865 ± 0.020 μm) ..... 128*
*5.2.3. VIIRS I3 and M10 Bands (1.61 ± 0.03 μm) ..... 131*
*5.2.5. VIIRS I5 Band (11.45 ± 0.95 μm) ..... 150*
*5.2.6. VIIRS Day Night Band (DNB) ..... 156*
5.3. VIIRS IMAGERY ASSIST DATA ..... 159
*5.3.1. VIIRS M1 – M4 Bands (0.412 ± 0.010 μm, 0.445 ± 0.009 μm, 0.488 ± 0.010 μm, 0.555 ± 0.010 μm) ..... 160*
*5.3.2. VIIRS M9 Band (1.378 ± 0.0075 μm) ..... 163*

**CHAPTER 6 ..... 167**

**MULTICOLOR COMPOSITES OF MULTISPECTRAL IMAGERY ..... 167**

6.1. INTRODUCTION ..... 167
6.2. COLOR COMPOSITES OF (0.64μM, 0.865μM, AND 12.0 μM) SURFACE VEGETATION AND CLOUD CLASSIFICATIONS ..... 169
6.3 COLOR COMPOSITES (3.7 μM ALBEDO, 0.865μM, 12.0 μM) FOR SNOW DETECTION ..... 171
6.4. COLOR COMPOSITES OF (0.64 μM, 0.64μM, 3.7μM ALBEDO) SNOW MAPPING THROUGH THIN CIRRUS CLOUDS ..... 173
6.5. COLOR COMPOSITES OF (0.412 μM, 0.865 μM, AND 0.64 μM) CLOUDS OVER ARID REGIONS ..... 175

**CHAPTER 7 ..... 177**

**CASE STUDIES IN THE USE OF MULTICOLOR COMPOSITES FOR SCENE INTERPRETATION ..... 177**

7.1 OVERVIEW ..... 177
7.2 MAS DATA OVER ALASKA ..... 178
*COLOR COMPOSITE #1: IDENTIFICATION OF VEGETATED SURFACES ..... 180*
*COLOR COMPOSITE #2: IDENTIFICATION OF SNOW AND ICE FEATURES ..... 182*
*COLOR COMPOSITE #3: CLOUD TYPE CLASSIFICATION – PART I ..... 184*
*COLOR COMPOSITE #4: CLOUD TYPE CLASSIFICATION – PART II ..... 187*
7.3 MAS SUCEES DATA COLLECTED OVER COLORADO ..... 189
*COLOR COMPOSITE #1: IDENTIFICATION OF VEGETATED SURFACES ..... 191*
*COLOR COMPOSITE #2: IDENTIFICATION OF SNOW AND ICE FEATURES ..... 193*
*Color Composite #3: CLOUD TYPE CLASSIFICATION – PART I ..... 195*

*Color Composite #4: CLOUD TYPE CLASSIFICATION – PART II* ..... *198*

**CHAPTER 8** ..... **201**

**AUTOMATED 3-DIMENSIONAL CLOUD ANALYSES FROM NPOESS** ..... **201**

8.1 ARCHITECTURE FOR 3-DIMENSIONAL CLOUD ANALYSES ..... 201
8.2 AUTOMATED CLOUD DETECTION ..... 203
*8.2.1 Single Channel Cloud Detection Algorithms* ..... *204*
*8.2.2 Multispectral Channel Cloud Detection Algorithms* ..... *204*
*8.2.3 Spatial Cloud Classifier Algorithms* ..... *207*
8.3 CLOUD TOP PHASE CLASSIFICATIONS ..... 207
8.4 CLOUD OPTICAL (THICKNESS AND PARTICLE SIZE) PROPERTIES ..... 213
*8.4.1 Retrieval for Water Clouds During Daytime Conditions* ..... *213*
*8.4.2 Retrieval for Ice Clouds Microphysical Properties* ..... *217*
8.4.2.1 Retrieval of Ice Cloud Properties in Daytime Imagery ..... 218
8.4.2.2 Retrieval of Ice Cloud Properties in Nighttime Imagery ..... 219
8.5 CLOUD TOP (TEMPERATURE, PRESSURE, AND HEIGHT) PARAMETERS ..... 222
8.6 CLOUD BASE HEIGHTS ..... 223
*8.6.1 Cloud base heights retrieved for water clouds* ..... *223*
*8.6.2 Cloud base heights retrieved for ice clouds* ..... *224*
*8.6.3 Ancillary Data and Products from Other Sensors* ..... *224*
*8.6.4 Integration of VIIRS, CMIS, and Conventional Cloud Base Observations* ..... *226*

**CHAPTER 9** ..... **228**

**REFERENCES** ..... **228**

**Page vii: [3] Deleted** **keithh** **11/27/2004 11:56:00 AM**

TABLE 1.1 GUAM DMSP TROPICAL CYCLONE POSITION STATISTICS FOR 1972. ..... 38
TABLE 2.1 – OVERVIEW OF THE US CIVILIAN POLAR METEOROLOGICAL PROGRAMS (KRAMER 2002). ..... 44
TABLE 2.2 – SPECTRAL CHANNEL WAVELENGTHS OF THE AVHRR ..... 48
TABLE 2.3 CHRONOLOGICAL OVERVIEW OF DMSP SERIES SATELLITES ..... 52
TABLE 2.4 COMPARISON OF TWO SENSORS – NOAA AVHRR/2 AND DMSP/OLS (KRAMER 2002) ..... 52
TABLE 2.5 BAND CHARACTERISTICS FOR MODIS DATA PRODUCTS (NASA MODIS WEBSITE) ..... 52
TABLE 2.6 MODIS DATA PRODUCTS ACCORDING TO APPLICATION CLASS. ..... 52
TABLE 2.7 - OVERVIEW OF POLAR-ORBITING METEOROLOGICAL SATELLITE SERIES (KRAMER 2002) ..... 52
TABLE 2.8 OVERVIEW OF METOP-1 PAYLOAD COMPLIMENT (KRAMER 2002). ..... 52
TABLE 2.9 OVERVIEW OF GEOSTATIONARY METEOROLOGICAL SATELLITES (KRAMER 2002). ..... 52
TABLE 3.1 ATTRIBUTE REQUIREMENTS FOR EACH VIIRS BAND CLASSIFIED AS IMAGERY ..... 52
TABLE 3.2. NPOESS REQUIREMENTS FOR MANUALLY-GENERATED CLOUD COVER EDR. ..... 52
TABLE 3.3. NPOESS REQUIREMENTS FOR MANUALLY-GENERATED CLOUD TYPE EDR. ..... 52
TABLE 4.1. COMPARISONS OF MANUALLY-GENERATED CLOUD MASK AND SIMULATION BINARY CLOUD MASK FOR SYNTHETIC VIIRS IMAGERY SHOWN IN FIGURE 4.7. ..... 52
TABLE 4.2. VIIRS IMAGERY BANDS NEEDED TO SATISFY EACH NPOESS VIIRS REQUIREMENT FOR MANUALLY-GENERATED CLOUD COVER AND CLOUD TYPE EDRS. ..... 52
TABLE 4.3. VIIRS IMAGERY AND IMAGERY ASSIST BAND SELECTED TO SATISFY NPOESS REQUIREMENTS. ..... 52
TABLE 4.4 VIIRS SPECTRAL BAND OPTICAL REQUIREMENTS ..... 52
TABLE 4.5 OPTICALLY BLURRED IFOV REQUIREMENTS. ..... 52
TABLE 4.6 MODERATE RESOLUTION BAND MTF REQUIREMENTS ..... 52
TABLE 4.7. CROSS-TRACK AGGREGATION FACTORS. ..... 52
TABLE 4.8. HSI REQUIREMENTS FOR SINGLE-GAIN MODERATE RESOLUTION BANDS. ..... 52
TABLE 4.9 HSI REQUIREMENTS FOR DUAL-GAIN MODERATE RESOLUTION BANDS. ..... 52
TABLE 4.10 HSI REQUIREMENTS FOR IMAGING BANDS ..... 52
THE DYNAMIC RANGE OF THE VIIRS REFLECTIVE AND EMISSIVE BANDS IS SHOWN IN TABLES 4.17 AND 4.18. ..... 52

TABLE 4.11 DYNAMIC RANGE REQUIREMENTS FOR VIIRS SENSOR REFLECTIVE BANDS. ....52
TABLE 4.12 DYNAMIC RANGE REQUIREMENTS FOR VIIRS SENSOR EMISSIVE BANDS. ....52
TABLE 4.13 SENSITIVITY REQUIREMENTS FOR VIIRS SENSOR REFLECTIVE BANDS. ....52
TABLE 4.14 SENSITIVITY REQUIREMENTS FOR VIIRS SENSOR EMISSIVE BANDS. ....52
TABLE 4.15 POLARIZATION SENSITIVITY REQUIREMENTS. ....52
TABLE 4.16 VIIRS DETECTOR NEΦ REQUIREMENTS. ....52
TABLE 4.17 BANDS AND DETECTORS DEFINED ....52
TABLE 4.18 ABSOLUTE RADIOMETRIC CALIBRATION UNCERTAINTY OF SPECTRAL RADIANCE FOR MODERATE RESOLUTION EMISSIVE BANDS. ....52
TABLE 4.19 RADIOMETRIC CALIBRATION UNCERTAINTY FOR IMAGING EMISSIVE BANDS. ....52
TABLE 4.20 RADIOMETRIC CALIBRATION UNCERTAINTY FOR DAY/NIGHT BAND ....52
TABLE 4.21 STRUCTURED SCENE REQUIREMENTS. ....52
TABLE 5.1. BANDPASSES OF INSTRUMENTS THAT APPROXIMATE VIIRS IMAGERY RESOLUTION BANDS. ....52
TABLE 5.2. BANDPASSES OF SENSORS THAT CLOSELY APPROXIMATE VIIRS MODERATE RESOLUTION BANDS. ....52
TABLE 7.1. FEATURE DETECTION AND IDENTIFICATION BASED UPON INTERPRETATION OF FIGURE 7.1. ....52
TABLE 7.2. FEATURE DETECTION AND IDENTIFICATION BASED UPON INTERPRETATION OF FIGURE 7.3. ....52
TABLE 7.3. FEATURE DETECTION AND IDENTIFICATION BASED UPON INTERPRETATION OF FIGURE 7.4. ....52
TABLE 7.4. FEATURE DETECTION AND IDENTIFICATION BASED UPON INTERPRETATION OF FIGURE 7.5. ....52
TABLE 7.5. FEATURE DETECTION AND IDENTIFICATION BASED UPON INTERPRETATION OF FIGURE 7.7. ....52
TABLE 7.6. FEATURE DETECTION AND IDENTIFICATION BASED UPON INTERPRETATION OF FIGURE 7.8. ....52
TABLE 7.7. FEATURE DETECTION AND IDENTIFICATION BASED UPON INTERPRETATION OF FIGURE 7.9. ....52
TABLE 7.8. FEATURE DETECTION AND IDENTIFICATION BASED UPON INTERPRETATION OF FIGURE 7.10. ....52
TABLE 8.1 FREQUENCY OF OCCURRENCE OF CLOUD TYPES FROM CURRENT MODIS ALGORITHMS AND THOSE DEVELOPED BY PAVOLONIS AND HEIDINGER (2004) FOR 8-DAY PERIOD. ....52
TABLE 8.2. PREDICTED CLOUD THICKNESS FOR EXPECTED OPTICAL DEPTHS, (10 FOR ICE AND 64 FOR WATER CLOUDS) WHICH MIGHT BE RETRIEVED FROM MODIS IMAGERY ....52
TABLE 8.3 CHARACTERISTICS OF CLOUD BASE HEIGHT OBSERVATIONS. ....52

**Page vii: [4] Deleted keithh 11/27/2004 11:56:00 AM**

TABLE 1.1 GUAM DMSP TROPICAL CYCLONE POSITION STATISTICS FOR 1972. ....31
TABLE 2.1 – OVERVIEW OF THE US CIVILIAN POLAR METEOROLOGICAL PROGRAMS (KRAMER 2002). ....36
TABLE 2.2 – SPECTRAL CHANNEL WAVELENGTHS OF THE AVHRR ....40
TABLE 2.3 CHRONOLOGICAL OVERVIEW OF DMSP SERIES SATELLITES ....44
TABLE 2.4 COMPARISON OF TWO SENSORS – NOAA AVHRR/2 AND DMSP/OLS (KRAMER 2002). ....47
TABLE 2.5 BAND CHARACTERISTICS FOR MODIS DATA PRODUCTS (NASA MODIS WEBSITE). ....49
TABLE 2.6 MODIS DATA PRODUCTS ACCORDING TO APPLICATION CLASS. ....51
TABLE 2.7 - OVERVIEW OF POLAR-ORBITING METEOROLOGICAL SATELLITE SERIES (KRAMER 2002). ....53
TABLE 2.8 OVERVIEW OF METOP-1 PAYLOAD COMPLIMENT (KRAMER 2002). ....56
TABLE 2.9 OVERVIEW OF GEOSTATIONARY METEOROLOGICAL SATELLITES (KRAMER 2002). ....58
TABLE 3.1 ATTRIBUTE REQUIREMENTS FOR EACH VIIRS BAND CLASSIFIED AS IMAGERY ....68
TABLE 3.2. NPOESS REQUIREMENTS FOR MANUALLY-GENERATED CLOUD COVER EDR. ....71
TABLE 3.3. NPOESS REQUIREMENTS FOR MANUALLY-GENERATED CLOUD TYPE EDR. ....71
TABLE 4.1. COMPARISONS OF MANUALLY-GENERATED CLOUD MASK AND SIMULATION BINARY CLOUD MASK FOR SYNTHETIC VIIRS IMAGERY SHOWN IN FIGURE 4.7. ....90
TABLE 4.2. VIIRS IMAGERY BANDS NEEDED TO SATISFY EACH NPOESS VIIRS REQUIREMENT FOR MANUALLY-GENERATED CLOUD COVER AND CLOUD TYPE EDRS. ....98
TABLE 4.3. VIIRS IMAGERY AND IMAGERY ASSIST BAND SELECTED TO SATISFY NPOESS REQUIREMENTS. ....99
TABLE 4.4 VIIRS SPECTRAL BAND OPTICAL REQUIREMENTS ....105
TABLE 4.5 OPTICALLY BLURRED IFOV REQUIREMENTS. ....107
TABLE 4.6 MODERATE RESOLUTION BAND MTF REQUIREMENTS ....108
TABLE 4.7. CROSS-TRACK AGGREGATION FACTORS. ....109
TABLE 4.8. HSI REQUIREMENTS FOR SINGLE-GAIN MODERATE RESOLUTION BANDS. ....109
TABLE 4.9 HSI REQUIREMENTS FOR DUAL-GAIN MODERATE RESOLUTION BANDS. ....110
TABLE 4.10 HSI REQUIREMENTS FOR IMAGING BANDS ....110

THE DYNAMIC RANGE OF THE VIIRS REFLECTIVE AND EMISSIVE BANDS IS SHOWN IN TABLES 4.17 AND 4.18. ..... 110
TABLE 4.11 DYNAMIC RANGE REQUIREMENTS FOR VIIRS SENSOR REFLECTIVE BANDS. ..... 110
TABLE 4.12 DYNAMIC RANGE REQUIREMENTS FOR VIIRS SENSOR EMISSIVE BANDS. ..... 111
TABLE 4.13 SENSITIVITY REQUIREMENTS FOR VIIRS SENSOR REFLECTIVE BANDS. ..... 111
TABLE 4.14 SENSITIVITY REQUIREMENTS FOR VIIRS SENSOR EMISSIVE BANDS. ..... 112
TABLE 4.15 POLARIZATION SENSITIVITY REQUIREMENTS. ..... 113
TABLE 4.16 VIIRS DETECTOR NEΦ REQUIREMENTS. ..... 114
TABLE 4.17 BANDS AND DETECTORS DEFINED ..... 115
TABLE 4.18 ABSOLUTE RADIOMETRIC CALIBRATION UNCERTAINTY OF SPECTRAL RADIANCE FOR MODERATE RESOLUTION EMISSIVE BANDS. ..... 118
TABLE 4.19 RADIOMETRIC CALIBRATION UNCERTAINTY FOR IMAGING EMISSIVE BANDS. ..... 118
TABLE 4.20 RADIOMETRIC CALIBRATION UNCERTAINTY FOR DAY/NIGHT BAND ..... 118
TABLE 4.21 STRUCTURED SCENE REQUIREMENTS. ..... 119
TABLE 5.1. BANDPASSES OF INSTRUMENTS THAT APPROXIMATE VIIRS IMAGERY RESOLUTION BANDS. ..... 124
TABLE 5.2. BANDPASSES OF SENSORS THAT CLOSELY APPROXIMATE VIIRS MODERATE RESOLUTION BANDS. ..... 159
TABLE 7.1. FEATURE DETECTION AND IDENTIFICATION BASED UPON INTERPRETATION OF FIGURE 7.1. ..... 181
TABLE 7.2. FEATURE DETECTION AND IDENTIFICATION BASED UPON INTERPRETATION OF FIGURE 7.3. ..... 183
TABLE 7.3. FEATURE DETECTION AND IDENTIFICATION BASED UPON INTERPRETATION OF FIGURE 7.4. ..... 186
TABLE 7.4. FEATURE DETECTION AND IDENTIFICATION BASED UPON INTERPRETATION OF FIGURE 7.5. ..... 188
TABLE 7.5. FEATURE DETECTION AND IDENTIFICATION BASED UPON INTERPRETATION OF FIGURE 7.7. ..... 192
TABLE 7.6. FEATURE DETECTION AND IDENTIFICATION BASED UPON INTERPRETATION OF FIGURE 7.8. ..... 194
TABLE 7.7. FEATURE DETECTION AND IDENTIFICATION BASED UPON INTERPRETATION OF FIGURE 7.9. ..... 197
TABLE 7.8. FEATURE DETECTION AND IDENTIFICATION BASED UPON INTERPRETATION OF FIGURE 7.10. ..... 199
TABLE 8.1 FREQUENCY OF OCCURRENCE OF CLOUOD TYPES FROM CURRENT MODIS ALGORITHMS AND THOSE DEVELOPED BY PAVOLINIS AND HEIDINGER (2003) FOR 8-DAY PERIOD. ..... 211
TABLE 8.2. PREDICTED CLOUD THICKNESS FOR EXPECTED OPTICAL DEPTHS, (10 FOR ICE AND 64 FOR WATER CLOUDS) WHICH MIGHT BE RETRIEVED FROM MODIS IMAGERY ..... 225
TABLE 8.3 CHARACTERISTICS OF CLOUD BASE HEIGHT OBSERVATIONS. ..... 226

**Page xi: [5] Deleted** **keithh** **11/27/2004 11:56:00 AM**

FIGURE. 1.1 COMPARISON OF THE NH ANOMALY CORRELATION FROM OPERATIONAL AND REANALYSIS FORECASTS FOR 500 MB. (KALNAY, 1998). ..... 29
FIGURE 1.2 COMPARISON OF OPERATIONAL AND REANALYSIS 5-DAY FORECAST ANOMALY CORRELATIONS FOR THE NORTHERN HEMISPHERE AND THE SOUTHERN HEMISPHERE AT 500 MB. (KALNAY, 1998). ..... 30
FIGURE 1.3 SIMULATIONS DEMONSTRATE THE IMPACT OF SENSOR NEΔT ON SST ANALYSES USING 2-CHANNEL AND 3-CHANNEL MULTICHANNEL SEA SURFACE TEMPERATURE ALGORITHMS. ..... 33
FIGURE 1.4 SIMULATIONS DEMONSTRATE THE IMPACT OF AN IMPERFECT CLOUD MASK ON MEETING SEA SURFACE TEMPERATURE (SST) REQUIREMENTS OF 0.5 K. SST ACCURACY IS STRONGLY IMPACTED IF CLOUDS FAIL TO BE DETECTED IN THE CLOUD MASK BUT NO IMPACT IS NOTED IF THE MASK OVER-DETECTS THEM. ..... 35
FIGURE 1.5 CONCENTRATION OF ATMOSPHERIC CO2 AT MAUNA LOA OBSERVATORY, HAWAII EXPRESSED AS A MOLE FRACTION IN PARTS PER MILLION OF DRY AIR FOR THE PERIOD 1958-1990 (LIOU 1992). ..... 36
FIGURE 1.6 MODEL ON THE EVOLUTION OF TROPICAL STORMS USED IN INTENSITY ANALYSIS BASED UPON THE DVORAK METHOD (RAO, 1990). ..... 38
FIGURE 1.7 MODIS TERRA WATER VAPOR IMAGERY OVER NORTHERN POLAR REGIONS (LEFT PANEL) AND WIND FIELDS (~~LOW-LEVEL WIND~~, ~~MID-LEVEL WIND~~, ~~HIGH-LEVEL WIND~~) DERIVED FROM ANALYSES (RIGHT PANEL) OF CLOUD MOVEMENTS OBSERVED IN SUCCESSIVE ORBITS ..... 41
FIGURE 1.8 IMPROVEMENTS IN FORECAST SCORES (ANOMALY CORRELATION) AT ECMWF FOR THE 1000 HPA (LEFT) AND 500 HPA (RIGHT) GEOPOTENTIAL HEIGHT OVER THE ARCTIC (TOP) AND NORTHERN HEMISPHERE (BOTTOM), FOR MODEL FORECASTS WITH (RED) AND WITHOUT (BLUE) THE MODIS POLAR WINDS. ..... 41
FIGURE 2.1 ILLUSTRATION OF THE AVHRR INSTRUMENT (FROM KRAMER, 2002). ..... 47
FIGURE 2.2 SCHEMATIC ILLUSTRATION OF DMSP BLOCK 5D-3 SPACECRAFT MODEL ( KRAMER, 2002). ..... 52
FIGURE 2.3 ILLUSTRATION OF THE EOS AQUA SATELLITE AND SENSORS (KRAMER, 2000). ..... 52

FIGURE 2.4 INTEGRATED CONCEPT OF NOAA/EUMETSAT METEOROLOGICAL POLAR SATELLITES (KRAMER,2002). ....52
FIGURE 2.5. SKETCH OF METOP-1 (FROM FIGURE 204 KRAMER, 2002) ....52
FIGURE 2.6 COVERAGE OF THE GEOSYNCHRONOUS SATELLITES ASSOCIATED WITH THE COORDINATION OF GEOSTATIONARY METEOROLOGICAL SATELLITES (RAO, 2000). ....52
FIGURE 2.7 METEOROLOGICAL SATELLITES SUPPORTING THE WMO WORLD WEATHER WATCH PROGRAMME (WMO WEBSITE). ....52
FIGURE 2.8 TRANSITION OF NPOESS SATELLITES WITH EXISTING US POES SATELLITE SYSTEMS (IPO WEBSITE). ....52
FIGURE 3.1. HRCP CLOUD FORECAST RELIABILITY ESTABLISHED DURING 1990 CMEP STUDY (HUTCHISON AND JANOTA, 1989). ....52
FIGURE 4.1. SOLAR SPECTRAL IRRADIANCE DISTRIBUTION FOR TOP OF THE ATMOSPHERE (TOA) AND SEA LEVEL ALONG WITH PRIMARY ATMOSPHERIC ABSORPTION BANDS AND SPECIES. (FIGURE 2.6 FROM LIOU, 1980). ....52
FIGURE 4.2. CLOUDS AND SNOW ARE BRIGHT IN AVHRR IMAGERY CHANNEL 2 (0.9 μM) AT PANEL (A) AND CHANNEL 5 (12.0 μM) AT PANEL (B) OF A NOAA-12 SCENE COLLECTED ON MARCH 19, 1996 (HUTCHISON ET AL, 1997). ....52
FIGURE 4.3. CLOUDS SEEN IN THE 0.6 μM BAND (CHANNEL 1) OF THE AVHRR IMAGERY IN PANEL (A) ARE CONTAINED THE MANUALLY-GENERATED CLOUD ANALYSIS, ARE SHOWN AS RED, IN PANEL (B). ....52
FIGURE 4.4. SNOW NOW APPEARS BLACK IN PANEL (A) CONTAINING THE ALBEDO COMPONENT OF THE 3.7 μM BAND (CHANNEL 3) OF THE AVHRR IMAGERY WHILE PANEL (B) CONTAINS THE MANUALLY-GENERATED CLOUD ANALYSIS MADE USING THIS IMAGE. ....52
FIGURE 4.5. EXAMPLE OF A TOTAL CNC ANALYSIS CREATED BY MERGING CNC ANALYSES FROM INDIVIDUAL SPECTRAL BANDS SHOWN IN FIGURE 4.3 AND FIGURE 4.4 INTO A SINGLE CNC ANALYSIS. ....52
FIGURE 4.6. SYNTHETIC BACKGROUND SHOWN IN PANEL (A) ARE USED WITH CLOUD MASK, SHOWN IN PANEL (B) TO GENERATE SYNTHETIC VIIRS IMAGERY. ....52
FIGURE 4.7. SYNTHETIC 12.0 μM VIIRS IMAGE, MANUAL AND SYNTHETIC CLOUD MASKS, AND DIFFERENCE FIELDS SHOW LOCATIONS OF INACCURACIES IN MANUALLY-GENERATED CLOUD DATA PRODUCT. ....52
FIGURE 4.8. SPECTRAL SIGNATURES OF CLOUD PARTICLES AND SURFACE BACKGROUNDS IN 0.3 - 1.0 MICRON RANGE. (KEY: REFLECTIVITIES: VEGETATED LAND = GREEN, OCEAN = DARK BLUE, SNOW = WHITE, BARE SOIL OR SAND = YELLOW., SOLAR ILLUMINATION = GOLD AND ATMOSPHERIC TRANSMISSION = BLACK. VIIRS BANDS BLUE, SOLID TURQUOISE = INDEX OF REFRACTION FOR WATER DROPLETS, AND DASHED TURQUIOSE = INDEX OF REFRACTION FOR ICE.) ....52
FIGURE 4.9. SPECTRAL SIGNATURES OF CLOUD PARTICLES AND SURFACE BACKGROUNDS IN 1.0 - 3.0 MICRON RANGE. (KEY: REFLECTIVITIES OF, VEGETATED LAND = GREEN, OCEAN = DARK BLUE, SNOW = WHITE, BARE SOIL OR SAND = YELLOW. SOLAR ILLUMINATION = GOLD AND ATMOSPHERIC TRANSMISSION = BLACK. VIIRS BANDS ARE SHOWN IN LIGHTER BLUE SOLID TURQUOISE = INDEX OF REFRACTION FOR WATER DROPLETS, AND DASHED TURQUIOSE = INDEX OF REFRACTION FOR ICE.) ....52
FIGURE 4.10. SPECTRAL SIGNATURES OF CLOUD PARTICLES AND SURFACE BACKGROUNDS IN 3.0 - 5.0 MICRON RANGE. (KEY: REFLECTIVITIES OF, VEGETATED LAND = GREEN, OCEAN = DARK BLUE, SNOW = WHITE, BARE SOIL OR SAND = YELLOW. SOLAR ILLUMINATION = GOLD AND ATMOSPHERIC TRANSMISSION = BLACK. VIIRS BANDS ARE SHOWN IN LIGHTER BLUE SOLID TURQUOISE = INDEX OF REFRACTION FOR WATER DROPLETS, AND DASHED TURQUIOSE = INDEX OF REFRACTION FOR ICE.) ....52
FIGURE 4.11. SPECTRAL SIGNATURES OF CLOUD PARTICLES AND SURFACE BACKGROUNDS IN 5.0.- 15.0 MICRON RANGE. (KEY: REFLECTIVITIES OF, VEGETATED LAND = GREEN, OCEAN = DARK BLUE, SNOW = WHITE, BARE SOIL OR SAND = YELLOW. SOLAR ILLUMINATION = GOLD AND ATMOSPHERIC TRANSMISSION = BLACK. VIIRS BANDS ARE SHOWN IN LIGHTER BLUE SOLID TURQUOISE = INDEX OF REFRACTION FOR WATER DROPLETS, AND DASHED TURQUIOSE = INDEX OF REFRACTION FOR ICE.) ....52
FIGURE 4.12 VIIRS SENSOR BLOCK DIAGRAM. ....52
FIGURE 4.13 SUMMARY OF VIIRS DESIGN CONCEPTS AND HERITAGE. ....52
FIGURE 4.14 VIIRS DETECTOR FOOTPRINT AGGREGATION SCHEME FOR BUILDING IMAGERY "PIXELS". ....52
FIGURE 4.15 HORIZONTAL SAMPLING INTERVAL (HSI) FOR IMAGERY BANDS (AGGREGATION IN SCAN DIRECTION). ....52
FIGURE 4.16 VIIRS AGGREGATION AND BOW TIE PIXEL REDUCTION. ....52
FIGURE 4.17 DEPICTION OF SENSOR OPTICAL PERFORMANCE PARAMETERS. ....52

FIGURE 4.18 HSI FOR SINGLE-GAIN MODERATE RESOLUTION BANDS ....52
FIGURE 4.19 HSI FOR DUAL-GAIN MODERATE RESOLUTION BANDS. ....52
FIGURE 5.1. NORMALIZED DISTRIBUTION OF EMISSION SPECTRA FOR THREE BLACKBODIES WITH ABSOLUTE TEMPERATURES OF 6000 K (SUN), 770 K (FOREST FIRES), AND 300 K (EARTH'S SURFACE) SHOWS PRIMARY ENERGY SOURCES FOR EACH OF THE VIIRS SPECTRAL BANDS (SCORER, 1990). ....52
FIGURE 5.2. SIGNATURES OF CLOUDS AND LAND SURFACES TYPICAL OF THOSE PRESENT IN THE VIIRS I1 BAND ARE SEEN IN THE NOAA-12 AVHRR CHANNEL 1 IMAGERY COLLECTED NEAR SAN FRANCISCO, CA ON FEBRUARY 19, 1996 (HUTCHISON ET AL., 1997(A)). ....52
FIGURE 5.3. SIGNATURES OF CLOUDS AND LAND SURFACES TYPICAL OF THOSE PRESENT IN THE VIIRS I2 BAND ARE SEEN IN THE NOAA-12 AVHRR CHANNEL 1 IMAGERY COLLECTED NEAR SAN FRANCISCO, CA ON FEBRUARY 19, 1996 (HUTCHISON ET AL., 1997(A)). ....52
FIGURE 5.4. SIGNATURES OF CLOUDS AND LAND SURFACES TYPICAL OF THOSE PRESENT IN THE VIIRS I2 BAND ARE SEEN IN THE SEAWIFS DATA COLLECTED OVER SOUTHWESTERN US ON JULY 13, 2001 AS ALSO SHOWN IN FIGURE 5.23. ....52
FIGURE 5.5. THEMATIC MAPPER DATA COLLECTED OVER THE SIERRA NEVADA MOUNTAINS SHOW THE VALUE OF 1.61 μM IMAGERY FOR DIFFERENTIATING BETWEEN WATER CLOUDS (BRIGHT IN BOTH BANDS) AND SNOW (BLACK IN ONLY THE 1.61 μM IMAGE). ....52
FIGURE 5.6. ATMOSPHERIC ATTENUATION IN AVHRR 3.7, 10.8, AND 11.8 μM IR CHANNELS AS A FUNCTION OF TOTAL ATMOSPHERIC WATER VAPOR (HUTCHISON ET AL., 1995). ....52
FIGURE 5.7. SUN GLINT IN AVHRR CHANNEL 2 AND CHANNEL 3 BANDS OF NOAA-15 MISSION OVER SOUTHEASTERN UNITED STATES. ....52
FIGURE 5.8. STRATUS OVER SAN FRANCISCO BAY AND COASTAL CALIFORNIA IN NIGHTTIME 3.7 μM AND 11 μM IMAGERY COLLECTED BY NOAA-14. ....52
FIGURE 5.9. CHANNELS 1,3, AND 5 OF NOAA-12 IMAGERY COLLECTED AT ABOUT 7:05 AM PST ON MARCH 19, 1996 OVER WESTERN UNITED STATES AND PACIFIC COASTAL REGIONS. ....52
FIGURE 5.10. NOAA-12 SCENE COLLECTED AT ABOUT 7:05 AM LOCAL PST (1505 GMT) ON ....52
MARCH 19, 1996 OVER WESTERN UNITED STATES AND PACIFIC COASTAL REGIONS (HUTCHISON AND LOCKE, 1997). ....52
FIGURE 5.11. NOAA-12 SCENE COLLECTED AT ABOUT 7:58 AM LOCAL (1558 GMT) ON MARCH 12, 1996 OVER WESTERN UNITED STATES AND PACIFIC COASTAL REGIONS (HUTCHISON ET AL., 1997(B)). ....52
FIGURE 5.12. AMBIGUITIES IN SPECTRAL SIGNATURES CAN IMPACT A-PRIORI CLOUD TOP PHASE ANALYSES OF THIS NOAA-12 AVHRR SCENE COLLECTED AT 1558 GMT ON MARCH 12, 1996. ZOOMING IN ON THE LOWER-RIGHT QUADRANT OF CHANNEL 5, (A), AND CHANNEL 3A, (B), SHOWS THE DIFFICULTY IN MANUALLY CLASSIFYING CIRRUS SINCE ICE APPEARANCE CHANGES AS OPTICAL THICKNESS DECREASES FROM (A) TO (B) (HUTCHISON ET AL, 1997). ....52
FIGURE 5.13. SIMULATED AVHRR ($T_{3.7}$-$T_{11.0}$) BRIGHTNESS TEMPERATURE DIFFERENCE VERSUS OPTICAL THICKNESS OF CIRRUS IN MID-LATITUDE WINTER ATMOSPHERE WITH CLOUD TEMPERATURE OF 236K AND RADII OF 20 AND 40 MICRONS (HUTCHISON ET AL., 1997). ....52
FIGURE5.14. SIMULATED AVHRR (CHANNEL 3 MINUS CHANNEL 5) BRIGHTNESS TEMPERATURE DIFFERENCE VERSUS CHANNEL 4 TEMPERATURE FOR CIRRUS OF VARIABLE EMISSIVITY AT 10 KM IN SUB-ARCTIC WINTER ATMOSPHERE (HUTCHISON ET AL., 1997). ....52
FIGURE 5.15. SMOKE PLUMES FROM SEVERAL FOREST FIRES (INCLUDING THE ONE NEAR LOS ALAMOS, NEW MEXICO) ARE EVIDENT IN CHANNEL 2 OF THE NOAA-12 AVHRR SCENE COLLECTED AT 2319 GMT ON MAY 11, 2000. ....52
FIGURE 5.16. HOT SPOTS IN THE FOREST FIRES ARE EVIDENT IN CHANNEL 3 OF THE NOAA-12 AVHRR SCENE COLLECTED AT 2319 GMT ON MAY 11, 2000. SEVERAL IN THE MOUNTAINS OF MEXICO SHOW NO PLUMES. ....52
FIGURE 5.17. GOES-EAST VISIBLE AND IR IMAGERY OF TEXAS ON APRIL 4, 2001 AT 1600 GMT SHOW EXTENSIVE WATER CLOUDS OVER THE EASTERN AND THIN CIRRUS CLOUDS OVER WESTERN TEXAS. ....52
FIGURE 5.18. BRIGHTNESS TEMPERATURES IN AVHRR CHANNEL 4 IMAGERY OF VARIOUS CLOUDS LOCATED OVER TEXAS AT 1127 GMT ON APRIL 4, 2001. ....52
FIGURE 5.19. RADIOSONDE FOR CORPUS CHRISTI, TEXAS AT 1200 UTC ON APRIL 4, 2001 ALONG WITH THERMODYNAMIC (SKEWT-LOGP) CHART OF THESE DATA SHOW CLOUD TOP TEMPERATURE OF 19.6C. ....52
FIGURE 5.20. SPECTRAL RESPONSE OF THE DAYTIME/NIGHTTIME VISIBLE IMAGERY BAND, COMPARED WITH THE LUNAR SIGNAL. ....52

FIGURE 5.21. SIGNAL TO NOISE RATIO PERFORMANCE OF THE DAYTIME/NIGHTTIME VISIBLE IMAGERY UNDER QUARTER-MOON ILLUMINATION CONDITIONS, AS A FUNCTION OF SCAN ANGLE. ....52
FIGURE 5.22 – F13 OLS VISIBLE (HRD) IMAGE FOR THE FIRST TERMINATOR CROSSING OF THE JULY 20, 2001 1131 UT ORBIT. ....52
FIGURE 5.23. SEAWIFS DATA FROM THE 0.412 μM AND 0.488 μM BANDPASSES ARE SHOWN FOR THE WESTERN US AND NORTHERN MEXICO ON JULY 13, 2001 AT 1954 GMT. ....52
FIGURE 5.24. SEAWIFS DATA IN THE 0.555 μM AND 0.765 μM BANDS ARE SHOWN FOR THE SCENE OVER THE WESTERN US AND NORTHERN MEXICO ON JULY 13, 2001 AT 1954 GMT. ....52
FIGURE 5.25. THE TWO-WAY CLEAR-SKY TRANSMITTANCES FOR ENERGY ARRIVING AT SATELLITE ALTITUDE IN THE 1.38 μM REGION FOR A PERFECT REFLECTOR LOCATED AT DIFFERENT ALTITUDES. CALCULATIONS BASED UPON SUB-ARCTIC SUMMER ATMOSPHERE AND LOWTRAN. (GAO ET AL., 1993). ....52
FIGURE 5.26. AVIRIS IMAGERY FOR VIIRS I2 AND M9 CHANNELS OVER COFFEVILLE, KS SHOWS VALUE OF MASKING SURFACE FEATURES FOR MANUAL INTERPRETATION OF THIN CIRRUS. ....52
FIGURE 5.27. AVIRIS IMAGERY FOR VIIRS I1 AND M9 CHANNELS OVER TEXAS GULF COAST REVEALS THAT LOW-LEVEL WATER CLOUDS ARE MASKED IN 1.38 μM IMAGERY. ....52
FIGURE 6.1. COLOR COMPOSITE TO EMPHASIZE VEGETATED LAND SURFACES CREATED BY ASSIGNING 0.64 μM BAND ASSIGNED TO RED AND GREEN GUNS OF CRT AND 0.865 μM ALBEDO BAND ASSIGNED TO BLUE GUN. ....52
FIGURE 6.2. PLACING THE 12.0 μM CHANNEL IN THE BLUE GUN OF FIGURE 6.1 PROVIDES VALUABLE DATA ON CLOUD TOP TEMPERATURES NEEDED FOR CLOUD TYPING. WARM, LOW LEVEL WATER CLOUDS APPEAR YELLOW WHILE COLDER ICE CLOUDS ARE BLUE. ....52
FIGURE 6.3. REPLACING THE BAND IN THE RED GUN OF FIGURE 6.2 WITH THE 3.7 ALBEDO CHANNEL ALLOWS SNOW TO BE DIFFERENTIATED FROM LOWER-LEVEL WATER CLOUDS, THIN CIRRUS, AND THICKER CIRRUS WHILE MAINTAINING INFORMATION ON CLOUD TOP TEMPERATURES AND VEGETATED LAND SURFACES (RED = 3.7 μM ALBEDO, GREEN = 0.865 μM, BLUE = 12.0 μM). ....52
FIGURE 6.4. COLOR COMPOSITE RED = 0.64 μM BAND, GREEN = 0.64 μM BAND, BLUE = 3.7 μM ALBEDO BAND) FOR THE MANUAL DETECTION AND MAPPING OF SNOW THROUGH CIRRUS CLOUDY CONDITIONS (HUTCHISON AND LOCKE, 1997). ....52
FIGURE 6.5. COMPOSITE IMAGE (RED = 0.412 μM, GREEN = 0.865 μM, BLUE = 0.64 μM) FOR THE DETECTION CLOUDS OVER HIGHLY REFLECTIVE, ARID OR SEMI-ARID REGIONS. ....52
FIGURE 7.1. GRAY-SCALE MAS IMAGERY COLLECTED OVER THE NORTH SLOPE OF ALASKA DURING FLIGHT TRACK #01 ON JUNE 7, 1995. DATA SHOWN ARE THOSE MODIS AND VIIRS CHANNELS NEEDED TO INTERPRET CLOUD AND SURFACE FEATURES IN THE SCENE. ....52
FIGURE 7.2. COLOR COMPOSITE (RED = 0.645μM, GREEN = 0.845 μM, BLUE = 0.645 μM) SHOWS MOST OF THE SURFACE IS (GREEN) HIGHLY VEGETATED. ....52
FIGURE 7.3. COLOR COMPOSITE (RED = 0.645μM, GREEN = 0.845 μM, BLUE = 1.61 μM) SHOWS SNOW, ICE, AND GLACIATED CLOUDS AS YELLOW. NOTICE THE SMOOTH TEXTURE ASSOCIATED WITH CIRRUS CLOUDS. ....52
FIGURE 7.4. COLOR COMPOSITE (RED = 0.645 μM, GREEN = 1.88 μM, BLUE = 11.45 μM) PROVIDES VALUABLE INFORMATION FOR CLOUD TYPE, SURFACE, AND ATMOSPHERIC MOISTURE CLASSIFICATIONS. ....52
FIGURE 7.5. COLOR COMPOSITE (RED = 0.645 μM, GREEN = 0.865 μM, BLUE = 11.45 μM) PROVIDES USEFUL INFORMATION ON SURFACE FEATURES AND CLOUD TOP TEMPERATURES AND HEIGHTS. ....52
FIGURE 7.6. GRAY-SCALE IMAGERY COLLECTED OVER COLORADO DURING FLIGHT TRACK #26 OF THE MODIS AIRBORNE SIMULATOR ON JULY 5, 1995. DATA SHOWN ARE THOSE MODIS AND VIIRS CHANNELS NEEDED TO INTERPRET FEATURES IN THE SCENE. ....52
FIGURE 7.7. COLOR COMPOSITE (RED = 0.645μM, GREEN = 0.845 μM, BLUE = 0.645 μM) SHOWS MOST OF THE SURFACE IS NOT (GREEN) HIGHLY VEGETATED. ....52
FIGURE 7.8. COLOR COMPOSITE (RED = 0.645μM, GREEN = 0.845 μM, BLUE = 1.61 μM) SHOWS SNOW, ICE, AND GLACIATED (OPTICALLY-THIN) CLOUDS AS YELLOW. THICKER CLOUDS REMAIN WHITE. ....52
FIGURE 7.9. COLOR COMPOSITE (RED = 0.645 μM, GREEN = 1.88 μM, BLUE = 11.45 μM) PROVIDES INFORMATION ON CLOUD TYPE, SURFACE, AND ATMOSPHERIC MOISTURE CLASSIFICATIONS. ....52
FIGURE 7.10. COLOR COMPOSITE (RED = 0.645 μM, GREEN = 0.865 μM, BLUE = 11.45 μM) PROVIDES USEFUL INFORMATION ON SURFACE FEATURES AND CLOUD TOP TEMPERATURES AND HEIGHTS. ....52

FIGURE 8.1 OVERVIEW OF AN APPROACH TO RETRIEVING 3-DIMENSIONAL CLOUD FIELDS FROM SATELLITE DATA (HUTCHISON, 2002). ....52
FIGURE 8.2 BI-SPECTRAL REFLECTANCES RATIO (BSRR) IN THE FORWARD AND NON-FORWARD SCATTERING DIRECTIONS FOR OPTICALLY-THICK CLOUDS (▲)AND CLOUD–FREE PIXELS (+) OVER OCEAN SURFACES AS A FUNCTIONS OF COSINE SOLAR ZENITH ANGLE (FROM HUTCHISON AND HARDY, 1995)....52
FIGURE 8.3 BRIGHTNESS TEMPERATURE DIFFERENCES (BTD) BETWEEN NIGHTTIME 3.7 μM MINUS 11.0 μM FOR THIN CIRRUS CLOUDS (▲) AND CLOUD CLOUD–FREE PIXELS (+) ARE SHOWN IN THE LEFT PANEL AS A FUNCTION OF TOTAL ATMOSPHERIC WATER CONTENT. IN THE RIGHT PANEL, 11.0 μM MINUS 3.7 μM BTDS ARE SHOWN FOR STRATUS CLOUDS (▲) AND CLOUD-FREE (+) PIXELS IN NIGHTTIME AVHRR IMAGERY (FROM HUTCHISON AND HARDY, 1995). ....52
FIGURE 8.4 CLOUD PHASE CLASSIFICATION FROM THE FUSION OF SPECTRAL SIGNATURES IN AVHRR IMAGERY AND CLOUD TOP PRESSURES FROM CO2 SLICING OF HIGH RESOLUTION IR SOUNDER DATA. (FROM HUTCHISON ET AL., 1997A) S & K = SAUNDERS AND KRIEBEL (1988); BSRR = BISPECTRAL REFLECTANCE RATIO ....52
FIGURE 8.5 ANALYSIS OF CLOUD PHASE CLASSES FROM GLOBAL TERRA MODIS DATA USING CURRENT MODIS ALGORITHM (MENZEL ET AL., 2002). ....52
FIGURE 8.6 ANALYSIS OF CLOUD PHASE CLASSES FROM GLOBAL TERRA MODIS DATA USING PAVOLONIS AND HEIDINGER ALGORITHM (PAVOLONIS AND HEIDINGER 2004). ....52
FIGURE 8.7. ARCHITECTURE FOR THE RETRIEVAL OF WATER CLOUD MICROPHYSICAL PROPERTIES DURING DAYTIME AND NIGHTTIME CONDITIONS. CTT = CLOUD TOP TEMPERATURE (OU ET AL., 2002) ....52
FIGURE 8.8. OVERVIEW OF THE WATER CLOUD SOLAR RETRIEVAL ALGORITHM. $A_G(\Lambda)$ = SURFACE ALBEDO FOR WAVELENGTH Λ (OU ET AL., 2002) ....52
FIGURE 8.9. SUN SATELLITE GEOMETRY. (OU ET AL., 2002)....52
FIGURE 8.10. THEORETICAL RELATIONSHIP BETWEEN THE REFLECTION FUNCTION AT 0.664 μM AND (A) 1.621 μM AND (B) 2.142 μM FOR VARIOUS VALUES OF $\tau_C$ (AT 0.664 μM) AND $R_E$ WHEN $\theta_0$ =26°, θ = 40° AND ϕ = 42°. (KING ET AL., 1997) ....52
FIGURE 8.11. ARCHITECTURE FOR THE RETRIEVAL OF ICE CLOUD MICROPHYSICAL PROPERTIES FROM VIIRS DATA DURING DAYTIME CONDITIONS AND VIIRS DATA DURING NIGHTTIME. $T_C$, AND $D_E$ ARE CLOUD TOP TEMPERATURE AND ICE CRYSTAL DIAMETER (FIGURE 4.11 FROM OU ET AL., 2002)....52
FIGURE 8.12 PROCESSING SEQUENCE FOR RETRIEVAL OF ICE CLOUD OPTICAL PROPERTIES IN DAYTIME CONDITIONS. ....52
FIGURE 8.13 PROCESSING SEQUENCE FOR RETRIEVAL OF ICE CLOUD OPTICAL PROPERTIES IN NIGHTTIME CONDITIONS. ....52
FIGURE 8.14 GEOMETRY FOR RETRIEVAL OF CLOUD BASE HEIGHT USING CLOUD TOP HEIGHT ALONG WITH CLOUD OPTICAL PROPERTIES THE OBTAIN CLOUD THICKNESS (HUTCHISON, 2002). ....52

**Page xi: [6] Deleted** **keithh** **11/27/2004 11:56:00 AM**

FIGURE. 1.1 COMPARISON OF THE NH ANOMALY CORRELATION FROM OPERATIONAL AND REANALYSIS FORECASTS FOR 500 MB. (KALNAY, 1998). (QUERY: WHAT ARE THE NUMBERS UP THE RIGHT-HAND SIDE OF THE FIGURE?) ....22
FIGURE 1.2 COMPARISON OF OPERATIONAL AND REANALYSIS 5-DAY FORECAST ANOMALY CORRELATIONS FOR THE NORTHERN HEMISPHERE AND THE SOUTHERN HEMISPHERE AT 500 MB. (KALNAY, 1998). ....23
FIGURE 1.3 SIMULATIONS DEMONSTRATE THE IMPACT OF SENSOR NEΔT ON SST ANALYSES USING 2-CHANNEL AND 3-CHANNEL MULTICHANNEL SEA SURFACE TEMPERATURE ALGORITHMS. ....26
FIGURE 1.4 SIMULATIONS DEMONSTRATE THE IMPACT OF AN IMPERFECT CLOUD MASK ON SATISFYING NPOESS SST REQUIREMENTS OF 0.5 K ACCURACY. ....27
FIGURE 1.5 CONCENTRATION OF ATMOSPHERIC CO2 AT MAUNA LOA OBSERVATORY, HAWAII EXPRESSES AS A MOLE FRACTION IN PARTS PER MILLION OF DRY AIR FOR THE PERIOD 1958-1990 (LIOU 1992). ....28
FIGURE 1.6 MODEL ON THE EVOLUTION OF TROPICAL STORMS USED IN INTENSITY ANALYSIS BASED UPON THE DVORAK METHOD (RAO, 2000) ....30
FIGURE 1.7 MODIS TERRA WATER VAPOR IMAGERY OVER NORTHERN POLAR REGIONS (LEFT PANEL) AND WIND FIELDS (LOW-LEVEL WIND, MID-LEVEL WIND, HIGH-LEVEL WIND) DERIVED FROM ANALYSES (RIGHT PANEL) OF CLOUD MOVEMENTS OBSERVED IN SUCCESSIVE ORBITS ....33
FIGURE 1.8 IMPROVEMENTS IN FORECAST SCORES (ANOMALY CORRELATION) AT ECMWF FOR THE 1000 HPA (LEFT) AND 500 HPA (RIGHT) GEOPOTENTIAL HEIGHT OVER THE ARCTIC (TOP) AND NORTHERN

HEMISPHERE (BOTTOM), FOR MODEL FORECASTS WITH (RED) AND WITHOUT (BLUE) THE MODIS POLAR WINDS. ....33
FIGURE 2.1 ILLUSTRATION OF THE AVHRR INSTRUMENT (FROM KRAMER, 2002). ....39
FIGURE 2.2 SCHEMATIC ILLUSTRATION OF DMSP BLOCK 5D-3 SPACECRAFT MODEL ( KRAMER, 2002). ....44
FIGURE 2.3 ILLUSTRATION OF THE EOS AQUA SATELLITE AND SENSORS (KRAMER, 2000). ....49
FIGURE 2.4 INTEGRATED CONCEPT OF NOAA/EUMETSAT METEOROLOGICAL POLAR SATELLITES (KRAMER,2002). ....55
FIGURE 2.5. SKETCH OF METOP-1 (FROM FIGURE 204 KRAMER, 2002) ....56
FIGURE 2.6 COVERAGE OF THE GEOSYNCHRONOUS SATELLITES ASSOCIATED WITH THE COORDINATION OF GEOSTATIONARY METEOROLOGICAL SATELLITES (RAO, 2000). ....60
FIGURE 2.7 METEOROLOGICAL SATELLITES SUPPORTING THE WMO WORLD WEATHER WATCH PROGRAMME (WMO WEBSITE). ....61
FIGURE 2.8 TRANSITION OF NPOESS SATELLITES WITH EXISTING US POES SATELLITE SYSTEMS (IPO WEBSITE). ....64
FIGURE 3.1. HRCP CLOUD FORECAST RELIABILITY ESTABLISHED DURING 1990 CMEP STUDY (HUTCHISON AND JANOTA, 1989). ....73
FIGURE 4.1. SOLAR SPECTRAL IRRADIANCE DISTRIBUTION FOR TOP OF THE ATMOSPHERE (TOA) AND SEA LEVEL ALONG WITH PRIMARY ATMOSPHERIC ABSORPTION BANDS AND SPECIES. (FIGURE 2.6 FROM LIOU, 1980). ....83
FIGURE 4.2. CLOUDS AND SNOW ARE BRIGHT IN AVHRR IMAGERY CHANNEL 2 (0.9 μM) AT PANEL (A) AND CHANNEL 5 (12.0 μM) AT PANEL (B) OF A NOAA-12 SCENE COLLECTED ON MARCH 19, 1996 (HUTCHISON ET AL, 1997). ....85
FIGURE 4.3. CLOUDS SEEN IN THE 0.6 μM BAND (CHANNEL 1) OF THE AVHRR IMAGERY IN PANEL (A) ARE CONTAINED THE MANUALLY-GENERATED CLOUD ANALYSIS, ARE SHOWN AS RED, IN PANEL (B). ....85
FIGURE 4.4. SNOW NOW APPEARS BLACK IN PANEL (A) CONTAINING THE ALBEDO COMPONENT OF THE 3.7 μM BAND (CHANNEL 3) OF THE AVHRR IMAGERY WHILE PANEL (B) CONTAINS THE MANUALLY-GENERATED CLOUD ANALYSIS MADE USING THIS IMAGE. ....86
FIGURE 4.5. EXAMPLE OF A TOTAL CNC ANALYSIS CREATED BY MERGING CNC ANALYSES FROM INDIVIDUAL SPECTRAL BANDS SHOWN IN FIGURE 4.3 AND FIGURE 4.4 INTO A SINGLE CNC ANALYSIS. ....87
FIGURE 4.6. SYNTHETIC BACKGROUND SHOWN IN PANEL (A) ARE USED WITH CLOUD MASK, SHOWN IN PANEL (B) TO GENERATE SYNTHETIC VIIRS IMAGERY. ....88
FIGURE 4.7. SYNTHETIC 12.0 μM VIIRS IMAGE, MANUAL AND SYNTHETIC CLOUD MASKS, AND DIFFERENCE FIELDS SHOW LOCATIONS OF INACCURACIES IN MANUALLY-GENERATED CLOUD DATA PRODUCT. ....89
FIGURE 4.8. SPECTRAL SIGNATURES OF CLOUD PARTICLES AND SURFACE BACKGROUNDS IN 0.3 - 1.0 MICRON RANGE. (KEY: REFLECTIVITIES: VEGETATED LAND = GREEN, OCEAN = DARK BLUE, SNOW = WHITE, BARE SOIL OR SAND = YELLOW., SOLAR ILLUMINATION = GOLD AND ATMOSPHERIC TRANSMISSION = BLACK. VIIRS BANDS BLUE, SOLID TURQUOISE = INDEX OF REFRACTION FOR WAER DROPLETS, AND DASHED TURQUIOSE = INDEX OF REFRACTION FOR ICE.) ....94
FIGURE 4.9. SPECTRAL SIGNATURES OF CLOUD PARTICLES AND SURFACE BACKGROUNDS IN 1.0 - 3.0 MICRON RANGE. (KEY: REFLECTIVITIES OF, VEGETATED LAND = GREEN, OCEAN = DARK BLUE, SNOW = WHITE, BARE SOIL OR SAND = YELLOW. SOLAR ILLUMINATION = GOLD AND ATMOSPHERIC TRANSMISSION = BLACK. VIIRS BANDS ARE SHOWN IN LIGHTER BLUE SOLID TURQUOISE = INDEX OF REFRACTION FOR WAER DROPLETS, AND DASHED TURQUIOSE = INDEX OF REFRACTION FOR ICE.) ....95
FIGURE 4.10. SPECTRAL SIGNATURES OF CLOUD PARTICLES AND SURFACE BACKGROUNDS IN 3.0 - 5.0 MICRON RANGE. (KEY: REFLECTIVITIES OF, VEGETATED LAND = GREEN, OCEAN = DARK BLUE, SNOW = WHITE, BARE SOIL OR SAND = YELLOW. SOLAR ILLUMINATION = GOLD AND ATMOSPHERIC TRANSMISSION = BLACK. VIIRS BANDS ARE SHOWN IN LIGHTER BLUE SOLID TURQUOISE = INDEX OF REFRACTION FOR WAER DROPLETS, AND DASHED TURQUIOSE = INDEX OF REFRACTION FOR ICE.) ....96
FIGURE 4.11. SPECTRAL SIGNATURES OF CLOUD PARTICLES AND SURFACE BACKGROUNDS IN 5.0.- 15.0 MICRON RANGE. (KEY: REFLECTIVITIES OF, VEGETATED LAND = GREEN, OCEAN = DARK BLUE, SNOW = WHITE, BARE SOIL OR SAND = YELLOW. SOLAR ILLUMINATION = GOLD AND ATMOSPHERIC TRANSMISSION = BLACK. VIIRS BANDS ARE SHOWN IN LIGHTER BLUE SOLID TURQUOISE = INDEX OF REFRACTION FOR WAER DROPLETS, AND DASHED TURQUIOSE = INDEX OF REFRACTION FOR ICE.) ....97
FIGURE 4.12 VIIRS SENSOR BLOCK DIAGRAM. ....101
FIGURE 4.13 SUMMARY OF VIIRS DESIGN CONCEPTS AND HERITAGE. ....102

FIGURE 4.14 VIIRS DETECTOR FOOTPRINT AGGREGATION SCHEME FOR BUILDING IMAGERY "PIXELS". ..... 103
FIGURE 4.15 HORIZONTAL SAMPLING INTERVAL (HSI) FOR IMAGERY BANDS (AGGREGATION IN SCAN DIRECTION). ..... 104
FIGURE 4.16 VIIRS AGGREGATION AND BOW TIE PIXEL REDUCTION. ..... 104
FIGURE 4.17 DEPICTION OF SENSOR OPTICAL PERFORMANCE PARAMETERS. ..... 105
FIGURE 4.18 HSI FOR SINGLE-GAIN MODERATE RESOLUTION BANDS ..... 109
FIGURE 4.19 HSI FOR DUAL-GAIN MODERATE RESOLUTION BANDS. ..... 110
FIGURE 5.1. NORMALIZED DISTRIBUTION OF EMISSION SPECTRA FOR THREE BLACKBODIES WITH ABSOLUTE TEMPERATURES OF 6000 K (SUN), 770 K (FOREST FIRES), AND 300 K (EARTH'S SURFACE) SHOWS PRIMARY ENERGY SOURCES FOR EACH OF THE VIIRS SPECTRAL BANDS (SCORER, 1990). ..... 121
FIGURE 5.2. SIGNATURES OF CLOUDS AND LAND SURFACES TYPICAL OF THOSE PRESENT IN THE VIIRS I1 BAND ARE SEEN IN THE NOAA-12 AVHRR CHANNEL 1 IMAGERY COLLECTED NEAR SAN FRANCISCO, CA ON FEBRUARY 19, 1996 (HUTCHISON ET AL., 1997(A)). ..... 127
FIGURE 5.3. SIGNATURES OF CLOUDS AND LAND SURFACES TYPICAL OF THOSE PRESENT IN THE VIIRS I2 BAND ARE SEEN IN THE NOAA-12 AVHRR CHANNEL 1 IMAGERY COLLECTED NEAR SAN FRANCISCO, CA ON FEBRUARY 19, 1996 (HUTCHISON ET AL., 1997(A)). ..... 129
FIGURE 5.4. SIGNATURES OF CLOUDS AND LAND SURFACES TYPICAL OF THOSE PRESENT IN THE VIIRS I2 BAND ARE SEEN IN THE SEAWIFS DATA COLLECTED OVER SOUTHWESTERN US ON JULY 13, 2001 AS ALSO SHOWN IN FIGURE 5.23. ..... 130
FIGURE 5.5. THEMATIC MAPPER DATA COLLECTED OVER THE SIERRA NEVADA MOUNTAINS SHOW THE VALUE OF 1.61 μM IMAGERY FOR DIFFERENTIATING BETWEEN WATER CLOUDS (BRIGHT IN BOTH BANDS) AND SNOW (BLACK IN ONLY THE 1.61 μM IMAGE). ..... 132
FIGURE 5.6. ATMOSPHERIC ATTENUATION IN AVHRR 3.7, 10.8, AND 11.8 μM IR CHANNELS AS A FUNCTION OF TOTAL ATMOSPHERIC WATER VAPOR (HUTCHISON ET AL., 1995). ..... 134

FIGURE 5.7. SUNGLINT

**Page xi: [7] Deleted** **keithh** **11/27/2004 11:56:00 AM**

IN AVHRR CHANNEL 2 AND CHANNEL 3 BANDS OF NOAA-15 MISSION OVER SOUTHEASTERN UNITED STATES. ..... 138
FIGURE 5.8. STRATUS OVER SAN FRANCISCO BAY AND COASTAL CALIFORNIA IN NIGHTTIME 3.7 μM AND 11 μM IMAGERY COLLECTED BY NOAA-14. ..... 140
FIGURE 5.9. CHANNELS 1,3, AND 5 OF NOAA-12 IMAGERY COLLECTED AT ABOUT 7:05 AM PST ON MARCH 19, 1996 OVER WESTERN UNITED STATES AND PACIFIC COASTAL REGIONS. ..... 141
FIGURE 5.10. NOAA-12 SCENE COLLECTED AT ABOUT 7:05 AM LOCAL PST (1505 GMT) ON ..... 143
MARCH 19, 1996 OVER WESTERN UNITED STATES AND PACIFIC COASTAL REGIONS (HUTCHISON AND LOCKE, 1997). ..... 143
FIGURE 5.11. NOAA-12 SCENE COLLECTED AT ABOUT 7:58 AM LOCAL (1558 GMT) ON MARCH 12, 1996 OVER WESTERN UNITED STATES AND PACIFIC COASTAL REGIONS (HUTCHISON ET AL., 1997(B)). ..... 144
FIGURE 5.12. AMBIGUITIES IN SPECTRAL SIGNATURES CAN IMPACT A-PRIORI CLOUD TOP PHASE ANALYSES OF THIS NOAA-12 AVHRR SCENE COLLECTED AT 1558 GMT ON MARCH 12, 1996. ZOOMING IN ON THE LOWER-RIGHT QUADRANT OF CHANNEL 5, (A), AND CHANNEL 3A, (B), SHOWS THE DIFFICULTY IN MANUALLY CLASSIFYING CIRRUS SINCE ICE APPEARANCE CHANGES AS OPTICAL THICKNESS DECREASES FROM (A) TO (B) (HUTCHISON ET AL, 1997). ..... 145
FIGURE 5.13. SIMULATED AVHRR ($T_{3.7}$-$T_{11.0}$) BRIGHTNESS TEMPERATURE DIFFERENCE VERSUS OPTICAL THICKNESS OF CIRRUS IN MID-LATITUDE WINTER ATMOSPHERE WITH CLOUD TEMPERATURE OF 236K AND RADII OF 20 AND 40 MICRONS (HUTCHISON ET AL., 1997). ..... 147
FIGURE5.14. SIMULATED AVHRR (CHANNEL 3 MINUS CHANNEL 5) BRIGHTNESS TEMPERATURE DIFFERENCE VERSUS CHANNEL 4 TEMPERATURE FOR CIRRUS OF VARIABLE EMISSIVITY AT 10 KM IN SUB-ARCTIC WINTER ATMOSPHERE (HUTCHISON ET AL., 1997). ..... 147
FIGURE 5.15. SMOKE PLUMES FROM SEVERAL FOREST FIRES (INCLUDING THE ONE NEAR LOS ALAMOS, NEW MEXICO) ARE EVIDENT IN CHANNEL 2 OF THE NOAA-12 AVHRR SCENE COLLECTED AT 2319 GMT ON MAY 11, 2000. ..... 148

FIGURE 5.16. HOT SPOTS IN THE FOREST FIRES ARE EVIDENT IN CHANNEL 3 OF THE NOAA-12 AVHRR SCENE COLLECTED AT 2319 GMT ON MAY 11, 2000. SEVERAL IN THE MOUNTAINS OF MEXICO SHOW NO PLUMES. ..... 149
FIGURE 5.17. GOES-EAST VISIBLE AND IR IMAGERY OF TEXAS ON APRIL 4, 2001 AT 1600 GMT SHOW EXTENSIVE WATER CLOUDS OVER THE EASTERN AND THIN CIRRUS CLOUDS OVER WESTERN TEXAS. ..... 153
FIGURE 5.18. BRIGHTNESS TEMPERATURES IN AVHRR CHANNEL 4 IMAGERY OF VARIOUS CLOUDS LOCATED OVER TEXAS AT 1127 GMT ON APRIL 4, 2001. ..... 154
FIGURE 5.19. RADIOSONDE FOR CORPUS CHRISTI, TEXAS AT 1200 UTC ON APRIL 4, 2001 ALONG WITH THERMODYNAMIC (SKEWT-LOGP) CHART OF THESE DATA SHOW CLOUD TOP TEMPERATURE OF 19.6C. ..... 155
FIGURE 5.20. SPECTRAL RESPONSE OF THE DAYTIME/NIGHTTIME VISIBLE IMAGERY BAND, COMPARED WITH THE LUNAR SIGNAL. ..... 156
FIGURE 5.21. SIGNAL TO NOISE RATIO PERFORMANCE OF THE DAYTIME/NIGHTTIME VISIBLE IMAGERY UNDER QUARTER-MOON ILLUMINATION CONDITIONS, AS A FUNCTION OF SCAN ANGLE. ..... 157
FIGURE 5.22 – F13 OLS VISIBLE (HRD) IMAGE FOR THE FIRST TERMINATOR CROSSING OF THE JULY 20, 2001 1131 UT ORBIT. ..... 158
FIGURE 5.23. SEAWIFS DATA FROM THE 0.412 μM AND 0.488 μM BANDPASSES ARE SHOWN FOR THE WESTERN US AND NORTHERN MEXICO ON JULY 13, 2001 AT 1954 GMT. ..... 161
FIGURE 5.24. SEAWIFS DATA IN THE 0.555 μM AND 0.765 μM BANDS ARE SHOWN FOR THE SCENE OVER THE WESTERN US AND NORTHERN MEXICO ON JULY 13, 2001 AT 1954 GMT. ..... 162
FIGURE 5.25. THE TWO-WAY CLEAR-SKY TRANSMITTANCES FOR ENERGY ARRIVING AT SATELLITE ALTITUDE IN THE 1.38 μM REGION FOR A PERFECT REFLECTOR LOCATED AT DIFFERENT ALTITUDES. CALCULATIONS BASED UPON SUB-ARCTIC SUMMER ATMOSPHERE AND LOWTRAN. (GAO ET AL., 1993). ..... 164
FIGURE 5.26. AVIRIS IMAGERY FOR VIIRS I2 AND M9 CHANNELS OVER COFFEVILLE, KS SHOWS VALUE OF MASKING SURFACE FEATURES FOR MANUAL INTERPRETATION OF THIN CIRRUS. ..... 165
FIGURE 5.27. AVIRIS IMAGERY FOR VIIRS I1 AND M9 CHANNELS OVER TEXAS GULF COAST REVEALS THAT LOW-LEVEL WATER CLOUDS ARE MASKED IN 1.38 μM IMAGERY. ..... 166
FIGURE 6.1. COLOR COMPOSITE TO EMPHASIZE VEGETATED LAND SURFACES CREATED BY ASSIGNING 0.64 μM BAND ASSIGNED TO RED AND GREEN GUNS OF CRT AND 0.865 μM ALBEDO BAND ASSIGNED TO BLUE GUN. ..... 168
FIGURE 6.2. PLACING THE 12.0 μM CHANNEL IN THE BLUE GUN OF FIGURE 6.1 PROVIDES VALUABLE DATA ON CLOUD TOP TEMPERATURES NEEDED FOR CLOUD TYPING. WARM, LOW LEVEL WATER CLOUDS APPEAR YELLOW WHILE COLDER ICE CLOUDS ARE BLUE. ..... 169
FIGURE 6.3. REPLACING THE BAND IN THE RED GUN OF FIGURE 6.2 WITH THE 3.7 ALBEDO CHANNEL ALLOWS SNOW TO BE DIFFERENTIATED FROM LOWER-LEVEL WATER CLOUDS, THIN CIRRUS, AND THICKER CIRRUS WHILE MAINTAINING INFORMATION ON CLOUD TOP TEMPERATURES AND VEGETATED LAND SURFACES (RED = 3.7 μM ALBEDO, GREEN = 0.865 μM, BLUE = 12.0 μM). ..... 171
FIGURE 6.4. COLOR COMPOSITE RED = 0.64 μM BAND, GREEN = 0.64 μM BAND, BLUE = 3.7 μM ALBEDO BAND) FOR THE MANUAL DETECTION AND MAPPING OF SNOW THROUGH CIRRUS CLOUDY CONDITIONS (HUTCHISON AND LOCKE, 1997). ..... 173
FIGURE 6.5. COMPOSITE IMAGE (RED = 0.412 μM, GREEN = 0.865 μM, BLUE = 0.64 μM) FOR THE DETECTION CLOUDS OVER HIGHLY REFLECTIVE, ARID OR SEMI-ARID REGIONS. ..... 175
FIGURE 7.1. GRAY-SCALE MAS IMAGERY COLLECTED OVER THE NORTH SLOPE OF ALASKA DURING FLIGHT TRACK #01 ON JUNE 7, 1995. DATA SHOWN ARE THOSE MODIS AND VIIRS CHANNELS NEEDED TO INTERPRET CLOUD AND SURFACE FEATURES IN THE SCENE. ..... 179
FIGURE 7.2. COLOR COMPOSITE (RED = 0.645μM, GREEN = 0.845 μM, BLUE = 0.645 μM) SHOWS MOST OF THE SURFACE IS (GREEN) HIGHLY VEGETATED. ..... 180
FIGURE 7.3. COLOR COMPOSITE (RED = 0.645μM, GREEN = 0.845 μM, BLUE = 1.61 μM) SHOWS SNOW, ICE, AND GLACIATED CLOUDS AS YELLOW. NOTICE THE SMOOTH TEXTURE ASSOCIATED WITH CIRRUS CLOUDS. ..... 182
FIGURE 7.4. COLOR COMPOSITE (RED = 0.645 μM, GREEN = 1.88 μM, BLUE = 11.45 μM) PROVIDES VALUABLE INFORMATION FOR CLOUD TYPE, SURFACE, AND ATMOSPHERIC MOISTURE CLASSIFICATIONS. ..... 185
FIGURE 7.5. COLOR COMPOSITE (RED = 0.645 μM, GREEN = 0.865 μM, BLUE = 11.45 μM) PROVIDES USEFUL INFORMATION ON SURFACE FEATURES AND CLOUD TOP TEMPERATURES AND HEIGHTS. ..... 187

FIGURE 7.6. GRAY-SCALE IMAGERY COLLECTED OVER COLORADO DURING FLIGHT TRACK #26 OF THE MODIS AIRBORNE SIMULATOR ON JULY 5, 1995. DATA SHOWN ARE THOSE MODIS AND VIIRS CHANNELS NEEDED TO INTERPRET FEATURES IN THE SCENE. ....190
FIGURE 7.7. COLOR COMPOSITE (RED = 0.645μM, GREEN = 0.845 μM, BLUE = 0.645 μM) SHOWS MOST OF THE SURFACE IS NOT (GREEN) HIGHLY VEGETATED. ....191
FIGURE 7.8. COLOR COMPOSITE (RED = 0.645μM, GREEN = 0.845 μM, BLUE = 1.61 μM) SHOWS SNOW, ICE, AND GLACIATED (OPTICALLY-THIN) CLOUDS AS YELLOW. THICKER CLOUDS REMAIN WHITE. ....193
FIGURE 7.9. COLOR COMPOSITE (RED = 0.645 μM, GREEN = 1.88 μM, BLUE = 11.45 μM) PROVIDES INFORMATION ON CLOUD TYPE, SURFACE, AND ATMOSPHERIC MOISTURE CLASSIFICATIONS. ....195
FIGURE 7.10. COLOR COMPOSITE (RED = 0.645 μM, GREEN = 0.865 μM, BLUE = 11.45 μM) PROVIDES USEFUL INFORMATION ON SURFACE FEATURES AND CLOUD TOP TEMPERATURES AND HEIGHTS. ....198
FIGURE 8.1 OVERVIEW OF AN APPROACH TO RETRIEVING 3-DIMENSIONAL CLOUD FIELDS FROM SATELLITE DATA (HUTCHISON, 2002). ....203
FIGURE 8.2 BI-SPECTRAL REFLECTANCES RATIO (BSRR) IN THE FORWARD AND NON-FORWARD SCATTERING DIRECTIONS FOR OPTICALLY-THICK CLOUDS (▲)AND CLOUD–FREE PIXELS (+) OVER OCEAN SURFACES AS A FUNCTIONS OF COSINE SOLAR ZENITH ANGLE (FROM HUTCHISON AND HARDY, 1995). ....206
FIGURE 8.3 BRIGHTNESS TEMPERATURE DIFFERENCES (BTD) BETWEEN NIGHTTIME 3.7 μM MINUS 11.0 μM FOR THIN CIRRUS CLOUDS (▲) AND CLOUD CLOUD–FREE PIXELS (+) ARE SHOWN IN THE LEFT PANEL AS A FUNCTION OF TOTAL ATMOSPHERIC WATER CONTENT. IN THE RIGHT PANEL, 11.0 μM MINUS 3.7 μM BTDS ARE SHOWN FOR STRATUS CLOUDS (▲) AND CLOUD-FREE (+) PIXELS IN NIGHTTIME AVHRR IMAGERY (FROM HUTCHISON AND HARDY, 1995). ....206
FIGURE 8.4 CLOUD PHASE CLASSIFICATION FROM THE FUSION OF SPECTRAL SIGNATURES IN AVHRR IMAGERY AND CLOUD TOP PRESSURES FROM CO2 SLICING OF HIGH RESOLUTION IR SOUNDER DATA. (FROM HUTCHISON ET AL., 1997A) S & K = SAUNDERS AND KRIEBEL (1988); BSRR = BISPECTRAL REFLECTANCE RATIO ....209
FIGURE 8.5 ANALYSIS OF CLOUD PHASE CLASSES FROM GLOBAL TERRA MODIS DATA USING CURRENT MODIS ALGORITHM (MENZEL ET AL., 2002). ....210
FIGURE 8.6 ANALYSIS OF CLOUD PHASE CLASSES FROM GLOBAL TERRA MODIS DATA USING PAVOLINIS AND HEIDINGER ALGORITHM (PAVOLINIS AND HEIDINGER 2003). ....211
FIGURE 8.7. ARCHITECTURE FOR THE RETRIEVAL OF WATER CLOUD MICROPHYSICAL PROPERTIES DURING DAYTIME AND NIGHTTIME CONDITIONS. CTT = CLOUD TOP TEMPERATURE (OU ET AL., 2002) ....214
FIGURE 8.8. OVERVIEW OF THE WATER CLOUD SOLAR RETRIEVAL ALGORITHM. $A_G(\Lambda)$ = SURFACE ALBEDO FOR WAVELENGTH Λ (OU ET AL., 2002) ....215
FIGURE 8.9. SUN SATELLITE GEOMETRY. (OU ET AL., 2002) ....215
FIGURE 8.10. THEORETICAL RELATIONSHIP BETWEEN THE REFLECTION FUNCTION AT 0.664 μM AND (A) 1.621 μM AND (B) 2.142 μM FOR VARIOUS VALUES OF $\tau_C$ (AT 0.664 μM) AND $R_E$ WHEN $\theta_0$ =26°, θ = 40° AND ϕ = 42°. (KING ET AL., 1997) ....216
FIGURE 8.11. ARCHITECTURE FOR THE RETRIEVAL OF ICE CLOUD MICROPHYSICAL PROPERTIES FROM VIIRS DATA DURING DAYTIME CONDITIONS AND VIIRS DATA DURING NIGHTTIME. $T_C$, AND $D_E$ ARE CLOUD TOP TEMPERATURE AND ICE CRYSTAL DIAMETER (FIGURE 4.11 FROM OU ET AL., 2002). ....218
FIGURE 8.12 PROCESSING SEQUENCE FOR RETRIEVAL OF ICE CLOUD OPTICAL PROPERTIES IN DAYTIME CONDITIONS. ....219
FIGURE 8.13 PROCESSING SEQUENCE FOR RETRIEVAL OF ICE CLOUD OPTICAL PROPERTIES IN NIGHTTIME CONDITIONS. ....221
FIGURE 8.14 GEOMETRY FOR RETRIEVAL OF CLOUD BASE HEIGHT USING CLOUD TOP HEIGHT ALONG WITH CLOUD OPTICAL PROPERTIES THE OBTAIN CLOUD THICKNESS (HUTCHISON, 2002). ....223

**Page xiii: [8] Deleted** **keithh** **11/27/2004 12:38:00 PM**

Meteorological satellites have been flown in near-Earth orbit since the launch of Television and Infrared (IR) Observing System (TIROS)-1 by the National Aeronautics and Space Administration (NASA) of the United States (US) in 1960. In the mid-1960s, the US Department of Defense (Do

**Page xiii: [9] Deleted** **keithh** **11/27/2004 12:19:00 PM**

D) launched its first meteorological satellite under the Defense Meteorological Satellite Program (DMSP). These early satellite sensors collected data in only one broadband visible and one broadband IR channel, e.g. 0.5-1.0 and 10-12 μm regions of the electromagnetic spectrum. Early applications of these data included their use in automated cloud models at the US Air Force Weather Central and the manual interpretation of meteorological conditions by weather forecasters around the globe. A satellite meteorological handbook was developed as the first significant attempt to document the manual interpretation of clouds and weather patterns in satellite imagery (Dickenson, et al., 1974; Brandli, 1976). Several cloud detection problems associated with these early satellites sensors included the automated and manual detection of stratus in nighttime imagery, differentiation between snow and clouds in daytime imagery, and the automated detection of thin cirrus clouds in daytime and nighttime imagery.

The Advanced Very High Resolution Radiometer (AVHRR) was the first truly operational cloud imaging instrument to be flown on a polar-orbiting meteorological satellite. The first AVHRR was carried on the experimental TIROS-N spacecraft in 1978 and it then became an operational system when flown on the National Oceanographic and Atmospheric Administration (NOAA)-6 spacecraft in 1979. In addition to providing imagery of clouds and the development of weather systems in the visible and near-infrared wavelength ranges, the AVHRR was also designed to provide improved data for sea surface temperature analyses. NOAA scientists postulated that these sea surface temperature analyses could be analyzed with a 1.0 K accuracy using improved atmospheric corrections made possible by viewing the ocean at two separate IR wavelengths.

Many years after the launch of the NOAA-7 in 1981, which carried the first 5-channel AVHRR instrument, scientists continue to find new applications for the data from this instrument. In addition, the US Air Force pioneered the use of meteorological satellite data in the analysis of tropical storms and hurricanes with the higher resolution data collected by the DMSP Operational Line Scan (OLS) system. In 1994 there was a Presidential Decision Directive in the US to combine the DMSP and NOAA polar-orbiting meteorological satellite systems into a single system, the (US) National Polar-orbiting Operational Environmental Satellite System (NPOESS). The NPOESS Integrated Program Office (IPO), consisting of personnel from NOAA, Do

**Page xiii: [10] Deleted** **keithh** **11/27/2004 12:28:00 PM**

D and NASA, was created to develop, acquire, and operate this next generation of US polar-orbiting meteorological satellites.

In the meantime, EUMETSAT, the European organization which has a long track record in operating geostationary meteorological satellites, had begun planning MetOp, a Meteorological Operational series of polar-orbiting spacecraft similar to the US NOAA spacecraft. In 1998 a cooperation agreement was signed with the objective of joining the space segment of the emerging MetOp programme with the NPOESS program to form a fully coordinated service, thus sharing the costs between the US and Europe.

The electro-optical imagery knows as the Visible/Infrared Imager/Radiometer Suite (VIIRS) has been specifically designed to meet a subset of the totality of user requirements defined by NPOESS. The first VIIRS instrument is scheduled to fly on the NASA NPOESS Preparatory Project (NPP) in 2006 and further VIIRS instruments are planned to be flown on all the spacecraft of the NPOESS program. VIIRS will collect data in 22 spectral bands in the visible, near-IR, mid-IR, and long-wave IR regions of the electromagnetic spectrum. Its heritage is from the NASA MODerate-resolution Imaging Spectroradiometer (MODIS), the Sea-viewing Wide Field-of-view Sensor (SeaWiFS), AVHRR and the DMSP OLS instrument

**Page xiii: [11] Deleted** keithh 11/27/2004 12:35:00 PM

s.

In recent decades, there has been an ever-increasing wealth of information collected by meteorological satellites that carry mult

**Page xiii: [12] Deleted** keithh 11/27/2004 12:01:00 PM

ispectral sensors to view the Earth-atmosphere system in a large number of discrete wavelengths. However, no single reference has been written to introduce users of these data to the next generation instrument or help those new in the field to exploit more fully these data once they become available. It is hoped that this text will serve as a useful guide for the VIIRS sensor and the interpretation of VIIRS heritage imagery, especially for those interested in cloud detection and cloud typing under global conditions.

**Page xiii: [13] Formatted** keithh 11/27/2004 1:08:00 PM

Font: (Default) Times New Roman

**Page xiii: [14] Formatted** keithh 11/27/2004 1:10:00 PM

Font: (Default) Times New Roman

**Page xiii: [15] Formatted** keithh 11/27/2004 1:10:00 PM

Font: (Default) Times New Roman

**Page xiii: [16] Deleted** keithh 11/27/2004 1:10:00 PM

providing the funding used to prepare the original manuscript that forms the core segment of this book and to